Methods Development and Validation for Large Scale Simulations of Dense Particulate Flow Systems in CFD-DEM Framework

Husam A. Elghannay

Dissertation submitted to the faculty of the Virginia Polytechnic Institute and State University in partial fulfillment of the requirements for the degree of

Doctor of Philosophy

In

Mechanical Engineering

Danesh K. Tafti, Chair

Francine Battaglia

Mark R. Paul

Rui Qiao

Saad A. Ragab

Madhava Syamlal

February 26, 2018

Blacksburg, Virginia, USA

Keywords: CFD-DEM, Simulation of Particulate Flow Systems, Sediment Transport, Representative Particle Model, History Force Modeling, Time Driven Hard Sphere

Copyright 2018, Husam A. Elghannay

Methods Development and Validation for Large Scale Simulations of Dense Particulate Flow Systems in CFD-DEM Framework

Husam A. Elghannay

ABSTRACT

Computational Fluid Dynamics Coupled to Discrete Element Method (CFD-DEM) is widely used in simulating a large variety of particulate flow system. This Eulerian-Lagrangian technique tracks all the particles included in the system by the application of point mass models in their equation of motion. CFD-DEM is a more accurate (and more expensive) technique compared to an Eulerian-Eulerian representation. Compared to Particle Resolved Simulations (PRS), CFD-DEM is less expensive since it does not require resolving the flow around each particles and thus can be applied to larger scale systems. Nevertheless, simulating industrial and natural scale systems is a challenge for this numerical technique. This is because the cost of CFD-DEM is proportional to the number of particles in the system under consideration. Thus, massively parallel codes are used to tackle these problems with the help of supercomputers.

In this thesis, the CFD-DEM capability in the in-house code Generalized Incompressible Direct and Large Eddy Simulation of Turbulence (GenIDLEST) is used to investigate large scale dense particulate flow systems. Central to the contributions made by this work are developments to reduce the computational cost of CFD-DEM. This includes the development and validation of reduced order history force model for use in large scale systems and validation of the representative particle model, which lumps multiple particles into one, thus reducing the number of particles that need to be tracked in the system. Numerical difficulties in the form of long integration times and instabilities encountered in fully coupling the fluid and particle phases in highly energetic systems are alleviated by proposing a partial coupling scheme which maintains the accuracy of full-

coupling to a large extent but at a reduced computational cost. The proposed partial-coupling is found to have a better convergence behavior compared to the full coupling in large systems and can be used in cases where full coupling is not feasible or impractical to use. Alternative modeling approaches for the tangential treatment of the soft-sphere impact model to avoid storing individual impact deformation are proposed and tested. A time advancement technique is developed and proposed for use in dense particulate systems with a hard-sphere impact model. The new advancement technique allows for the use of larger time steps which can speed-up the time to solution by as much as an order of magnitude.

Methods Development and Validation for Large Scale Simulations of Dense Particulate Flow Systems in CFD-DEM Framework

Husam A. Elghannay

GENERAL AUDIENCE ABSTRACT

Computational Fluid Dynamics Coupled to Discrete Element Method (CFD-DEM) is widely used in simulating a large variety of particulate flow system. Nevertheless, simulating industrial and natural scale systems is a challenge for this numerical technique. This is because the cost of CFD-DEM is proportional to the number of particles in the system under consideration. The current work aims to provide alternative efficient models that can reduce the computational requirement of CFD-DEM. This includes reducing the computational time to run the calculation, reducing the memory requirement, or providing an alternative method to get reasonably accurate predictions when the proper implementation fails to converge.

Different elements of CFD-DEM were targeted in the current work. The testing and validation work covered different applications and ranged over wide operation conditions. Comparisons with available experimental and numerical work was conducted to evaluate the suggested methods. Good to reasonable agreement was achieved with the suggested models and treatments. Savings in calculation time and resources varies depending on what elements/models are being used. A significant reduction of the calculation time and memory resources was achieved with the use of a reduced order force model. The savings in computational time and memory resources opens the door for using the proposed models in applications with large dense systems of particles where other models become impractical to use.

Dedication

Dedicated to my parents, family, and all of those who have ever wished me success

Acknowledgments

I would like to express my gratitude to my advisor, Professor Danesh Tafti, for his trust, support and guidance during my PhD journey. His immense knowledge, enthusiasm, experience and vision helped me in directing and shaping my research. I am also grateful to all of my committee members, Professor Francine Battaglia, Professor Mark Paul, Professor Rui Qiao, Professor Saad Ragab, and Dr. Madhava Syamlal, for their interest in my research and for the privilege granted to me by their participation in my educational process.

I am indebted to my parents, no words can express my gratitude for their sacrifice, endless love and support. Their presence is always felt by me in spite of the distance between us. I owe my success to them. I wish to acknowledge all of my teachers and mentors since my early educational stages, it is the knowledge and values that they imparted to me that made me who I am today. Special thanks to my loving and supportive wife, Huda, who continuously and patiently took care of my environment, myself, and our kids. To all my beloved siblings, relatives and friends I provide my heart-felt gratitude for their encouragement and unlimited support.

The research in this thesis benefited from the brilliant feedback and suggestions from the many remarkable individuals whom I interacted with during my stay in the High-Performance CFD-lab. I am particularly grateful to the assistance given by Dr. Surya Deb, in helping me learn the specifics of CFD-DEM capability. He along with Drs. Nagendra Krishnamurthy and Amit Amrikar helped me going through the challenging initial stage of learning how to use, edit and debug the powerful in-house code that I used.

I am appreciative to The Libyan Ministry of Higher Education for granting me a full scholarship to pursue my PhD studies in Virginia Tech. I am also grateful to the Mechanical Engineering at Virginia Tech for awarding me a one year Hord fellowship. I would like to acknowledge the use of the large computational resources provided by The Advanced Research Computing at Virginia Tech. I would also like to extend my thanks to the Information Technology and help desk personnel's at the Mechanical Engineering Department at Virginia Tech for their skillful handling of technical difficulties. Special appreciation to James Archual and Ben Boe for being around and handling technical problems swiftly.

Table of Contents

ABSTRACT ..... **ii**

GENERAL AUDIENCE ABSTRACT ..... **iv**

Dedication ..... **v**

Acknowledgments ..... **vi**

Table of Contents ..... **vii**

List of Figures ..... **xiii**

Preface ..... **xxiv**

Chapter 1 ..... **1**

Introduction **1**

Chapter 2 ..... **8**

DEM Predictions of NETL Small Scale Challenge Problem **8**

2.1 Abstract 9

2.2 Introduction 9

2.3 Experiment (problem Setup) 10

2.3.1 Facility description 10

2.3.2 Operation conditions 12

2.4 Numerical Technique 12

2.4.1 Governing equations 12

2.4.2 Algorithm overview 14

2.4.3 Simulation parameters 14
2.5 Results and Discussions 15
2.5.1 Pressure results 16
2.5.2 Velocity results 21
2.6 Conclusions 26
2.7 Nomenclatures 27
Chapter 3 28
Development and Validation of a Reduced Order History force Model 28
3.1 Abstract 29
3.2 Introduction 29
3.3 Numerical Method 31
3.3.1 Gravity force 32
3.3.2 Drag force 32
3.3.3 Added mass 33
3.3.4 Fluid-stress force 33
3.3.5 History force 34
3.4 Mathematical Formulation 35
3.4.1 Concept of decay function 36
3.4.2 Model formulation 38
3.5 Validation with Experiment 41
3.5.1 Settling spheres 42
3.5.2 Oscillating sphere 48
3.5.3 Bouncing spheres 52
3.6 Computational resources 55
3.7 Summary and Conclusions 57

Chapter 4 ..... **59**

LES-DEM Simulations of Sediment Transport **59**

4.1 Abstract 60

4.2 Introduction 60

4.3 Governing Equations and Mathematical Formulation 65

4.3.1 Fluid equations 65

4.3.2 Particle dynamical equation 67

4.3.3 Dual-grid formulation 70

4.3.4 Representative particle model 71

4.4 Simulation Details 73

4.5 Results and Discussion 79

4.5.1 Effect of coupling strategy 79

4.5.2 Effect of coarse graining 83

4.5.3 Entrainment of particles 87

4.6 Conclusions 90

Chapter 5 ..... **92**

Sensitivity of Numerical Parameters on DEM Predictions of Sediment Transport **92**

5.1 Abstract 93

5.2 Introduction 93

5.3 Governing equations 96

5.4 Simulation Details 98

5.5 Results 103

5.6 Conclusions 110

5.7 Nomenclature 111

Chapter 6 113

Revised Partial Coupling for Dense Fluid-Particulate Systems 113

6.1 Abstract 114

6.2 Introduction 114

6.3 Mathematical Formulation 118

6.3.1 Particle dynamical equation 118

6.3.2 Fluid equations 119

6.3.3 Base and revised partial coupling 120

6.4 Simulation Details and Results 121

6.4.1 Bubbling fluidized bed 121

6.4.2 Sediment transport in turbulent open channel 126

6.4.3 Convergence and stability of calculations 130

6.4.4 Speed-up of calculations 131

6.5 Conclusions 132

Chapter 7 134

Alternate Tangential Impact Treatment for the Soft-Sphere Collision Model 134

7.1 Abstract 135

7.2 Introduction 135

7.3 Mathematical Formulation 137

7.3.1 Particle Dynamical Equation 137

7.3.2 Collision Mechanics 137

7.4 Model Predictions 141

7.4.1 Model comparison and particle level validation 141

7.4.2 Proper implementation of the tangential linear soft sphere model 150

7.4.3 Alternate formulation 155
7.4.4 Validation on inelastic impacts 159
7.5 Conclusions 163
Chapter 8 164
Comparison of a Physics Based Hard-sphere Model with the Soft Sphere Model 164
8.1 Abstract 165
8.2 Introduction 165
8.3 Governing Equations and Mathematical Formulation 168
8.3.1 Fluid Equations 168
8.3.2 Particle Dynamical Equation 169
8.3.3 Soft Sphere Model 171
8.3.4 Hard Sphere Impulse Based Model 172
8.4 Results 177
8.4.1 Evaluation of Relocation Technique 178
8.4.2 Bubbling fluidized bed 186
8.4.3 Transport and deposition of micron sized sand particles in a ribbed duct 192
8.5 Summary and Conclusions 202
Chapter 9 203
Summary and Conclusions 203
References 210
Appendix A 223
On the Improvement of CFD-DEM Coarse Graining Predictions 223
Abstract 224

Nomenclature 224
Introduction 226
Materials and Methods 228
Results 234
Conclusions 250
Appendix B 252
Evaluation of Coarse Graining DEM Using Representative Particle Model 252
Abstract 253
Introduction 253
Mathematical Formulation 254
Governing Equations 254
Representative Particle Model 255
Simulation Details and Results 256
Unidirectional Flow Channel 256
Pseudo-3D Fluidized bed 258
Discussions and Conclusions 260

List of Figures

Figure 2. 1. SSCP-I test unit and measurement locations. 11

Figure 2. 2. Comparison between measured and simulated time series of pressure drop between first and second pressure ports above the distributor a) U=2.19 m/s, b) U=3.28 m/s, U=4.38 m/s. 16

Figure 2. 3. Comparison between measured and simulated data for a) mean and b) rms pressure drop 0.0413 to 0.3461 above the distributor. 17

Figure 2. 4. Simulation results of average void fraction across the bed for the three cases. 18

Figure 2. 5. Snap shots showing flow structures for the three cases. 20

Figure 2. 6. Comparison between measurement and simulation of averaged vertical velocity at measurement location across width of the bed. 21

Figure 2. 7. Comparison between measurement and simulation of averaged horizontal velocity at PIV windows. 23

Figure 2. 8. Mean solids velocity vectors for the first 60 cm of the bed. Horizontal lines show vertical extent of measurement window. 23

Figure 2. 9. Comparison between measurement and simulation of vertical velocity rms at PIV windows. 24

Figure 2. 10. Comparison between measurement and simulation of horizontal velocity rms at PIV window. 24

Figure 2. 11. Comparison between measurement and simulation vertical velocity skewness at PIV windows. 25

Figure 2. 12. Comparison between measurement and simulation horizontal velocity skewness at PIV windows. 25

Figure 2. 13. Comparison between measurement and simulation; kurtosis of vertical velocity at PIV windows. 25

Figure 2. 14. Comparison between measurement and simulation; kurtosis of horizontal velocity at PIV windows. 25

Figure 3. 1. Integration kernel of the history force at different Reynolds numbers. 39

Figure 3. 2. Flow chart of current model. 40

Figure 3. 3. Decay function vs. proposed fit functions. 41

Figure 3. 4. Comparison of experiment with current model at constant density ratio (~3.7) and different Reynolds numbers. 44

Figure 3. 5. Comparison of experiment with current model at constant density ratio (~2.47) and different Reynolds numbers. 45

Figure 3. 6. Comparison of experiment with current model at constant density ratio (~1.16) and different (low) Reynolds numbers. 46

Figure 3. 7. Comparison of experiment with current model at same Reynolds numbers $Re_{p,term}$~30 and different density ratio. 47

Figure 3. 8. Comparison of current model with Mordant & Pinton data. 48

Figure 3. 9. Measured vs. calculated force on oscillating sphere at different amplitudes and frequencies. 51

Figure 3. 10. Rebound trajectories for spheres at different Reynolds numbers and constant density ratio (S~8). 53

Figure 3. 11. Rebound trajectories for spheres at different density ratios and the same impact Reynolds number ($Re_{p,impact}$ ~100)..... 54

Figure 3. 12. Comparison of CPU time required to calculate the history time..... 56

Figure 4. 1. Schematic of the soft-sphere collision model..... 68

Figure 4. 2. Simulation domain of unidirectional turbulent channel flow test cases. Particles are colorized using their streamwise velocity with respect to the friction velocity (Case 1). 74

Figure 4. 3. Transport regime for the selected cases: Bagnold (1966), van Rijn (1984), and Shields (from Brownlie, 1982). 78

Figure 4. 4. Evolution of flowrate and sediment flux for τ^*~ 1.34 case (i.e., Case 9). 79

Figure 4. 5. Comparison of sediment transport rate results (MPM refers to the Meyer-Peter and Muller (1948) bedload formula, Engelund-Hansen refers to the Engelund and Hansen (1967) total load formula)..... 80

Figure 4. 6. Friction factor, C_f, vs. normalized shear velocity. The dashed line approximates the friction factor for a fixed rough wall..... 82

Figure 4. 7. Comparison of friction factor results when using an equal number of particles in both regimes using the RP Model. 84

Figure 4. 8. Domain averaged sediment properties for bedload simulations, left; solid fraction of particles, right; solids velocity. 86

Figure 4. 9. Domain averaged sediment properties for suspended-load simulations, left; volume fraction of particles, right; solids velocity. 86

Figure 4. 10. Instantaneous particles stream wise velocity and fluid fluctuations for τ^*~ 0.021.. 88

Figure 4. 11. Quadrant analysis of the flow signal above the bed for τ^*~ 0.021. 89

Figure 5. 1. Computational Domain (flow is in the positive x-direction), particles (shown to scale) are colorized with respect to their velocity normalized by the friction velocity. 99

Figure 5. 2. Location of the computational experiments on the Shields diagram (red line shows Brownlie's fit (1982)) along with criteria for the transition to suspended flow by van Rijn (1984) and Bagnold (1966). Arrows show the selected cases for the sensitivity. 102

Figure 5. 3. Effect of changing numerical parameters on a) mean flow velocity and b) particle flux for τ^*~0.021. 105

Figure 5. 4. Effect of changing numerical parameters on a) flowrate and b) particle flux for τ^*~0.288 (legend as indicated in Figure 5.3.a). 106

Figure 5. 5. Effect of changing numerical parameters on a) flowrate and b) particle flux for τ^*~1.56 (legend as indicated in Figure 5.3.a). 107

Figure 5. 6. Non-dimensional sediment transport vs. Shields parameter for selected numerical experiments. 108

Figure 6. 1. Comparison of domain averaged particles velocity for the different coupling approaches. 123

Figure 6. 2. Comparison of averaged void fraction (top) and solids velocity (bottom) for (a) fully coupled simulation, (b) base partial coupling, and (c) revised partial coupling. 123

Figure 6. 3. Comparison of averaged interstitial fluid velocity for fully coupled simulation (left), base partial coupling (middle) and revised partial coupling (right). 124

Figure 6. 4. Comparison of averaged interstitial fluid velocity for fully coupled simulation (left), averaged projected interstitial velocity of the revised partial coupling (middle) and the difference between the two (right). 125

Figure 6. 5. Pressure drop signal of the bubbling fluidized bed at the last 5s of simulations using different coupling methods. 126
Figure 6. 6. Calculation domain for the turbulent open channel flow. 127
Figure 6. 7. Temporal evolution of *(a)* friction coefficient (C_f) and *(b)* particle flux for case-3 (τ^*~1.56)..... 130
Figure 6. 8. Sample of convergence for successive 25 time step for the sediment transport simulation (τ^*~1.56) for a strict convergence criterion using full coupling and revised partial coupling..... 131
Figure 7. 1. Schematic diagram of soft-sphere collision model (left) and coordinate system (right). 139
Figure 7. 2. Comparison of current model with experimental results of an elastic oblique impact. 143
Figure 7. 3. Comparison between tangential force trends for the three models at different impact angles (a) 4 degrees, (b) 10 degrees, (c) 20 degrees, (d) 50 degrees. 145
Figure 7. 4. Variation of tangential displacement and the slip velocity during an elastic oblique impact at different angles. 146
Figure 7. 5. Initial (left) and final (right) condition of sphere travelling on wall experiment in absence of rolling friction. 147
Figure 7. 6. Dynamics of a 10 mm sphere moving on a flat plate without rolling friction and sliding friction factor of 0.7. Top: Model-A, Middle: Model-B, Bottom: Model-C. 149
Figure 7. 7. Comparison of the tangential force for particle on wall experiment for the three models. The transition region is exaggerated on right plot for models B and C. 150

Figure 7. 8. Non-dimensional time to reach pure rolling condition for sphere traveling on a flat plate experiment. 150
Figure 7. 9. Comparison of model-A and Model-AA with other models and experimental data of an elastic oblique impact. 153
Figure 7. 10. Comparison between tangential force trends of Model-A and Model-AA at impact angles (a) 10 degrees, (b) 20 degrees. 154
Figure 7. 11. Dynamics of a 10 mm sphere moving on a flat plate using model-AA (left), close up of the slip velocity as it reaches rolling condition is shown on right plot. 155
Figure 7. 12. Performance of the proposed surrogate tangential soft-sphere models on oblique impact results (a) tangential COR, and (b) rebound angular velocity. 159
Figure 7. 13. Comparison of the tangential COR (left) and rebound rotational speed (right) for inelastic impact with no initial spin. 161
Figure 7. 14. Comparison of results of inelastic oblique impact with initial spin. a) tangential COR b) rebound rotational speed. 162
Figure 8. 1. Schematic drawing of the soft-sphere impact model. 172
Figure 8. 2. Hard sphere collision model implementation. (a) ghost particles and internal particles on a processor. (b) Collisions only with ghost particles (c) Collisions only with internal particles. 176
Figure 8. 3. Algorithmic elements of hard sphere model implementation. 177
Figure 8. 4. Stack of 10 particles in under the influence of gravity. 178
Figure 8. 5. Pattern of velocity track at different COR for a stack of ten particles placed on top of each other. 180
Figure 8. 6. Exaggerated view of the velocity fluctuations for selected cases. 181

Figure 8. 7. Position of the topmost particles from the initial condition for different coefficients of restitutions (Exaggerated view on bottom figure). 183
Figure 8. 8. Effect of time step on the velocity and position of the top most particle in a fully dissipative system a) non-dimensional velocity, b) total overlap of the particles stack. 184
Figure 8. 9. Initial position of particles in 3D settling bed test. 186
Figure 8. 10. Vertical location of center of gravity of a settling bed of particles 186
Figure 8. 11. Comparison between averaged void friction (top) and solids velocity (bottom) between *(a)* soft-sphere with COR=0.98 using Δt of ~5μs (b) hard sphere with COR=0.98 using Δt of ~5μs, (c) hard sphere with variable COR using Δt of ~5μs, and (d) hard sphere with variable COR using Δt of ~125μs 188
Figure 8. 12. Comparison between averaged void fraction (ε) at 16.4 mm (left) and 32.2 mm (right) above the distributor. 189
Figure 8. 13. Comparison of averaged solids velocity at a) 15 b), 25 and c) 35 mm above the distributor. Legends are the same as Figure 8.12. 190
Figure 8. 14. Comparison of the variation of COR of particle-wall impact for the hard sphere and soft sphere simulations. 191
Figure 8. 15. Comparison between averaged void fraction (top) and solid velocity (bottom) of hard-sphere (left) and soft-sphere (right). Simulations are run on two processors with periodicity in the z-direction. 192
Figure 8. 16. Computational domain for periodic ribbed duct. 195
Figure 8. 17. Cross sectional view shows the averaged flow velocity in the domain. 195
Figure 8. 18. Comparison between mean flow stream turbulent intensity at different locations with experimental data. 196

Figure 8. 19. Instantaneous particle location in the middle 50% of the duct at times 8.8 ms, 26.5 ms, and 44.1 ms (left to right) after the injection of the particles for 1 μm (top), and 20 μm (bottom). 199

Figure 8. 20. Instantaneous plan view of the location of particles between rib height and wall at times 8.8 ms, 26.5 ms, and 44.1 ms (left to right) after the injection of the particles for 1 μm (top), and 20 μm (bottom). 199

Figure 8. 21. Formation of particle agglomerates with exposure time for 20 μm particles. 200

Figure 8. 22. Representative normal restitution coefficients of particle-wall impacts for 1 μm and 20 μm particles..... 201

Figure A. 1. Unscaled system of spheres (left) lumped in one representative sphere (right) moving with average velocity. 231

Figure A. 2. Averaged voidage (top) and solids velocity (bottom) for unscaled simulation (right), RP model (l=2; middle) and (l=3; left). 236

Figure A. 3. Comparison of average void fraction at 16.4 mm above the distributor (left) and 31.2 mm above the distributor (right). 237

Figure A. 4. The periodic fluidized bed system. 239

Figure A. 5. Time series of vertical particle flux for decoupled ideal and real systems for both unscaled and scaled simulation. 240

Figure A. 6. Comparison between average void fraction and solids velocity for both ideal and dissipative spheres. 241

Figure A. 7. Results from extrapolation of particle velocity and random walks concepts. 245

Figure A. 8. Calculations domain for Sakai simulation. 247

Figure A. 9. Kriging and co-kriging for pressure drop (left) and bed height (right) for a pseudo-2D fluidized bed..... 248
Figure A. 10. Simulation domain of unidirectional flow simulation. 249
Figure A. 11. Kriging and co-kriging models for sediment transport (left) and friction factor (right) of a psudo-2D fluidized bed. 249
Figure B. 1. Simulation domain for unidirectional open channel flow simulation..... 257
Figure B. 2. Comparison between scaled and unscaled simulations for open channel simulation: a) sediment transport and b) friction factor. 258
Figure B. 3. Calculations domain for psudu-3D fluidized bed case. 259
Figure B. 4. Code-to-code comparisons to Pseudo-3D fluidized bed simulation at different scaling factors: a) bed height, b) pressure drop. 260

List of Tables

Table 2. 1. Numerical parameter used in the simulation. 15

Table 3. 1. Sphere and fluid properties for the selected settling sphere experiments. 43

Table 3. 2. Experimental parameters for oscillating sphere experiments. 49

Table 3. 3. Sphere and fluid properties for the selected bouncing sphere experiments*. 53

Table 4. 1. Simulation parameters for the different test cases. 74

Table 4. 2. Comparison of baseline grid results with finer grid results for most energetic suspended-load simulation. 76

Table 4. 3. Numerical parameters of particles. 77

Table 4. 4. Quantitative analysis of particle movement and fluid signal. 90

Table 5. 1. Simulation parameters for different cases. 100

Table 5. 2. Comparison of baseline grid results with fine grid results for most energetic suspended load simulation using partial coupling. 101

Table 5. 3. Numerical parameters used in the reference calculation. 102

Table 5. 4. Mean base-calculation parameters with standard deviation for 10 s averaging period. 104

Table 5. 5. Deviations in sediment transport (q*) and mean flow velocity (ub) from base-value calculation with a change in one numerical parameters. 109

Table 6. 1. Simulation parameters used for Muller's experiment [170]. 121

Table 6. 2. Numerical parameters of particles. 127

Table 6. 3. Simulation conditions for the selected cases. 129

Table 6. 4. Mean friction factor (C_f) and sediment transport for the three selected cases. 129

Table 6. 5. Averaged performance for 2.5 seconds of real time for all considered simulations. 132

Table 7. 1. Simulation parameters for the oblique impact case. 142

Table 7. 2. Description of different elastic impact regimes. 157

Table 7. 3. Simulation parameters for the inelastic oblique impact case. 160

Table 8. 1. Simulation parameters used for 3D settlement of particles and fluidized bed simulations. 185

Table 8. 2. Materials properties used in the simulations 196

Table 8. 3. Simulation conditions for the periodic ribbed channel. 196

Table 8. 4. Number of impacts per 10 time steps as percentage of total number of injected particles. 200

Table A. 1. Simulation parameters used for Muller's simulation. 235

Table A. 2. Simulation parameters of the particles. 247

Table B. 1. Numerical parameters for open channel flow. 257

Table B. 2. Simulation parameters for psudu-3D fluidized bed case. 259

Preface

This dissertation is submitted for the degree of Doctor of Philosophy in Mechanical Engineering at Virginia Tech. The research described herein was conducted under the supervision of Professor Danesh K. Tafti between August 2012 and February 2018. The dissertation takes the Manuscript Format where every core chapter is either a published work or submitted for consideration of publication. The research is computational in nature where the in-house code GenIDLEST, developed by Dr. Tafti, was used in conducting all the numerical experiments. Dr. Danesh K. Tafti, as the primary advisor of Husam Elghannay provided scientific guidance and took part in reviewing and organization of all the chapters. Dr. Kuahai Yu, is the lead developer of the physics-based impact model described in Chapter-8, and took part in reviewing the manuscript.

Husam A. Elghannay

March 2018

Chapter 1
Introduction

Two-approaches are commonly used to study granular/particulate flows, namely the Eulerian-Eulerian description (or the two-fluid-model, TFM) and the Eulerian-Lagrangian approach. In TFM both the carrier and disperse phases are treated as two interpenetrating continuous phases while Newton's second law is used in the Eulerian-Lagrangian approach to solve the motion of individual particles. There are two paths that can be used in Eulerian-Lagrangian description, in one method the flow around each particle is resolved (Particle Resolved Simulations or PRS) and the fluid-particle forces can be calculated by integrating fluid forces on the particle surface. In the second approach, force models are used to account for the various fluid forces acting on the particle (point mass approach). When applied to dense particulate flow systems, this approach is known as Computational Fluid Dynamics Coupled to Discrete Element Method (CFD-DEM). CFD-DEM is widely used in simulating a large variety of particulate flow systems. This Eulerian-Lagrangian technique tracks all the particles in the system by the application of point mass models in their equation of motion. CFD-DEM is a more accurate (and more expensive) technique compared to Eulerian-Eulerian representation. Compared to PRS, CFD-DEM is less expensive since it does not require resolving the flow around each particle and thus can be applied to large scale flow systems. Nevertheless, simulating industrial and natural scale systems is a challenge for this numerical capability. This is because the cost of CFD-DEM is proportional to the number of particles in the system under consideration. Massively parallel codes are used to tackle these problems with the help of supercomputers.

In this work, the CFD-DEM capability in the in-house code Generalized Incompressible Direct and Large Eddy Simulation of Turbulence (GenIDLEST) is used to investigate large scale dense particulate flow systems. The existing implementation was first further ***validated in the small scale blind challenge problem*** [1]. The blind test was setup by National Energy and Technology Laboratory (NETL) to validate multiphase flow solvers. Good to reasonable agreement was

achieved by comparing different parameters of interest to the experimental measurements at various operating conditions.

Different numerical techniques that can reduce the cost of the calculation (time and/or memory requirements) are proposed and validated. Five different aspects of CFD-DEM formed the topics of the current research: reducing the cost of CFD-DEM by coarse graining or lumping particles together; development and validation of a history force model that is feasible to use in large scale systems; investigating the impact of reducing the inherent coupling between the disperse and continuous phases and improving the quality of prediction when the full coupling between the dispersed and continuous phases is compromised; development of alternative tangential impact models for the soft-sphere collision frame work that eliminate the need to store contact information for each interacting pair of particles; and development of a new advancement technique for time-driven hard-sphere based dense flow simulations.

Lumping particles in representative particles or clouds (known as coarse graining) can help in saving the computational time at the expense of some accuracy. ***Representative particle model*** (RPM) was implemented in the in-house code and code-to-code comparisons were made to validate the implementation. The numerical approach itself is developed by other researchers and attempts are made in the current work to validate its applicability to different systems and to identify and reduce sources of error that had an adverse impact on the quality of the predictions.

In many systems when the particle/fluid density ratio is not very large the history force can be significant and cannot be neglected. Typical calculation of this force requires storing and using the information of the particles throughout the whole simulation or at least store hundreds or thousands of previous/most-recent time steps. ***A reduced order model for the calculation of history force is developed and validated*** in this work for use in simulations where large number of particles are integrated over long times.

Energetic flow systems can show difficult convergence behavior (or fail to converge) which may require a reduction of the degree of coupling between the continuous and dispersed phases. This challenge was encountered in sediment transport simulations in turbulent open channel. The effects of full and reduced coupling, using representative particle model and ***sensitivity of the different numerical parameters*** were investigated. Results pertaining to sediment transport in different flow

regimes and channel roughness were compared to empirical formulas and published work that use reduced coupling. Moreover, insights into the behavior of channel friction factor and the role of turbulent structures on particle motion were gained. In light of these studies a modification of the reduced coupling was proposed and tested. The ***revised partial coupling*** showed improved predictions in different applications over the base reduced/partial coupling.

The soft-sphere impact model is typically used with DEM to resolve collisions. Resolving the contact mechanics in the tangential direction requires storing deformation information of each contact. Different forms of tangential impact treatment in the literature were found to perform differently for different particle-level experiments where the performance varied from being the same as the rigid body theory limit to totally erratic behavior. The reason of the unexpected deviation is discussed along with the proper implementation. Two different alternative treatments are suggested for use without the need to store contact information. The suggested methods are tested in particle-level experiments and found to provide good to reasonable agreement with experiments.

Lastly, a time driven advancement technique is proposed for use with hard sphere impact model for dense particle flow systems. The advancement technique along with the accompanying parallelization method are presented and tested. A physics-based impact model in which the coefficient of restitution is a function of the material properties and impact velocity is implemented and used in the current work. The current model and time integration technique were used in studying bubbling fluidized beds and the dispersion of particles in a ribbed channel and allowed for using reasonably large time steps which are not achievable with the soft sphere model.

Main contributions of the current work can be summarized as follows:

- Development and validation of a reduced order history force model: The calculation of the history force typically requires storing and using relative velocity information during the life time of the particle. For a large number of particles integrated over long times, history force calculation can become prohibitively expensive. The current work presents a new modeling approach to calculate the history force in which a decay function is applied to a stored cumulative value of the history force. The model shows very good agreement with the experiments of settling spheres and reasonable/good agreement with oscillating and

bouncing sphere experiments. The proposed model significantly reduces the computational resources required to calculate the history force especially when large number of particles need to be integrated over long times.

- Investigation of the effect of using reduced/partial coupling on the simulations of the sediment transport in open turbulent channel flow: In this work, a fully-coupled Computational Fluid Dynamics (CFD) model and Discrete Element Method (DEM) are used to simulate a unidirectional turbulent open-channel flow over the full range of sediment transport regimes. The fluid and particles are computed on separate grids using a dual-grid formulation to maintain consistency and avoid instability issues. The results of coupling the dispersed phase to a multiphase flow solver that uses volume-averaged Navier-Stokes equations are compared to those obtained from coupling through drag to a single phase flow solver. The simulation results of sediment transport from both coupling techniques show good agreement with empirical formulas in the bedload regime, but under-predict sediment transport in the suspended load regime. In the suspended load regime, using partial coupling, the rate of sediment transport was found to be under-predicted as compared to full-coupling. A sensitivity analysis was conducted and showed that the under-predicted sediment transport in the suspended load regime can be bridged by moderately decreasing the friction factor of the particles from 0.6 to 0.25. The impact of the same change in bed-load regime is not as significant. Both the coefficient of restitution and the particle stiffness show less significant to negligible impact as compared to the friction factor. Investigating the outcome of the difference between the full coupling and the base partial coupling motivated the development of a revised partial coupling. In the proposed revised particle coupling a modified fluid velocity is used in point force models to compensate for the omission of the void fraction in the fluid governing equations. The effectiveness of this method is demonstrated in a fluidized bed and in sediment transport simulations. In both cases it is shown that the use of the proposed method gives very good comparisons with the fully-coupled simulations while reducing the fluid calculation time by factors ranging from 1.35 to 4.35 depending on the flow conditions.
- Development of alternative tangential treatment for soft-sphere collision models: The contact mechanics in the normal and tangential directions is modelled by a spring, damper and dashpot system. The current work evaluates existing modelling strategies in the

tangential direction. Existing models require storing the cumulative tangential deformation during the course of the collision for each collision pair. The paper evaluates two existing tangential models (A and B) from the literature and develops alternative methods which do not require storing the tangential deformation (C and D). The models are tested for two canonical single particle experiments of oblique impacts on a surface and sliding particle on a surface. It is shown that neither of the two models A nor B validate with both the test cases. However, limiting the tangential deformation in model A validates both experiments. In Model C, the tangential displacement is approximated as the product of the characteristic time of collision with the instantaneous particle tangential velocity. In Model D, the instantaneous ratio of the tangential to normal impulse is used to characterize the impact according to Maw et al.'s [2] analysis. It is shown that both models give reasonably good predictions in the two test cases with the quality of predictions as good or better than Models A and B which require the storage of the tangential deformation.

- Comparison of physics based hard-sphere model with the soft sphere model. The application of a three dimensional physics-based hard-sphere impact model to many-particle systems is presented. The hard sphere model is used with conventional time-advancement which is not event driven. A particle relocation technique based on using both pre- and post-collision velocities is developed and validated. Also developed is a parallelization scheme which overcomes the inherent sequential nature of processing collisions with the hard sphere model. The relocation technique is tested in a one-dimensional stack of particles and in the three-dimensional settling of a bed of particles. The technique demonstrates its ability to prevent excessive overlaps and maintaining stable stacks of particles at coefficients of restitutions ranging from 0.0 to 0.98. The model is validated in a bubbling fluidized bed and shows no discernable differences with the soft sphere model but at a computational cost about 23 times less than that of the soft sphere model. The model is used to investigate particle agglomeration in a turbulent ribbed duct flow using LES for particles of size 1 μm and 20 μm. It was found that the 20 μm particles were more prone to agglomerate in regions of low velocity at the upstream and downstream corners of the rib-wall junction. The hard sphere model enabled time steps an order of magnitude larger than that permissible for the soft sphere model which resulted in speedups of up to 20 times.

The structure of the thesis is as follows, Chapter 2 presents the blind predictions of our in-house code GenIDLEST (Generalized Incompressible Direct Large Eddy Simulation for Turbulence) to the small scale challenge problem (SSCP-I) set by NETL (National Energy and Technology Lab.) of the DOE (Department of Energy) to provide additional validation for the CFD-DEM implementation. The development and validation of a reduced order history force model is presented in Chapter 3. The application of fully coupled CFD-DEM simulations to the sediment transport in a unidirectional open turbulent channel is presented in Chapter 4 with comparisons to empirical formulas and concluding remarks on the entrainment of particles. The sensitivity of different numerical parameters on the prediction of sediment transport is provided in Chapter 5. The outcomes of the revised partial coupling in different application and flow regimes is the topic of Chapter 6. Chapter 7 presents alternative tangential impact treatment for soft-sphere collision model. The application of a physics based hard sphere impact model to dense particulate flow systems and the introduction of a new time advancement technique for the hard sphere model is presented in Chapter 8. Finally, summary and concluding remarks are provided in Chapter 9.

Validation and evaluation of the implementation of coarse graining method using the representative particle model along with methods suggested to improve the accuracy of the representative particle model predictions are provided in Appendices A and B.

The work resulted in the following peer-reviewed journal publications:

- Elghannay, Husam A., and Danesh K. Tafti. "Development and validation of a reduced order history force model." *International Journal of Multiphase Flow* 85 (2016): 284-297.
- Elghannay, Husam, and Danesh Tafti. "LES-DEM simulations of sediment transport." *International Journal of Sediment Research* (2017).
- Elghannay, Husam A., and Danesh K. Tafti. "Sensitivity of numerical parameters on DEM predictions of sediment transport." Particulate Science and Technology (2017): 1-9.
- Yu, Kuahai, Husam A. Elghannay, and Danesh Tafti. "An impulse based model for spherical particle collisions with sliding and rolling." *Powder Technology* 319 (2017): 102-116.
- Elghannay, Husam A., and Danesh K. Tafti. "Revised Partial Coupling for Dense Fluid-Particulate Systems." (submitted to Powder Tech, Sept. 2017).

- Elghannay, Husam A., and Danesh K. Tafti. "Alternate Tangential Impact Treatment for the Soft-Sphere Collision Model". (submitted to Powder Tech, Jan. 2018).
- Elghannay Husam A., Yu, Kuahai, and Danesh Tafti. "Comparison of a physics based hard-sphere model with the soft sphere model", (submitted to Powder Tech, Feb. 2018).

The following conference papers were written and published during this work:

- Elghannay, Husam A., and Danesh K. Tafti. "DEM Predictions of NETL Small Scale Challenge Problem." *ASME 2014 4th Joint US-European Fluids Engineering Division Summer Meeting collocated with the ASME 2014 12th International Conference on Nanochannels, Microchannels, and Minichannels*. American Society of Mechanical Engineers, 2014.
- Elghannay, Husam, Kuahai Yu, and Danesh Tafti. "On the Improvement of CFD-DEM Coarse Graining Predictions." *ASME 2016 Fluids Engineering Division Summer Meeting collocated with the ASME 2016 Heat Transfer Summer Conference and the ASME 2016 14th International Conference on Nanochannels, Microchannels, and Minichannels*. American Society of Mechanical Engineers, 2016.
- Elghannay, Husam A., and Danesh K. Tafti. "Evaluation of Coarse Graining DEM Using Representative Particle Model." *International Conference on Discrete Element Methods*. Springer, Singapore, 2016.
- Yu, Kuahai, Husam A. Elghannay, and Danesh Tafti. "Three dimensional particle-particle impact model based on impact force analysis". The *7th International Conference on Discrete Element Methods*, Dalian, China, August 1-4, 2016.

Chapter 2

DEM Predictions of NETL Small Scale Challenge Problem

Husam A. Elghannay[*] and Danesh K. Tafti[*]

[*]Department of Mechanical Engineering
Virginia Polytechnic Institute and State University
Blacksburg, Virginia 24061

Citation:

Elghannay, Husam A., and Danesh K. Tafti. "DEM Predictions of NETL Small Scale Challenge Problem." ASME 2014 4th Joint US-European Fluids Engineering Division Summer Meeting collocated with the ASME 2014 12th International Conference on Nanochannels, Microchannels, and Minichannels. American Society of Mechanical Engineers, 2014.

2.1 Abstract

The Discrete Element Method (DEM) coupled to Computational Fluid Dynamics (CFD) is used to predict dense fluid-particle system in a *blind* study using the in-house code GenIDLEST (Generalized Incompressible Direct and Large Eddy Simulation of Turbulence). The experimental measurements were performed at the Department of Energy's (DOE's) National Energy Technology Laboratory (NETL) at three different superficial velocities in a 0.076m×0.23m×1.22m bubbling fluidized bed with 3.26 mm Nylon beads. Experimental measurements include the mean and rms of pressure drop between specific locations, the first four moments of solid velocity components, and time series of pressure drop at selected locations in the bed. The predictions capture the trends in the change in bed hydrodynamics with an increase in the superficial velocity. While good qualitative agreement is found with experiments, quantitative agreement is fair. Factors that might cause deviations in predictions are discussed.

2.2 Introduction

Simulating the physics of fluidized beds is challenged by the complex interaction between fluid and solid phases. Two numerical approaches commonly used in simulating dense particle-laden flows are the two-fluid model (TFM) and the discrete element method coupled to computational fluid dynamics (DEM-CFD) method. In the TFM both the carrier and disperse phases are treated as two interpenetrating continuous phases while Newton's second law is used in the DEM-CFD approach to solve the motion of individual particles. Though DEM simulations are more accurate and have the ability to numerically account for several realistic behavior in particulate systems [3-5], TFM is less expensive and can be reasonably applied to many industrial scale problems.

Several techniques were tried to experimentally validate numerical models applied to particulate flow systems in laboratory and industrial scale fluidized beds. These techniques include single-point measurement of pressure fluctuation, 2D particle image velocimetry (PIV), x-ray tomography and Magnetic resonance (MR) [6-9].

The ideal of developing a fluidization modelling challenge problem was first proposed in Fluidization VII in 1992. The first challenge problem conducted by Particulate Solid Research Inc. (PSRI) consisted of two industrial scale circulating fluidized bed (CFB) units (riser diameters of 0.2 m and 0.4 m) with two different materials and at different operation conditions. Results from ten groups responding to the first challenge problem were presented at Fluidization VIII in 1995

and only three were reported successful. It was concluded that "Models were not sophisticated enough to be used to predict all the hydrodynamics in a circulating fluidized bed" [10, 11].

The second challenge problem was issued by PSRI in 2001 for the same industrial unit and the same type of materials but with change in the entrance region. Thirteen different results from different groups were presented at Fluidization X in Beijing, China [12]. Modelling results poorly captured radial profiles for the solids flux and particle velocity with percentage error ranging from 77 to 334%. It was concluded that; "Models still needed substantial development to be able to predict CFB hydrodynamics" [10, 12].

Later in 2010, the third challenge problem was generated by the U.S. Department of energy's (DOE's) National Energy Technology Laboratory (NETL) in collaboration with PSRI. The challenge problem comprised two systems, NETL's CFB riser (16m long and 0.305 m in diameter) and PSRI's bubbling fluidized bed BFB (9m long and 0.92 m in diameter). After a first blind testing of all models the experimental data was publicly released and the modeller's were allowed to tune their models and to submit refined results [13]. Five groups responded to NETL's problem whereas only three participated in simulating PSRI's system. Overall assessment of all simulation results were presented at the Circulating Fluidized Bed X Conference held in Sun River Valley, Oregon, USA in May 2011[14]. Some reasonable results for simulating challenging problem III were published/presented [13, 15].

In May 2013 NETL collaborated with a scientific advisory committee released a small scale challenge problem based on experimental measurements in a 0.076m×0.23m×1.22m rectangular bubbling fluidized bed [16]. The purpose of SSCP-I is to improve the reliability of computational modeling of multiphase flows by validating with accurate and well defined experimental data. In this paper, our blind CFD-DEM predictions using the in-house code GenIDLEST (Generalized Incompressible Direct and Large Eddy Simulation of Turbulence) [17] are compared to experimental measurements of the SSCP-I fluidized bed at three different superficial velocities.

2.3 Experiment (problem Setup)

2.3.1 Facility description

A schematic drawing of the experimental bed along with measurement locations is shown in Fig. 2.1. The rectangular bed is equipped with a number of pressure transducers at both sides of the bed

at three different elevations. The pressure transducers are used to measure statistics of axial pressure gradients for various flow conditions.

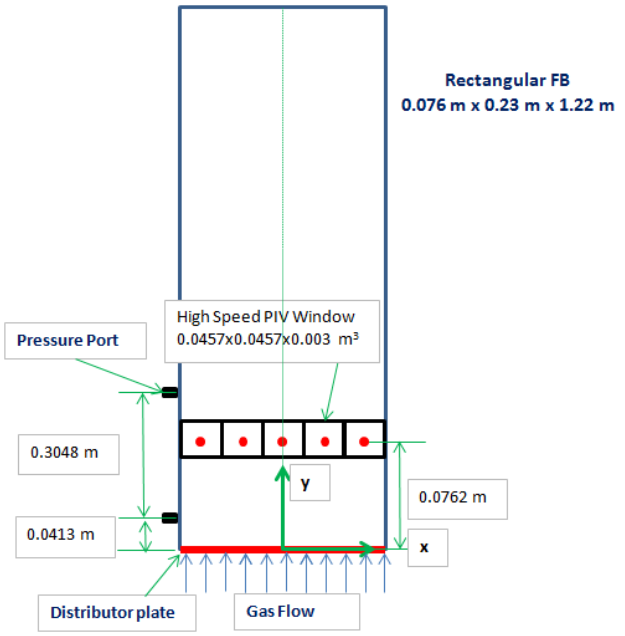

Figure 2. 1. SSCP-I test unit and measurement locations.

The first pressure port is located at 0.0413 m above the distributer while a second pressure port is located at 0.3048 m above the first one. A third pressure port is located at 0.0603 m below the distributer (not shown). No lid was utilized at the top of the bed so that exit pressure can be assumed atmospheric. A low frequency (1 Hz) transducer was used to measure the mean pressure drop across two heights and a high speed pressure transducer (100-1kHz) was used for rms and time series measurements.

High speed PIV [8] is utilized for obtaining individual particle velocity data at a sampling rate of 1 to 1.5 kHz. Five measurement windows (0.0457 m x0.0457 m) are distributed along the width of the bed. The height of the center of high speed measurement window is 0.0762 m above the distributor plate (Fig. 2.1). The measurement technique involves tracking individual particles in the field of view whose centroids are less than 3mm from the wall. The velocity of all particles that reside in a particular window at every time step is aggregated to obtain the particle velocity distribution for that window. The measured data includes the first four moments of the horizontal and vertical velocity distribution in the measurement window at all the flow conditions.

2.3.2 Operation conditions

The granular material used in the experiment were Nylon beads of uniform size and high sphericity (0.93-0.95). The particles are 3.256 mm in diameter with density of 1131 kg/m^3 (Geldart group D particles). Three different flow conditions are provided for superficial velocities 2.19 m/s, 3.28 m/s and 4.38 m/s. The bed is filled with a solids weight of 1.9 kg in each case and the minimum fluidization velocity is estimated to be 1.05 m/s. The flow conditions correspond to 2, 3 and 4 times the minimum fluidization velocity.

2.4 Numerical Technique

The in-house code flow solver GenIDLEST was coupled with an implementation of DEM to solve for individual particle motion for simulating particulate flows. Serial and parallel DEM implementation was validated in previous work [18, 19].

2.4.1 Governing equations

The Eulerian-Lagrangian framework involves solving the volume averaged Navier-Stokes equations derived by Anderson and Jackson [20] for the carrier phase. Model B of Gidaspow is adapted in which the pressure drop is accounted for only by the fluid. The continuous phase is governed by:

$$\frac{\partial(\varepsilon\rho_g)}{\partial t} + \vec{\nabla}.(\varepsilon\rho_g\vec{u}) = 0 \tag{2.1}$$

$$\frac{\partial(\varepsilon\rho_g\vec{u})}{\partial t} + \vec{\nabla}.(\varepsilon\rho_g\vec{u}\vec{u}) = -\vec{\nabla}p + \vec{\nabla}.(\varepsilon\bar{\bar{\tau}}) + \rho_g\vec{g} - \vec{f}_{Drag} \tag{2.2}$$

where $\varepsilon, \rho_g, \vec{u}, p, \bar{\bar{\tau}}$ and $\vec{f}_{Drag}$ are the volume fraction, density, fluid interstitial velocity, pressure, viscous shear stress and drag force per unit volume respectively. The drag force represents the particle fluid interaction and is defined as:

$$\vec{f}_{Drag} = \sum_{n=1}^{N_p} \beta \frac{V_p}{\varepsilon(1-\varepsilon)}(\vec{u} - \vec{v}_p) \tag{2.3}$$

where β, V_p and $\vec{v}_p$ are the momentum exchange coefficient, the particle volume, and the particle velocity, respectively. N_p represents the number of particles in each computational cell. A combination of Ergun and Wen & Yu drag correlation with a blending function to avoid discontinuity is used for the momentum exchange coefficient [21].

$$\beta = W\beta_{Ergun} + (1 - W)\beta_{Wen-Yu} \tag{2.4}$$

$$\beta_{Ergun} = 150\mu\frac{(1-\varepsilon)^2}{\varepsilon d_p^2} + 1.75(1-\varepsilon)\frac{\rho_g}{d_p}\left|\vec{u} - \vec{v}_p\right| \tag{2.5}$$

$$\beta_{Wen-Yu} = \frac{3}{4}C_D\frac{(1-\varepsilon)\varepsilon}{d_p}\rho_g\left|\vec{u} - \vec{v}_p\right|\varepsilon^{-2.65} \tag{2.6}$$

where W is the blending function given by:

$$W = \frac{\tan^{-1}\big(150(\varepsilon - 0.8)\big)}{\pi} + 0.5 \tag{2.7}$$

$$C_D = \begin{cases} 24\big(1.0 + 0.15Re_p^{0.687}\big)/Re_p, & Re_p < 1000 \\ 0.44, & Re_p \geq 1000 \end{cases} \tag{2.8}$$

where Reynolds number Re_p is defined as;

$$Re_p = \frac{\varepsilon\rho_g d_p\left|\vec{u} - \vec{v}_p\right|}{\mu_g} \tag{2.9}$$

in the above equations d_p represents the particle diameter, C_D is the drag coefficient solid phase, and μ_g denotes the fluid viscosity.

The motion of each particle is governed by Newton's law;

$$m_p\frac{d\vec{v}_p}{dt} = V_p\big(\rho_p - \rho_g\big)\vec{g} + \vec{F}_{p,drag} + \sum\vec{F}_{p,collision} \tag{2.10}$$

$$I_p\frac{d\vec{\omega}_p}{dt} = \vec{T}_{p,collision} \tag{2.11}$$

where m_p, I_p and ω_p, are the particle's mass, mass moment of inertia, the angular velocity, respectively. $F_{p,\text{collision}}$, and $T_{p,collision}$ stand for the force and torque resulting from the particle collisions with walls or with each other. Soft or hard sphere models are commonly used to model particle-particle interactions in DEM simulations. The soft sphere approach is used to account for multiple interactions occurring at the same time which are predominant in dense fluidized beds. The contact force in the soft sphere model is decomposed into a normal force component and a tangential force component. Normal and tangential force component are modelled using spring-dashpot-slider system. Details of the soft sphere model can be found in [22, 23].

2.4.2 Algorithm overview

A semi-implicit fractional step method is used to solve the flow field on a non-staggered finite-volume grid. The flow field is advanced in time using calculated void fractions and drag forces from the previous time step. A detailed description of the numerical algorithm coupling the fluid and solid equations is described in [18].

An explicit Euler method is used to advance the particles in time. The continuous and disperse phases are coupled via the drag force and void fractions. The void fractions are calculated based on particle locations. In this step the volume of all particles whose centroids are located in a given cell is distributed using weighting factors to the cell vertices. The collective solid volume at the cell vertices is then divided by the volume of the cell averaged to calculate the solid and void fraction in the cell. The drag force acting on each particle is calculated using the calculated void fraction and cell-centered fluid velocity. The cumulative drag force in a given computational fluid cell is the sum of the drag force on all particles residing in that cell. The same procedure used for calculating the void fraction at the fluid cell center is used for calculating the integrated drag force acting on the fluid cell.

2.4.3 Simulation parameters

Typically in gas fluidized beds in the bubbling regime, the interstitial gas flow is assumed laminar. In this paper, however, not only is the Reynolds number based on the hydraulic diameter of the bed without accounting for the particles is well into the turbulent region for an equivalent channel flow (Re_D~16,700 for lowest superficial velocity), but also the calculated Archimedes number using the given particle and gas properties (Ar~1.4×10^6) indicates that the presence of the particles will result in near fully turbulent flow at the onset of fluidization (critical Ar ~ 1.6×10^6) [24]. This, however, is not the same as the turbulent fluidization regime which lies between bubbling and fast fluidization regimes [25]. In light of this, to account for subgrid turbulence, the Dynamic Smagorinsky model was used [26]. The time step was selected to be about 15 times the critical collision time as proposed by [23]. The top and bottom boundaries were assumed as permeable walls allowing for a uniform gas flow velocity equal to the superficial velocity. A permeable wall was used at the top to prevent particles from being ejected from the bed during initial transients. Alternative boundary conditions (e.g. outflow) can be used at the top wall; the top boundary condition is assumed far enough to not affect the bed hydrodynamics. A no-slip boundary

condition was used for fluid velocities at the side walls. Simulation parameters are summarized in table 2.1.

Table 2. 1. Numerical parameter used in the simulation.

Parameter	value
Particles	
Sphericity	1
Number	92948
Diameter	3.256 mm
Density	1131 kg/m^3
Coefficient of stiffness*	800 kN/m^3
Coefficient of restitution	0.84
Coefficient of friction	0.35
Fluid (air)	
Viscosity	1.8× 10^{-5} Pa.s
Density	1.205 kg/m^3
Computation Domain dimensions $(L_x \times L_y \times L_z)$	0.23m×1.22m×0.076m
Cell in x-direction	40
Cell in y-direction	100
Cell in z-direction	6
Time step	2 × 10^{-5}

* assumed to be the same in the normal and tangential directions

2.5 Results and Discussions

The simulations were run for a total time between 13-15 s. To eliminate the effect of initial transients the first 3-5 seconds of the simulation were not included in the analysis. The successive 10 seconds of simulation where sampled at 50Hz sampling rate and submitted for comparison with temporal measurements of pressure drop across the first two pressure ports and velocity data at each PIV window. To reduce the time of the calculations, the domain was decomposed into two blocks in the x-direction to ensure load balance in each block. The BlueRidge supercomputer provided by Virginia Tech's Advanced Research Computing was used to run the simulations. BlueRidge is a 318-node Linux cluster with each node outfitted with two Intel(R) Xeon(R) CPU E5-2670 CPUs @ 2.60GHz and 64 gigabytes of memory for a total of 5,088 cores and 20.4 TB of memory systemwide. It took about 47 minutes of wall clock time to run 1 second of simulation (lesser for higher superficial velocity).

2.5.1 Pressure results

At fluidization the total pressure drop across the bed should be able to support the weight of the particles inside the bed. The pressure drop across the bed was found to be 1.096 kPa, 1.155 kPa and 1.108 kPa for a superficial velocity of 2.19 m/s, 3.28 m/s and 4.38 m/s respectively which are slightly above the pressure due to the solids weight (1.081 kPa). The slight difference is because of the pressure drop in the riser itself which increases with the increase in the fluid velocity. Pressure probes where inserted in computational cells located two cells away from the wall at the same level as the experimental pressure transducers. Comparisons between measurement and simulation of time series results of pressure drop between the first two ports (0.0413 to 0.3461 above the distributor) are presented in Figs. 2.2 (a-c).

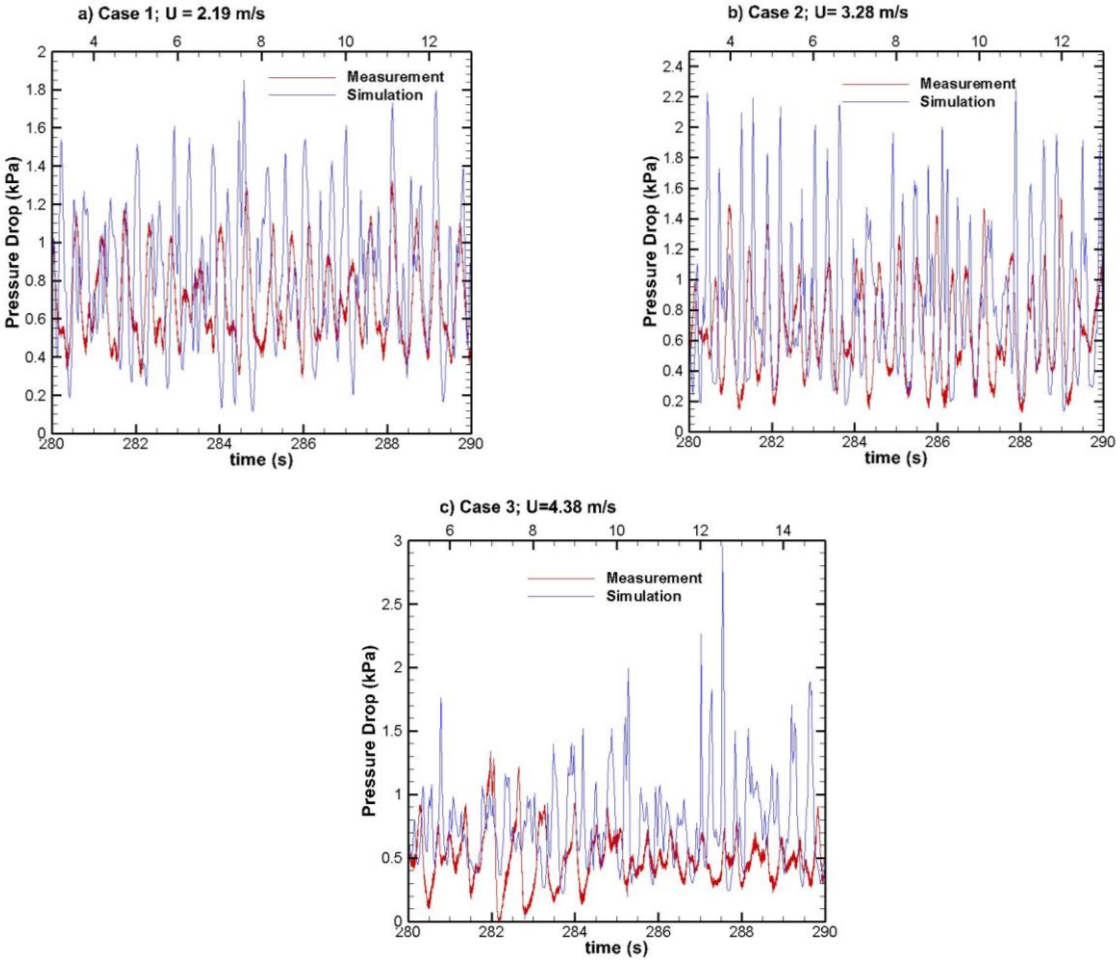

Figure 2. 2. Comparison between measured and simulated time series of pressure drop between first and second pressure ports above the distributor a) U=2.19 m/s, b) U=3.28 m/s, U=4.38 m/s.

The main and secondary abscissa displays the actual measurement time and the simulation time respectively. As compared to measurements it can be seen that all simulations show higher pressure fluctuations. The simulated pressure time series was averaged to obtain the mean pressure for each case. Differences in mean and rms values of pressure are presented in bar charts in Figs. 2.3.a and 2.3.b. The calculated mean pressure drop from transient data in the specified level are 0.832, 0.825 and 0.768 kPa for superficial velocities of 2.19, 3.28 and 4.38 m/s respectively. The corresponding measured values are 0.69, 0.65 and 0.5 kPa for cases 1, 2, and 3, respectively. This accounts for differences of about 21 %, 27 % and 54% with increasing superficial velocity. The corresponding measured rms values are 0.18, 0.32, 0.23 kPa compared to calculated values of 0.365, 0.471 and 0.357 kPa for case 1, 2 and 3 respectively. Case 1 shows the largest difference in pressure rms values among the three simulations (just above 100%). At intermediate velocity (U=3.28 m/s) the difference is about 47% and 55% difference was found in the higher superficial velocity condition (U=4.38 m/s).

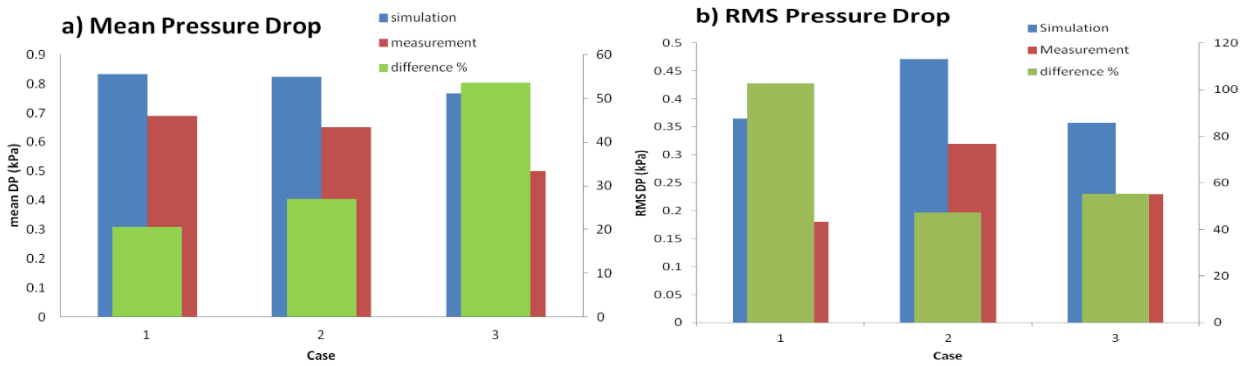

Figure 2. 3. Comparison between measured and simulated data for a) mean and b) rms pressure drop 0.0413 to 0.3461 above the distributor.

The pressure drop between the second port and the exit pressure (atmospheric) was too small for the instrumentation to measure for the first two cases (2.19 m/s and 3.28 m/s superficial velocity). For the third case (U=4.38 m/s) measurements of mean pressure drop indicated 0.07 kPa with an error band of about 0.05 kPa (70%). The predicted mean pressure drop was about 0.131 kPa which is very close to the uncertainty limit in mean measurements.

Neglecting the pressure drop due to fluid friction at the walls of the channel; the pressure drop between two levels in a gas fluidized bed is due to the weight of solids. Thus, the mean pressure

drop will tend to decrease between vertical sections as the bubbling activity increase between the two sections. While the absolute values of pressure difference in Fig. 2.3(a) are different between simulation and experiment, both follow the same trend of decreasing pressure drop with increase in fluidization velocity. Figure 2.4 shows the mean results for void fraction of the bed for the three cases. It can be seen that as the superficial velocity increases (from left to right) the bed height increases. It also can be seen that fluid void fractions are lower in the bed centre resulting from bubble formation and coalescence. The higher void fraction justifies the reduction in mean pressure drop between measurement locations. The low void fraction near the walls (blue colour) is a consequence of particles clustering and falling down at the sides of the bed.

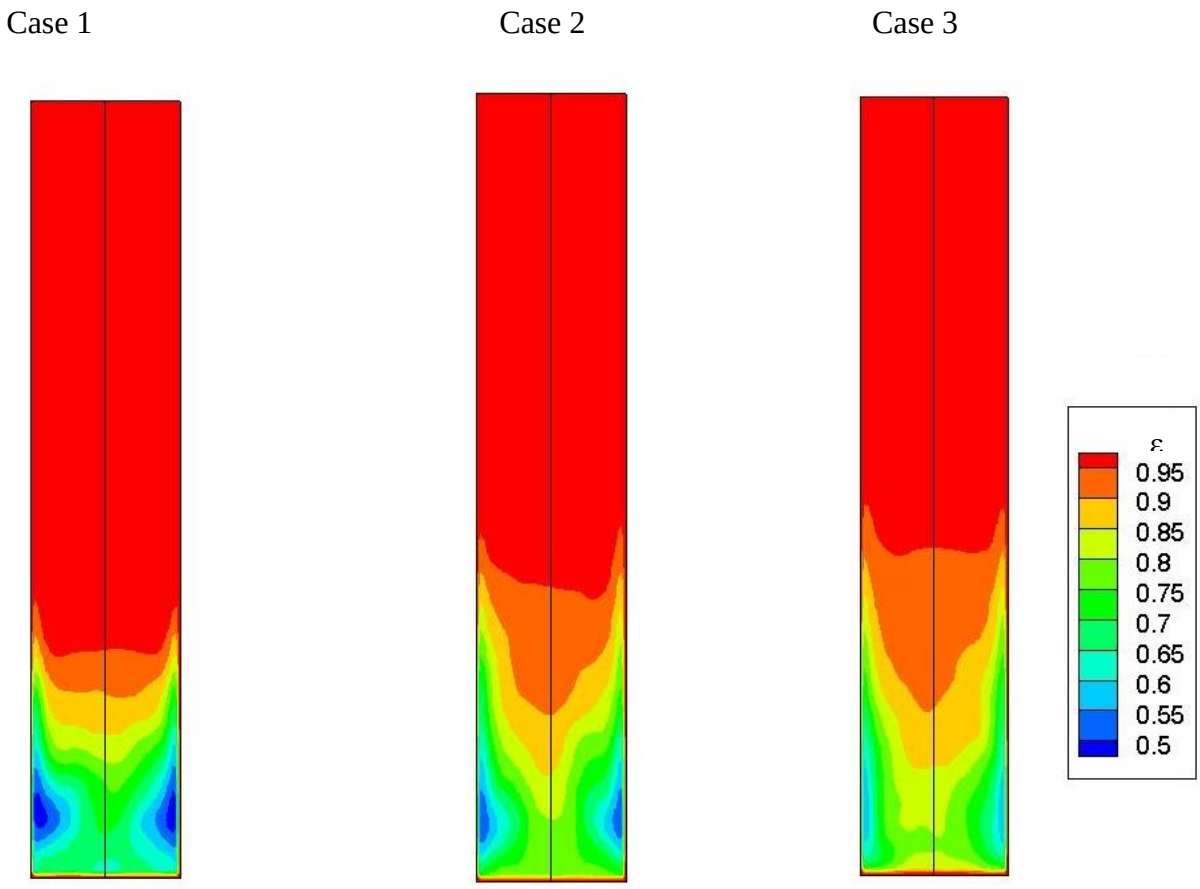

Figure 2. 4. Simulation results of average void fraction across the bed for the three cases.

Same as with the mean pressure drop, both the measurement and simulation show the same trend for the rms pressure drop also. As the superficial velocity increases to the intermediate velocity the rms value peaks and then drops with a further increase in superficial velocity. Fluctuations in pressure drop in fluidized bed are caused by formation of bubbles and slugs [22]. The drop in rms values of pressure might indicate a beginning of transition to the turbulent fluidization flow regime which is characterized by the break-up of large bubbles into smaller more frequent bubble formation. Several transition criteria based on different measurement techniques including pressure fluctuation and total bed expansions have been utilized [25] in the literature. The beginning of the transition to turbulent fluidization is marked as the gas velocity at which the standard deviation of pressure fluctuation reaches a maximum whereas the end of transition is denoted by levelling of the standard deviation of the pressure fluctuations [25].

Figure 2.5 shows instantaneous snapshots of some existing flow structures for the three cases spaced 0.1 s apart. At superficial velocity of 2.19 m/s bubbles are formed above the distributor plate and grow in size as a result of bubble coalescence and finally a dome can be seen as the bubble erupts at the bed surface. At higher superficial velocity (U=3.28 m/s) the bed height increases with more heterogeneous mixing can be observed. More aggressive bubbles and slugs are formed above the distributor with stronger mixing characteristics. Interaction of the formed larger bubbles produces a frequent splashing of large bubbles at the bed surface followed by drop in bed height. With further increase in the superficial velocity (U=4.38 m/s) more bubbles are formed above the distributor with more heterogeneous mixing.

Case 1

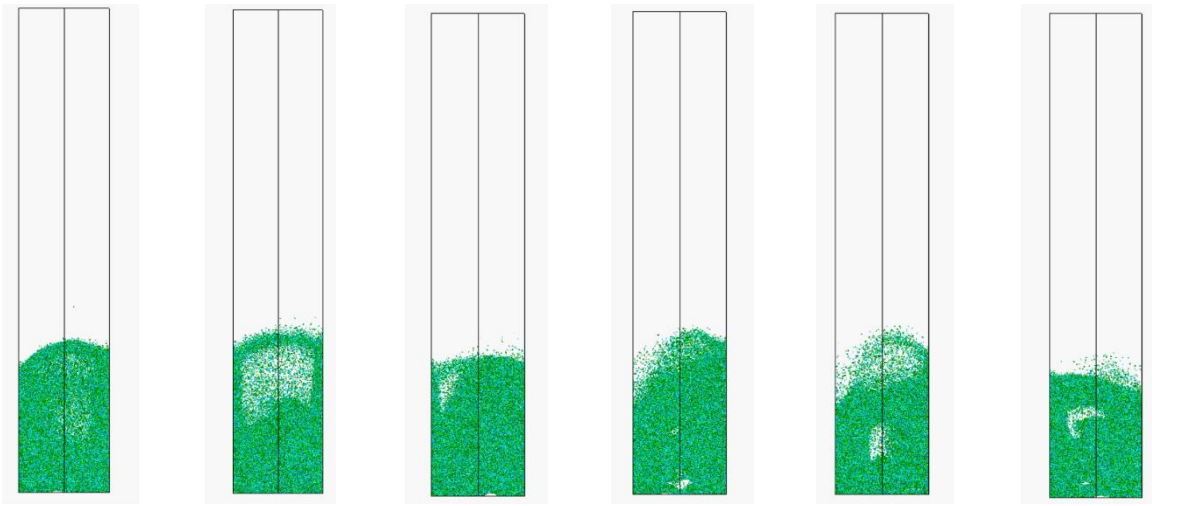

Case 2

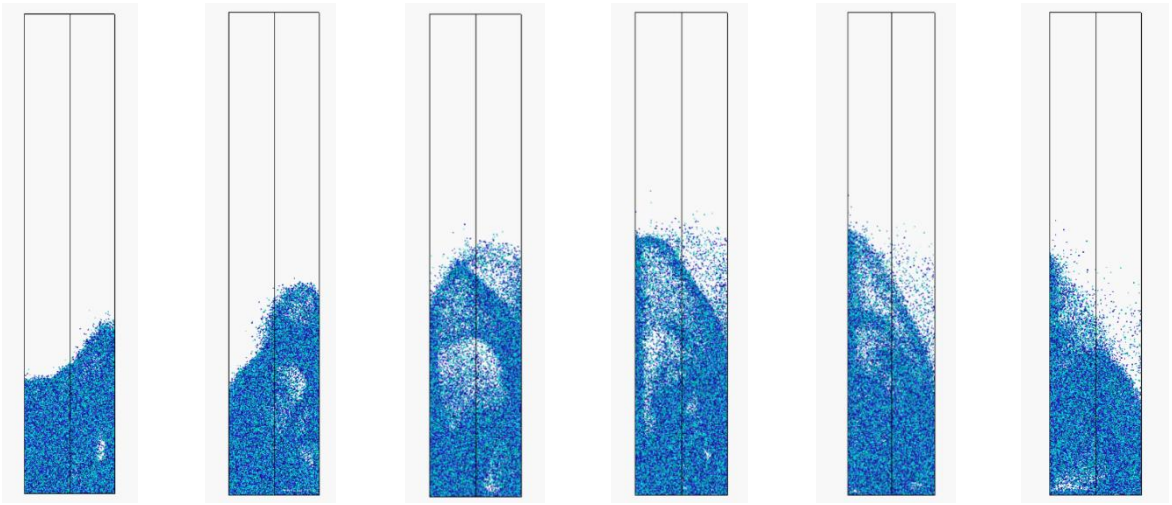

Case 3

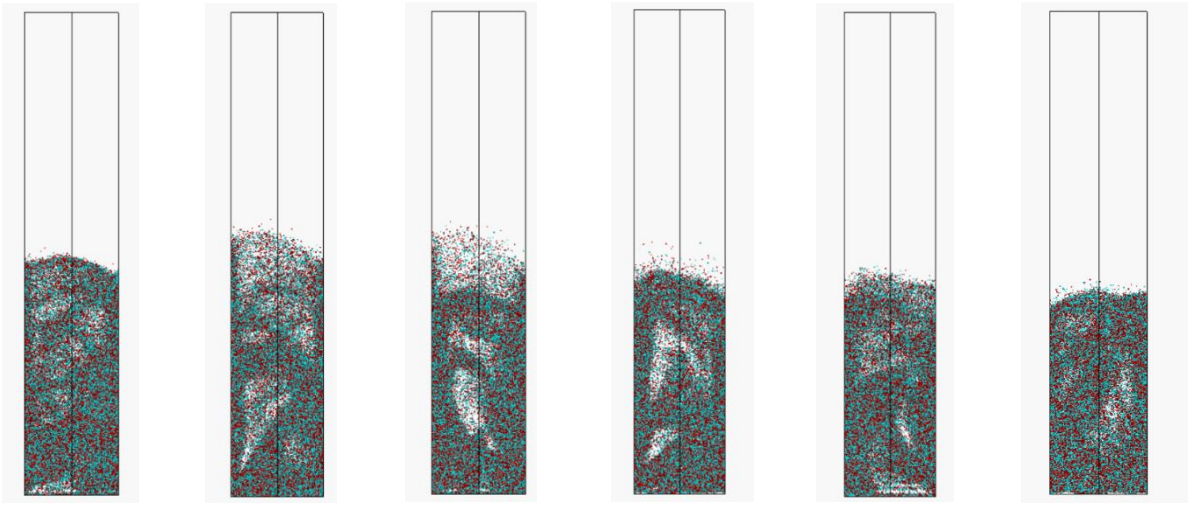

Figure 2. 5. Snap shots showing flow structures for the three cases.

2.5.2 Velocity results

Mean, rms, skewness and kurtosis of vertical and horizontal velocity are measured at the locations shown in Figure 2.1. Because the measurements use a local averaging window method [27] to calculate the frame averaged velocity for each measurement window, we tried to emulate the same procedure is used for the simulations. At each time step, the frame averaged particle velocity is calculated. The fluctuating velocity component of each particle is calculated by subtracting the frame averaged value from the instantaneous particle velocity. This is used to calculate the high-order moments instantaneously which are then time averaged. The mean velocity is also obtained by time-averaging the instantaneous frame averaged value. In the simulations, the depth of the domain is three times the particle diameter which corresponds to the depth of the fluid cell inside the wall, whereas the experiments only consider a depth of one particle diameter. The simulation results are averaged over 10 seconds. Comparisons between measured and simulated averaged vertical velocity across the width of the bed wall are presented in Figs. 2.6 (a-c).

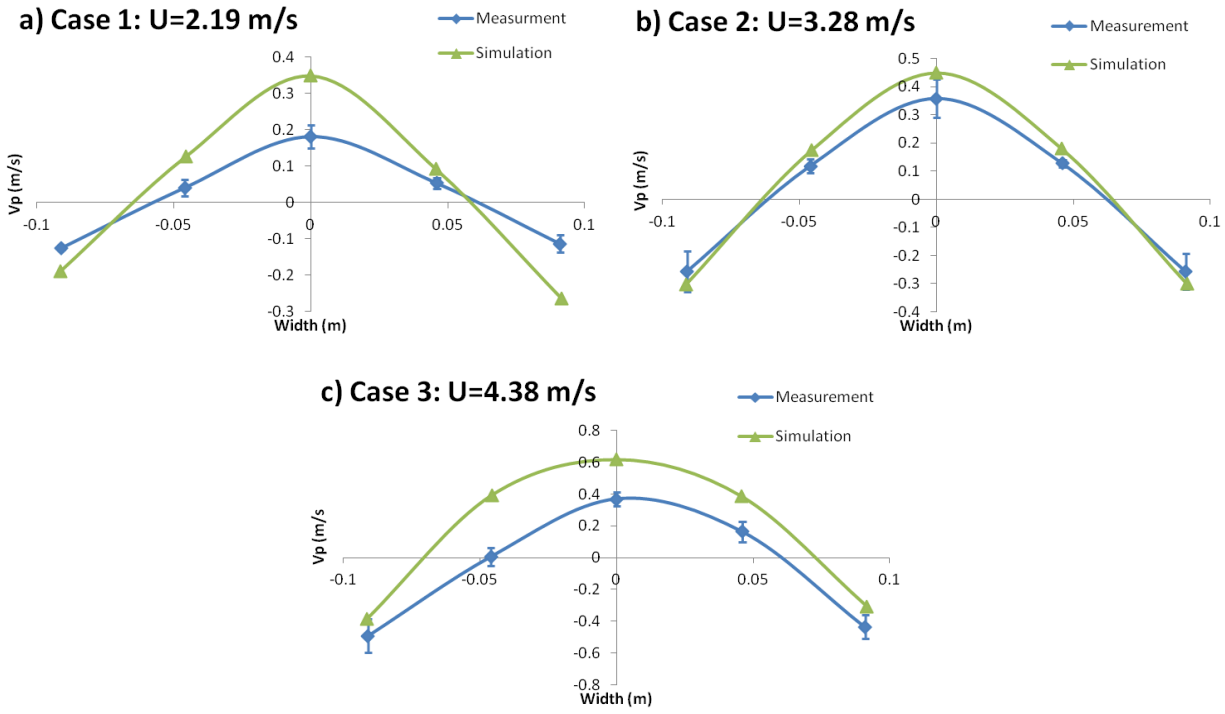

Figure 2. 6. Comparison between measurement and simulation of averaged vertical velocity at measurement location across width of the bed.

Averaged measurement and simulation results are assumed to be in the centre of each PIV measurement window. Error bars represent the 95% Confidence Index of measurement. As can be

seen from these figures, the velocity profiles from both measurement and simulation indicate an upward velocity in the centre of the bed and a negative (downward) velocity near the side walls. As the superficial velocity increases, there is less particle clustering at the side walls in the region above the distributor (blue regions in Fig. 2.4) and the falling solids velocity increases as indicated in Fig. 2.6 (a-c). While both simulation and experiment show an increase in peak velocity as the superficial velocity increases, the rate of increase between Case 2 and 3 is much smaller in the experiments.

Although good agreement is achieved along the bed width for the intermediate velocity (U=3.28 m/s) the peak velocity is over-predicted in the bed centre for the other two cases. One factor that might affect the simulation results near walls is that the computational grid near the wall is quite coarse at three times the particle diameter. It is certain that the fluid boundary layer is not resolved by this grid which could lead to higher fluid velocities and lead to higher particle velocities also. The discrepancy near walls has been observed in other numerical investigations as well [6, 18].

Figures 2.7(a-c) show the distribution of the horizontal velocity in the bed at the measurement windows. While Case 1 and 2 show the correct trends between experiments and simulations (in spite of large quantitative differences), Case C shows the opposite trend – while the simulation indicates particle movement from the sides to the centre of the bed, the experiments indicate the reverse flow from the centre to the sides. To explain these differences further, Fig. 2.8 shows the solid velocity vectors plotted in the vicinity of the wall with the vertical extent of the measurement window (horizontal lines).

It can be seen from Fig. 2.8 that, in all cases, the solid circulation pattern is the same; particles are pushed upward and outward at the centre of the bed and collapse into the bed along the side walls moving downward under the influence of gravity till they reach near the bottom of the bed when they are entrained back to the centre of the bed in a circulating pattern. The location of the measurement windows indicates that at that vertical distance the simulated flow is always inward, while if the windows were placed higher in the bed, the flow would be outward as seen in the experiments. It can also be seen that as the fluidization velocity increases the core recirculation region moves closer to the distributor plate.

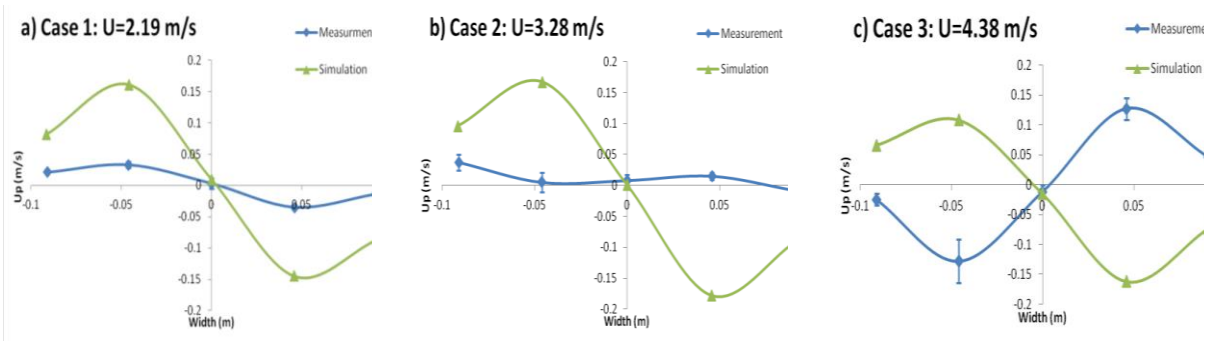

Figure 2. 7. Comparison between measurement and simulation of averaged horizontal velocity at PIV windows.

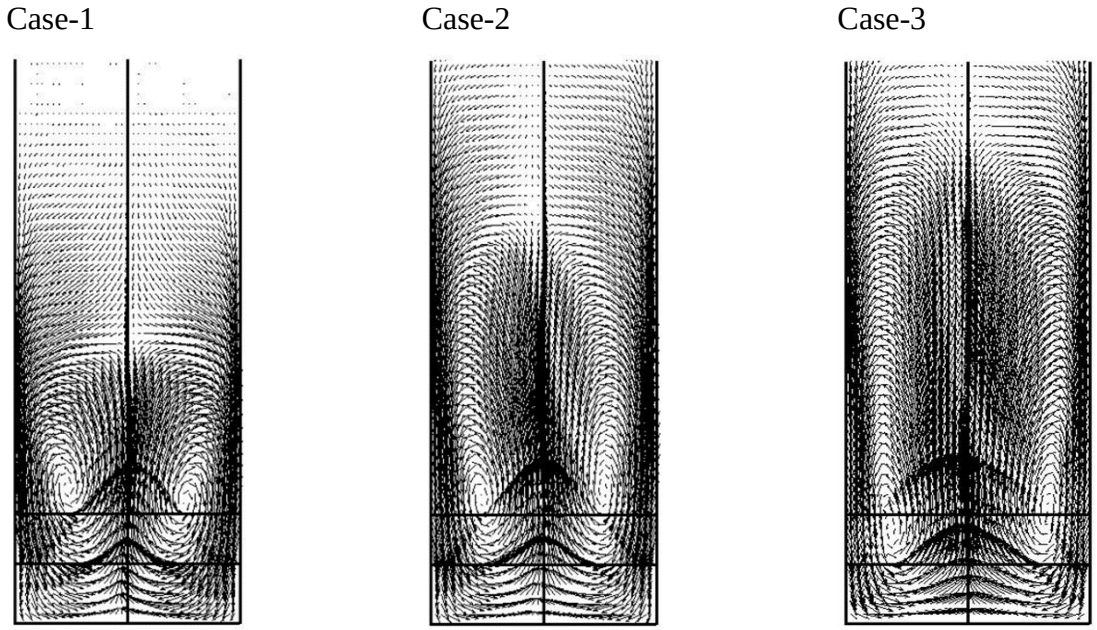

Figure 2. 8. Mean solids velocity vectors for the first 60 cm of the bed. Horizontal lines show vertical extent of measurement window.

It can be deduced from the measurements, that a weak inward flow does exist for Case 1, which gets weaker for Case 2, and switches to outward flow for Case 3. This implies that as the fluidization velocity increases, either the recirculating pattern ceases to exist or it moves down near to the baseplate below the measurement window location. Indeed this is seen in the experiment [28]. The rms values of the vertical velocity component are shown in Figs. 2.9 (a-c). The predictions capture the trend but under-predict the values. On the other hand, the rms values for the horizontal velocity component in Figs. 2.10 (a-c) are over-predicted by the simulations. Physically, the rms velocities are fluctuations about the mean and can be correlated to the collision frequency between particles. Particles moving in a cluster without collisions will exhibit low rms

fluctuations whereas colliding particles with random velocity distributions will tend to have higher rms values. Based on this reasoning the simulations results imply less or weaker collisions in the vertical direction and stronger or more collisions in the horizontal direction than the experiments. Among the three cases higher deviations can be noticed at the lower velocity (2.19 m/s).

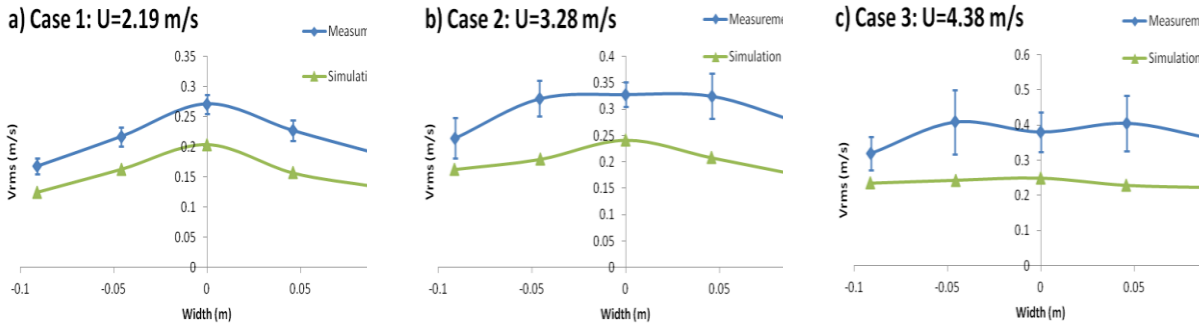

Figure 2. 9. Comparison between measurement and simulation of vertical velocity rms at PIV windows.

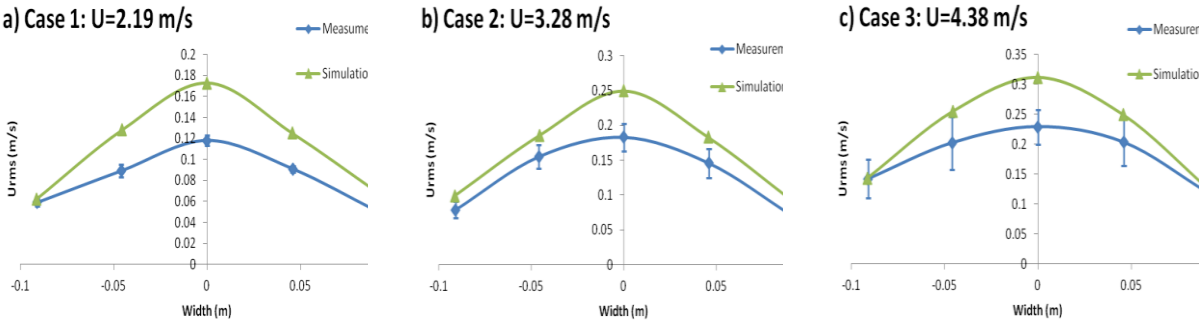

Figure 2. 10. Comparison between measurement and simulation of horizontal velocity rms at PIV window.

Skewness is a measure of asymmetry about the mean value whereas the fourth central moment (kurtosis or flatness) is a measure of extent of sharpness about the mean value. In all cases, predictions are in better agreement with experiments at the centre of the bed whereas the discrepancies increase near the side walls. Interestingly, both simulated skewness and flatness (Figs. 2.11-2.14) exhibit values close to 0 and 3 which imply a Gaussian distribution, whereas the experimental values show considerable deviation from these values as the walls are approached.

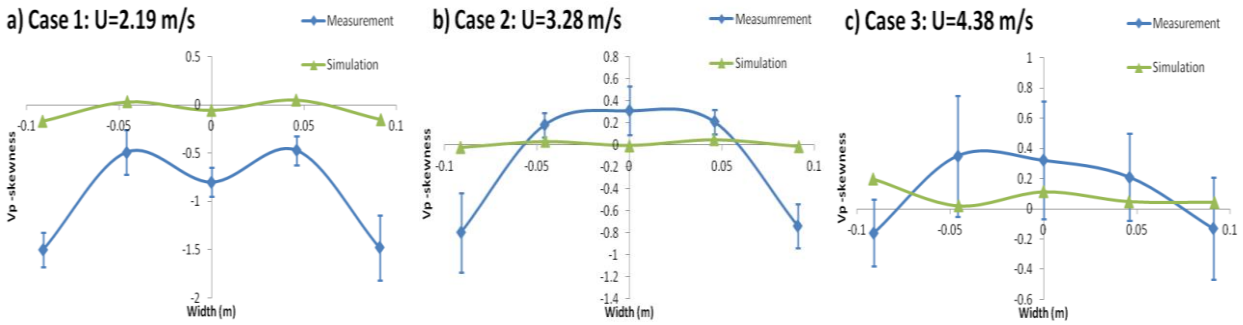

Figure 2. 11. Comparison between measurement and simulation vertical velocity skewness at PIV windows.

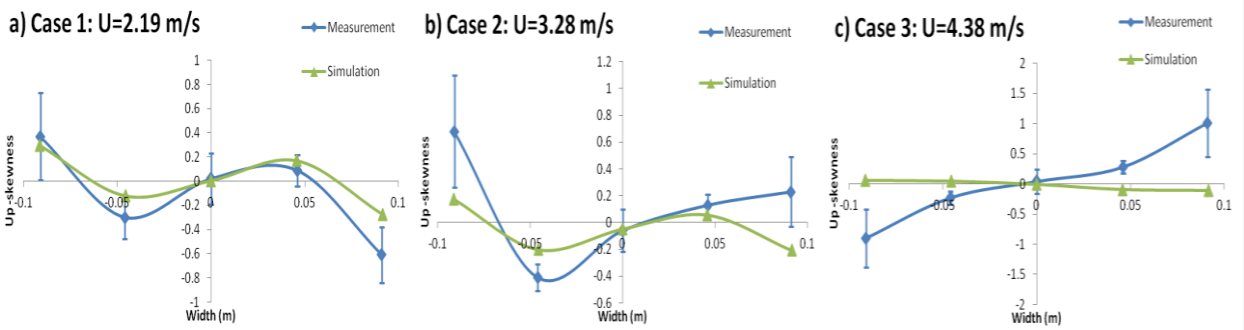

Figure 2. 12. Comparison between measurement and simulation horizontal velocity skewness at PIV windows.

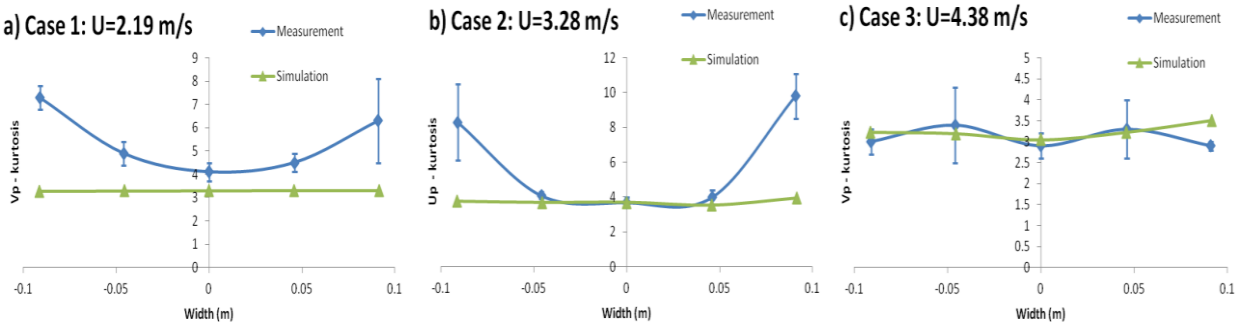

Figure 2. 13. Comparison between measurement and simulation; kurtosis of vertical velocity at PIV windows.

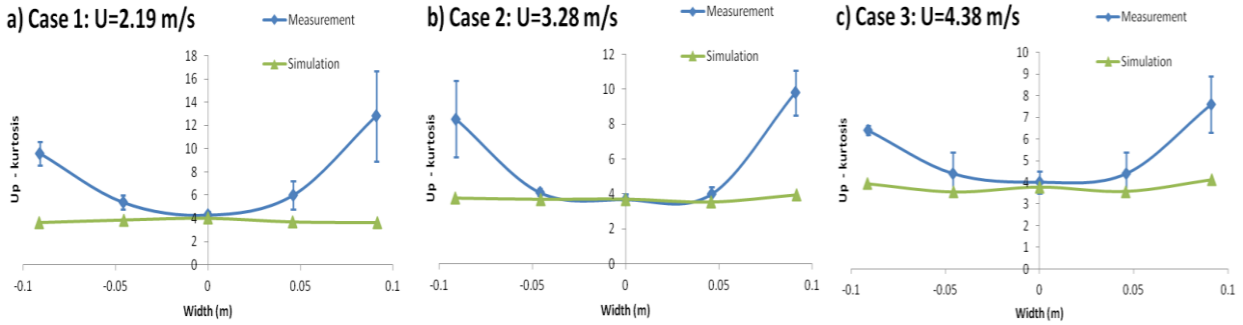

Figure 2. 14. Comparison between measurement and simulation; kurtosis of horizontal velocity at PIV windows.

Beside the inability of the simulations to predict these higher moments, which are difficult to predict even in single phase turbulent flows with second-order numerics, some other contributing factors to the discrepancies could be caused by the non-uniformity of the base flow in the experiments and the fact that the simulation results extend three particle diameters into the bed from the wall while the experimental field of view only extends one particle diameter. Thus the simulation results could be skewed toward a Gaussian distribution more than the experiments.

2.6 Conclusions

In this paper, blind DEM-CFD predictions using the in-house code GenIDLEST are compared to experimental measurements of a small scale challenge problem set by NETL for validating multiphase flow codes. The experiment comprises a bubbling fluidized bed with Geldart group D particles at three superficial velocities. Comparisons of mean and rms of velocity and pressure along with third and fourth-order moments of velocity components are presented. In spite of quantitative differences between the measured and simulated values of mean and rms pressure, there is agreement in the changing trends as fluidization velocity increases. The mean vertical velocities are represented reasonably well by the simulations, whereas the simulated trends in the horizontal velocity are different than experiments. The rms velocities are predicted with reasonable accuracy. The simulated skewness and flatness indicate a close to Gaussian distribution for the vertical and horizontal velocities. This agrees reasonably well with the experiments at the center of the bed, but larger differences exist at the side walls. Where appropriate, the possible reasons for the discrepancies are discussed.

CFD-DEM clearly falls into the realm of complex multi-physics simulations, with drag models, methods used to transfer fluid-to-particle and particle-to-fluid quantities, size of fluid and particle grid [18] influencing the prediction accuracy. This is further complicated by the stochastic nature of the calculations where there is no linear path between cause and effect. Considering all these challenges, GenIDLEST performed reasonably well with good qualitative agreement but fair quantitative agreement with experiments.

2.7 Nomenclatures

C_D	drag coefficient (-)
d_p	particle diameter (m)
e	coefficient of restitution (-)
f	force per computational cell volume (N/m^3)
F_p	force on particle (N)
g	acceleration of gravity (m/s)
I_p	particle moment of inertia ($kg.m^2$)
m_p	mass of particle (kg)
N_p	number of particles in computational cell (-)
p	pressure (N/m^2)
Re	Reynolds number (-)
t	time (s)
T_p	torque on particle (N.m)
u	fluid velocity (m/s)
v_p	particle velocity (m/s)
V_p	particle volume (m^3)
W	smoothing factor (-)

Greek letters

β	momentum exchange coefficient ($kg/(m^3.s)$
ε	computational cell void fraction (-)
ρ	density (kg/m^3)
τ	viscous shear tensor (Pa.s)
ω	rotational velocity (s^{-1})

Chapter 3

Development and Validation of a Reduced Order History force Model

Husam A. Elghannay[*] and Danesh K. Tafti[*]

[*]Department of Mechanical Engineering
Virginia Polytechnic Institute and State University
Blacksburg, Virginia 24061

Citation:

Elghannay, Husam A., and Danesh K. Tafti. "Development and validation of a reduced order history force model." *International Journal of Multiphase Flow* 85 (2016): 284-297.

3.1 Abstract

The history force model accounts for temporal development in fluid gradients in the viscous region surrounding a particle in point particle methods. The calculation of the history force typically requires storing and using relative velocity information during the life time of the particle. For a large number of particles integrated over large times, history force calculation can become prohibitively expensive. The current work presents a new modeling approach to calculate the history force in which a decay function is applied to a stored cumulative value of the history force. The proposed formulation is equivalent to applying the same function obtained from a constant acceleration assumption to a running average of the acceleration within the memory time of the particle. The new force model is validated with experimental measurements of settling spheres at Reynolds numbers ranging from around one to a few hundreds and at density ratios from 1.2 to about 9.32. More validation work was carried-out with experimental measurements of oscillating spheres at different frequencies and amplitudes, as well as bouncing spheres at different Reynolds numbers and density ratios. The model shows very good agreement with the experiments of settling spheres and reasonable/good agreement with oscillating and bouncing sphere experiments. The proposed model significantly reduces the computational resources required to calculate the history force especially when large number of particles need to be integrated over long times.

3.2 Introduction

Point force models are widely used in simulating natural and industrial particulate flow systems because they allow for simulating relatively large number of particles for long times. In this approach, the fluid-particle interaction force is accounted by a linear combination of different force models. Among the different force models, history force is considered as the most computationally expensive as it typically requires storing and using relative velocity information during the life-time of the particle. The calculation of the history force using this approach, however, requires significant computing resources. For example, it would require 1.2GB of memory to store a single precision value of relative velocity in three dimensions to simulate 100,000 particles for 1000 time steps [29]. Moreover, the inclusion of the history force may render the entire computation impractical when large number of particles are simulated [30].

In part, the work on development of history force models was motivated by the need to efficiently model sediment transport [30-33]. In one mode of sediment transport, sediment particles move by

jumping along the channel bottom wall (bed of particles) or by taking projectile trajectories (saltating). Thus, researchers have extensively focused on simulating the motion of saltating particles to develop sediment transport formulas or to improve existing models of sediment transport [34-37].

Though some researchers completely neglect the history force in their numerical modeling of solid particles in sediment transport simulations (e.g., [38-41]), numerical and empirical evidence suggests that the history force plays an important role in the transport of relatively small sediment particles moving near the bed. Comparing laboratory observations with numerical results provides evidence that while the history force is negligible for gravels moving as bedload; it becomes extremely important for sand [32, 33]. The history force was found to be significant to correctly describe the particle trajectory for a high Reynolds number of 4000 [31, 42], and appreciable for Reynolds numbers smaller than or of the order of one for large density ratios [43].The length and height of a single particle jump can be under-predicted by about 40% and 15%, respectively when the history force is neglected in the case of sand [32] and the cumulative effect of such differences for multiple jumps can lead to very large errors in predictions of sediment transport [31].

Many researchers have acknowledged the fact that reducing the computational cost associated with the history force would be beneficial and have worked towards developing less computationally intensive methods for modeling the history/Basset force. Michaelides [44] used Laplace transform to recast the linear equations of particle motion in a simplified creeping flow velocity field. He reported 6-11 times faster simulations with no need to store the velocity with the new method. His procedure, however, does not apply to non-linear equations or in random velocity fields [30, 31].

Gonzalez et al. [30, 31] were the first to use a series expansion of the semi-derivative formula for the history force in creeping flow as proposed by Tatom [45]. They also introduced a "memory time period" during which the history of the particle affected the current particle motion. The use of the semi-derivative formulation was found to reduce the computational cost by 20% compared to conventional techniques, and a time reduction of 10%-30% of the original simulation time was realized when the concept of memory time period was employed [31].

The justification for the use of memory time lies in the fact that particle behaviour at earlier times have a smaller contribution to the history force integral [34] at the current time. Mordant and

Pinton [42] noted that the history force at finite particle Reynolds number (as defined in Eq. (3.5)) can be well presented by the creeping flow expression for short intervals and becomes negligible thereafter [29]. Such findings inspired the development of a window model in which the history force was integrated over a prescribed finite time using the Basset kernel [29]. The truncation of integration time can yield more than an order of magnitude savings in CPU time compared to conventional history force calculations [29]. The model performed well for settling spheres with Reynolds numbers ranging from 9 to 853 and density ratios from 1.17 to 9.32. For oscillating particles the window model produced reasonable results only when changes in relative particle acceleration over the integration window were limited [29]. To further increase the accuracy of the window model, Van Hinsberg et al. [46] proposed the use of an exponential function to represent the tail rather than truncating it.

Although the use of the window model significantly reduces the computational time and memory requirements for calculating the history force, depending on Reynolds number and time step used, the model still requires storing particle information for few hundreds of time steps. Such requirement is still considerable for simulating natural and industrial processes with number of particles in order of millions or more. The objective of the current work is to seek a more efficient computational model in terms of memory resources and calculation time.

3.3 Numerical Method

In Lagrangian approaches, the path of each particle is predicted by the integration of its equation of motion resulting from the application of Newton's law of motion. In the point force (or point mass) model, the forces are described as a linear combination of individual contributions of different forces. A rigorously derived equation of motion for small particles in non-uniform flow derived by Maxey and Riley [47] forms a baseline equation of motion to which other force contributions are added. Neglecting forces arising from non-continuum effects, rotating reference frames, and lift forces, the equation of motion of particles interacting with other particles or walls can be written as

$$\frac{d\vec{u}_p}{dt} = \vec{f}_{Grav} + \vec{f}_{Drag} + \vec{f}_{Addm} + \vec{f}_{FS} + \vec{f}_{Hist} + \sum \vec{f}_{Contact} \qquad (3.1)$$

where the forces per unit mass on the right-hand-side are due to gravity, drag, added mass, fluid-stress, history, and collision forces, respectively. For collision forces, soft or hard sphere models

are commonly used to model particle interactions with other particles or with solid boundary in point force simulations. The soft sphere approach is used in the current work in which the contact force is decomposed into a normal force component and a tangential force component. The normal and tangential force components are modelled using a spring-dashpot-slider system. Details about the soft sphere model can be found in [22, 23]. In what follows, force models for solid spherical particles are presented.

3.3.1 Gravity force

Gravity force herein accounts for the weight of the particle (per unit mass of the particle) and is given by

$$\vec{f}_{Grav} = \vec{g} \tag{3.2}$$

where g is the gravitational acceleration.

3.3.2 Drag force

The drag force accounts for the quasi-steady viscous dissipation due to skin friction and form drag of the particle in uniform flow. The drag force is often a key element in interaction of dense granular flows. For the current work it will be modeled using the form

$$\vec{f}_{Drag} = \frac{3C_D\rho_f}{4d_p\rho_p}\left|\vec{u} - \vec{u}_p\right|\left(\vec{u} - \vec{u}_p\right) \tag{3.3}$$

where $\vec{u}\ and\ \vec{u}_p$ is the fluid velocity at the particle location and the particle velocity respectively. ρ_f, ρ_p, C_D and d_p are the fluid density, particle density, the drag coefficient, and the particle diameter. The drag coefficient for a sphere can be expressed as

$$C_D = \begin{cases} 24\left(1.0 + 0.15Re_p^{0.687}\right)/Re_p, & Re_p < 1000 \\ 0.44, & Re_p \geq 1000 \end{cases} \tag{3.4}$$

In which the particle Reynolds number Re_p is calculated as

$$Re_p = \frac{d_p\left|\vec{u} - \vec{u}_p\right|}{\nu_f} \tag{3.5}$$

where ν_f denotes the fluid kinematic viscosity.

3.3.3 Added mass

The added mass effect accounts for the force required to accelerate/decelerate the fluid surrounding the particle. A general formula derived by Lamb (1945) [48] for an isolated particle in creeping flow limit (Re_p <<1) is given by

$$\vec{f}_{Addm} = c_{\forall} \frac{\rho_f}{\rho_p} \left[\frac{D\vec{u}}{Dt} - \frac{d\vec{u}_p}{dt} \right] \tag{3.6}$$

Here $c_{\forall}$ is the added mass coefficient which is equal to 0.5 for a spherical particle, and the derivative *Du/Dt* is the change in fluid velocity following the particle path. Several studies have shown that the added-mass term predicted by creeping flow and potential flow theory works remarkably well for finite-Reynolds-number flows over a wide range of relative accelerations [49-52].

3.3.4 Fluid-stress force

The fluid stress force accounts for the fluid stress-gradients acting across the volume occupied by the particle. The fluid-stress force acting on a particle surrounded by a flow combines the effects of pressure gradients and viscous stresses of the fluid

$$\vec{f}_{FS} = \frac{1}{\rho_p} \left(-\vec{\nabla} p + \vec{\nabla} . \bar{\bar{\tau}} \right) \tag{3.7}$$

where the right hand side (RHS) can be replaced by the acceleration of the fluid and gravity force

$$\rho_f \left(\frac{D\vec{u}}{Dt} - \vec{g} \right) = -\vec{\nabla} p + \vec{\nabla} . \bar{\bar{\tau}} \tag{3.8}$$

Substituting Eq. (3.8) in (3.7) we get

$$\vec{f}_{FS} = \frac{\rho_f}{\rho_p} \left(\frac{D\vec{u}}{Dt} - \vec{g} \right) \tag{3.9}$$

Hence, the fluid-stress force contains the effect of both the buoyancy force and the unsteady force. The term $\frac{\rho_f}{\rho_p} D\vec{\boldsymbol{u}}/Dt$ is referred to as the unsteady force and can be calculated separately from the buoyancy effect which can be combined with the gravity force (Eq. (3.2)) in a submerged weight of the particle. The gravity force can be then expressed as

$$\vec{f}_{Grav,net} = \left(1 - \frac{\rho}{\rho_p}\right)\vec{g} \tag{3.10}$$

If shear stresses are negligible (e.g. gas fluidized beds) this force can be represented by pressure gradients alone

$$\vec{f}_{Pressure} = -\frac{1}{\rho_p}\vec{\nabla}p \tag{3.11}$$

3.3.5 History force

The history force model accounts for the temporal evolution of the viscous region near the particle (boundary layer) when the particle undergoes unsteady motion. The history force can be thought to be the unsteady part of the quasi-steady drag force (described earlier). This "unsteady" force model decays with time as the particle reaches an equilibrium condition (e.g., constant velocity). Basset (1888) [53] was the first to formulate the history force for spherical particles in creeping flow conditions. A general form of the history force can be written as

$$\vec{f}_{History} = -\frac{18\pi\nu_f\rho_f}{d_p^2\rho_p}\int_0^t K(t-\tau)\frac{d\vec{u}_{rel}(\tau)}{d\tau}d\tau \tag{3.12}$$

where $\vec{u}_{rel} = \vec{u} - \vec{u}_p$ is the relative velocity. For spheres in creeping flow the integration kernel, *K*, as formulated by Basset is given as

$$K_{Basset}(t-\tau) = \left[\frac{4\pi(t-\tau)}{\tau_d}\right]^{-1/2} \tag{3.13}$$

where τ_d is the diffusive time scale of the particle defined as

$$\tau_d = \frac{d_p^2}{\nu_f} \tag{3.14}$$

This force is difficult to evaluate and its value depends on the acceleration history up to the present time [54]. In the limit of creeping flow, Basset kernel indicates that the force decays at a rate ~ $\sqrt{t}$. Odar & Hamilton [55] proposed a correction of Basset history force for finite Reynolds number by using an empirical fitting parameter. The formula of Odar and Hamilton was widely accepted for many years [56]. Mei and Adrian pointed out that that the formulation of Odar and Hamilton was not physically or mathematically justified [57] since they assumed the decay rate at finite Reynolds number to be the same as that in the creeping flow limit.

Mei et al. [50], Mei and Adrian [57] determined that the short time behavior is consistent with the Basset kernel decay rate of ~ $t^{-1/2}$ as per Eq. (3.13), while the long time decay-rate is proportional to t^{-2}. For a finite Reynolds numbers they proposed the following kernel formula with constants c_1 = 2 and c_2 = 0.105 to match their resolved oscillating flow simulations

$$K_{MA}(t-\tau) = \left\{ \left[4\pi \frac{(t-\tau)}{\tau_d} \right]^{\frac{1}{2c_1}} + \left[\pi \frac{(t-\tau)^2}{\tau_d^2} \left(\frac{Re_p(\tau)}{0.75 + c_2 Re_p(\tau)} \right)^3 \right]^{\frac{1}{c_1}} \right\}^{-c_1} \qquad (3.15)$$

The above kernel combines both the short time limit of Basset (first term on RHS) and long time limit (second term on RHS). It can be seen that for small Reynolds numbers (Re_p< 0.1) the second term on RHS will be negligible and the decay rate will retrieve the Basset kernel. For time scales much smaller than the diffusion time scale (small $(t-\tau)/\tau_d$), the Basset kernel decay rate dominates since $((t-\tau)/\tau_d)^2$ is small. As the relative time $(t-\tau)/\tau_d$ increases, the long-time decay rate dominates. The diffusion time indicates the time during which the gradients diffuse with time during the unsteady process - the shorter the diffusion time, the particle reaches equilibrium with the fluid much faster; and larger the change in the relative velocity gradients between particle and fluid, the more significant the history force. As noted by Loth [58], the history force is related to the time-scales for convection and diffusion of momentum away from particles. For finite Reynolds particle numbers, convection effects help the temporal development of velocity gradients in the vicinity of the particle. The increase in Reynolds number thus implies a less significant history force.

Based on a large set of experimental data of settling particles Dorgan and Loth [29] found that c_1 = 2.5 and c_2 = 0.2 provide slightly better predictions. Laurence and Mei [59] found that depending on the type of motion the long time asymptotic behavior of the kernel may be t^{-2} of t^{-1} or even exponential. Similar conclusions reached by other investigators [60, 61] suggest the use of slightly different values of constants c_1 and c_2, however, the form of Equation (3.15) is generally accepted [29].

3.4 Mathematical Formulation

The current work deals with developing an efficient history force model that can be used for industrial and natural systems. The model targets saving both memory resources and the calculation time and can be used for particles with finite Reynolds numbers. The current model

assumes that the history force can be calculated by imposing a proper decay rate to the sum of history force increments. Derivation of the imposed "decay function" is presented.

3.4.1 Concept of decay function

For simplicity let us first consider the case in which history force can be represented by Basset formula

$$\vec{f}_B = C_B \int_0^t \frac{\frac{\partial \vec{u}_{rel}}{\partial \tau}}{\sqrt{t-\tau}} d\tau \tag{3.16}$$

where C_B is a constant defined as $C_B = \frac{-18\rho_f}{\rho_p\sqrt{4\pi\tau_d}}$. The above formula of Basset force (Eq. (3.16)) at time *t* can be expanded as [62]

$$\vec{f}_B = C_B \left[\frac{\Delta\vec{u}_{rel(1)}}{\sqrt{t_n - t_{n-1}}} + \frac{\Delta\vec{u}_{rel(2)}}{\sqrt{t_n - t_{n-2}}} + \cdots . + \frac{\Delta\vec{u}_{rel(n-1)}}{\sqrt{t_n - t_1}} + \frac{\Delta\vec{u}_{rel(n)}}{\sqrt{t_n}} \right] \tag{3.17}$$

It can be seen that the impact of the change in relative velocity that takes place at the n^{th} time step in the past ($\Delta\vec{u}_{rel(n)}$) will have less impact on the history force at time t_n compared to the more recent changes in velocity ($\Delta\vec{u}_{rel(1)}$). As time elapses the significance of initial changes in velocity will decay at a rate proportional to the square root of time. Considering the motion of a settling sphere at low Reynolds number as an example, as the particle starts reaching an equilibrium condition, the most recent changes in relative velocity will diminish; thus *Eq. (3.17) represents a decaying Basset force*. Assuming a constant time step we can rewrite Eq. (3.17) as

$$\vec{f}_B = C_B \left[\frac{\Delta\vec{u}_{rel(n)}}{\sqrt{n\Delta t}} + \frac{\Delta\vec{u}_{rel(n-1)}}{\sqrt{(n-1)\Delta t}} + \cdots . + \frac{\Delta\vec{u}_{rel(2)}}{\sqrt{2\Delta t}} + \frac{\Delta\vec{u}_{rel(1)}}{\sqrt{\Delta t}} \right] \tag{3.18}$$

For the general case, Eq. (3.18) will require $\Delta\vec{u}_{rel}$ to be stored at each time step. By assuming constant acceleration $\left(\frac{\Delta\vec{u}_{rel}}{\Delta\tau} = const\right)$ we can write

$$\vec{f}_B = C_B \frac{\Delta\vec{u}_{rel}}{\sqrt{\Delta t}} \left[1 + \frac{1}{\sqrt{2}} + \frac{1}{\sqrt{3}} + .. + \frac{1}{\sqrt{n}} \right] \tag{3.19}$$

Or more generally

$$\vec{f}_B = C_B \frac{\Delta\vec{u}_{rel}}{\sqrt{\Delta t}} \left[\sum_{i=1}^{n_{tot}} \frac{1}{\sqrt{n_i}} \right] \tag{3.20}$$

Here, n_{tot} is the total number of time-steps. Eq. (3.20) mathematically represents the Basset force for a particle moving with constant acceleration. In this limiting case, the history force can be calculated without a need to store any time-dependent data. A function can be fitted to the number of time steps *n* for the sum between brackets, and the expression does not require storage of any particle information. For varying acceleration, however, Eq. (3.20) uses the current acceleration (or current change in velocity) without real consideration to the change in acceleration; this implies that if the particle reaches an equilibrium condition ($\Delta\vec{u}_{rel(1)} = 0$), the history force will be zero. The history force at such condition is however not zero as can be seen from equation (3.18), since the particle will feel some force from previous changes in velocity gradients. A better approximation would be to use an averaged acceleration instead of the instantaneous acceleration such that

$$\vec{f}_B = C_B \frac{\overline{\Delta\vec{u}_{rel}}}{\sqrt{\Delta t}} \left[\sum_{i=1}^{n_{tot}} \frac{1}{\sqrt{n_i}} \right] \tag{3.21}$$

where

$$\overline{\Delta\vec{\boldsymbol{u}}_{rel}} = \frac{\sum_{i=1}^{n_{tot}} \Delta\vec{\boldsymbol{u}}_{rel}}{n_{tot}} \tag{3.22}$$

rearranging Eq. (3.21) we can write

$$\vec{f}_B = \frac{\left[\sum_{i=1}^{n_{tot}} \frac{1}{\sqrt{n_i}} \right]}{n_{tot}} \frac{C_B}{\sqrt{\Delta t}} \sum_{i=1}^{n_{tot}} \Delta\vec{u}_{rel} \tag{3.23}$$

or in the general form

$$\vec{f}_B = g(n). \sum_{i=1}^{n_{tot}} \Delta\vec{f}_B \tag{3.24}$$

here

$$\Delta\vec{\boldsymbol{f}}_B = C_B \frac{\Delta\vec{\boldsymbol{u}}_{rel}}{\sqrt{\Delta t}} \tag{3.25}$$

is a representation of the change in basset force for the current time step (Eq. (3.19) for one time step) and the function *g(n)* is defined as

$$g(n_{tot}) = \frac{\sum_{i=1}^{n_{tot}} \frac{1}{\sqrt{n_i}}}{n_{tot}} \tag{3.26}$$

Except for the first time step, Eq. (3.26) will be less than unity and will be termed as the "decay function" since it enforces a certain decay to a stored cumulative value. The use of Eq. (3.26) allows for a large reduction in the memory requirement as it requires storing only the non-decaying cumulative history force components (three additional variables per particles in 3D simulation) without any dependence on the simulation length. The reduction in calculation time will be discussed in a later section. A final general form applicable for finite Reynolds number and validation of the current model is discussed in the next sections.

3.4.2 Model formulation

An approximation of the decay function for finite Reynolds number (for Mei and Adrian kernel) is not as straight forward as the Basset kernel. The Basset kernel (Eq. 3.13) implies a decrease in the memory effects at a rate proportional to the inverse square root of time ($t^{-1/2}$). For finite particle's Reynolds numbers the Mei and Adrian kernel (Eq. (3.15)), suggests that the decay rate will be proportional to inverse square root of time for elapse times less than some "history time" and proportional to the inverse square of time for times larger than the history time (Fig. 3.1). Events which took place at times older than the history time window have a fast decay rate and can be neglected. The concept of neglecting events in time frames older than history time "or memory time" for finite Reynolds number was first used by [29]. Based on the above discussion, it is reasonable to assume that the decay function derived in the earlier section (Eq. (3.24)) can be imposed on the stored cumulative value till the history time is reached. The history time based on Mei and Adrian kernel [29] is given by

$$\tau_h = \tau_d \left(\frac{0.632}{Re_p} + 0.087 \right)^2 \tag{3.27}$$

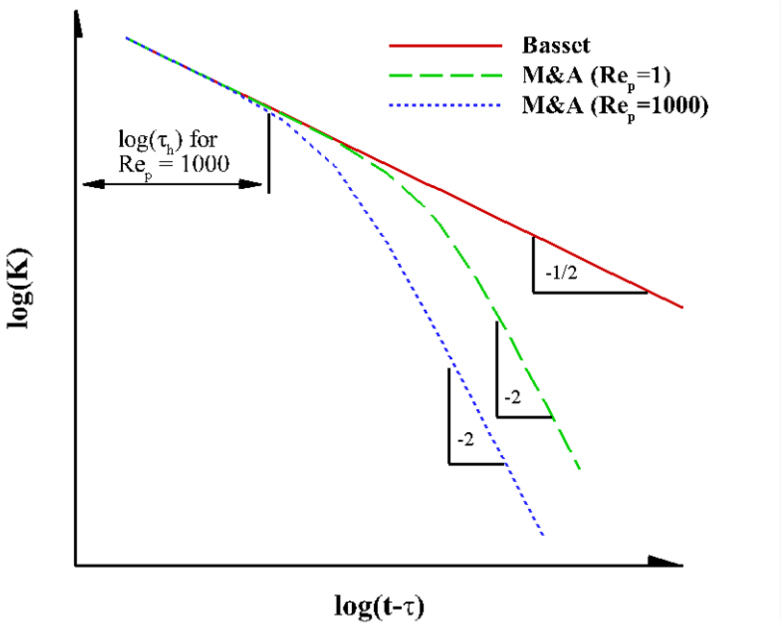

Figure 3. 1. Integration kernel of the history force at different Reynolds numbers.

The current model only accounts for the most recent events that have taken place within the history time. These events have a decay rate which is proportional to the inverse of square root of time (Basset kernel). Similar to the window model [29], earlier events will have a higher decay rate (ultimately proportional to the inverse of square of time) and are assumed negligible as compared to the more recent ones. The calculation of the history force is performed by multiplying the stored accumulated incremental history force by the decay function as long as the history time is not reached. When time reaches/exceeds the history time, the stored cumulative value should be updated to include the most recent running average. For instance, if the particle Reynolds number is constant after reaching the history time (terminal condition), the stored cumulative value should be decreased by a weight equivalent to one time step before adding the most recent time step to the stored cumulative value. Similarly, if the Reynolds number is increasing, the history time will decrease and the stored cumulative value should be decreased accordingly. In the current formulation this is done by multiplying the history time for the current step by the history time of the previous time step for cases with increasing Reynolds numbers. A flow chart of the calculation procedure is shown in Figure 3.2 below.

Both the travel time and history time (Eq. (3.27)) are first calculated. The travel time here is the time from the initial time step of interest, n_o, to the current time step. The incremental Basset force

from the current time step is calculated (Eq. (3.25)). If the travel time has not exceeded the history time (i.e., the history time has not been reached), then the incremental history force from the current time step is added to the cumulative history force. The cumulative history force here includes all events in the calculated travel time. Thus all the time steps in the travel time are considered in the decay function when applied to the cumulative value. If the history time is exceeded or reached ($t_t \geq t_h$), then the cumulative history force is reduced proportional to the ratio between the new and the previous history time (no reduction takes place if the particle Reynolds number remains the same). The time steps in the memory time are calculated based on the new history time. Before adding the current Basset increment to the cumulative value, an equivalent of one-time step is removed from the cumulative history force. Then the time step from which the calculation of the history time is of interest is updated.

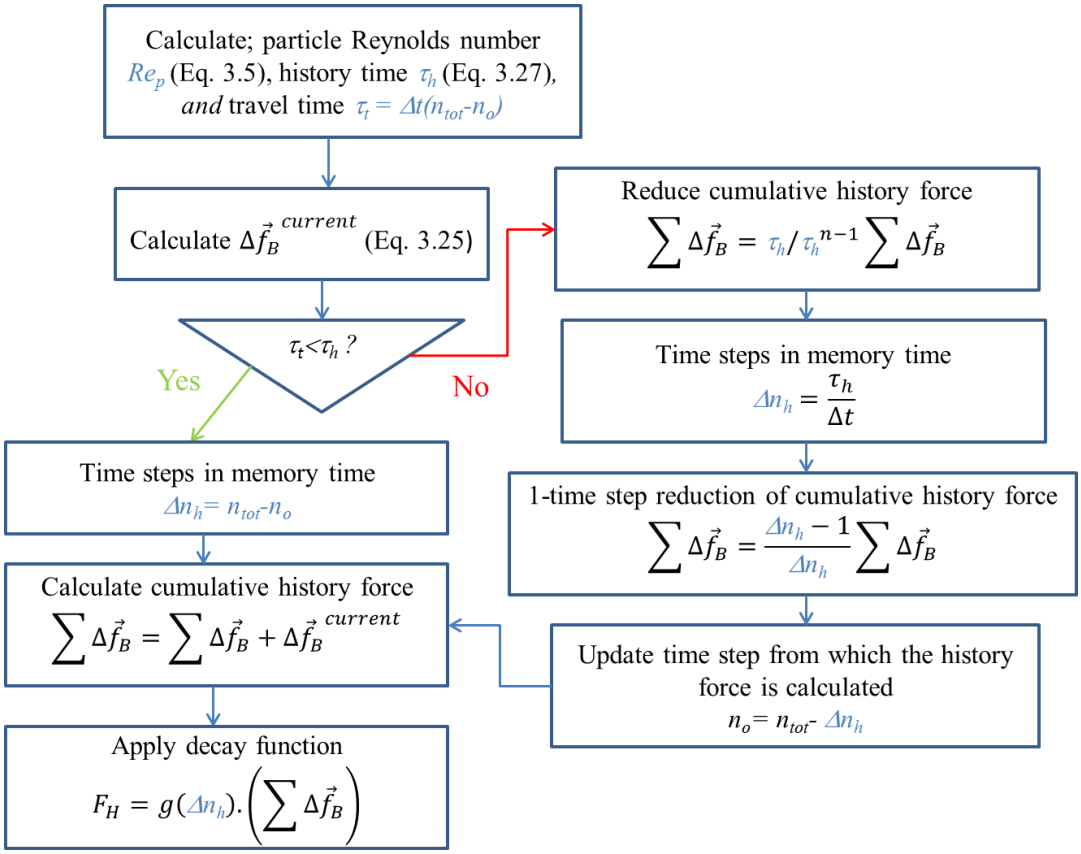

Figure 3. 2. Flow chart of current model.

The last aspect to be addressed here is a general formulation to reduce the cost of calculating of the new history force model. To avoid the overhead of calculating the decay function (Eq. 3.26) at

each time step we can fit it to the number of time steps *n*. The following piece-wise fit function is found reasonably accurate in representing the decay function

$$g_1(n) = \begin{cases} 1.04n^{-0.305}, & n \leq 10 \\ 1.53n^{-0.46}, & 2000 \geq n > 10 \\ 1.78n^{-0.49}, & 10000 \geq n > 2000 \\ 2n^{-0.5}, & \infty \geq n > 10000 \end{cases} \tag{3.28a}$$

An approximate single expression fit of the decay function can be written as

$$g_1(n) = 0.9279\left(\frac{2n-1}{n}\right)n^{-\left(\frac{n}{2n-1}\right)} + 0.001531 \tag{3.28b}$$

Figure (3.3) show the calculated decay function along with the above fit functions. The piece-wise function was used in the current work.

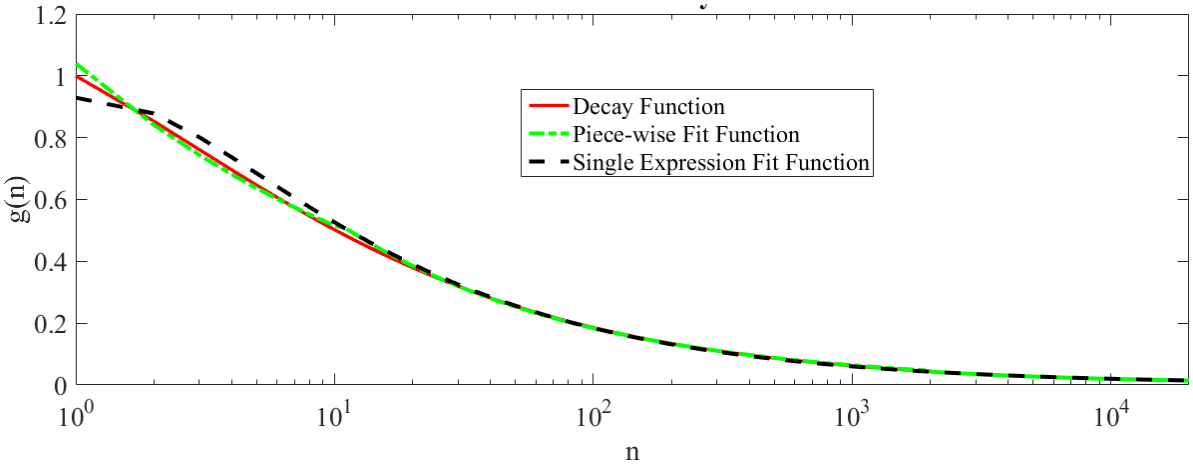

Figure 3. 3. Decay function vs. proposed fit functions.

3.5 Validation with Experiment

Three differrent sets of simulations are considered for validating the proposed history force model - settling particles, oscillating spheres, and bouncing spheres. In the first validation set of experiments we compare our simulation results with measurements of the motion of a settling particle released from rest. On each plot, the experimental measurement will be compared to results from activating drag and gravity (includes buoyancy effects) only, activating added mass along with drag and gravity forces, and activating the history force from current model along with all other forces. In the oscillating sphere validation cases, the sphere is forced to move in a prescribed oscillating mode and the overall force acting on it is measured. The measured overall force on the

osillating sphere is compared to the sum of the predicted hydrodynamic forces. In the bouncing sphere validation cases, particles are released from rest and allowed to collide with a solid boundary (wall). The rebound trajectory when activating different force models is compared to the experimental data at different Reynolds numbers and density ratios to show the impact of each force.

3.5.1 Settling spheres

In these simulations the particles (spheres) are released from rest under the effect of gravity and their velocity is monitored and recorded untill they reach their terminal velocity. By doing so it is possible to collect information related to the unsteady part of the motion of settling spheres. Selected experiments from Moorman [63], Pinton & Mordant [42] and Ten Cate et. al [64] are simulated to cover a range of particle Reynolds numbers (from ~1- 280) and density ratios (~1.2-9.2). The specifications and main characterisics of selected experiments are summarized in Table 4.1. The velocity variation in the Figures is normalized by the terminal velocity, and time is normalized by the diffusion time (as per Eq. (3.14)) as given in Table 3.1.

Figures 3.4, 3.5 and 3.6 show a comparison of simulations at three different density ratios ($S = \rho_f / \rho_p$) of 3.7, 2.47 and 1.12, respectively. Simulation results are shown in each figure for cases in which only drag and gravity forces are active, drag, gravity and added mass forces are active, and when all forces are active (current model). The results cover a range of terminal Reynolds numbers ranging from nearly 1 to about 280. Figure 3.7, shows comparisons for settling particles at different density ratios and approximately the same Reynolds number of ~30. Two additional validation cases from Mordant and Pinton at different Reynolds numbers and density ratios are presented in Fig. 3.8. The point at which the history time is first reached can be seen as a discontinuity at small Reynolds number (most obvious in case E1 of Fig. 3.6). This behavior can be attributed to the fact that the history force is truncated when the history time is reached. To account for truncation of the tail (high decay rate part in Mei and Adrian kernel) once the history time is reached, the cumulated history force (on which the decay function is applied) is reduced by two mechanisms. In one mechanism, the cumulative history force is reduced in proportionality to the ratio of the history time of the current time step to the history time of the pervious time step. The other reduction technique is done by reducing the cumulative history force by one step before adding the most recent one (which is smaller as compared to averaged cumulative value). The

transition from continuous addition of increments to the cumulative history force to the reduction of cumulative history force is not smooth and particles which show/undergo quick/fast change in their acceleration will show more notable discontinuity.

Moorman's Run #31 (Figure 3.5) and Ten Cate et al.'s Experiment E1 (Figure 3.6) experiments show some notable deviation in the region where history time is reached. Both cases have a particle Stokes number (defined as $\rho_p d V_{term}/(18\mu_f)$) of ~0.12 and 0.1, respectively, which are the lowest amongst all the simulations. The small Stokes number indicates that the particle will have a fast response time and hence the constant acceleration assumption might not hold within the memory time of the particle. It should be mentioned that the constant acceleration assumption is also used in deriving the history time formula (Eq. (3.26)) [29] which might also require no large changes in acceleration within the window time for the history time to be accurate. The model, however, shows very good comparison as compared to experimental data of settling spheres for most of the cases. It should be mentioned here that the fit function of (Equation 3.28a) is used in the presented results. The time steps used were less than 0.01 of the particle time scale.

Table 3. 1. Sphere and fluid properties for the selected settling sphere experiments.

Run #	$Re_{p,term}$	d(mm)	ρ_p (kg/m^3)	ρ_f (kg/m^3)	ν_f (m^2/s)	τ_d(s)
Moorman						
10	31.5	11.1	7782.2	850.4	2.7e-4	0.4553
19	181	15.88	3076.8	834.9	7.2e-5	3.502
21	67	9.51	3076.8	834.9	7.2e-5	1.256
22	28	6.37	3076.8	834.9	7.2e-5	0.564
27	29	12.71	3076.8	1247.2	1.49e-4	1.087
29	6	6.37	3076.8	1247.2	1.49e-4	0.273
30	4.2	6.37	3076.8	1252.4	1.88e-4	0.216
31	0.9	6.37	3076.8	1257.5	4.49e-4	0.09
Mordant and Pinton						
CASE-1	41	0.5	2560	1000	1e-6	0.25
CASE-4	260	0.8	7710	1000	1e-6	0.64
Cate et. al.						
E1	1.5	15	1120	970	3.85e-4	0.585
E2	4.1	15	1120	965	2.2e-4	1.024
E3	11.6	15	1120	962	1.17e-4	1.915

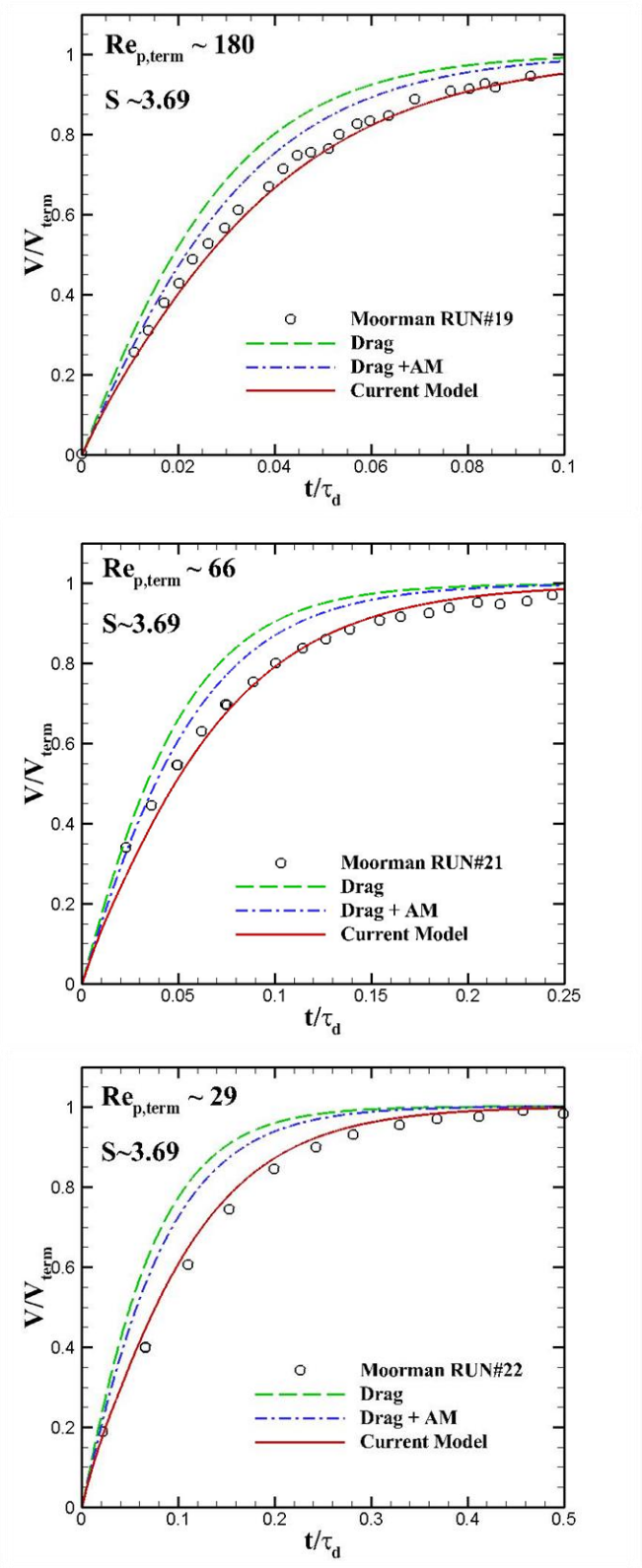

Figure 3. 4. Comparison of experiment with current model at constant density ratio (~3.7) and different Reynolds numbers.

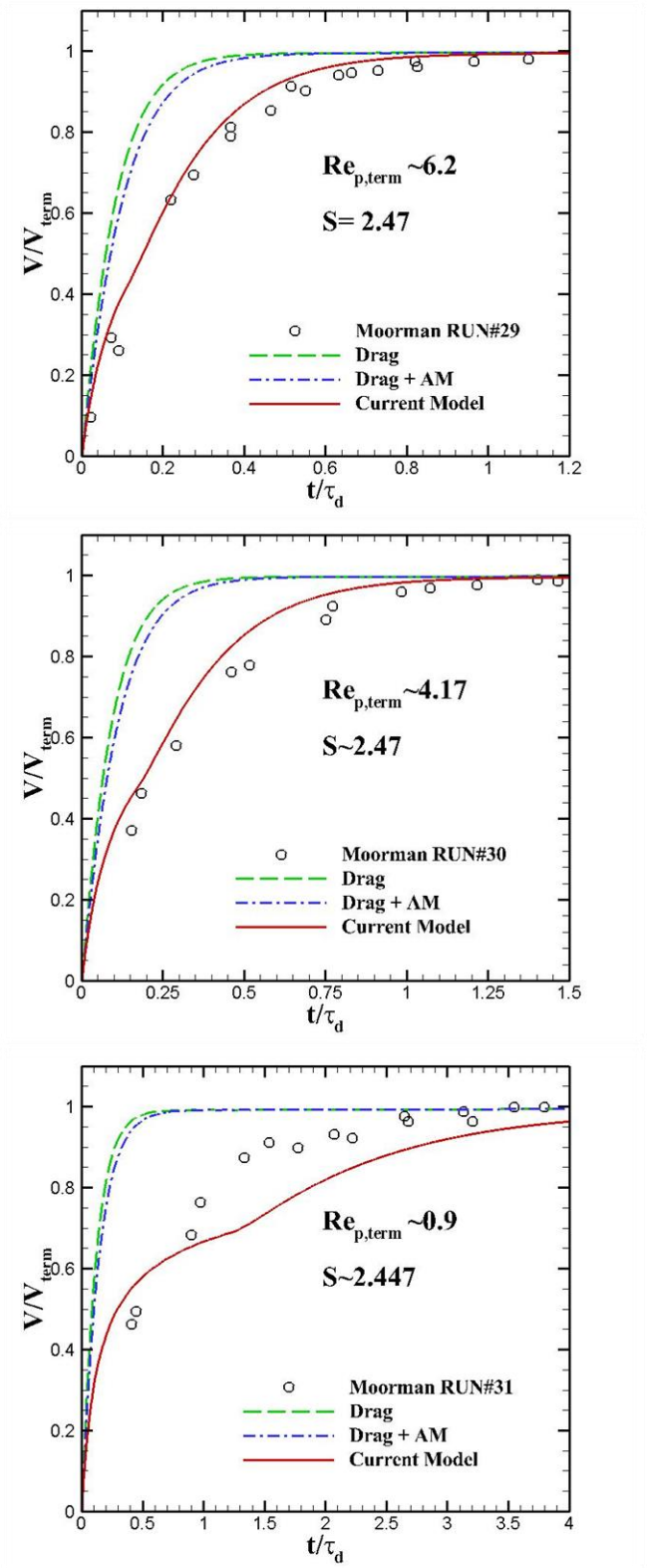

Figure 3. 5. Comparison of experiment with current model at constant density ratio (~2.47) and different Reynolds numbers.

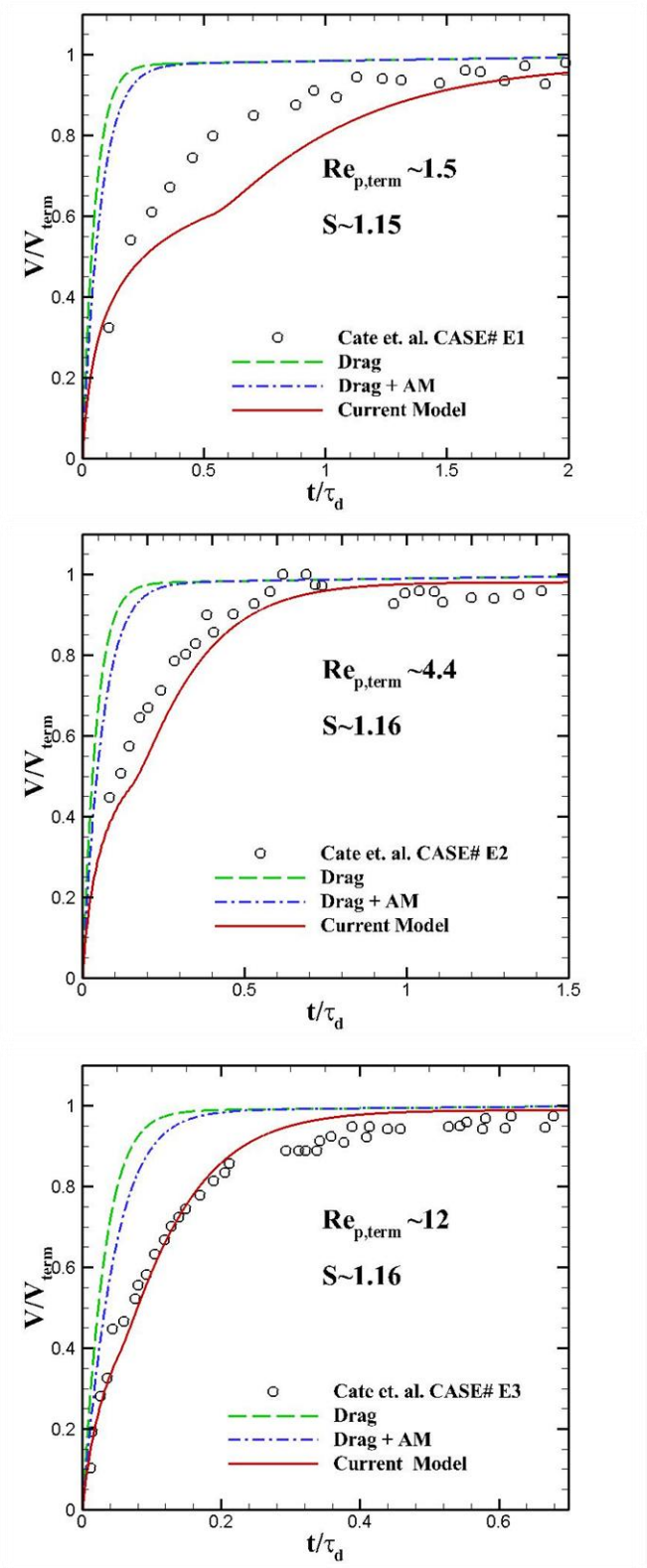

Figure 3. 6. Comparison of experiment with current model at constant density ratio (~1.16) and different (low) Reynolds numbers.

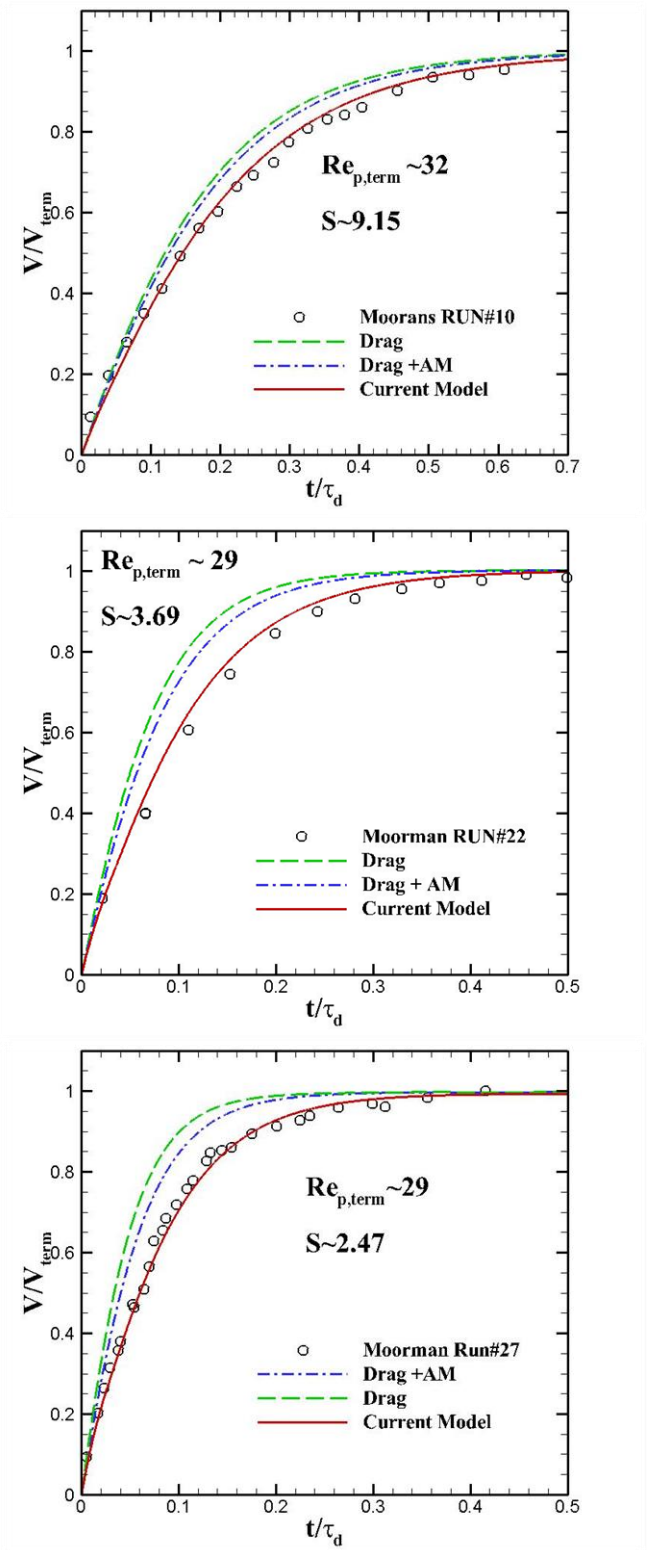

Figure 3. 7. Comparison of experiment with current model at same Reynolds numbers $Re_{p,term}$~30 and different density ratio.

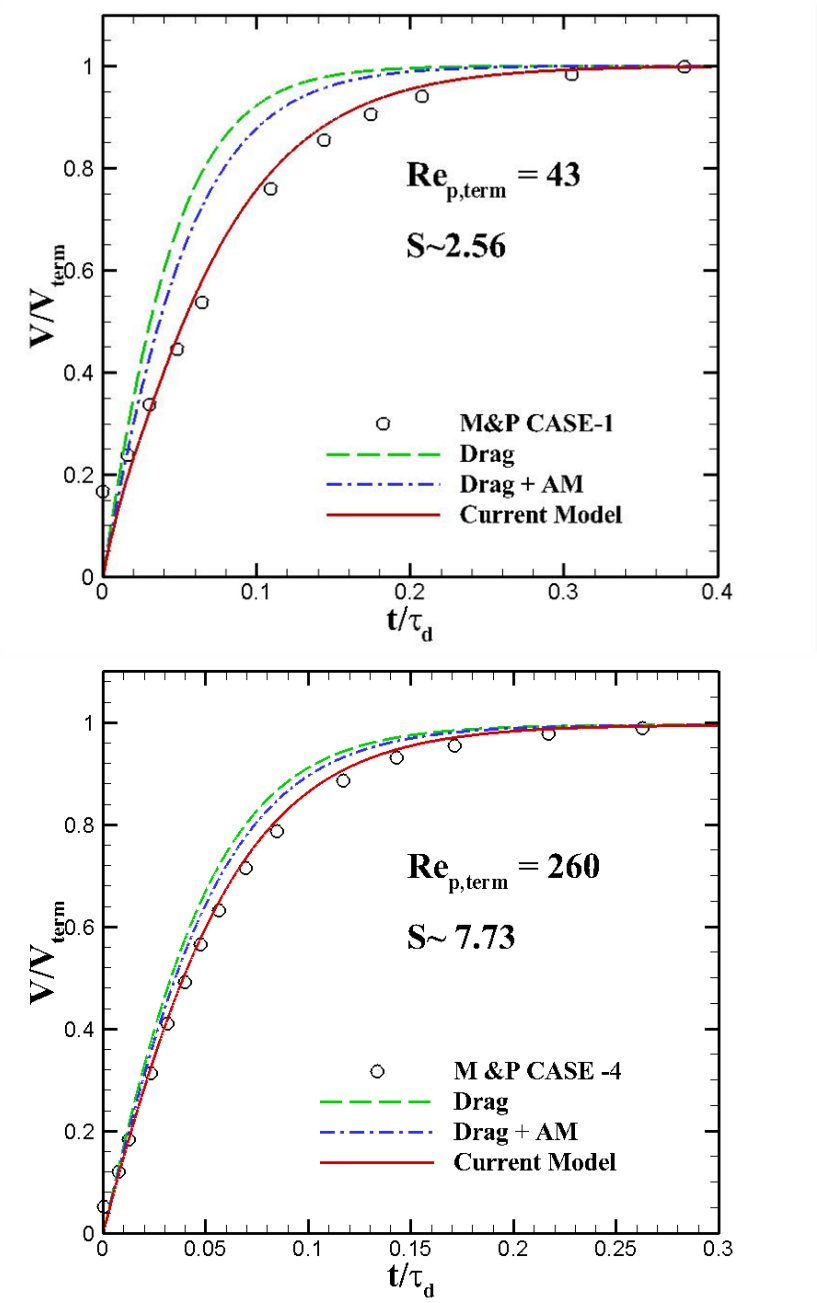

Figure 3. 8. Comparison of current model with Mordant & Pinton data.

3.5.2 Oscillating sphere

Selected cases from the experimental work of Odar and Hamilton [55] are considered for validation of the current model. The experiments are conducted by oscillating a 2.5 inch hollow sphere at different frequencies and amplitudes. The prescribed motion of the oscillating sphere is given by $A_o cos(\omega t)$, where A_o is the amplitude of the periodic motion and ω is the rotational speed of the

oscillation. The apparatus allows for the frequency to be varied from as low as 1.67 rad/s up to 16.4 rad/s with amplitudes of 1, 2, 3 or 4 inches (2.54, 5.08, 7.62 and 10.16 cm). The effective mass of the moving sphere system was found to be 0.128 grams, with an effective solid-to-fluid density ratio of S=1.07. The work of Odar and Hamilton also provided individual calculated hydrodynamic force components such as drag, added mass, and history force during the oscillation. Their formulation of the added mass was incorrect since the added mass coefficient was considered as a variable. Since these values were used to calculate the history force, as a result their history force values were in error too. A correction of the analysis of Odar and Hamilton by using a constant added mass coefficient was performed by Michaelides [65] for a number of experiments. Hence, in the current work only the measured total force of Odar and Hamilton's work is used and compared to the sum of the modeled individual force components. The parameters of the selected experiments are listed in Table 3.2. The Reynolds number is based on the maximum velocity of the oscillating particle (occurs at $\omega t=\pi/2$) and the corresponding Strouhal number is calculated using the following formula [29]

$$St = \frac{\omega d_p}{2V_{rms}} \tag{3.29}$$

where V_{rms} is the root mean square of the wave velocity.

Table 3. 2. Experimental parameters for oscillating sphere experiments.

Run #	Frequency (rad/s)	diameter (mm)	Strouhal number	$Re_{p,max}$
9	4.61	50.8	0.9	16.7
18	11.9	50.8	0.9	43
29	5.0	25.4	1.74	9.22
38	13.3	25.4	1.77	24.1
50	5.1	76.2	0.59	27.65
56	9.37	76.2	0.59	51
65	5.63	101.6	0.44	40.7
68	7.63	101.6	0.45	55

Figure 3.9 shows the calculated individual force components on the oscillating sphere for one cycle. The forces are non-dimensionalized with respect to the effective weight of the moving mass. The inertia force shown here is a result of the motion of the effective mass of the oscillating system which will also be part of the total measured force. The sum of all forces is compared to the

measured force provided by Odar and Hamilton. It can be seen that all forces are of the same magnitude, and the calculated overall force agrees well with the experiments except near the peaks, which are underrepresented by the model. The deviations increase with an increase in the amplitude of oscillation from about 10% to roughly 20% at 4" amplitude (Run#65 and 68). It should be mentioned here that, such deviations can also be attributed to uncertainty in the experiment, the uncertainty in the drag correlation, and the history force model of Mei and Adrian. A difference of 10% can exist between the measured force and the total calculated force even when the full velocity information of the particle is stored and used to calculate the history force using Mei and Adrian integration kernel (Eq. (3.15)) [29]. The maximum value of the total force occurs just after the particle changes the direction of its motion (this corresponds to the zero velocity and zero drag location). The total predicted force shows a sharp change near the apex as a result of the abrupt change in history force calculated using the current model. The abrupt change in the modeled cumulative history force is attributed to the increase in Reynolds number which triggers an adjustment in the cumulative history force caused by the corresponding decrease in history time, and the fact that the newly added incremental history force will have an opposite sign as compared to the stored value.

Overall, the predicted force compares well with the experiments, in spite of the differences near the peak. In cases of abrupt change of motion where the particle is in direct interaction with its wake, Lawrence and Mei [59] showed that the decay rate of the history force will be much faster at a rate proportional to the inverse of time. As such, the integration kernel of Mei and Adrian (Eq. (3.15)) may not be appropriate [29]. Results from using Mei and Adrian kernel for Odar and Hamilton's oscillating sphere experiments, however, showed that the applicability of the Mei and Adrian kernel is still valid since reasonable agreement was achieved in the selected cases of these experiments. Dorgan and Loth [29] suggest that the change in the decay rate due to the ingestion in the wake would become more evident for cases with higher Strouhal number ($St >> 1$).

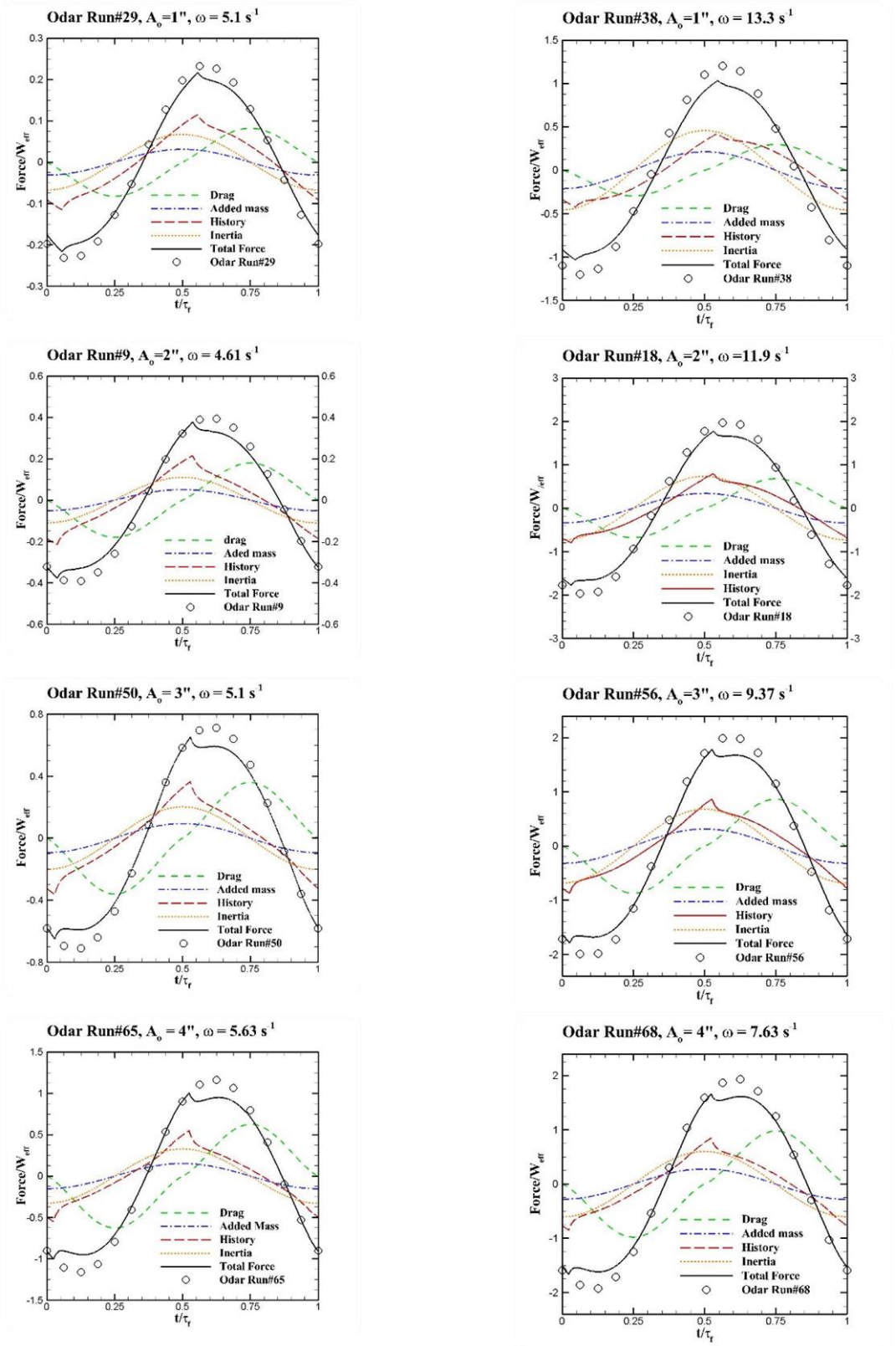

Figure 3. 9. Measured vs. calculated force on oscillating sphere at different amplitudes and frequencies.

3.5.3 Bouncing spheres

Experiments of Gondret [66] are selected to evaluate the performance of the decay function model for bouncing spheres. Seven experiments are selected in which solid particles bounce in liquids. The liquids in the experiment are water and silicone oils of different densities and viscosities. The key parameters of the simulations are listed in Table 4.3, where the Reynolds number is based on the particle radius and impact velocity. The soft sphere collision model [23] is used with a spring stiffness of 800 N/m to model the collisions. The time step of these simulations is made smaller than the critical collision time scale [22] by more than 15 times and was less than 0.001 of the particle time scale. To start a simulation, the sphere is released from rest and is allowed to move under the effect of gravity and buoyancy. The initial height is set such that it ensures an impact velocity equal to the rebound velocity of the experiment, implying a perfectly elastic collision. All forces of interest are activated just before the collision. The history force in this case is assumed to reach its terminal velocity with zero value at the incipience of collision.

Figures 3.10(a-d), show the first rebound of simulations of steel spheres in oil. The rebound height (h) is non-dimensionalized by the particle radius, and the particle radius and the impact velocity (U_i), (based on impact Reynolds numbers as listed in Table 3.3) are used to non-dimensionalize the time scale. The density ratio is approximately the same (~8), whereas the impact Reynolds number is different between cases. The simulation results are shown for cases when only gravity (includes buoyancy) is active; gravity and drag forces are active; gravity, drag and added mass, and the last case with all forces active including the history force as calculated from the current model. As noted by Gondret, it can be seen from the simulation results that as the Reynolds number increases, the drag force increases. The added mass effect, however, is the same since the density ratio is kept the same. The added mass seems to give energy to the bouncing sphere as it bounces to heights larger than that with gravity and drag forces only. The effect of added mass in a particle decelerating in a still fluid can be thought to be the same as the effect of accelerating fluid surrounding a stationary particle. As can be seen from Figure 3.10, the history force seems to be over predicted by the current model for case 10A (Reynolds number of 394) by about 10%, but shows good comparison for the remaining cases.

Table 3. 3. Sphere and fluid properties for the selected bouncing sphere experiments*.

Fig #	$Re_{p,impact}$	d_p(mm)	ρ_s (kg/m^3)	ρ_f (kg/m^3)	μ_f (m^2/s)	τ_d (s)	$Re_{p,rebound}$
Gondret							
10A	394	5	7800	920	0.005	4.6	369
10B-11B	106	6	7800	953	0.02	1.715	84
10C	55	4	7800	953	0.02	0.762	39
10D	15	6	7800	965	0.01	0.347	7
11A	108	5	14970	953	0.02	1.191	96
11C	119	6	2500	935	0.01	3.366	89
11D	91	5	1410	920	0.005	4.6	57

* Reynolds number based on particle radius

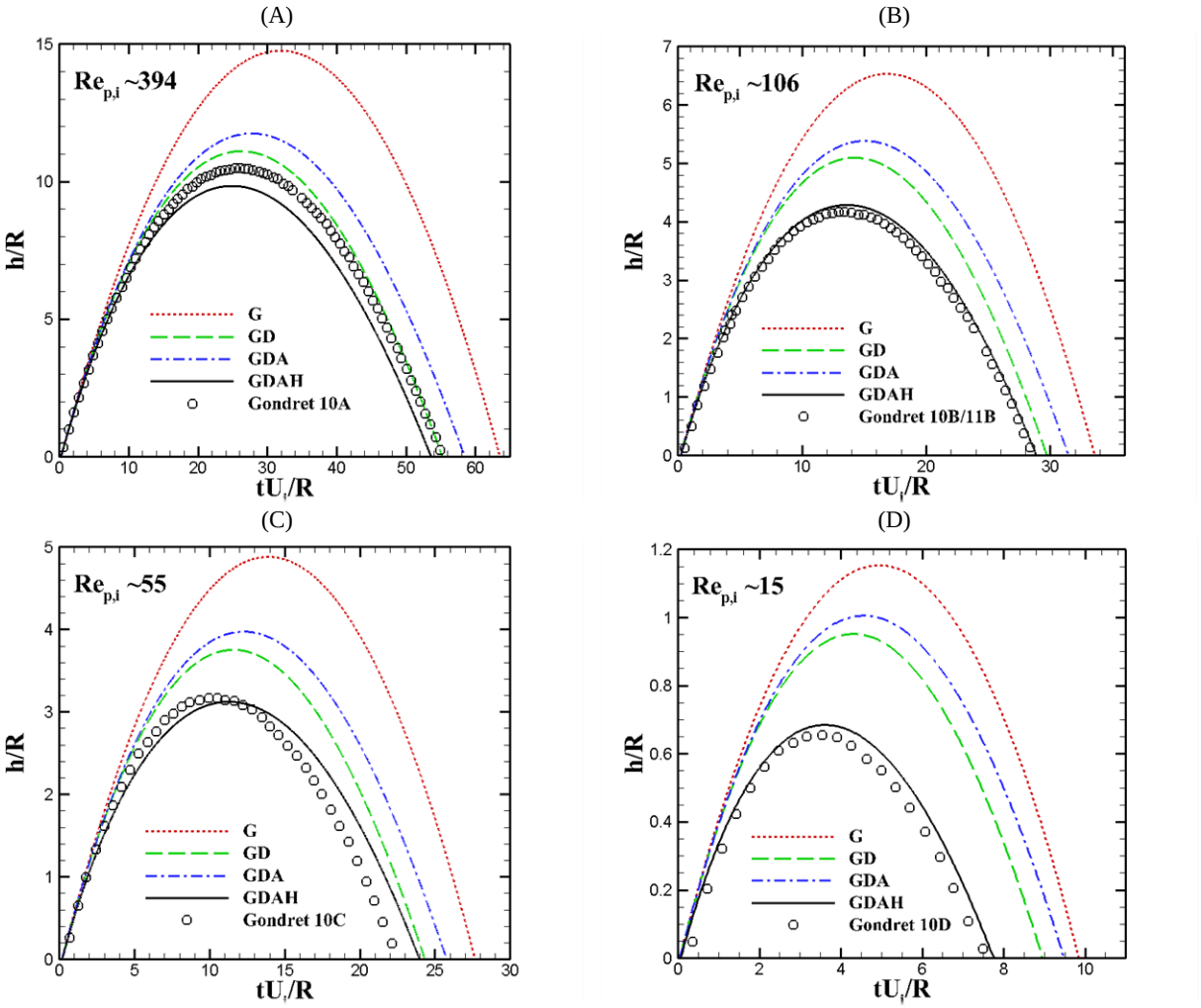

Figure 3. 10. Rebound trajectories for spheres at different Reynolds numbers and constant density ratio (S~8).

Figures 3.11(a-d) present the rebound trajectories at approximately the same impact Reynolds number but at different density ratios. It can be seen that the current model under predicts the history force by about 10% for case 11A, but shows good agreement for cases 11B and 11C. For case 11D, however, it can be seen that the current model over predicts the force such that the rebound height is underestimated by about 50%.

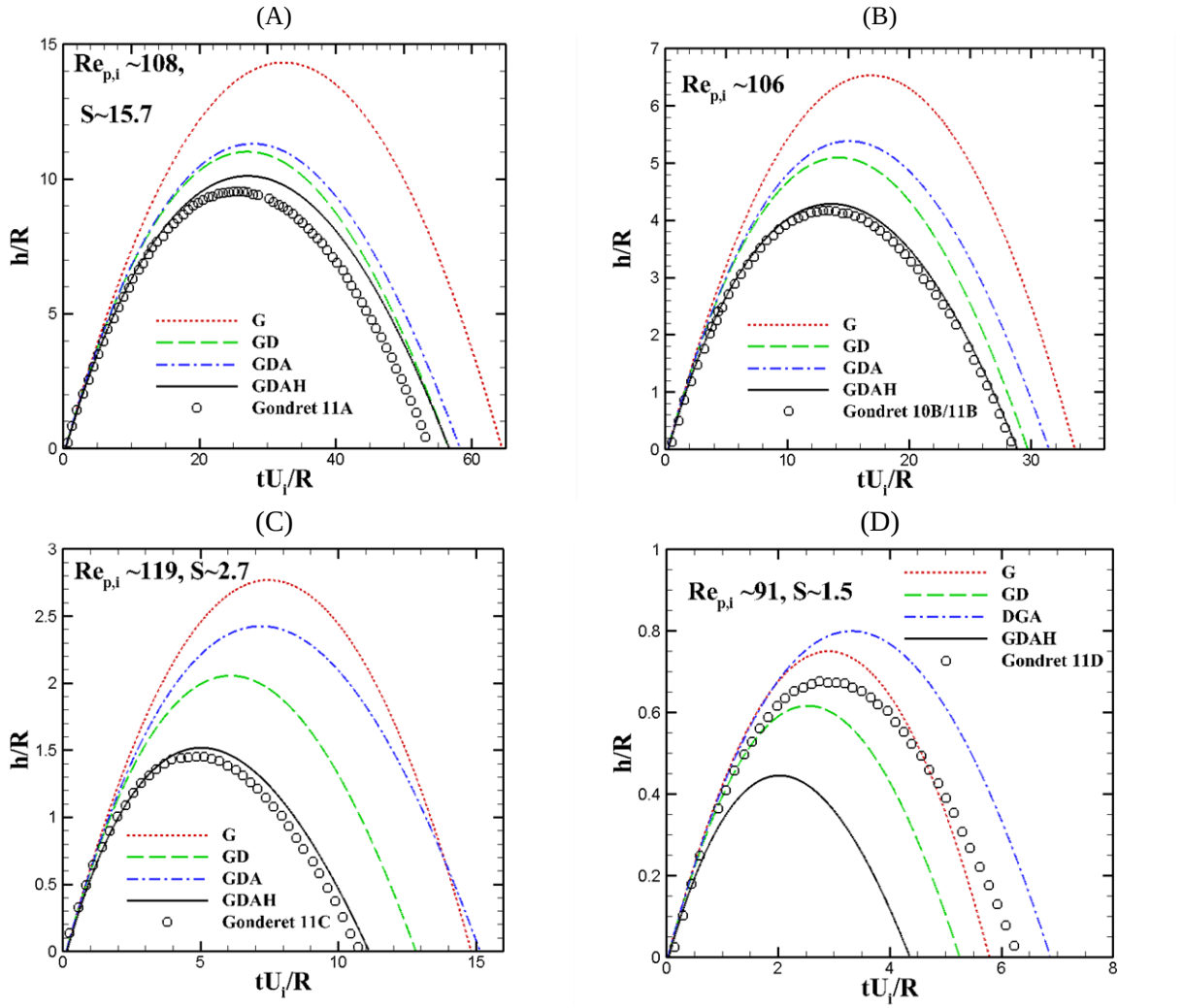

Figure 3. 11. Rebound trajectories for spheres at different density ratios and the same impact Reynolds number ($Re_{p,impact}$ ~100).

This can be due to the fact that the particle is being ingested into its wake in this impulsive motion. It is suggested that because the rebound of the particle is taking place near the wall, it will have longer interaction time with its own wake on its way to the wall. As discussed in the previous section, according to the findings of Mei and Lawrence [59] the long time decay rate of cases with sudden stops or reversal in motion become proportional to the inverse of time and the use of Mei

and Adrian kernel (Eq. (3.15)) becomes inappropriate. Comparison of the current model results in other bouncing sphere cases, however, suggests that the use of inverse of square root time decay rate of Mei and Adrian kernel may still be appropriate for similar situations. It is suggested that there might be other parameters which determine whether the wake will alter the decay rate of an oscillating or bouncing sphere. For instance, Dorgan and Loth [29] suggest that the Strouhal number of the oscillating particle has to be large enough to violate the applicability of Mei and Adrian kernel. In the current bouncing sphere experiments, the for case 11D, the rebound height is found/estimated to be the smallest as compared to the length scale of the wake among all cases (ratio ~0.27, second smallest for 11C is ~0.52, others are more than 1.5) which may indicate stronger impact of the wake on the rebounding trajectory. The ratio of wake length to the particle diameter was roughly estimated using findings of Taneda [67] as

$$\frac{L_w}{d} \sim 1.45 \times \log\left(Re_p/24\right) \tag{3.30}$$

Other than Case 11D, the model generally shows reasonably good agreement compared to experiments. The activation of all unsteady forces improves the prediction as compared to drag and gravity effects only. In all the rebound cases it can be seen that the activation of added mass force without the history force can lead to more deviations as compared to neglecting unsteady forces altogether (i.e. activation of drag, gravity and buoyancy only). It should be noted that some cases show deviation in the calculation of terminal velocity which can be due to uncertainty in experimental measurements or due to uncertainties in the drag model or differences in parameters used in the simulation and the actual parameters of the experiments. Noting that, the history force model is activated just before the collision such that the particle starts the collision with no prior history.

3.6 Computational resources

The current model greatly reduces the memory requirements to calculate the history force. In the current formulation only five variables need to be stored per particle for the entire simulation, three variables for the cumulative value of the history force in each direction for a three dimensional simulation, together with two additional variables to store the previous history time of the particle and the starting time step. These memory resources should be compared to 3n (where n is the number of time steps) for the full calculation (savings ~O(n)) of the history force. The reduction

in floating point operations depends on how long the simulation is run. For example the floating point operations required to calculate the Basset force for 3D simulation is about 70 different operations using Eq. (3.28a). On the other hand, the traditional 3D calculation of the history force using the Basset kernel will require about 4+21(n) different floating point operations. It is also interesting to compare the current model to the window model [29]. In the window model the history force is calculated by only using the particle information for the previous memory "history" time using the Basset kernel. It is estimated that the calculation will require 25+21(n_h) different floating point operations where n_h is the number of time steps to reach the history time.

Figure 3.12, shows the CPU time required to calculate the history force per time step for a selected case using the three different calculation techniques, the full history force calculation, the window model, and the current model. For the former two calculations, mock subroutines were used in which only information of current and previous time step are used. For full calculation of the history force, only Basset kernel (less expensive) was considered.

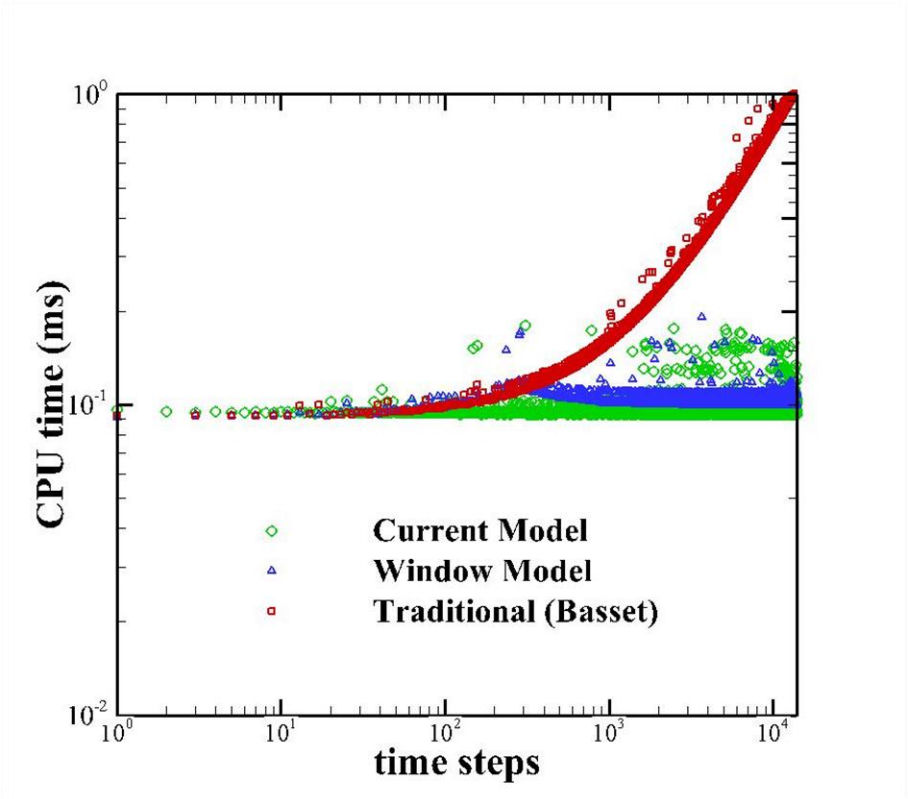

Figure 3. 12. Comparison of CPU time required to calculate the history time.

It can be seen from Fig. 3.12 that the full calculation can be done faster than or at about the same time as the current model only at the very first few time steps. However, the full model becomes a lot more expensive as the simulation proceeds in time ~ O(n). The window model follows the same trend as the full force calculation until the history time is reached; as the particle attains a higher Reynolds number the corresponding history time decreases. It can be clearly seen that the current model significantly reduces the CPU time for long integration times as compared to the traditional calculation and also compared to the window model. The scatter in the points shown is because of change in compute machine performance. Some of the calculations of the current model (scattered) seem to be slower than the window model. The authors attribute this to the fact that the current model involves more expensive arithmetic calculations compared to the window model (i.e., multiplication, division and exponents takes more floating operations per second as compared to addition) thus showing more sensitivity to changes in machine performance. It should be noted here that the window model will differ in computational complexity depending on the Reynolds number whereas the current model exhibits the same behavior independent of the Reynolds number.

3.7 Summary and Conclusions

In this work a new modeling approach for history force is proposed. The new model saves both CPU time and memory resources. The model shows very good agreement with settling particle simulations for a wide range of Reynolds number ranging from ~1 to ~ 260. Some deviation was noticed at smaller Reynolds numbers ~1, which can be attributed to the rapid change in acceleration in a short time which may not be consistent with the assumptions made in deriving the current formulation.

The model also shows good agreement when compared to available experimental data of oscillating spheres at different frequencies and amplitudes, and spheres rebounding from a wall over a wide range of Reynolds numbers and density ratios. The current model efficiently calculates the history force in terms of both memory resources and calculation time. The memory resources are reduced to saving only 5 parameters per particle for the whole simulation compared to 3n per particle when using the full force calculation method using the Basset kernel and few hundreds per particle when using the window model [29]. The large savings in memory resource and computational time makes this formulation a good candidate for use in application where large

number of particles are simulated for long times. Validating the performance of the model in a complex flow-field is difficult to tackle and was not tested. The validation of the model in basic modes of motion, however, indicates that it could produce quantitative/qualitative agreement in a combination of these modes. The model was developed and validated assuming/using a constant time step. The applicability of the model is limited to cases where Basset or Mei and Adrain kernel are applicable (e.g. Mei and Adrian kernel may not be applicable if the particle is ingested into its own wake). The model deviates from experiments when large variations in acceleration take place within the memory time period. These deviations where noted as discontinuities for settling spheres with small Stokes numbers (~0.1).

Chapter 4

LES-DEM Simulations of Sediment Transport

Husam A. Elghannay* **and Danesh K. Tafti***

*Department of Mechanical Engineering
Virginia Polytechnic Institute and State University
Blacksburg, Virginia 24061

Citation:

Elghannay, Husam, and Danesh Tafti. "LES-DEM simulations of sediment transport." *International Journal of Sediment Research* (2017).

4.1 Abstract

In this work, a fully-coupled Computational Fluid Dynamics (CFD) model and Discrete Element Method (DEM) are used to simulate a unidirectional turbulent open-channel flow over the full range of sediment transport regimes. The fluid and particles are computed on separate grids using a dual-grid formulation to maintain consistency and avoid instability issues. The results of coupling the dispersed phase to a multiphase flow solver that uses volume-averaged Navier-Stokes equations are compared to those obtained from coupling through drag to a single flow solver. The current work also examines the applicability and limitations of lumping particles as a representative particle to reduce the cost of simulations. Insight to the impact of different turbulent events to the entrainment of particles is also given. The simulation results of sediment transport from both coupling techniques show good agreement with empirical formulas in the bedload regime, but under-predict sediment transport in the suspended load regime. In the suspended load regime, using partial coupling, the rate of sediment transport was found to be under-predicted as compared to full-coupling. The deviation in results in the suspended load regime was found to increase with increases in the applied shear stress. Both coupling methods revealed the same effect on the friction factor where friction increases in the bedload regime and decreases in the suspended load regime reaching a maximum at the transition between regimes. This result is contrary to past studies which have shown a discrete jump in the friction factor at the transition. Lumping particles as representative particles is shown to reduce the simulation cost by more than a factor of 5 when using a scaling factor of 2. By doing a quadrant analysis on information obtained from particle and flow field results, it was found that most of the particles are entrained by more frequent sweep events.

4.2 Introduction

Sediment transport is vitally important in many geological and engineering applications. Understanding the underlying physics of sediment transport is important to identify the conditions under which erosion and deposition take place. Two aspects are of vital importance to sediment engineers: the condition at which the magnitude of hydrodynamic forces become capable of entraining sediment particles (the *critical condition* or *threshold condition*), and the transport rate of the solids in the flow. Many experimental and theoretical efforts have been done during the past several decades to determine the condition of incipient motion and the sediment transport rate. An

extensive recent review of the most used methods to calculate the incipience of particle motion can be found in Dey [68]. A review of the most commonly used sediment transport formulas along with their range of applicability can be found in Chanson [69]. Among the various parameters proposed and used to predict the incipience of motion the most commonly used approaches are either based on mean flow velocity or the bed shear stress. Recent research work suggests that the entrainment of sediment particles relates to the impact of large impulse forces for short times during turbulent events [e.g., 70].

Two-approaches are commonly used to study granular/particulate flows, namely the Eulerian-Eulerian description and the Eulerian-Lagrangian approach. Most Eulerian-Eulerian sediment transport models in use solve the Reynolds Averaged continuity and Navier-Stokes (RANS) equations of the carrier fluid along with the mass balance equation for the sediment [71]. With the introduction of closures, the sediment mass balance (or continuity) equation is usually interpreted in the form of a convection-diffusion equation which solves for the sediment concentration. Large-Eddy Simulation (LES) was recently integrated in this description [e.g., 72, 73]. Another Eulerian-Eulerian approach is the Two-Fluid-Model (TFM) in which a volume averaged Navier-Stokes equation is used to solve the dispersed phase [e.g., 20]. In the TFM, additional closure models are required to account for the continuum properties of the dispersed phase (i.e. pressure and viscosity). These closure models typically use theoretical or semi-empirical correlations [74]. In a Partial-Two-Fluid-Model, the mass and momentum of the two phases are combined and solved for the mixture [75]. Different research groups [76, 77] applied a RANS model of the carrier fluid to account for turbulence and showed good comparison to empirical correlations (and Eulerian-Lagrangian descriptions) of sediment transport in the bedload and suspended-load regimens.

In Eulerian-Eulerian models, the bed morphology (or elevation) is calculated by solving the mass balance equation at the surface using the Exner [78] or Exner-Paola equation [79]. The process of solving for morphodynamics is usually associated with the use of additional closures (e.g. sand-slide algorithm to control the repose angle of sand). Using these techniques, Eulerian-Eulerian descriptions have been used to predict morphodynamic and sand-wave formation along with scour around piers [80-83].

Although Eulerian-Eulerian methods are appealing as they allow for simulating industrial and possibly natural scale phenomena, Eulerian-Largangian descriptions allow for better

representation of particle-wall interactions with large variability in particle size [58]. The use of Eulerian-Lagrangian descriptions for single and multiple saltating sediment particles has been the topic of intensive research work [e.g., 33, 84]. Such simulations are typically run with a fixed fluid velocity profile imposed over the particle bed and an initial velocity is given to the saltating particles under consideration. A stochastic collision model is usually applied when particles are in contact with the bed to determine the initial condition of the next saltation trajectory.

Various modeling approaches have been used to simulate multiple particle systems. These range from modeling the fluid with two-dimensional moving slabs [85, 86] or advecting a point measurement of fluid velocity above the bed of particles [38] or using an averaged velocity profile [87]. Qualitative and quantitative agreement when reported by using these models.

Chang and Scotti [88] did LES-Discrete Element Method (DEM) simulations to analyze the trajectories of individual particles released in a turbulent flow over a wavy wall. Though the grid spacing was about an order of magnitude larger than the sediment diameter, only one-way coupling between the fluid and dispersed phase was used (particle-particle interactions are not considered either). Fourteen thousand, four hundred particles were uniformly distributed on a section of a ripple surface and were released in the flow once a specified threshold was exceeded. The vertical structures on the upslope are shown to control the amount of sediment entrained and the particle trajectories. The same model was used in [89] to investigate the role of coherent structures in the lifting and dispersal of sediment under pulsating flow conditions.

Durán et al. [90] coupled DEM with RANS to examine the influence of the grain to fluid density ratio on the sediment transport for the transition from bed load to saltation. In their model, they coupled a Reynolds averaged description of the carrier flow in a pseudo two-dimensional continuum with a DEM. They proposed a Prandtl-like differential mixing length for turbulence closure. Fifteen thousand spherical particles were considered with small variability in the diameter (d_{max} ~1.2 d_{mean}, where d_{max} is the maximum diameter and d_{mean} is the mean diameter). The particles and fluid were coupled via drag and pressure forces. The model was able to produce the qualitative behavior of bedload transport at a particle to fluid density ratio close to unity and saltation of particles in air (Aeolian transport) at a large particle to fluid density ratio. The particle flux with air and water showed agreement with experimental observations.

Escauiaza and Sotiropoulos [91] used Detached Eddy Simulation (DES) to study the effect of horseshoe vortical structures on sediment transport in the vicinity of a cylindrical pier. Up to 10^5 particles were placed upstream of the vertically mounted cylinder in a rectangular channel. The particles were assumed not to affect the fluid (one-way coupling) in their model, however, the particle-particle and particle-wall interactions were considered. Their results showed that the location of particle ejections appeared to coincide with the onset of the turbulent horseshoe vortex instability. Good qualitative agreement was found with experimental observations of scouring conditions near the threshold condition.

Nabi et al. [92] used four different sub-models to describe sediment transport, namely pickup, transport over the bed, suspended transport, and deposition. Sliding is ignored for sediment pickup and sediment transported over the bed is modeled as a layer that moves in the direction of the exerted force. The average saltation height, length, and velocity show agreement with experimental results. The model was used along with LES on a Cartesian grid with local refinement to simulate the formation and migration of dunes and was able to capture the realistic physics [93]. The model was also used to simulate the development morphodynamics of bed forms and local scour at submerged piers and showed good agreement with experimental data [93, 94].

Schmeeckle [41] combined LES with DEM to simulate unidirectional transport in an open channel. He did 11 experiments spanning a region of no motion to energetic suspension. Only drag, gravity, buoyancy, and pressure forces were considered with the solid phase being coupled through drag to the fluid solver. A drag model based on experimental observation developed by Schmeeckle [95] was adapted which gives the drag force as a function of particle Reynolds number (but not the void fraction). The LES-DEM showed good capability of predicting bedload sediment transport rates. The same approach was used later by Schmeeckle [96] to investigate the interaction between the bedload motion and turbulence in a backward facing step. Their quadrant analysis results were consistent with the findings of the experimental work of Nelson et al. [97] where sweeps and upward interactions were found to entrain most of the transported sediment.

Resolved flow simulations were also used to study sediment transport using Lattice-Boltzmann simulations or coupled Immersed Boundary Method (IBM) to Direct Numerical Simulation (DNS-IBM) in open horizontal channel flow [e.g., 98], laminar channel flow [99] or turbulent channel flow [100]. Good qualitative comparisons are reported in these studies for the onset of erosion and

transport rate. These simulations, however, are computationally expensive and are subject to one or more of the following constraints: limited number of particles, low submergence rate (small domain), relatively small Reynolds numbers, or relatively small integration time.

The state of the art of Computational Fluid Dynamic-Discrete Element Method (CFD-DEM) modeling efforts extends to using a fluid grid larger than particle size [90] and using RANS in solving the flow field or coupling the discrete phase through drag to a single phase solver [41]. By doing so, it is possible to avoid numerical stability issues occurring from discontinuities in void fraction, which would occur in a fully coupled solver if the particle size was of the same order or larger than the grid size. The use of RANS, however, neglects the unsteady nature of the fluid, which plays an important role in the entrainment and suspension of particles. On the other hand, in wall-resolved methods such as LES, using one-way coupling neglects the feedback from particles to the continuous phase, and only coupling the two phases through drag is incomplete. An alternate treatment is required for more appropriate coupling of the particles to a multiphase flow solver when the size of the dispersed phase diameter is larger than the required grid size.

In most past LES-DEM applications, the inherent coupling between the solid and fluid phases was reduced to one-way coupling or by coupling particles to a single phase solver only through drag force feedback. The primary interest of this paper is to extend the state-of-the-art of simulating sediment transport by using LES with a dual-grid-formulation [18] of DEM as a tool to allow proper coupling between the continuous and the dispersed phase. The differences in the two coupling formulations is investigated, namely coupling the particles to a multiphase flow solver and coupling the particles only through drag to a single phase flow solver. In the former, the volume averaged Navier-Stokes Equations [20] are solved for the continuous phase and source terms from particles are fed back into the momentum equation of the carrier fluid (referred to as full coupling). In the latter, source terms from particles are included in the momentum equations, however, the continuous phase is modeled using Navier-Stokes equations for a single phase (referred to as reduced/partial-coupling). The reduced-coupling formulation was used by Schmeeckle [41] to avoid stability issues that could arise from using a multiphase flow solver with particle sizes larger than the grid size. The dual-grid formulation [18] is used herein to overcome such stability issues. It should be noted that after the completion of this work, the authors have

become aware of a recent work by Sun and Xiao [101] in which a different technique is used to overcome the same stability issue.

In addition to investigating the coupling between phases, the paper also investigates methods to reduce the cost of the DEM. Since the computational cost of tracking each individual particle scales with the order of the number of particles [102], the applicability and limitation of using a Representative Particle Model (RPM) on simulating sediment transport flows also is considered. In this model, particles are lumped together as representative particles to reduce the number of simulated particles and permit investigating larger, more realistic, systems which otherwise would not be possible to simulate or would come at a considerable computational cost.

These enabling features are applied to sediment transport in a turbulent channel flow across a range of conditions from essentially no motion to strong suspension. The structure of the paper is as follows: Section 4.3 presents the governing equations along with additional numerical tools that are used in this work. It includes the numerical aspects of the flow solver, particle equation of motion (EOM) with point force models, the dual-grid formulation, and finally the representative particle model. The simulation details are given in Section 4.4, while the results section (Section 4.5) includes subsections related to the comparison of sediment transport and channel friction results from using different coupling strategies and using a representative particle model. Findings from the current numerical simulations regarding the entrainment of particles by different turbulent events are also presented in this section. Concluding remarks are given in Section 4.6.

4.3 Governing Equations and Mathematical Formulation

The methodology applies an Eulerian-Lagrangian approach involving tracking the individual motion of each particle. The flow is not resolved around the particle surface; instead, point-force expressions are used to account for different fluid-particle interactions. The fluid governing equations along with the particle equations of motion and the coupling strategy are first presented, followed by the description of the dual-grid formulation and the representative particle model.

4.3.1 Fluid equations

The carrier phase is modeled using volume averaged Navier-Stokes equations derived by Anderson and Jackson [20] for multiphase flows. The current implementation of the continuous phase is governed by Model-B of Gidaspow [21] in which the pressure drop is accounted for only

by the fluid. Under the assumption of fully-developed flow the modified fluid equations are written as

$$\frac{\partial(\varepsilon\rho)}{\partial t} + \vec{\nabla}.(\varepsilon\rho\vec{u}) = 0 \tag{4.1}$$

$$\frac{\partial(\varepsilon\rho\vec{u})}{\partial t} + \vec{\nabla}.(\varepsilon\rho\vec{u}\vec{u}) = -\vec{\nabla}p + \vec{\nabla}.(\varepsilon\bar{\bar{\tau}}) + \rho\vec{g} - \sum_{i=1}^{n_p} \frac{m_{p,i}\vec{f}_{drag,i}}{\forall_{cell}} + \beta_x\vec{e}_x \tag{4.2}$$

where $\varepsilon, \rho, \vec{u}, p,$ and $\bar{\bar{\tau}}$ are the fluid void fraction in each computational cell, fluid density, fluid interstitial velocity, modified fluctuating pressure, and viscous shear stress, respectively, and t is time. While $m_p, \vec{f}_{drag}, \vec{g}, \forall_{cell}$, and n_p are the particle mass, the drag force per unit mass of the particle, the gravitational acceleration, the volume of the computational cell, and the number of particles residing in a computational cell, and *i* represents each individual particle. β_x is the mean pressure drop across the domain in the x-direction (constant) $\beta_x = -\Delta P_x/L_x$, where P is the total pressure, L_x is the domain extent in the flow direction (x in the current work), and $\vec{e}_x$ is the unit vector of the flow direction. The void fraction accounts for the presence of particles in the fluid volume. In contrast, a single phase flow solver does not account for the presence of the dispersed phase (hence, $\varepsilon = 1$ in equations 1 and 2). The shear stress tensor, $\bar{\bar{\tau}}$ in Eq. 4.2, is written as

$$\bar{\bar{\tau}} = (\mu + \mu_t)\vec{\nabla}\vec{u} \tag{4.3}$$

where μ is the dynamic viscosity of the fluid and μ_t is the subgrid-scale turbulent viscosity which is calculated using the dynamic Smagorinsky model [26, 103] in the current work. A local value of the dynamic constant is calculated and is constrained to values between 0 and 0.04. The second to last term on the right-hand side (RHS) of Eq. 4.2 accounts for the interaction forces between the dispersed phase and the continuous fluid phase and it together with the void fraction fully couples the fluid equations with the dispersed phase. The last term in Eq. 4.2 is required to simulate a streamwise periodic channel flow. It accounts for the mean pressure gradient which is applied to the streamwise momentum equation to drive the flow. Following the treatment of Patankar et al. [104], the pressure can be decomposed into a mean and fluctuating periodic component

$$P(\vec{x}, t) = P_{ref} - \beta_x x + p(\vec{x}, t) \tag{4.4}$$

where p is the modified fluctuating pressure, $\vec{x}$ is the position vector, and P_{ref} is the reference pressure. The modified fluctuating pressure *(p)* is used in Eq. (4.2). The flowrate adjusts as the

flow develops until the losses in the domain are balanced by the mean pressure drop. More details on the turbulent fluid flow solver are described in [105].

4.3.2 Particle dynamical equation

In the DEM, the path of each particle is predicted by the integration of its equation of motion resulting from the application of Newton's law of motion. A rigorously derived equation of motion for small particles in non-uniform flow derived by Maxey and Riley [106] forms the baseline equation of motion to which other force contributions are added. The equation of motion of particles moving under the influence of drag ($\vec{f}_{drag,i}$) and gravity ($\vec{f}_{grav,i}$) forces along with contact forces ($\vec{f}_{contact,i}$) can be expressed as

$$\frac{d\vec{u}_{p,i}}{dt} = \vec{f}_{grav,i} + \vec{f}_{drag,i} + \sum \vec{f}_{contact,i} \tag{4.5}$$

where the force components in the equation are per unit mass of the particle and u_p represents the particle velocity. The contact force in Eq. 4.5 accounts for both particle-particle interactions and particle-wall interactions. The soft sphere approach [22] is used to account for multiple interactions occurring at the same time which is predominant in dense particle concentrations. The contact force in the soft sphere model is decomposed into a normal force component and a tangential force component. Normal and tangential force components are modeled using a spring-dashpot-slider system as sketched in Fig. 4.1. The contact force components in the normal ($\vec{F}_n$) and tangential ($\vec{F}_t$) directions to the collision plane are expressed as

$$\vec{F}_n = -k_n\vec{\delta}_n - \eta_n\vec{u}_{p,n} \tag{4.6}$$

$$\vec{F}_t = \begin{cases} -k_t\vec{\delta}_t - \eta_t\vec{u}_{p,t} & for\ \left(|\vec{F}_t| < \mu_f|\vec{F}_n|\right) \\ -\mu_f|\vec{F}_n| & for\ \left(|\vec{F}_t| \geq \mu_f|\vec{F}_n|\right) \end{cases} \tag{4.7}$$

where k, δ, η, and μ_f above are the spring constant, particle contact displacement, coefficient of viscous dissipation, and friction coefficient, respectively. In Eqs. 4.6 and 4.7, the subscripts n and t represent the normal and tangential components of the various terms. The viscous dissipation coefficient is given by

$$\eta = 2\alpha\sqrt{\frac{m_{eff}k}{1+\alpha^2}} \tag{4.8}$$

where m_{eff} is the effective mass of the colliding pair

$$m_{eff} = \frac{m_{p1} \times m_{p2}}{m_{p1} + m_{p2}} \tag{4.9}$$

and α can be determined from the restitution coefficient as

$$\alpha = \frac{-\ln(e)}{\pi} \tag{4.10}$$

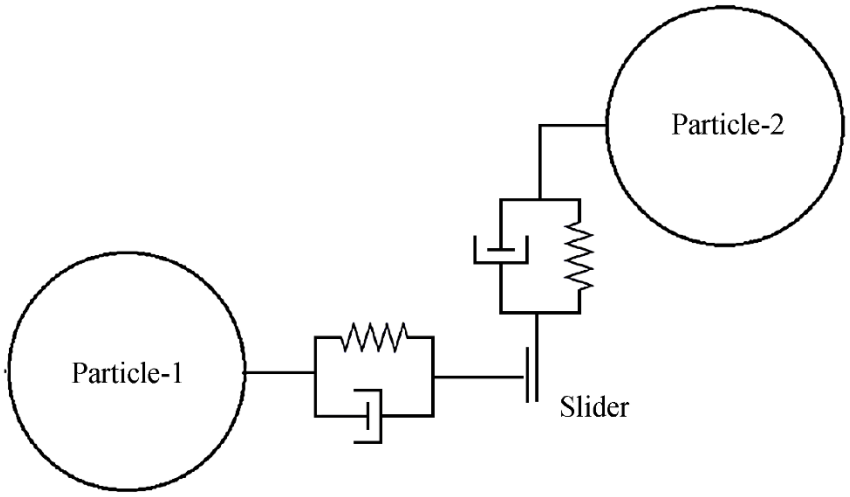

Figure 4. 1. Schematic of the soft-sphere collision model.

The rotational motion of the particles is governed by

$$\frac{d\vec{\omega}_{p,i}}{dt} = \frac{\vec{T}_{p,collision,i}}{I_p} \tag{4.11}$$

where I_p and ω_p, are the particle's mass moment of inertia and angular velocity, respectively. $T_{p,collision}$ is the torque resulting from particle collisions with walls or with each other. Individual force models used in the current work for solid spherical particles is presented briefly in the next sub-sections.

Gravity force herein includes both gravity and buoyancy effects. The submerged weight of the particle (per unit mass of the particle) is given by

$$\vec{f}_{grav} = \left(1 - \frac{\rho}{\rho_p}\right)\vec{g} \tag{4.12}$$

where ρ_p is the density of the particle and g is the gravitational acceleration (= 9.81 m/s^2). The drag force accounts for the quasi-steady drag in uniform flow and is often a key element in the interaction of dense granular flows and is modeled using the form

$$\vec{f}_{Drag} = \frac{\beta}{\varepsilon(1-\varepsilon)\rho_p}\left(\vec{u} - \vec{u}_p\right) \tag{4.13}$$

where β and $\vec{u}_p$ are the momentum exchange coefficient and the average fluid velocity. A combination of the Ergun [107] formula for dense mixtures $\varepsilon < 0.8$ and the Wen and Yu [108] drag correlation for dilute mixtures $\varepsilon > 0.8$ is used for the momentum exchange coefficient with a blending function to avoid discontinuity [21].

$$\beta = W\beta_{Ergun} + (1 - W)\beta_{Wen-Yu} \tag{4.14}$$

$$\beta_{Ergun} = 150\mu\frac{(1-\varepsilon)^2}{\varepsilon d_p^2} + 1.75(1-\varepsilon)\frac{\rho}{d_p}\left|\vec{u} - \vec{u}_p\right| \tag{4.15}$$

$$\beta_{Wen-Yu} = \frac{3}{4}C_D\frac{(1-\varepsilon)\varepsilon}{d_p}\rho\left|\vec{u} - \vec{u}_p\right|\varepsilon^{-2.65} \tag{4.16}$$

where d_p is the particle diameter, and the blending function, W, is defined as

$$W = \frac{\tan^{-1}\left(150(\varepsilon - 0.8)\right)}{\pi} + 0.5 \tag{4.17}$$

and the drag coefficient C_D is defined as

$$C_D = \begin{cases} 24\left(1.0 + 0.15Re_p^{0.687}\right)/Re_p, & Re_p < 1000 \\ 0.44, & Re_p \geq 1000 \end{cases} \tag{4.18}$$

where C_D is the drag coefficient. The particle Reynolds number, Re_p, is calculated as

$$Re_p = \frac{\varepsilon\rho d_p\left|\vec{u} - \vec{u}_p\right|}{\mu} \tag{4.19}$$

Other forces, which could be relevant, are the lift force (due to velocity gradients or Magnus effects), the added mass force, the Basset/history force, and the unsteady force. Mathematical formulation of these point mass force models for finite Reynolds number can be found in [58]. Since one of the main objectives of the current work is to examine differences between using

different coupling strategies, only coupling through drag is considered in the current work. It should be noted that the traditional calculation of the history force can make the whole calculation impractical for cases in which a large number of particles are integrated over a long time [109]. The history force is neglected in most CFD-DEM simulations that include a large number of particles [e.g., 91, 92, 101]. However, comparisons of modeling results to experimental measurement [66, 109] show that the trajectories of the particles bouncing from a wall in a viscous fluid are better represented by drag and gravitational forces only as compared to the consideration of part of the unsteady forces (i.e. including added mass and neglecting history forces). In light of these reasons, both added mass and history forces have been neglected.

4.3.3 Dual-grid formulation

Turbulent transport plays a key role in many industrial and natural particulate flow systems including sediment flow requiring the resolution of turbulent flow structures. Thus, dense fluid grid densities are required near surfaces. On the other, hand DEM modeling requires the grid to be large enough for proper volume averaging and to prevent sharp changes in the void fraction field. This is encountered in sediment flows since the grid required to resolve turbulent structures is typically smaller than the sediment size. To resolve this contradictory requirement, a coarse particle grid is mapped to the finer fluid grid to allow for proper coupling and better stability. While the particle dynamical equations are solved on the coarser particle grid, the turbulent fluid flow equations are solved on the finer fluid grid [18]. In the dual-grid formulation, the turbulent flow field is advanced in time on the fluid grid using calculated void fractions and source terms from particles from the previous time step. At this stage, the updated fluid velocities are transferred to the coarser particle grid. The transferred fluid velocity together with the particle velocity and void fraction are used to calculate the drag force on the particles. The particles are then advanced in time after calculating other relevant forces such as gravitational and collisional forces. As the particles are moved to new locations, the void fraction field is updated on the particle grid and transferred to the fluid grid together with the source terms. Both calculated void fractions and source terms are used in solving the fluid equations at the next time step. This method of full coupling, i.e., via both, particle drag and void fractions is used in the current work.

4.3.4 Representative particle model

Unlike simulating dilute particle mixtures without collisions, the DEM in dense mixtures, which resolves individual particle collisions, is dominated by the search for neighbors and the small time scale of the modeled collisions, giving it high spatial and temporal computational complexity. Thus, while tens of millions of particles can be reasonably accommodated in dilute suspension calculations as in Ferrante and Elghobashi [110] who considered 80 million particles, CFD-DEM in dense mixtures is limited to at most a few million particles using parallel processing techniques [e.g., 111]. Thus, to extend the applicability of the DEM to a large number of particles, methods that reduce its computational complexity have been attempted [112, 113]. The method used in the current work is based on lumping particles together into representative particles. Two different techniques are used for the representation of lumped particles; in one method increasing the particle size is associated with changing the particle and fluid properties according to similarity models [114-116] and in the second approach the physical particle and fluid properties are retained [117, 118].

These models have been used in fluidized bed systems [e.g., 5], spouted beds [114], and pneumatic conveyance systems [118]. Qualitative and quantitative agreement is reported with the use of different scaling factors (ratio between the representative particle diameter to the original particle diameter) up to 16. A scaling factor of 5 allowed for simulating up to 25 million particles in a fluidized bed with good quantitative agreement reported. To the best of the authors' knowledge, the applicability of the model to sediment transport has not been reported so far. In the current use of the representative particle model (RP model), both the fluid and particle properties are retained while the particle diameter is increased.

Consider a particle moving under drag and buoyancy effects only (Eq. 4.11). The equation of motion of the original particles assuming binary collision between particles

$$m_p \frac{d\vec{u}_p}{dt} = V_p(\rho_p - \rho)\vec{g} + \vec{F}_{p,drag} + \vec{F}_{coll,t} + \vec{F}_{coll,n} \tag{4.20}$$

The left hand side (LHS) represents the rate of change in particle momentum and the terms in the right hand side (RHS) represent the net particle weight, the drag force ($\vec{F}_{p,drag}$), and the normal ($\vec{F}_{coll,n}$) and ($\vec{F}_{coll,t}$) tangential collision forces. In Eq. (4.20), m_p and V_p are the mass and the

volume of the particle, respectively. The number of particles in each representative particle (or parcel),n_{pP}, can be found as

$$n_{pP} = \frac{m_{RP}}{m_p} = \left(\frac{d^{RP}}{d_p}\right)^3 = l^3 \tag{4.21}$$

where, m_{RP} and d^{RP} are the mass and diameter of the representative particle respectively, l is the scaling factor (or graining ratio). Taking the sum of both sides over the number of particles inside each computational parcel gives

$$m_p \sum_{n_{pP}} \frac{d\vec{u}_p}{dt} = n_{pP} V_p (\rho_p - \rho)\vec{g} + \sum_{n_{pP}} \left(\vec{F}_{p,drag} + \vec{F}_{coll,t} + \vec{F}_{coll,n}\right) \tag{4.22}$$

The velocities of the representative particles are,$\vec{u}^{RP}$, (where the superscript *RP* refers to the representative particles) assumed to be the average of the original scale particles

$$\vec{u}^{RP} = \frac{1}{n_{pP}} \sum_{n_{pP}} \vec{u}_p \tag{4.23}$$

Since the collective mass of the particles inside each parcel is equal to the representative particle mass (m_{RP}=n_{pP} m_p), Eq. 4.20 can be written as

$$m^{RP} \frac{d\vec{u}^{RP}}{dt} = V^{RP} (\rho_p - \rho)\vec{g} + \sum_{n_{pP}} \left(\vec{F}_{p,drag} + \vec{F}_{coll,t} + \vec{F}_{coll,n}\right) \tag{4.24}$$

Additionally, it is assumed that when two parcels collide, all original particles within the colliding parcels are undergoing the same collision (n_{pP} collisions occur) such that

$$\vec{F}^{RP}_{coll,n} = \sum_{n_{pP}} \vec{F}_{coll,n} = -k_n \sum_{n_{pP}} \vec{\delta}_n - \eta_n \sum_{n_{pP}} \vec{u}_{p,n} \tag{4.25}$$

Assuming the original and representative particles to have the same overlap $\delta_n = \delta_n^{RP}$, hence

$$\vec{F}^{RP}_{coll,n} = n_{pP} \left(-k_n \vec{\delta}_n - \eta_n \vec{u}_{p,n}\right) \tag{4.26}$$

such that an equivalent representative particle viscous dissipation (η_n^{RP}) and spring constant (k_n^{RP}) can be set as

$$k_n^{RP} = n_{pP} k_n \;\&\; \eta_n^{RP} = n_{pP} \eta_n \tag{4.27}$$

Then Eq. 4.26 can, thus, be written as

$$\vec{F}_{coll,n}^{RP} = -k_n^{RP}\vec{\delta}_n - \eta_n^{RP}\vec{u}_n^{RP} \tag{4.28}$$

Similar treatment is done in the tangential direction.

As for the rotational motion

$$\frac{d\vec{\omega}_p^{RP}}{dt} = \frac{\vec{T}_{p,coll}^{RP}}{I_p^{RP}} = \frac{\vec{r}_p^{RP} \times \vec{F}_{coll,n}^{RP}}{I_p^{RP}} \tag{4.29}$$

Equation 5.29 yields

$$\frac{d\vec{\omega}_p^{RP}}{dt} = \frac{1}{l}\frac{d\vec{\omega}_p}{dt} \tag{4.30}$$

The drag force for particles within each representative particle can be expressed as (recall Eq. 4.13)

$$\vec{F}_{Drag}^{RP} = \sum_{n_{pP}} \vec{F}_{Drag} = \frac{\beta V_p}{(1-\varepsilon)} \sum_{n_{pP}} (\vec{u} - \vec{u}_p) = \frac{\beta V^{RP}}{(1-\varepsilon)} (\vec{u} - \vec{u}^{RP}) \tag{4.31}$$

in which the momentum exchange coefficient β is assumed to be constant and evaluated for the original size particles.

4.4 Simulation Details

A unidirectional open channel flow simulation used by Schmeeckle [41] is selected for further investigation in this study. The simulations comprised of ten numerical experiments of 0.5 mm spheres of 2650 kg/m^3 density (medium sand) that cover the full range of sediment transport modes ranging from essentially no-motion to strong suspension. The simulations are performed in a turbulent open channel flow (Fig. 4.2) with a velocity slip condition imposed on the top boundary and a no slip condition on the bottom wall. The flow is periodic in both stream-wise and span-wise directions. The imposed mean pressure drop that balances the shear stress determines the value of the mass flowrate inside the channel (Eq. 4.10). The numerical experiments considered in the current work compromised of 5 simulations in the bedload regime and 5 simulations in the suspended load regime. The numerical parameters for the simulations are listed in Table 4.1. The bulk Reynolds number indicated in the table is based on the averaged/bulk velocity of the fluid (u_b) and the full channel height. The frictional Reynolds number if based on the shear velocity (u_τ). As commonly understood in the literature, the transition between the two regimes is assumed when the ratio of the shear velocity (u_τ) to the settling velocity (ω_s) is around unity. The settling velocity

for medium sand was calculated based on the empirical settling velocity formula of Dietrich [119] and found to be 0.057 m/s [41]. Simulations that cover the bedload regimes were performed using 115,728 particles whereas simulations in the suspended-load regime were performed with 330,028 particles.

Table 4. 1. Simulation parameters for the different test cases.

Case	Bedload					Suspended load				
	1	2	3	4	5	6	7	8	9	10
u_τ	0.013	0.0222	0.03	0.0392	0.0483	0.0618	0.0753	0.0835	0.0944	0.113
Re_τ	584	998	1346	1762	2170	3382	3754	4240	4680	5080
τ^*	0.0209	0.061	0.111	0.19	0.288	0.7	0.862	1.1	1.34	1.58
u_τ/ω_s	0.239	0.384	0.526	0.696	0.848	1.31	1.46	1.64	1.82	1.97
Re_b	7,820	1,1847	15,160	18,476	22,286	29,712	33,466	39,141	46,321	53,116

τ^* is the wall boundary shear stress

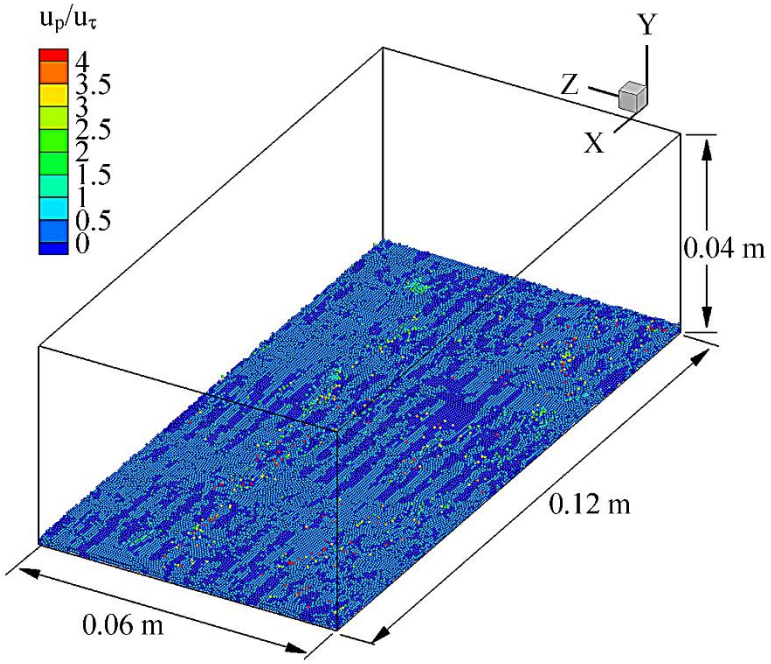

Figure 4. 2. Simulation domain of unidirectional turbulent channel flow test cases. Particles are colorized using their streamwise velocity with respect to the friction velocity (Case 1).

All the simulations were run in a domain of 0.12×0.06×0.04 m divided into 120, 60, 65 cells in the stream-wise (x), cross-stream (z) and vertical direction (y), respectively. The grid is uniformly spaced in both stream-wise and span-wise directions. The grid vertical spacing is 0.2 mm for the first 20 grid cells above the bottom wall, which is then gradually increased in size towards the top boundary. This particle bed height for bedload simulations (~ 2 mm) is encompassed in the uniform grid region. The domain and grid used are the same as that used by Schmeeckle [41] to ensure proper comparisons. The size of the near-wall grid used is 0.2 mm, which for the range of flow conditions considered in this study corresponds to Δy^+ ($\Delta y^+ = \Delta y_1 . u_\tau / \nu$) ranging between ~ 3 and 25 for Re_τ = 584 and 5080, respectively. The parameters used in the definition of y^+ are the friction velocity, u_τ, ($u_\tau = \sqrt{\tau_{wall}/\rho}$, where τ_{wall} is the wall shear stress) and the spacing of the first cell in the y-direction (Δy_1). The used values of y^+ may seem to be high for wall-resolved LES in a turbulent channel, however it is noted that the presence of the sediment bed damps the turbulence in the near-wall region. A grid refinement study performed by [41] for cases of τ^* ~ 0.288 and τ^* ~ 1.58 (Re_τ ~ 584 and 5080) showed that sediment transport did not exhibit any notable change by the refinement of the grid. Here, τ^* is the non-dimensional shear stress (aka Shields' parameter $\tau^* \equiv \frac{\rho u_\tau^2}{(\rho_s - \rho) g d_p}$).

To verify the adequacy of the baseline grid used, two finer grid calculations are performed for Re_τ=5080, the highest Reynolds number in this study (see Table 4.1). In the first-level finer grid the number of cells in the stream-wise direction was kept the same as the baseline grid, whereas the number of cells in both the cross-stream and vertical directions was increased to 150, resulting in a grid 5.8 times larger than the baseline grid. The near-wall grid size was reduced by a factor of 4 in the first 2 mm above the bottom wall (thus Δy^+ ~6 at Re_τ= 5080). In the second-level refinement, the streamwise number of cells was increased to 150 whereas the number of cells in the vertical direction was increased to 250, giving a grid (150×150×250) which is 12x finer than the baseline grid. The near wall cells were refined by a factor of 2 compared to the finer grid (8 times compared to the baseline grid in the first 2 mm above the bottom wall). Table 4.2 shows the results of the grid study with corresponding cell size in the x, z, and y directions in terms of percentage difference from the finest grid level which is considered the true solution. Both finer grid results are averaged for 10s after running the simulation for 10s of real time. The baseline grid

has errors of -13.7%, -0.22% and 0.11% in the particle flux, friction coefficient, and mean velocity, respectively with respect to the finest grid. Whereas the finer grid has errors of 7.9 %, 5.9% and -2.8%. While no clear convergence trend is noticed, the particle flux seems to be the most sensitive to the change in grid resolution but is bounded within ±15%, whereas the friction factor and the mean velocity are less sensitive to the grid resolution.

Taking into consideration the high cost of the simulations on the finest grid level and the fact that while grid independency is a measure of the accuracy of the results, other parameters such as friction between particles, μ_f, in Eq. (4.7) have a much larger impact on the results than the grid [120], we have used the baseline grid for all the calculations. Thus, with the use of the baseline grid, we submit to an uncertainty of ±15% in the particle flux, which notably varies over four orders of magnitude from 1×10^{-3} to >10 from bedload to suspended flow regimes.

Table 4. 2. Comparison of baseline grid results with finer grid results for most energetic suspended-load simulation.

	Baseline grid	Difference** %	Fine grid	Difference** %	Finest Grid
Cells	468,000 (120×60×65)	--	2,700,000 (120×150×150)	--	5,625,000 (150×150×250)
u_τ	0.113	--	0.113	--	0.113
Re_τ	5,080	--	5,080	--	5,080
τ^*	1.58	--	1.58	--	1.58
q^*	10.95	-13.7 %	13.68	7.9 %	12.68
C_f	0.0105	-0.22 %	0.0111	5.9 %	0.0105
u_b	1.104	0.11 %	1.0721	-2.8 %	1.103

** (grid result-finest grid result)/(finest grid result)

The simulation parameters pertaining to particle properties are listed in Table 4.3. The particle stiffness was set to an artificially low value, which is a standard practice, to soften the particles and to increase the time of collisions in the application of the soft sphere model [e.g., 22]. This

technique has been shown not to have much effect on the results with the caveat that the softening should be limited to prevent large unphysical overlaps between the spheres in contact (>10% of the radius). The other technique, which is used in the current simulations to work with disparities in the particle collision time scale and that of turbulence is the use of sub-stepping. In this technique, the particle is advanced multiple time steps during a fluid time step ($\Delta t_p = \Delta t_f / N_{sub}$, where Δt_p is the time step used for the particle calculation, Δt_f is the fluid –or calculation-time step, and N_{sub} is the number of particle sub-steps within a fluid time step) using a linearly interpolated fluid velocity between $n\Delta t_f$ *and* $(n+1)\Delta t_f$, where n indicates the number of the fluid time step. In the current work, the fluid time step, Δt_f, step was set to 5.3×10^{-4} s within which ten particle time step calculations are performed. Figure 4.3 shows the location of the selected computational experiments compared to the Shields diagram (Brownlie's fit [121]) along with criteria for the transition to suspended flow by Bagnold (1966) and van Rijn (1984) . It can be seen that all suspended load experiments have shear stresses higher than the Bagnold [122] Criterion of initiation of suspension. R_p indicated in the figure is the explicit particle Reynolds number (also known as Galileo number or the fall parameter) defined as $R_p = \sqrt{g\left(\frac{\rho_p}{\rho} - 1\right) d_p} d_p / \nu$ where ν is the kinematic viscosity of the fluid.

Table 4. 3. Numerical parameters of particles.

Parameter	Value
Particle diameter	0.5 mm
Coefficient of restitution	0.01
Particle density	2650 kg/m^3
Friction coefficient	0.6
Stiffness coefficient	100 (N/m)
Particle time step	5.3x10^{-5} s

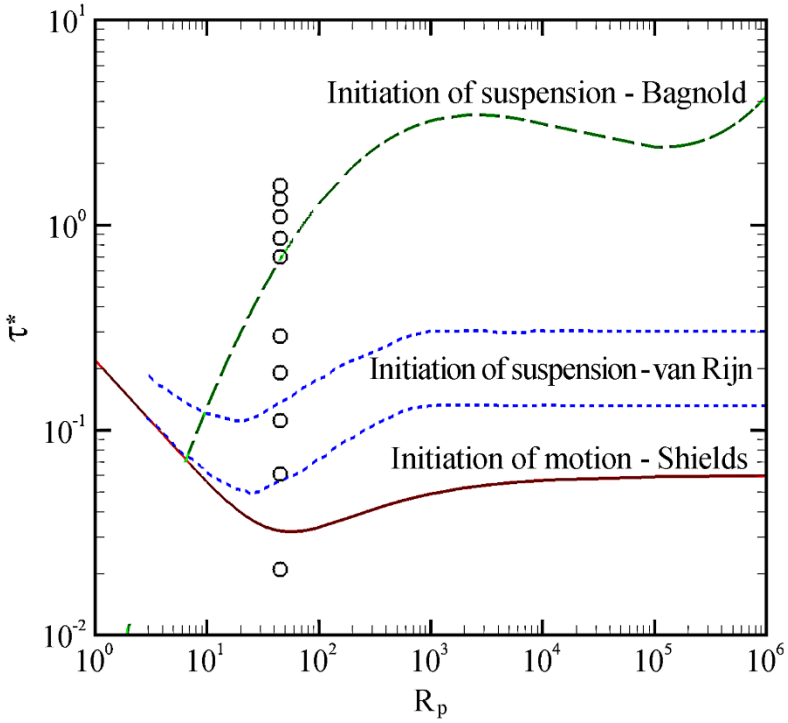

Figure 4. 3. Transport regime for the selected cases: Bagnold (1966), van Rijn (1984), and Shields (from Brownlie, 1982).

To initialize a simulation, particles were distributed above the bottom surface of the bed with their velocity equal to the fluid velocity. The initial mean velocity of the fluid was set to 16 times the friction velocity (u_τ) and the simulations were run for up to 30 s of real time. Figure 4.4 shows the time series results of mean flow velocity and sediment transport for a selected case. It can be seen that both particle flux and fluid velocity almost reach a stationary value after the first 10 seconds. The percentage change in fluid velocity in the last averaging period (20-30 s) compared to previously averaged results (10-20 s), shows that the change in flow velocity is about 6% or less, whereas almost all cases show a change of 13% or less for the particle flux in the same period. The physical time before averaging is equivalent to ~30-200 flow-throughs of the domain (highest for more energetic cases).

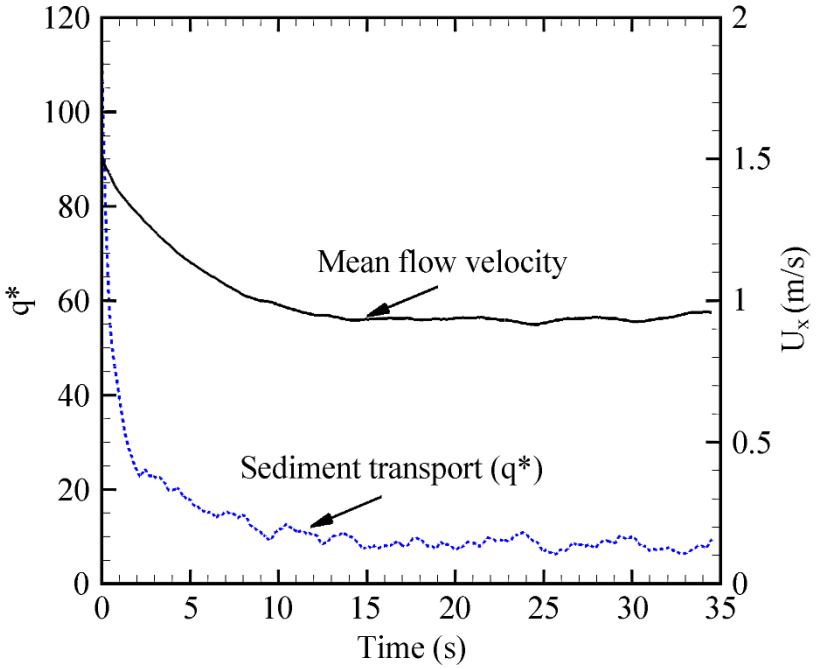

Figure 4. 4. Evolution of flowrate and sediment flux for τ^*~ 1.34 case (i.e., Case 9).

4.5 Results and Discussion

In the first section, the effect of using different coupling strategies is addressed. The main simulation results (sediment transport rate and friction factor) are presented using two different coupling methods. The next section presents the representative particle (RP) model as a less expensive method for making simulations with a large number of particles. The RP model predictions of sediment transport and friction factor are compared to unscaled simulations and the corresponding reduction in computational time is discussed. The effect of turbulent events on particle entrainment is discussed in the third section.

4.5.1 Effect of coupling strategy

The simulation experiments were done using two coupling strategies. In one method only the source terms from drag are fed back to the momentum equations while in the second approach both phases are coupled by drag forces (as source terms) and void fractions. The calculated average void fractions are used in calculating drag forces in both coupling strategies. In the current work, the dual-grid-formulation was used in both cases to allow for appropriate averaging of void fractions and to avoid stability issues. The first method was adapted in Schmeeckle's [41] work without using the dual-grid-formulation. The purpose here is to investigate the differences that

arise from using such an approach compared to the more appropriate four-way coupling. In the discussions that follow, the first method will be termed partial/reduced coupling whereas the second method will be termed full-coupling.

As stated previously, the simulations were run for 30 s of real time, unless noted otherwise and the presented results are averaged for the last 10 s. Figure 4.5 shows the non-dimensional solids transport rate (Einstein number) vs. the non-dimensional shear stress (Shield's parameter) using the two different coupling strategies, along with results from Schmeeckle [41]. The non-dimensional sediment transport $q*$ is defined as $q^* \equiv \frac{q_{sx}}{\left(\left(\frac{\rho_p}{\rho}-1\right)g d_p^3\right)^{1/2}}$, where q_{sx} is the total volumetric horizontal particle flux (summation of the particle velocity by the particle diameters for all particles) per unit horizontal area of the bed. The simulation results are compared to the prediction of the Meyer-Peter and Muller [123] (MPM) bedload transport equation ($q^* = 3.97(\tau^* - \tau_c^*)^{1.5}$) using a critical (entrainment threshold) shear stress (τ_c^*) of 0.05 [124] and the Engelund-Hansen [125] formula for total load ($q^* = \frac{0.05}{C_f} \times (\tau^*)^{2.5}$). C_f in the former equation is the generalized Darcy-Weisbach friction factor $C_f = (u_*/u_b)^2$.

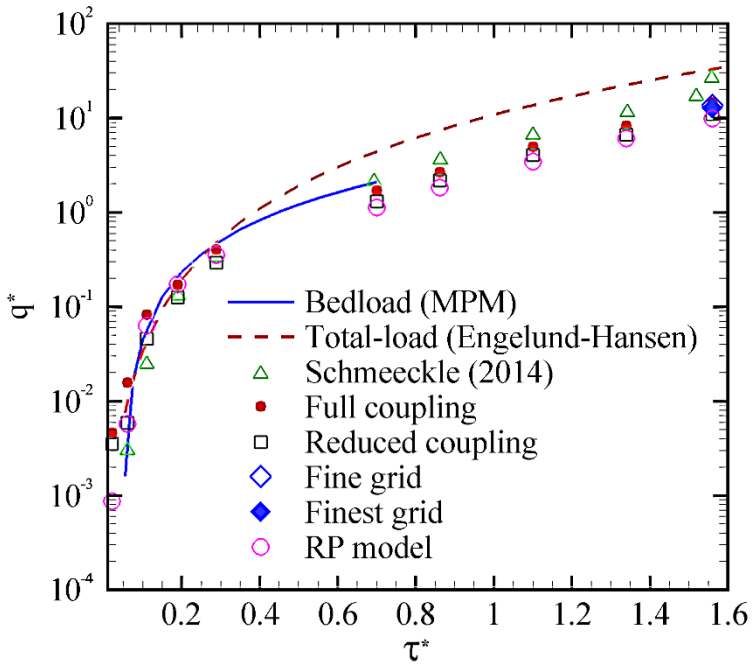

Figure 4. 5. Comparison of sediment transport rate results (MPM refers to the Meyer-Peter and Muller (1948) bedload formula, Engelund-Hansen refers to the Engelund and Hansen (1967) total load formula).

It can be seen that sediment transport using reduced coupling is lower than that predicted by full coupling. In the bedload regime, the predicted solids flux is in good agreement with the bedload transport formula. A small transport rate can be observed (q^*~4.6x10^{-3} or 5.5x10^{-4} kg/(m.s) for full coupling) at the first point of the bedload transport regime simulations. Although the shear stress at this point is less than the critical shear stress (τ^*~ 0.021 whereas τ_c^*~ 0.05), it does not necessarily imply zero particle transport. In fact, the small predicted transport rate is close to the general motion criterion of 4.1x10^{-4} kg/(m.s) set by U. S. Army Corps of Engineers (USACE) [126] to quantify the sediment transport at the initiation of particle motion. The slight over prediction might be due to using a uniform particle size instead of a distribution of particle sizes. The use of uniform particle sizes is found to decrease the critical shear stress [127]. Accordingly, the use of a particle size distribution is expected to increase the bed resistance to motion. It can be seen that the transport rate in the suspended-load regime is less than that predicted by the Engelund-Hansen [125] formula by roughly 50%. Current predictions are higher than the results provided by Schmeeckle [41] in the bedload regime but are lower in the suspended load regime. These differences can be attributed to the different drag model used by Schmeeckle [41] and the differences in the coupling.

Figure 4.6 shows the friction factor $C_f = (u_\tau/u_b)^2$ plotted versus the corresponding shear velocity non-dimensionalized with respect to the settling velocity of the particle. It can be seen from the figure that all friction factor estimates are larger than the Nikraduse friction coefficient for a fully rough channel with a fixed bed as indicated by the dashed line in Fig. 4.6 (C_f = 0.0036). This value is obtained by using the law of the wall ($u/u_\tau = 1/\kappa.ln(30y/k_s)$, where u is the fluid velocity, y is the distance perpendicular to the wall, κ=0.41 is the von Karmen constant and the relative roughness $k_s = d_p$). The results show the same trend as that obtained by Schmeeckle [41] but tend to be higher. Also, the transition in the friction factor as the flow transitions from the bedload to the suspended load regime is smoother compared to the abrupt change found by Schmeeckle [41].

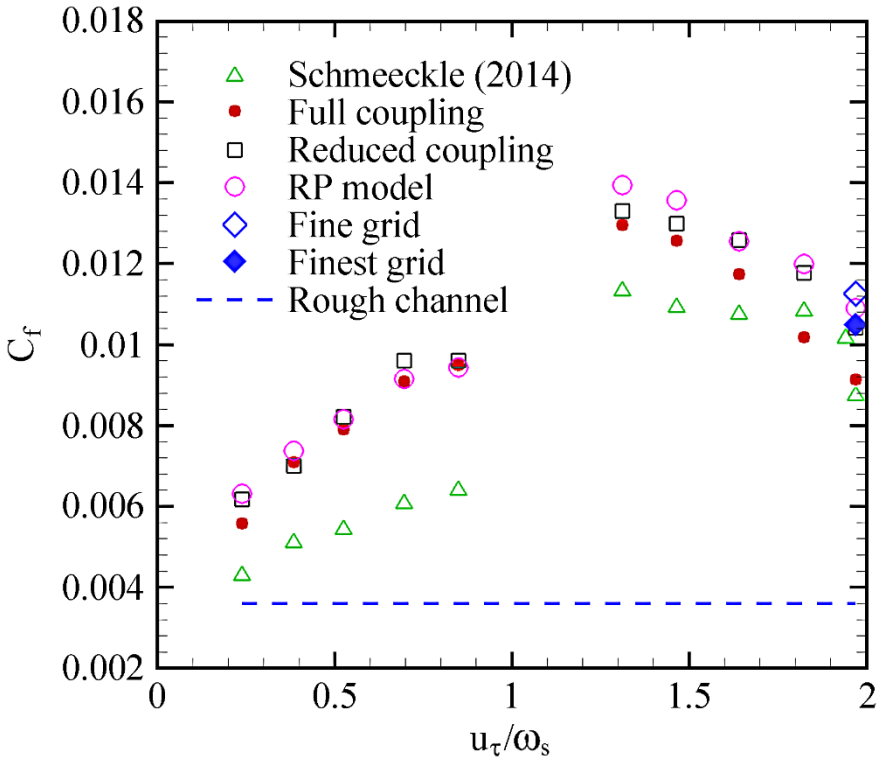

Figure 4. 6. Friction factor, C_f, vs. normalized shear velocity. The dashed line approximates the friction factor for a fixed rough wall.

It is shown in the next section that the apparent discontinuity in the friction factor observed in the current work and in the work of Schmeeckle [41] in transitioning from the bedload to the suspended load regime is a result of the different static bed heights used in the bedload and suspended load flow regimes. The same number of particles, and, hence, bed height across the full range of flows gives a much smoother distribution of C_f with a clear maximum at $u_\tau/\omega_s \sim 1$.

In the bedload regime where a bed surface can be distinguished and the flow above the bed is essentially single phase, both coupled and partially coupled calculations give the same results for the friction factor. Thus, partial coupling can be recommended for use in this regime. In the suspended load regime, however, the difference in the friction factor between the partial coupling and the full coupling increases as the flow rate increases. This can be explained by the increased mobility of the particles in the fully-coupled simulations. The increased mobility is a result of higher interstitial velocities caused by the blockage imposed by the particles, which is explicitly included in the fluid momentum equations through the void fraction. The increased mobility of

particles (indicated as an increase in the particle flux in Fig. 4.5) is associated with less energy extraction from the fluid, thus resulting in a reduction in the friction factor, C_f, (as can be seen in Fig. 4.6).

4.5.2 Effect of coarse graining

The use of the RP model reduces memory usage associated with storage of particle information. The speed-up obtained from using the RP model depends on various fluid, particle, and domain parameters, and can vary between simulations. For instance, consider the scaling factor of 2 in which eight particles are lumped in one representative parcel. The cost of DEM simulations will, thus, be reduced by a factor of more than 8 due to the reduction in the number of collisions and the number of ghost particles that need to be processed. The current fully coupled simulation showed a DEM speed-up of 13-16 times as compared to the original simulation. The corresponding overall speed-up was found to vary from 5 to as low as 2.5 times. The reduced speed-up is because the flow calculations do not scale down when using the RP model. For reduced coupling simulations in the bedload regime (not shown) it was found that the use of the RP model results in an overall speed-up of more than 5 times (DEM speed-up 16-18 times) (10 times speed up was obtained in some cases with reduced coupling). This is because in fully coupled simulations the DEM part consumes 66-81% (~75% on average) of the total simulation time, compared to 89-95% in the partial coupling case.

Comparison of results with original sized particles (fully coupled) with those of using a scaling factor of 2 (eight particles lumped in one representative particle) for transport rate and friction factor are shown in Figures 4.5 and 4.6, respectively. In these simulations, the particle grid in the dual-grid formulation was the same as that used with the original sized particle (i.e. the particle grid is mapped to three times the unscaled particle diameter). Good agreement is achieved for simulations in the bedload regime, however, the friction factor is over-predicted in the suspended-load regime where the representative particle model tends to under predict the transport rate (Figure 4.5). Such a decrease in particle flux indicates that an event that can entrain an un-scaled original particle may not be able to entrain lumped particles. The predicted friction factor is higher in the RP model as a result of less number of particles being suspended and transported in the flow (see Fig. 4.5). This supports the trend followed by the friction factor with wall shear velocity,

namely that as more particles are suspended and transported by the flow, the bed resistance decreases and so does the friction factor.

To confirm whether the abrupt jump in C_f during the transition from the bedload regime to the suspended load regime in Figure 4.6 was a result of the different number of particles in the two sets of simulations, a new set of simulations were performed with 330,024 particles over the whole range from bed to suspended load. The RP model was used for these simulations to reduce the cost. For continuity of results, an additional intermediate point was added between the two regimes in the RP model. Also, four additional points were added using the original particle size (shown as deltas in Fig. 4.7), two of them extending from the bed load to the suspended load regime with 115,000 particles, and the other two from the suspended to the bed load using 330,024 particles. The results are averaged for 5 seconds after running for 10 seconds of real time. In all cases, the results do not show any discontinuity in the friction factor during the transition from bed to suspended load regime and suggests that the discontinuity in friction factor between the two regimes in Figure 4.6 was a result of comparing two different systems, and that the particle bed height has a large impact on the calculated C_f. It is also very clear from the trends in all cases that the friction factor reaches a maximum at $u_\tau/\omega_s \sim 1$.

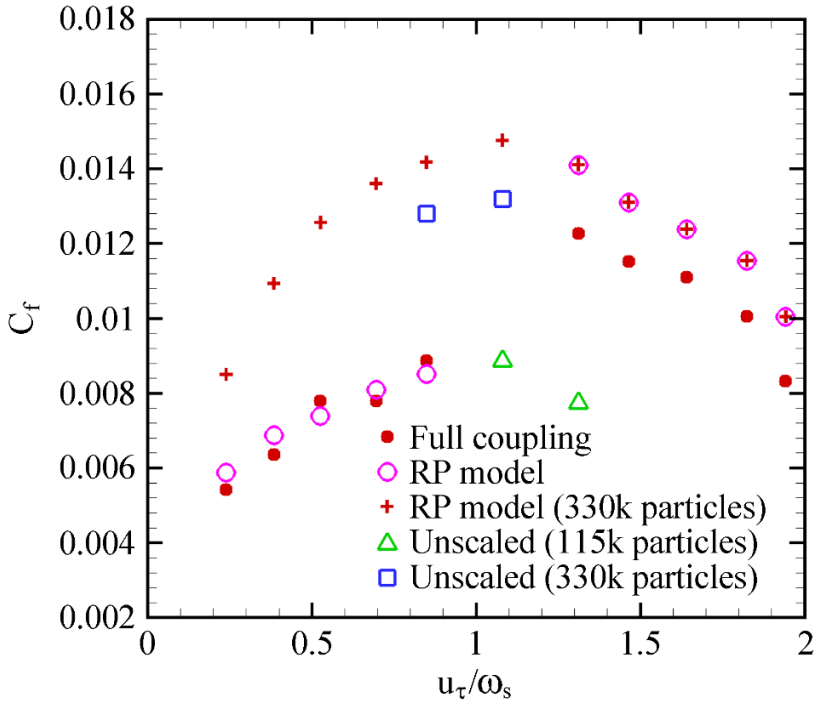

Figure 4. 7. Comparison of friction factor results when using an equal number of particles in both regimes using the RP Model.

This finding can be explained as follows, two different mechanisms are suggested/mentioned for the extraction of energy from the fluid by the particles. In the bedload regime, the increase in the friction factor is a result of the energy extracted by the particles with the increase in flow velocity. This will be the case since most of the particles are stationary and the transported sediment particles are moving at low velocities. This negligible collective mobility of the particles together with the fact that the thickness of the mobilized sediment layer will increase with an increase of flowrate leads to an increase in the friction factor in the bedload regime. The increased mobilization of the sediment layer is a result of particles hoping on the particle bed and the additional penetration of the fluid into the bed, which results in more particles interacting with the fluid and extracting more energy from the fluid. At some stage, the fluid mobilizes the full bed, maximizing the extracted energy. At this time the impact of increasing the flow velocity will be to increase the particle velocity, decreasing particle drag as a result and extracting less energy from the fluid. The latter mechanism dominates the behavior of the friction factor as the particles become suspended in the flow resulting in a decrease in the friction factor. A competition between the mechanisms determines whether the friction factor increases or decreases. The current simulations show that this condition is more likely to happen when the shear velocity is about the same as the free fall velocity of the particles. Thus, it can be concluded that the maximum friction coefficient occurs at the transition from bedload to suspended load.

Figures 4.8 and 4.9 present the averaged particle velocity along with the concentration for bedload and suspended load simulations, respectively. The averaged properties provided here are domain-averaged for a slab with a thickness equal to a particle diameter. The solids fraction in the bed is near the maximum packing fraction of spheres at around 0.74 in the bedload simulations when the bed is mostly stationary. This value is higher than a random close packing value of 0.634 because of the fact that up to 10% overlap may take place with the use of soft stiffness along with the fact that the whole volume of the particle is considered in the same computational cell at which the centroid of the particle is located. The particle velocities show that the top layer of particles starts accelerating almost parallel to the bed as the particles become mobile between $\tau^* \sim 0.021$ to $\tau^* \sim 0.061$. As the flow rate increases, particles start diffusing into the fluid by up to four particle diameters. The maximum average solids velocity is about twice the friction velocity. The suspended load simulations show similar trends with the particles reaching higher peak velocities.

The suspended particles mix more rigorously with the fluid, and consequently some of the particles are lifted to the full channel height at the extreme case tested ($\tau^* \sim 1.58$).

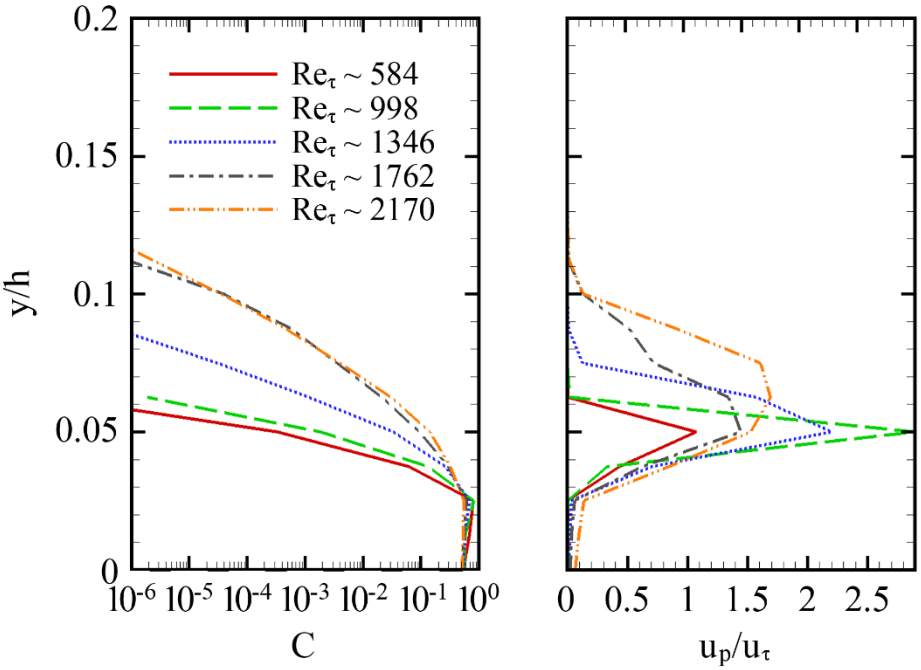

Figure 4. 8. Domain averaged sediment properties for bedload simulations, left; solid fraction of particles, right; solids velocity.

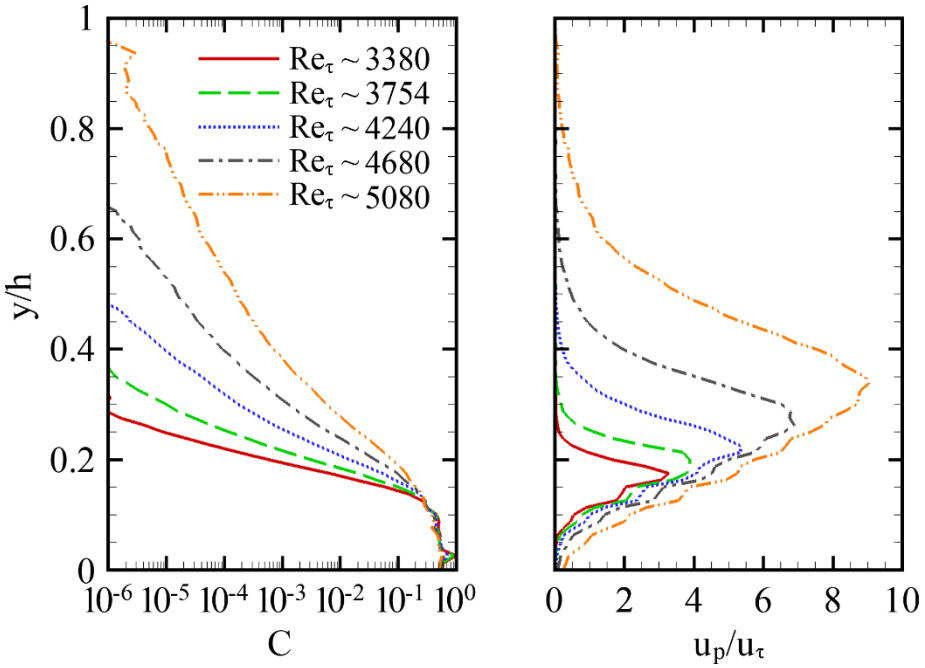

Figure 4. 9. Domain averaged sediment properties for suspended-load simulations, left; volume fraction of particles, right; solids velocity.

4.5.3 Entrainment of particles

It is quite well established that turbulent bursts and sweeps are the primary mechanisms of transport and generation of turbulent shear stress in the inner boundary layer, [e.g., 128, 129]. To get more insight into the role of these turbulent events in particle entrainment, the instantaneous stream wise and vertical fluctuating velocity components are recorded at a location just above the bed surface (probe located 3 mm from the bottom boundary). The probe is located above the bed and no lag between the fluid signal and particle transport is assumed. The corresponding particle flux and number of particles is measured in a control volume with a surface area of $1\times1cm^2$ surrounding the probe location and starting from a height which is 3 particle diameters above the bed. A bedload case with $\tau^*\sim 0.021$ (near critical shear stress) was selected where a 5 s time period was considered (10-15 s).

Figure 4.10 shows the probe velocity fluctuation signal over 5 s along with the corresponding average particle velocity in the control volume (u' and v' are the turbulent velocity fluctuations in the streamwise , x, direction , and vertical, y, directions, respectively). The number of particles inside the control volume indicates whether the increase in particle average velocity is because of the increase in the number of particles (possible rush of entrained particles with high speed from a neighboring event) or due to a current local event. Regions of significant increase in average particle velocity with an almost constant number of particles in the control volume are highlighted in the figure.

In the period 0.2-0.5 s, a series of successive sweeps ($u' > 0$, $v' < 0$) and ejections ($u' < 0$, $v' > 0$) take place with fluctuating fluid velocity components more than double the friction velocity. A relatively weak outward interaction ($u' > 0$, $v' > 0$) might be responsible for particles entrained at time ~1.1 s. The probe location experiences a long and strong sweep from 2 s to 2.3 s. This event mobilizes particles, increasing the particle flux. The number of particles in the monitored volume before this event indicates that most of the particles are embedded within the bed and are harder to dislodge compared to unsheltered particles. Some of the mobilized particles slow down and possibly settle as the sweep passes as can be seen after $t \sim 2.3$ s. This can be inferred from the decrease in the average particle flux at an almost constant number of particles. An ejection event following the strong sweep is capable of maintaining a certain amount of flux before the sweep event following at $t \sim 2.7$ s causes another increase in the particle flux. Other instances at which

ejections are associated with an increase in the particle flux can be seen at times 3.3 s and ~3.8 s. Similarly, a sweep at 2.7 s and ejections at times 1.5, 3.3 and 3.8 s seem to be responsible for particle entrainment. The findings are in agreement with results of Heathershaw and Throne [130] and Nelson et al. [97] where sweep and ejections are more frequent events and occupy most of the time spectrum.

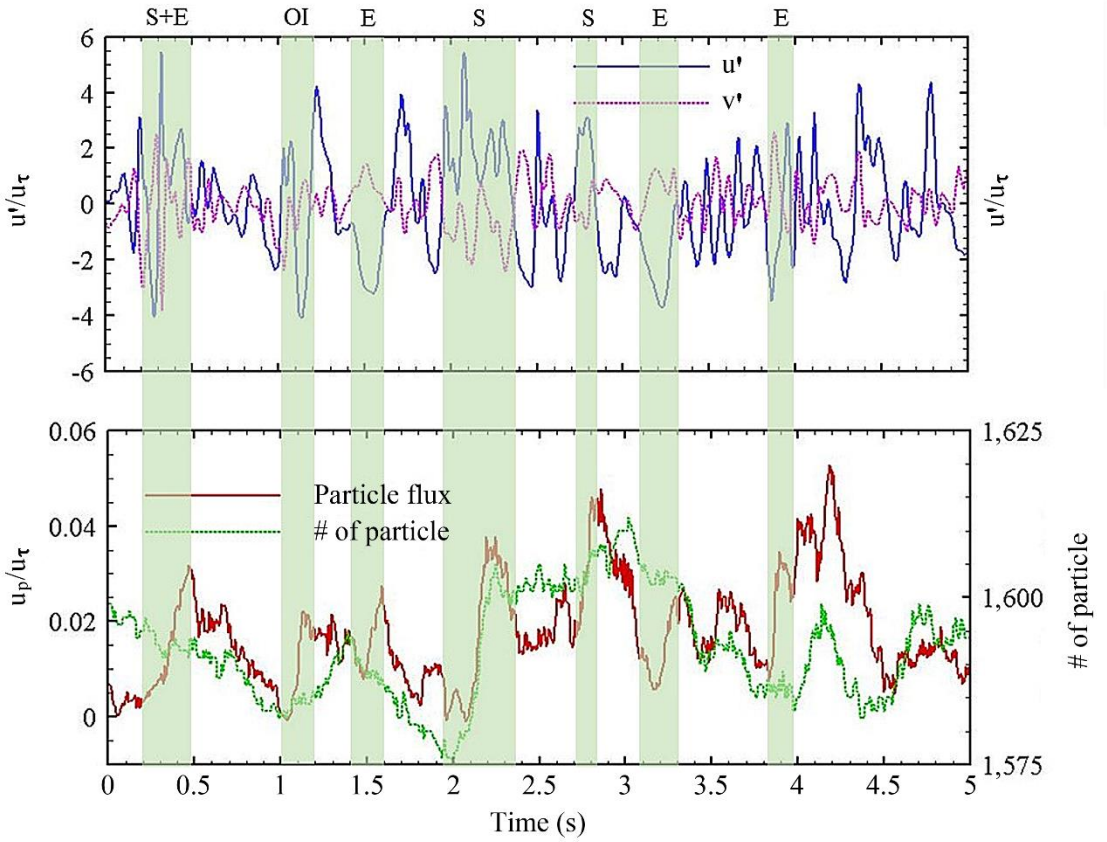

Figure 4. 10. Instantaneous particles stream wise velocity and fluid fluctuations for τ^{*}~ 0.021.

A quadrant analysis of the signal is provided in Fig. 4.11 where the events are colored by their corresponding normalized average sediment transport (divided by the maximum value of transport). A quantitative summary of the percentage of sediment entrained by each event and the percentage of time occupied by each event are listed in Table 4.4. Also provided is a measure of the integrated sediment transport per event in Table 4.4. The listed measure is the ratio between the percentages of the sediment transport (first row in Table 4.4) to the percentage of the event time (second row). It can be seen that sweeps and ejections are the most frequent events as

compared to inward and outward interactions. Unlike the findings of Heathershaw and Thorne [130], however, ejections in the current analysis are found to contribute almost equally as do sweeps to the entrainment of particles. Ejections were considered to be less effective in sediment transport as compared to sweeps and outward interactions [97, 130], but they were found to be dominating mechanisms for sediment transport by other investigators [131]. It can be seen from Table 4.4 that sweeps entrain the largest amount of sediment because of the high frequency at which they occur. This conclusion is in agreement with the finding of Nelson et al. [97]. The role of outward interactions ($u' > 0$, $v' > 0$) and inward interactions ($u' < 0$, $v' < 0$) seem to be collectively less influential to particle entrainment only because they are less frequent. As can be seen from the color-coding in Fig. 4.11, some instances of particle flux recorded for outward interactions seem to be close to the maximum entrained particle flux. The current results suggest that the entrainment of particles can be related to turbulent events which are basically large forces applied for short times (impulse). This would be in agreement with the hypothesis of the role of impulse in particle entrainment as suggested by Diplas et al. [70] and Dwivedi et al. [132] compared to the traditional criterion of averaged shear stress and velocity.

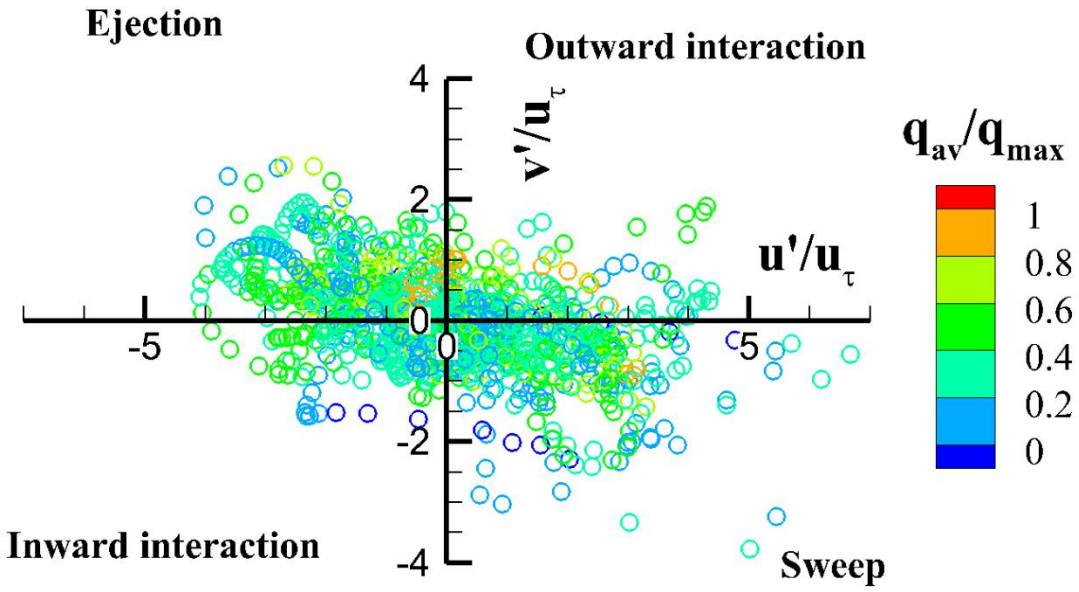

Figure 4. 11. Quadrant analysis of the flow signal above the bed for $\tau^* \sim 0.021$.

Table 4. 4. Quantitative analysis of particle movement and fluid signal.

Event	Outward interaction	Ejection	Inward interaction	Sweep
% sediment transport	19	29	14	38
% event time	16	27	15	42
A measure of integrated sediment transport during the event	116	109	93.3	90.6

4.6 Conclusions

In the current work, Computational Fluid Dynamics (CFD) was coupled with the Discrete Element Method (DEM) to simulate sediment transport in a turbulent open channel flow. Combining the DEM with LES poses contradictory requirements of a fine fluid grid to resolve small scale turbulent structures versus DEM requirements of a grid larger than the particle size for proper volume averaging to avoid near-discrete jumps in the void fraction field. To bypass this challenge, past work has used reduced or partial coupling between the continuous and dispersed phases. In the current work, a dual-grid formulation was used to allow for full four-way coupling. The differences between simulation results using partial and full coupling methods are given.

The predicted sediment transport rate was in good agreement with empirical bed load formula and showed a correct dependency in the suspended-load regime. Transport rates predicted by using partial coupling showed good agreement with full-coupling in the bedload regime, but under-predicted transport in the suspended load regime. The friction factor was found to increase in the bedload regime reaching a maximum when the friction velocity equaled the settling velocity, and then decrease in the suspended-load regime. The maximum resistance to flow, thus, takes place in the transition from the bedload to the suspended load regime. This is because of the competition between the increase in the energy extracted by the stationary sediment particles and the decrease in energy extracted by the suspended particles with the increase in flow energy.

A representative particle model with a scaling factor of 2 showed good performance in the bedload regime. The DEM was found to be about 10-16 times faster than the original un-scaled system.

The overall speed-up of the model, however, depended greatly on the ratio of time spent in DEM versus the fluid calculation and the overall speed-up ranged from less than 3 to more than 6 times the un-scaled simulation.

Finally, the information obtained from the simulation was used to gain insight into the process of particle entrainment. Particle entrainment happens in streaks along the length of the bed which is, qualitatively, in agreement with experiments [e.g., 133]. Both turbulent sweeps and ejections were found to collectively contribute more to the entrainment of particles because of their frequency of occurrence. On the other hand, outward interactions produce the same or possibly larger entrainment of particles but are less frequent.

Chapter 5

Sensitivity of Numerical Parameters on DEM Predictions of Sediment Transport

Husam A. Elghannay* **and Danesh K. Tafti***

*Department of Mechanical Engineering
Virginia Polytechnic Institute and State University
Blacksburg, Virginia 24061

Citation:

Elghannay, Husam A., and Danesh K. Tafti (2017): "Sensitivity of numerical parameters on DEM predictions of sediment transport", *Particulate Science and Technology*, DOI: 10.1080/02726351.2017.1352638.

5.1 Abstract

The current work presents a sensitivity study of selected numerical parameters on the LES-DEM predictions of sediment transport in a unidirectional open turbulent channel. The sensitivity of the particle friction factor, restitution coefficient and spring stiffness used in the soft sphere collision model are tested in the three regimes of sediment transport comprising of essentially no motion, bed-load, and suspended load flow regimes. The simulations are run for 10 s using base-values of the parameters of interest (reference calculation), then one parameter is changed at a time and the corresponding change in quantitative result is observed for the following 15 s where averaged results in the last 10 s are compared to the reference calculation. The sensitivity analysis shows that the under-predicted sediment transport in the suspended load regime can be bridged by moderately decreasing the friction factor of the particles from 0.6 to 0.25. The impact of the same change in bed-load regime is not as significant. Both the coefficient of restitution and the particle stiffness show less significant to negligible impact as compared to the friction factor.

5.2 Introduction

Simulation of sediment transport includes prediction of the fluid flow as well as particulate matter. Researchers are mostly interested in two aspects; the condition at which the sediment particles are set in motion (the *critical condition* or *incipience of motion threshold*), and the transport rate of the sediment particles. Many experimental and theoretical efforts have been conducted during the past several decades to determine the condition of incipient motion and the sediment transport rate. Both parameters are challenging to predict not only due to the involvement of the turbulence in the application, but also due to the many parameters that can affect them. To mention some, the variability of particle shape and size along with the presence of adhesion forces can affect the incipience of particle motion. Many criteria and methods are suggested and used to predict both quantities ranging from probabilistic or stochastic to deterministic approaches [134, 135]. An extensive review of the methods used in the estimation of both parameters is beyond the scope of this paper. The readers are referred to the work of [136] for a review of the most commonly used criteria for incipience of motion and to [69] for a review of the most commonly used sediment transport formulas along with their range of applicability.

Two numerical approaches are used to study sediment transport, the Eulerian-Eulerian approach, and the Eulerian-Lagrangin approach. In the first method, both the fluid and solid (continuous and

dispersed phases) are modelled using Eulerian descriptions where the Navier-Stokes equations are solved for each phase (thus it is also known as the Two-Fluid Model or TFM). This technique requires additional closure models to estimate the "viscosity" of the solids and to account for the collisions between the particles. On the other hand in the Eulerian-Lagrangian approach the fluid is solved using volume averaged Navier-Stokes Equation [20] while the dispersed phase is modeled by tracking the individual motion of the particles by solving their equation of motion. Forces on the particles can be directly calculated by integrating over the surface of the particles (known as resolved flow simulations). This procedure requires a fluid grid that is at least one order of magnitude smaller than the particle diameter which is impractical for systems of particles that include large number of particles or require integration for long times. Alternatively, a less expensive method is to approximate the particles as point masses and estimating the forces acting on the particles (known as CFD-DEM or Computational Fluid Dynamics coupled to Discrete Element Method or DEM).

Although TFM is appealing since it is computationally less expensive than CFD-DEM, it is problematic in several aspects such as handling particle-wall collisions and simulating particles with significant size or shape distributions [58]. The Eulerian-Lagrangian approach is generally more accurate and has the ability to account for several realistic behaviours in particulate systems. The application of the Eulerian-Lagrangian description is however restricted by the number of particles that can be simulated. Up to millions of particles were simulated using efficient parallelization techniques using CFD-DEM using large number of processors [19, 111, 137] In the following paragraphs previous Eulerian-Lagrangian models which were employed in simulating sediment transport are discussed.

Various Eulerian-Lagrangian modeling methods range from modeling the fluid with two-dimensional moving slabs [85, 86], advecting a measured transient fluid velocity above the bed of particles to drive the particles motion [38, 95] or using an averaged velocity profile [87]. These methods account for the change in fluid velocity caused by local momentum exchange with particles, or between fluid layers. Qualitative and quantitative agreement is reported by using these aforementioned models. More recently, the Lagrangian description of the particles (Discrete Element Method or DEM) has been coupled to Reynolds-Averaged Navier-Stokes (RANS), Large-Eddy Simulation (LES) or Direct Numerical Simulation (DNS) Eulerian descriptions of the fluid to simulate different applications related to sediment transport [41, 90, 138].

One of the important components of dense particle systems such as that encountered in sedimentation transport is modelling collisions between particles. Collision parameters used in the framework of the soft sphere model [22] such as restitution coefficient, spring stiffness and friction factor, however, have a degree of uncertainty associated with their values. Mostly a single value is used even when measurements show dependency of the parameters on experimental conditions. For example, researchers [139, 140] have measured various values for the effective normal coefficient of restitution of grains colliding within a range of 0.1-0.65 with the lower restitution coefficients measured at higher shear rates. Experimental measurements Gondret et al., [66] showed that the coefficient of restitution can be presented as a function of the impact Stokes number (defined as $St = \rho_p U_{impact}\, d_p/(9\mu)$, where ρ_p is the particle density, d_p is the particle diameter, U_{impact} is the impact velocity of the particle on the wall and μ is the kinematic viscosity of the fluid) and found that collisions are viscously damped if the impact Stokes number is less than 10. Similarly measured friction coefficients show a variation from 0.25-0.73 [140]. Moreover, the spring constant used in the soft sphere model has a direct impact on the allowable particle time step – using a lower spring constant increases the numerical collision time allowing larger time steps (hence can simulate longer physical times faster) and is thus desirable. DEM simulations have been shown to be quite insensitive to the value of the spring constant in energy systems in the absence of adhesion force [141].

Different conclusions are reported in the literature regarding the sensitivity of the numerical parameters used. For instance, tests with restitution coefficient (e) using three different values (e=0.15, 0.3, and 0.6 –for a particle diameter of around 1mm) showed the same statistically averaged results [98, 142]. Heald et al. [143] on the other hand, showed some dependency on restitution coefficient at low transport rate for three values of restitution coefficients of 0.3,0.5, and 0.7. While Jiang and Haff [85] reported some dependency on the friction factor, Drake and Calantoni [86] found that the friction factor is insignificant provided that it has a non-zero value. As for particle stiffness, Jiang and Haff [85] found similar hop patterns of the particle when they changed the particles stiffness by two orders of magnitude, showing its robustness. A similar conclusion was reached by Drake and Calantoni [86] where only negligible changes were found when the particle stiffness was changed by orders of magnitude while maintaining a maximum overlap of less than 0.5 % of the particle diameter.

From the former discussion it can be concluded that variation or uncertainty of physical properties exist. When simulating natural phenomena, however, these variations may not be faithfully accounted for in many Eulerian-Lagrangian descriptions. Conflicting conclusions regarding the sensitivity of some parameters is found in the literature and can be because of using different formulations or testing different systems. The current work investigates the sensitivity of critical parameters used in CFD-DEM simulations of sediment transport in various flow regimes in comparison to reported work in the literature.

5.3 Governing equations

An Eulerian- Lagrangian approach which involves tracking the individual motion of each particle is employed in the current work. The carrier phase is modeled using the volume averaged Navier-Stokes equations derived by Anderson and Jackson [20] for multiphase flows. Discrete particles are treated as point-masses and suitable force expressions are used to account for fluid-particle interactions. The current implementation of the continuous phase is governed by Model-B of Gidaspow [21] in which the pressure drop is accounted for only by the fluid:

$$\frac{\partial(\varepsilon\rho_f)}{\partial t} + \vec{\nabla}.(\varepsilon\rho_f\vec{u}) = 0 \tag{5.1}$$

$$\frac{\partial(\varepsilon\rho_f\vec{u})}{\partial t} + \vec{\nabla}.(\varepsilon\rho_f\vec{u}\vec{u}) = -\vec{\nabla}p + \vec{\nabla}.(\varepsilon\bar{\bar{\tau}}) + \rho_f\vec{g} - \sum_{i=1}^{n_p}\frac{\vec{F}_{i,Drag}}{\forall_{cell}} + \beta_x\vec{e}_x \tag{5.2}$$

Where $\varepsilon, \rho_f, \vec{u}, p, \bar{\bar{\tau}}$ and $\vec{F}_{Drag}$ are the void fraction, density, fluid interstitial velocity, fluctuating pressure, viscous stress and drag force due to the presence of particles, respectively. N_p represents the number of particles in each computational cell and V_{cell} represents the volume of the computational cell. The shear stress tensor is written as:

$$\bar{\bar{\tau}} = (\mu + \mu_t)\vec{\nabla}\vec{u} \tag{5.3}$$

where the subgrid-scale turbulent viscosity μ_t is calculated using the dynamic Smagorinsky model [26]. The last but one term on the right-hand side (RHS) of Eq. (5.2) accounts for the interaction forces between the dispersed phase and the continuous fluid phase (as a source term). The source terms from the drag force together with the void fraction fully couples the fluid equations with the dispersed phase. To simulate a stream wise periodic channel flow a mean pressure gradient is applied to the streamwise momentum equation to drive the flow. The flow-driving term is the last

term on the right hand side where the flow is in the x-direction in Eq. (5.2), $\beta_x = -\Delta P_x / L_x$ where ΔP_x is the pressure drop in the x-direction and L_x is the length of the domain in the x-direction. The flowrate adjusts as it develops until the losses in the domain are balanced by the applied pressure drop. More details on the turbulent fluid flow solver are described in [105].

The path of each particle is predicted by the integration of its equation of motion resulting from the application of Newton's law of motion. Neglecting forces arising from non-continuum effects or rotating reference frames, or unsteadiness of the particle or the flow field, the equations of motion of particles interacting with other particles or surfaces can be expressed as

$$m_p \frac{d\vec{v}_p}{dt} = V_p(\rho_p - \rho_f)\vec{g} + \vec{F}_{p,Drag} + \sum \vec{F}_{p,coll} \tag{5.4}$$

The history force is expensive to calculate for simulations with large number of particles integrated for a long time since it typically requires the storage and use of relative velocity information throughout the life-time of the particle [144]. The use of recently developed less expensive models [29, 109] was not considered in the current work. Based on the finding of experimental and numerical work [66] the activation of drag only gives better prediction compared to simulations in which part of the unsteady forces are considered (i.e. activation of added mass but not the history forces). The equation of motion in the rotational direction is expressed as

$$I_p \frac{d\vec{\omega}_p}{dt} = \vec{T}_{p,coll} \tag{5.5}$$

where m_p, I_p *and* ω_p, are the particle's mass, mass moment of inertial, the angular velocity, respectively. $F_{p,coll}$, and $T_{p,coll}$ stand for the force and torque resulting from the particle collisions with walls or with each other. The drag force represents the particle fluid interaction and is defined as

$$\vec{F}_{Drag} = \frac{\beta V_p}{\varepsilon(1-\varepsilon)}\left(\vec{u} - \vec{v}_p\right) \tag{5.6}$$

Where $\beta, V_p, \vec{u}$ and $\vec{v}_p$are the momentum exchange coefficient, the particle volume, the average fluid velocity, and the particle velocity, respectively. The momentum exchange coefficient was calculated using a combination between Ergun formula for dense particle concentration and Wen and Yu for dilute mixtures [21]. The soft sphere collision model is used to account for multiple

interactions occurring at the same time which is predominant in dense particle systems. The contact force in the soft sphere model is decomposed into a normal force component and a tangential force component. The contact force components in the normal and tangential direction to the collision plane are expressed as

$$\vec{F}_n = -k_n\vec{\delta}_n - \eta_n\vec{v}_{p,n} \tag{5.7}$$

$$\vec{F}_t = \begin{cases} -k_t\vec{\delta}_t - \eta_t\vec{v}_{p,t} & for\ \left(|\vec{F}_t| < f|\vec{F}_n|\right) \\ -f|\vec{F}_n| & for\ \left(|\vec{F}_t| \geq f|\vec{F}_n|\right) \end{cases} \tag{5.8}$$

where; k, δ, η and ϕ above are the spring constant, particle contact displacement, coefficient of viscous dissipation, and friction coefficient, respectively. In the above equations, $\vec{v}_{p,n}$ and $\vec{v}_{p,t}$ are the normal and tangential component of the particle velocity. For more details about the soft sphere collision model, the reader is referred to [18, 22]. A semi-implicit fractional step method is used to solve the flow field on a non-staggered finite-volume grid. The flow field is advanced in time using calculated void fractions and drag forces from the previous time step. A particle grid is mapped over the fluid fine grid to allow for appropriate volume averaging of void fraction and avoid stability issues. The particles are advanced in time using an explicit Euler method. For detailed description about the numerical algorithm and the coupling between the two phases, the reader is referred to [18].

5.4 Simulation Details

The simulations are performed in a turbulent open channel flow (Figure 5.1) for medium sand in water. Mono-sized spherical particles (no variations in particle diameter) with a diameter of 0.5 mm and density of 2650 kg/m^3 are used for all simulations. A velocity slip condition on the top boundary and a no-slip condition on the bottom wall are imposed. The flow is periodic in both stream-wise and span-wise directions. All the simulations were run in a domain of 0.12×0.06×0.04 m divided into 120, 60, 65 cells in the stream-wise (x), cross-stream (z) and vertical direction (y), respectively. The grid is uniformly spaced in both stream-wise and span-wise directions. The vertical spacing is 0.2 mm in size for the first 20 grid cells above the bottom wall which is then gradually increased in size towards the top boundary. The near wall grid size, hence the resolved turbulent structures, are smaller or on the order of the particle diameter. Structures of the size of the particle (and larger) are more influential to its motion [58]. The domain was decomposed into

16 blocks and the simulation was parallelized using Message Passing Interface (MPI). The number of particles simulated in each block is almost the same to ensure load balance between processors.

Ten numerical experiments where conducted comprising of 5 simulations in the bed-load regime and 5 simulations in the suspended load regime. The bed-load regime is characterized by the motion of the particles along the bed surface by rolling and sliding whereas in the suspended load regime particles can be supported for a long time in the flow. It is well accepted that the transition between the two regimes occurs when the ratio of the shear velocity (u_τ) to the settling velocity of the particles (ω_s) is around unity. Simulations that cover the bed-load regimes were performed using 115,728 particles whereas simulations in the suspended-load regime were performed with 330,028 particles. This was driven by the expensive nature of the calculations and the relative static nature of the bed in the bed load regime, not requiring as many particles as the suspended load regime in which the particles are lifted from the bed. The numerical parameters for the different simulations are listed in Table 5.1.

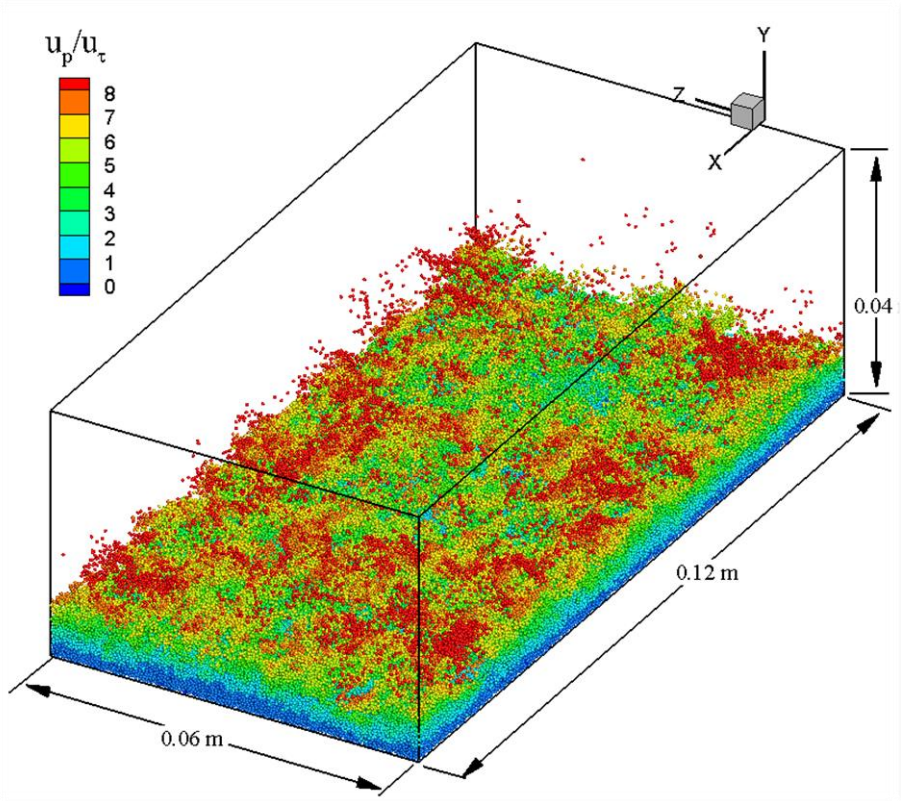

Figure 5. 1. Computational Domain (flow is in the positive x-direction), particles (shown to scale) are colorized with respect to their velocity normalized by the friction velocity.

Table 5. 1. Simulation parameters for different cases.

case	Bedload					Suspended load				
	1	2	3	4	5	6	7	8	9	10
u_τ (m/s)	0.013	0.0222	0.03	0.0392	0.0483	0.0618	0.0753	0.0835	0.0944	0.113
Re_τ	584	998	1346	1762	2170	3382	3754	4240	4680	5080
τ^*	0.0209	0.061	0.111	0.19	0.288	0.7	0.862	1.1	1.34	1.558
u_τ/ω_s	0.239	0.384	0.526	0.696	0.848	1.31	1.46	1.64	1.82	1.97
Re_b	7,820	1,1847	15,160	18,476	22,286	29,712	33,466	39,141	46,321	53,116

The size of the near-wall grid used is 0.2 mm, which for the range of flow conditions considered in this study corresponds to Δy^+ ranging between ~ 3 and 25 for Re_τ = 584 and 5080, respectively. To verify the adequacy of the baseline grid used, two finer grid calculations are performed for Re_τ=5080, the highest Reynolds number in this study (see Table 5.1). While all calculations presented in this paper use full coupling between the particles and the fluid flow (inclusion of particle effects through void fraction and drag term in Eqs. 5.1 and 5.2), the grid dependency study used partial coupling in which the effect of particles is fed back to the momentum equations only through the drag term. This results in slight under-prediction of sediment flux and flow rate compared to the fully coupled calculations [145] but should have an impact on the conclusions made from the grid dependency study. In the first-level finer grid the number of cells in the stream-wise direction was kept the same as the baseline grid, whereas the number of cells in both the cross-stream and vertical directions were increased to 150, resulting in a grid 5.8 times larger than the baseline grid. The near-wall grid size was reduced by a factor of 4 in the first 2 mm above the bottom wall (thus Δy^+ ~6 at Re_τ=5080). In the second-level refinement, the streamwise cells were increased to 150 whereas the number of cells in the vertical direction was increased to 250, giving a grid (150×150×250) which is 12 times finer than the baseline grid. The near wall cells were refined by a factor of 2 compared to the finer grid (8 times compared to the base-line grid in the first 2 mm above the bottom wall). Table 6.2 shows the results of the grid study with corresponding cell sizes in the x, z, and y directions in terms of percentage difference from the finest grid level which is considered the true solution. Both finer grid results are averaged for 10 s after running the simulation for 10 s of real time. The baseline grid has errors of -13.7% and 0.11% in the sediment flux and mean velocity, respectively with respect to the finest grid. Whereas the finer

grid has errors of 7.9 % and -2.8%. While no clear convergence trend is noticed, the sediment flux seems to be the most sensitive to the change in grid resolution but is bounded within ±15%, whereas the mean velocity is less sensitive to the grid resolution. Based on these results, we have used the baseline grid for all the calculations presented. This admits to an uncertainty of ±15% in the calculation of sediment flux noting that the sediment flux varies over four orders of magnitude going from the bed load to the suspended load regimes. The base grid resolves the structures that impact sediment transport, however, an even finer grid may result in producing more turbulent structures that can entrain more particles. The use of finer grid, however, adds significant computational cost. It is reasoned that the grid can be coarsened but not to exceed the order of the particle size to allow for faster estimates of the sediment transport with reasonable accuracy. It should be emphasised that due to the chaotic nature of the problem, empirical formulas that estimate the sediment transport have notable differences even in the bed-load regime [69].

Table 5. 2. Comparison of baseline grid results with fine grid results for most energetic suspended load simulation using partial coupling.

	Base-line grid	Difference** %	Fine grid	Difference** %	Finest Grid
cells	468,000 (120×60×65)	--	2,700,000 (120×150×150)	--	5,625,000 (150×150×250)
u_τ(m/s)	0.113	--	0.113	--	0.113
Re_τ	5,080	--	5,080	--	5,080
τ^*	1.58	--	1.58	--	1.58
q^*	10.95	-13.7 %	13.68	7.9 %	12.68
u_b(m/s)	1.104	0.11 %	1.0721	-2.8 %	1.103

** (grid result-finest grid result)/(finest grid result)

Figure 5.2 shows the location of the computational experiments on the Shields diagram (red line shows Brownlie's fit [121]) along with criteria for the transition to suspended flow by van Rijn [146] and Bagnold [147]. It can be seen that all suspended load experiments have shear stresses higher than Bagnold criterion for initiation of suspension [146]. For the current work, only three simulations are considered for further investigation (indicated in Figure 5.2). These are indicated in Table 5.1 by a bold font. The simulation parameters pertaining to the reference particle

properties are listed in Table 5.3. The particle stiffness was set to an artificially low value to soften the particles and to increase the time of collisions in the application of the soft sphere model. This technique has been shown not to have much effect on the results with the caveat that the softening be limited to prevent large unphysical overlap between the spheres in contact (>10% of the radius). In the current work, the fluid time step was set to 5.3×10^{-4} s within which ten particle time steps are taken.

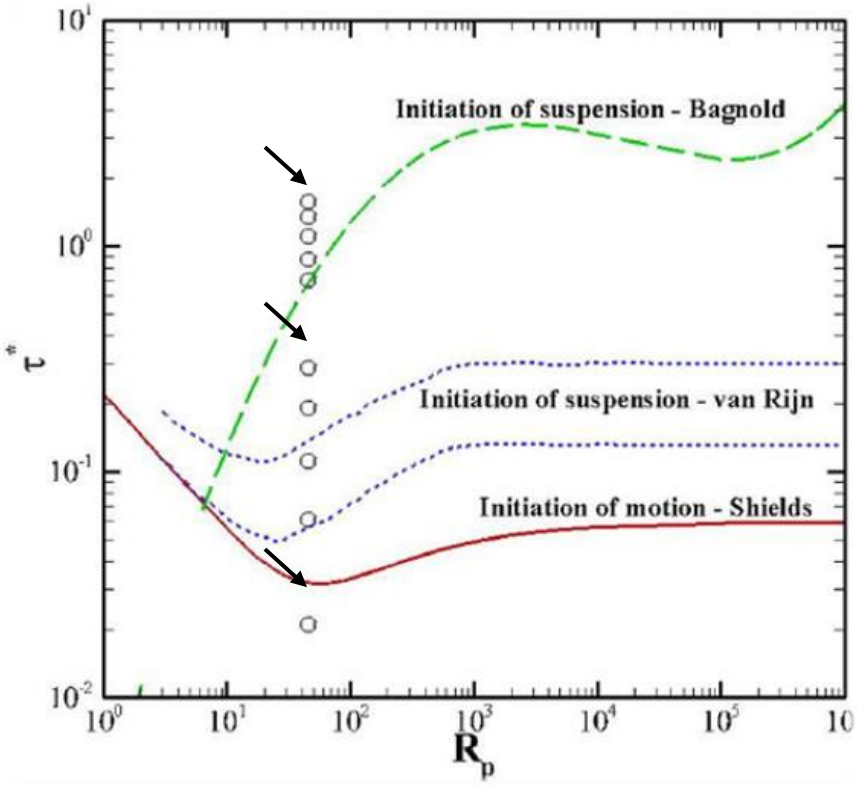

Figure 5. 2. Location of the computational experiments on the Shields diagram (red line shows Brownlie's fit (1982)) along with criteria for the transition to suspended flow by van Rijn (1984) and Bagnold (1966). Arrows show the selected cases for the sensitivity.

Table 5. 3. Numerical parameters used in the reference calculation.

Parameter	Value (unit)
Particle diameter	0.5 (mm)
Coefficient of restitution	0.01
Particle density	2650 (kg/m^3)
Friction coefficient	0.6
Stiffness coefficient	100 (N/m)
Particle time step	$5.3\text{x}10^{-5}$ (s)

5.5 Results

To investigate the sensitivity in the present framework, three different cases were selected, τ^*~0.021, 0.288 and 1.56. The selected cases represent one case near the threshold of motion, another at high bed-load and one at the most energetic suspended-load simulation (as indicated on Figure 5.2). The bed-load simulation with the smallest frictional velocity is theoretically at a shear stress below that required for particles entrainment. The simulations were run for 10 s using base reference values of the parameters of interest (as indicated in Table 5.3), then one numerical parameter was changed at a time and the corresponding change in the quantitative result of both sediment flux and flowrate are observed for the following 15 s. Unless stated otherwise, the results in the last 10 s are averaged and compared to base-value calculation averages during the same period. The base-value of the parameters under investigation for the reference cases are f=0.6, e=0.01, and k=100 N/m. Two different friction factors, 0.25 and 0.01, were tested. A friction factor of 0.25 was reported as a lower measured value of natural sediment particles by [140], however, lower (or even zero) friction factors are used by researchers, e.g. [87, 101]. A non-zero friction factor of 0.01 was selected to verify the conclusions reported in [86] that stated that the friction factor was insignificant provided that it had a non-zero value. Three additional values of the coefficient of restitution were adapted, 0.1, 0.6 and 1.0. The particle stiffness was decreased by one order of magnitude and increased by one order of magnitude (k=10 and 1000 N/m). For the more stiff case the number of particle sub-steps was increased to 32 (instead of 10) and the same fluid time step was maintained. The averaged results presented for the stiffness cases are only averaged for the 5 s after the change in the stiffness.

Table 5.4 presents the averaged main parameters of the reference calculation for the simulation period from 15-25 s. The standard deviation about the mean values of the flow velocity and particle flux are also indicated in Table 6.4 as a percentage of the mean value. The definition of the non-dimensional sediment flux q^* can be found in the nomenclature. It is found that variations of 10-15% in the particle flux exist even for small changes in the mean flowrate velocity. The variation of the mean flow velocity is less than 2% in the three calculations which indicates that the balance between the applied mean pressure gradient and the losses in the domain are in robust equilibrium. On the other hand, sediment transport is a sensitive quantity and variations less than the standard deviations shown in Table 4 are considered insignificant in the current sensitivity work.

Table 5. 4. Mean base-calculation parameters with standard deviation for 10 s averaging period.

τ^*	parameter	mean	Standard deviation/mean
0.021	Sediment transport (q^*)	4.42×10^{-3}	12.3%
	Mean flow velocity (u_b)	0.174	0.4%
0.288	Sediment transport (q^*)	0.3944	14.1%
	Mean flow velocity (u_b)	0.505	1.2%
1.56	Sediment transport (q^*)	15.0637	9.1%
	Mean flow velocity (u_b)	1.19	0.6%

Figures 5.3-5.5 show the temporal evolution of flow rate and sediment transport as a function of the simulation parameters for each of three cases. The trends are generally the same for all cases. Figure 5.3 shows the effect of changing the numerical parameters on the flowrate and particle flux near entrainment of particles threshold ($\tau^* \sim 0.021$). Among all calculations both a friction factor of 0.01 and a restitution coefficient of 1.0 show an increase in the mean flow velocity. The corresponding increase in particle flux is more obvious when f=0.01. Both the friction and restitution coefficient are directly related to the dissipation of the particle energy through collisions.

Similar conclusions can be seen from temporal trends at more energetic bed-load calculation (Figure 5.4 for $\tau^* \sim 0.288$). The impact of reducing the friction factor to 0.01 becomes more severe and the impact of reducing the friction factor to 0.25 on the particle flux exceeds the effect of assuming an elastic impact with restitution coefficient of 1.0. In the suspended load regime, the friction factor has a much larger impact on the results. Changing the coefficient of restitution from 0.01 to 1.0 also shows some impact which is, however, not as severe as the friction factor. Although some averaged results for f=0.01 have not attained a stationary state, a high sensitivity of the sediment transport and flow rate on the particle friction factor is established.

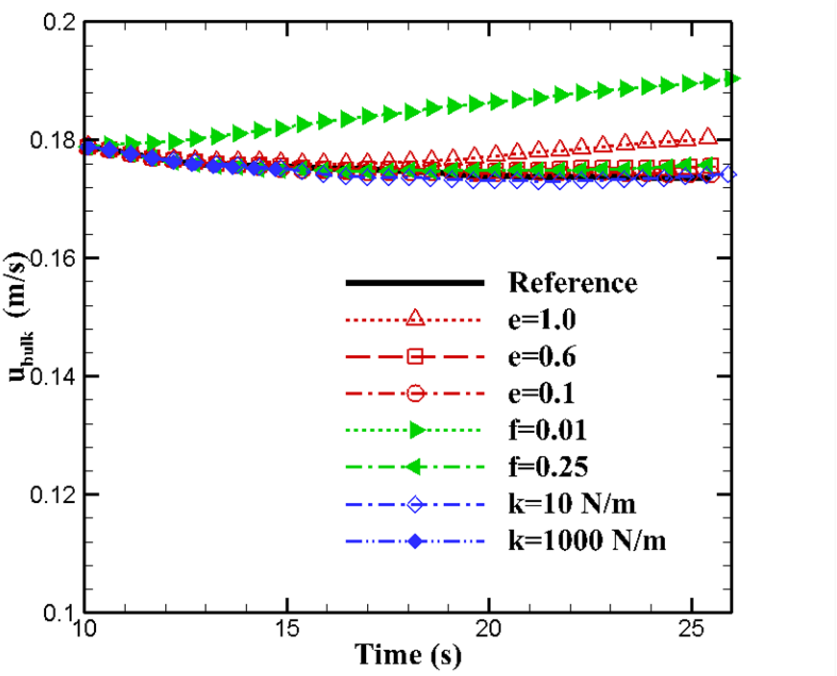

(a)

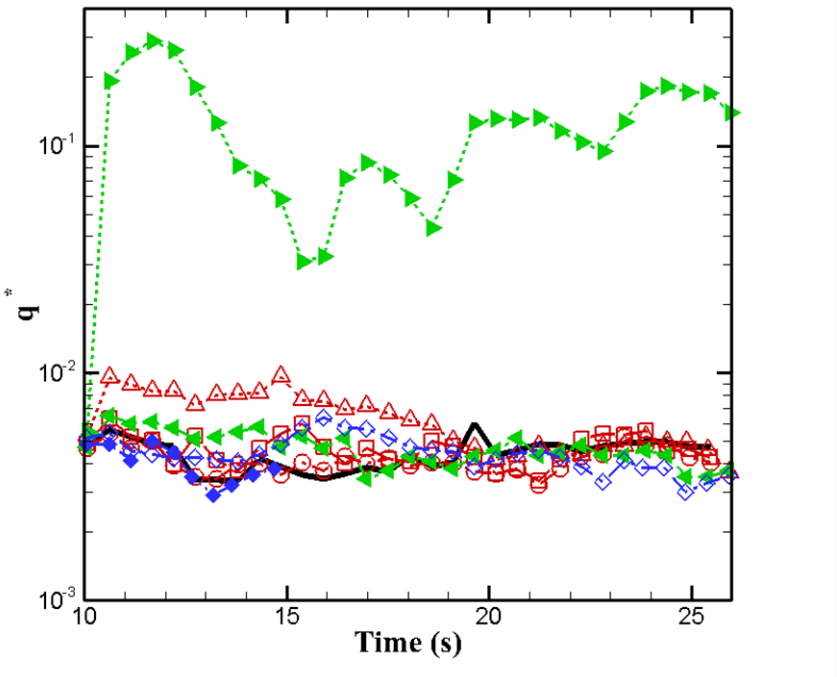

(b)

Figure 5. 3. Effect of changing numerical parameters on a) mean flow velocity and b) particle flux for τ^*~0.021.

(b)

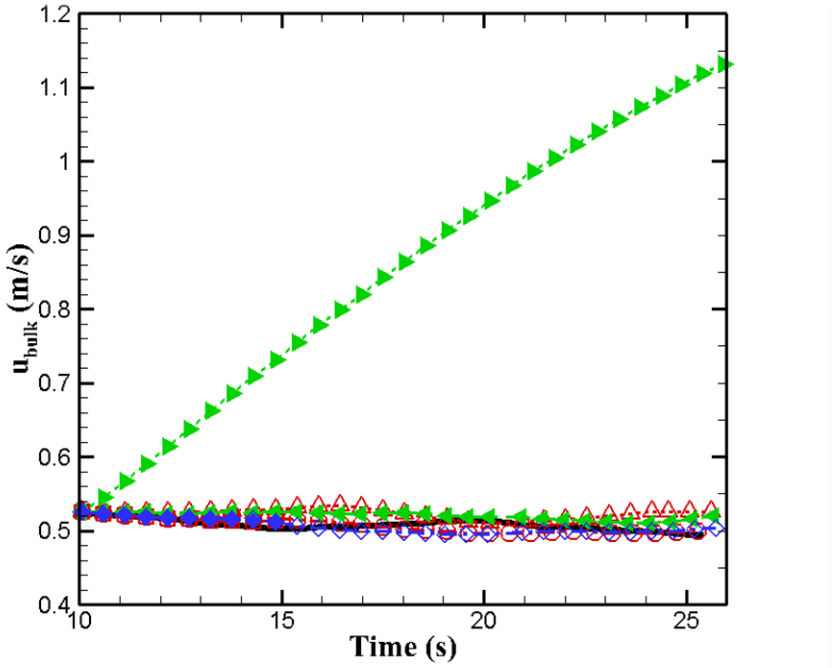

(a)

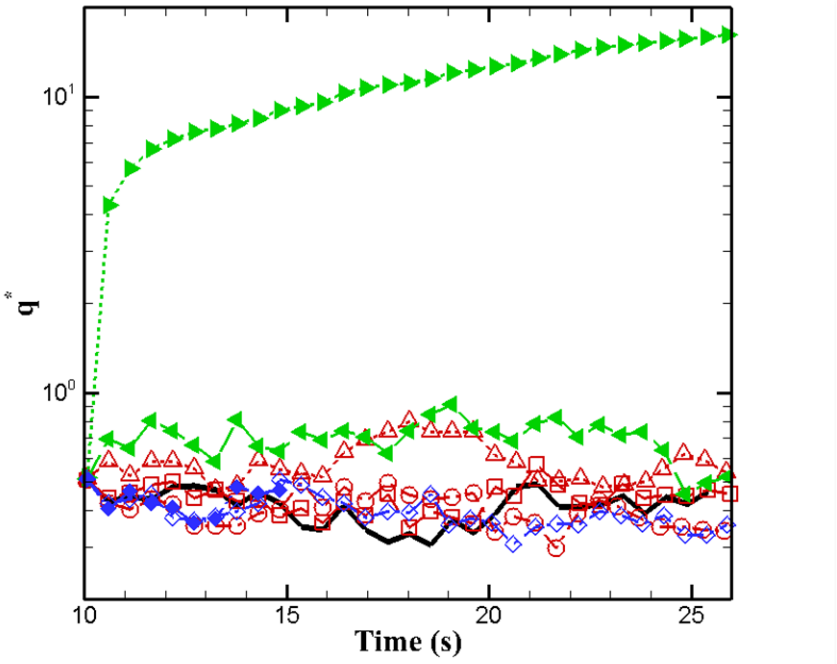

(b)

Figure 5. 4. Effect of changing numerical parameters on a) flowrate and b) particle flux for τ^*~0.288 (legend as indicated in Figure 5.3.a).

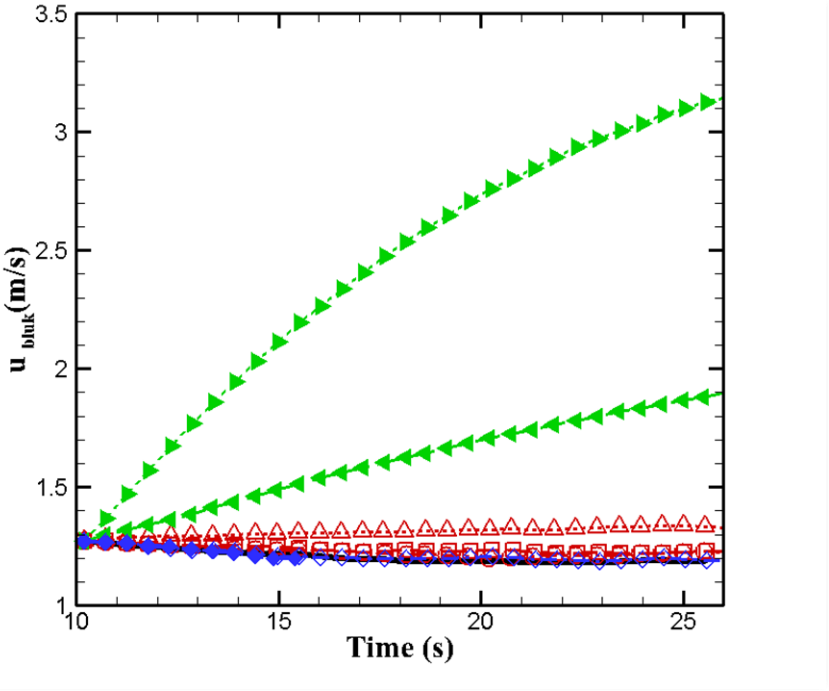

(a)

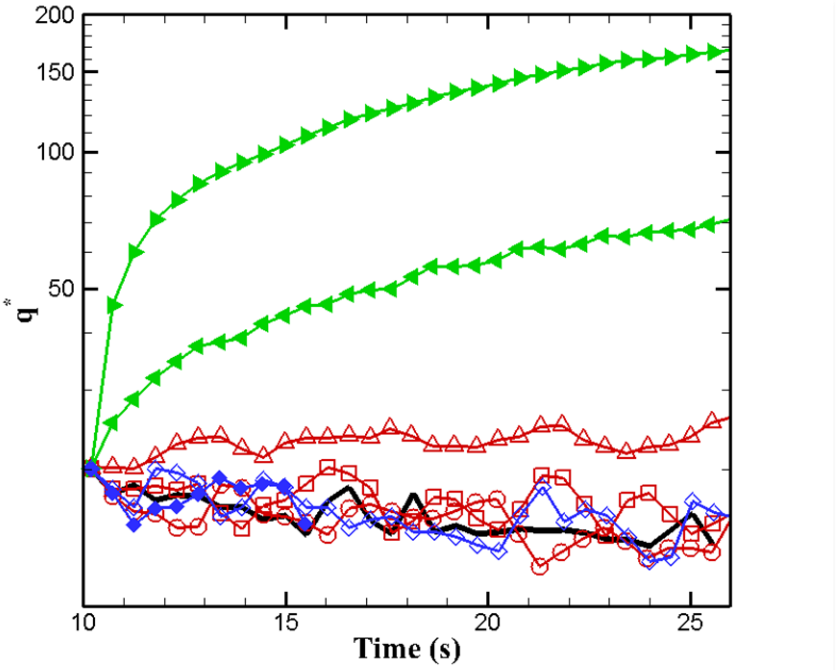

(b)

Figure 5. 5. Effect of changing numerical parameters on a) flowrate and b) particle flux for τ^*~1.56 (legend as indicated in Figure 5.3.a).

There is clear evidence that reducing particle friction results in higher particle flux in both bed-load and suspended load regimes. The corresponding increase in flowrate is a result of the reduced dissipation of energy during particle collisions and the increased mobility of the particle bed. Less mobile particles extract more energy from the fluid. The sediment transport rate obtained as indicated in Figure 5.6 for all 10 reference calculations is compared to empirical formulas (Muller-Peter-Meyer is used for bed-load regime and Engelund-Hansen for total load) [125, 148]. Figure 5.6 shows that the sediment transport results from simulations using base-value parameters are in good agreement with empirical formulas in the bed-load regime but under predict the correlation in the suspended load regime. The sensitivity analysis cases are mapped on the same figure. It is noteworthy that for the suspended load regime, reducing the friction factor from 0.6 to 0.25 can bridge the gap between the under-predicted simulation results in suspended load and the empirical total transport formula (in fact results tend to over-predict with f=0.25 as indicated in Figure 5.6). The impact of reducing the friction factor on bed-load results is not as large as in the case of suspended load except in the extreme case of f=0.01. It was found that reducing particle friction from 0.6 to 0.25 increased the particle flux by 80% and 295% for τ^*~ 0.288 and 1.56, respectively. The near threshold simulation (τ^*~ 0.021) did not show significant change. However, f=0.01 had a large impact on all the simulations with a large increase in sediment transport.

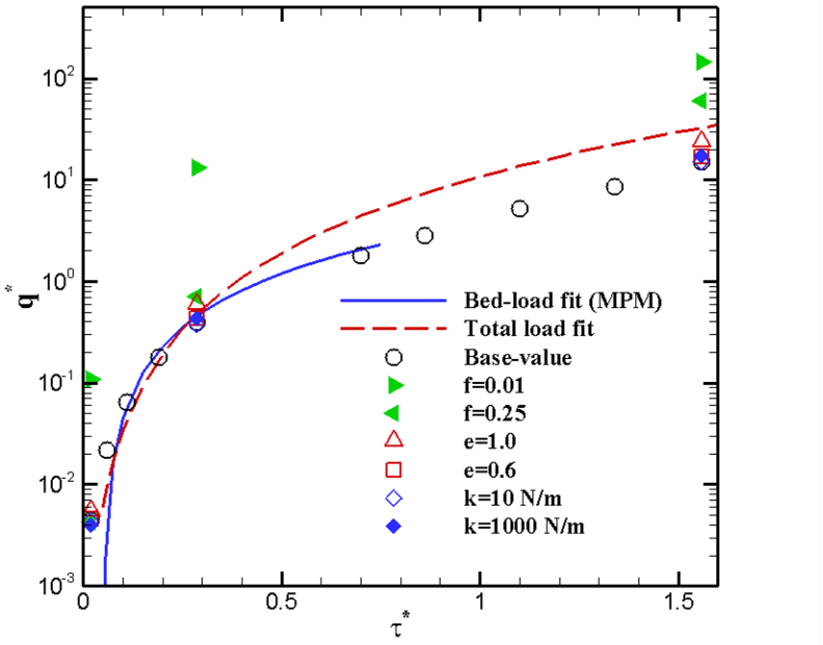

Figure 5. 6. Non-dimensional sediment transport vs. Shields parameter for selected numerical experiments.

Table 5.5 summarizes the sensitivity of the tested parameters on sediment transport and mean velocity. It is noted that parameters pertained to the dissipation of collision energy such as the restitution coefficient and particle friction factor have an impact on the simulation results. Between the restitution coefficient and the particle friction factor, the results are much more sensitive to the friction, especially in the suspended load regime. A change of two orders of magnitude of the particle stiffness shows a change of less than 10% which is within the standard deviation of the particle flux variability.

Table 5. 5. Deviations in sediment transport (q*) and mean flow velocity (ub) from base-value calculation with a change in one numerical parameters.

τ^*	parameter	e=1	e=0.6	e=0.1	f=0.01	f=0.25	k=10	k=1000
0.021	q^*	23.5%	2.5%	-7.5%	2375%	-3.4%	-1.3%	-9.4%
	u_b (m/s)	2.1%	0.5%	0.2%	7.2%	0.5%	-0.4%	-0.1%
0.288	q^*	50%	9.9%	1.2%	3208%	79.5%	-4.0%	-3.5
	u_b(m/s)	3.4%	2.2%	-0.9%	90%	2.7%	-1.1%	0.85%
1.56	q^*	57.6%	11.9%	-2.0%	854%	295%	0.74%	3.4%
	u_b (m/s)	11%	3.2%	2.3%	133%	45.2%	0.7%	-0.5%

Generally speaking, neither any obvious trend nor significant change was found for the spring stiffness on both the fluid average velocity and the particle flux. Reducing the collision dissipative properties by either increasing the restitution coefficient or reducing the friction factor is found to increase the average flowrate indicating that particle resistance to motion is smaller. When the restitution coefficient is increased or the friction factor is decreased, particles tend to lose less energy through collisions and hence become more mobile. The increase of particle mobility is associated with a reduction in the momentum extracted from the fluid which leads to an increase of the fluid average velocity (especially if the amount of entrained particles is significant).

The effect of friction factor was found to be the most significant among the parameters investigated. This can be attributed to the fact that friction factor constitutes one of the major resistances to particle motion. In fact results listed in Table 5 indicate that the high bedload simulation is more sensitive to the friction factor compared to the suspended load. This is because in the suspended bed the particles collide less frequently. For the near incipient motion a reduction

of the friction factor did not show significant effect on the results, and leads to the conclusion that a friction of 0.25 is enough to provide reasonable amount of resistance to the entrainment of particles. A rather small value of the friction factor (f=0.01) is, however, insufficient to provide enough resistance for the entrainment of particles leading to a huge increase of the particle flux and the average fluid velocity. The threshold at which the friction factor fails to maintain reasonable resistance is not investigated in the current work but is estimated to be smaller than 0.25. It should be mentioned that [149] analysed the effect of friction factor on the critical shear stress (threshold of particle movement) for spherical particles with friction factors ranging from 0.36-1.0 and found good agreement with Shields diagram at a fiction factor of ~0.47. Different conclusions, however, were found by [150] who analysed the incipient motion for ellipsoid particles, where the increase of friction factor can cause the initiation of motion to have different mechanics (i.e. start with rolling or sliding or a combination of them).

The simulations (and possibly the physical phenomenon) might show significant variation at such condition for small change in parameters which make the process of determination of the entrainment threshold a challenging task. For instance, Shields presented the entrainment threshold over a wide band [151], while Kramer [152] suggested a qualitative method to describe the entrainment of the particles based on visual observations. A limit of 4.1×10^{-4} kg/(m.s) of sediment transport flux is suggested by United States Army Corps of Engineers (USACE) [126]. Many other researchers suggest different ways to determine the threshold of entrainment of particles [149]. The entrainment of particles is also linked to the different turbulent events [97] and can be affected by sheltering of particles or their contact angles (or angle of inclination) [149, 153, 154]. In a physical situation, additional parameter can influence the initiation of sediment threshold such as the shape and variability of particle size and the presence of rolling friction and adhesion forces. The authors recommend using a friction factor of 0.25 and higher when simulating sediment transport or studying the entrainment threshold using Eulerian-Lagrangian descriptions.

5.6 Conclusions

The current work presents a sensitivity analysis of collision parameters on the numerical simulations of sediment transport using CFD-DEM framework. The sensitivity to friction factor, restitution coefficient and particle stiffness was examined for sediment transport cases in different flow regimes. It was found that the simulation results are sensitive to changes in friction factor in suspended load regime but show lesser sensitivity in the bed-load regime when moderate changes

in friction factor are considered. The increase in coefficient of restitution from the base value of 0.01 to 1.0, results in an increase in the particle flux and the flowrate. This is brought about by less dissipation of energy during collisions and a subsequent increase in the mobility of particles, which extract less energy from the fluid. Results from using restitution coefficient of 0.6 were, however, comparable to those from the reference calculation with a coefficient of restitution of 0.01. A change of the particle stiffness by two-orders of magnitude, shows insignificant impact on both particle transport and flow rate. Between the three parameters varied in the sensitivity analysis, the friction factor had the largest effect on the simulation results.

Different Eulerian-Lagrangian descriptions are used to study sediment transport in the literature ranging from coupling the particles (or DEM) to a fixed velocity profile to strongly coupling the particles to the fluid through resolved flow simulations. Although these models may show different sensitivities to the simulation parameters, the current conclusions are broadly applicable to other Eulerian-Lagrangian descriptions as well.

5.7 Nomenclature

A_s	surface area of bed [m^2]
e	coefficient of restitution [-]
F_n	normal contact force [N]
F_t	tangential contact force [N]
F_p	force on particle [N]
f	friction factor [-]
f_{drag}	drag imparted to fluid [N/m^3]
g	gravitational acceleration [m/s^2]
k	stiffness coefficient [N/m]
L_x	length of the domain in the x-direction [m]
m_p	mass of the particle [kg]
P	pressure of the fluid [Pa]
$q_*=q_{sx}/(g(\rho_p-\rho)d^3)^{0.5}$	non-Dimensional sediment flux
$q_{sx}=\sum u_p V_p/A_s$	sediment transport flux[m^2/s]

$R_p=(g(\rho_p-\rho)d^3)^{0.5}/\mu$	particle Reynolds number
u_b	Mean fluid velocity [m/s]
v_p	velocity of the particle [m/s]
V_p	volume of the particle [m^3]
ε	void fraction
δ_n	normal overlap between particles [m]
δ_t	tangential displacement [m]
η	viscous damping coefficient [N.s/m]
μ	dynamic viscosity of the fluid [Pa.s]
ρ	density of fluid [kg/m^3]
ρ_p	particle density [kg/m^3]
τ_g	shear stress tensor of fluid [N/m^2]
$\tau^*=\tau/(g(\rho_p-\rho)d)$	Shields parameter

Chapter 6

Revised Partial Coupling for Dense Fluid-Particulate Systems

Husam A. Elghannay[*] and Danesh K. Tafti[*]

[*]Department of Mechanical Engineering
Virginia Polytechnic Institute and State University
Blacksburg, Virginia 24061

Citation:

Paper submitted to Powder Tech (Sept. 2017).

6.1 Abstract

The Eulerian representation of the fluid in CFD-DEM simulations is typically made by solving volume averaged Navier-Stokes Equations. The full coupling between the dispersed phase and continuous phase is made by the exchange of source terms from the point-mass force models of the fluid-particle interaction forces as well as the void fraction calculated from the presence of the particles in the computational fluid cells. For dense particulate system, the full coupling approach can result in a slow convergence of the flow solver and can impact the robustness of the solver during the time-integration process. Although smoothing the void fraction can help stabilize the calculation, it can have a negative impact on the quality of the results. This situation manifests itself because point-mass force models (e.g. drag) typically use the local void fraction in their formulation. One option is to use partial coupling by neglecting the explicit effect of void fraction in the fluid momentum equations while retaining its effect on force models. Although the partial coupling is more stable and shows better convergence behavior, the mobility of the particles is found to be reduced as compared to the full-coupling approach.

In the current work, we propose a revised partial coupling in which a modified fluid velocity is used in point force models to compensate for the omission of the void fraction in the fluid governing equations. The effectiveness of this method is demonstrated in a fluidized bed and in sediment transport simulations. In both cases it is shown that the use of the proposed method gives very good comparisons with the fully-coupled simulations while reducing the fluid calculation time by factors ranging from 1.35 to 4.35 depending on the flow conditions.

6.2 Introduction

Two methods are typically used to simulate particulate flow systems namely the Eulerian-Eulerian approach and the Eulerian-Lagrangian approach. In the first method, also known as the Two-Fluid Model (TFM), both phases are modeled as two interpenetrating fluids using two sets of conservation equations. The latter method solves the volume averaged Navier-Stokes equations of the continuous phase while the particles are tracked by solving a dynamic equation based on Newton's second law of motion. Forces on each particle can be either solved by performing integration over the surface (Resolved Flow Simulations) or by using point model forces (Discrete Element Method). The TFM is appealing since it allows for simulating industrial and natural scale systems [81, 155]. This is because modeling the dispersed phase as a fluid is much less expensive

than the burden of tracking a large number of particles. However, modeling the dispersed phase as a continuum requires additional closure models (e.g. to estimate the solid viscosity) and the method is problematic when simulating particles with significant size or shape distribution or when handling particle-wall collision [58].

Although the Eulerian-Lagrangian approach includes a better representation of the physics, its application to industrial and to natural scales is impractical due to the large number of particles involved and the computational cost. The cost of Eulerian-Lagrangian approach (particle resolved simulations and CFD-DEM) scales with the number of particles to be simulated. Particle resolved simulations require a fluid grid that is at least one order of magnitude finer than the particle diameter and thus the method is quite restrictive in the size of the system that can be simulated. Simulation of thousands of particles using resolved flow simulation is reported for turbulent channel flow [156] and fluidized bed [157] applications. CFD-DEM, on the other hand, uses point mass particles and the particle forces are modeled. While millions of particles have been simulated using the CFD-DEM method when using large number of processors with efficient parallelization techniques [19, 111, 137], large system simulations are not that common. Thus it is important to reduce the cost of CFD-DEM simulations without sacrificing accuracy. One method that is used is to lump a group of particles into representative particles (swarms or parcels) to reduce the number of particles. In such simulations quick, but somewhat less accurate, estimates can be obtained [158].

At dilute concentration of the dispersed phase (volume concentration of the dispersed phase $<1\times10^{-3}$) interaction forces between the particles can be neglected resulting in two-way coupling between the fluid and the particles [159]. In this case the particles are coupled to a single phase flow solver using drag forces. At even lower concentration of particles (volume concentration of the dispersed phase $<1\times10^{-6}$) the feedback from the particles to the fluid can be further neglected resulting in one-way coupling. At dense concentration of the dispersed phase ($>1\times10^{-3}$) the interaction between the particles becomes important. The term four-way coupling is used to indicate that the particle-particle interaction force becomes important in addition to the two-way coupling [159].

The volume averaged Navier-Stokes equations are typically used for dense particulate flow systems [20]. Not only is the fluid momentum affected by the forces exerted on the particles but also by the flow blockage or solid fraction due to the presence of particles. Additionally, the point

mass force models (e.g. drag) are also affected by the flow blockage [e.g., 108, 160]. Thus for dense systems, the solid fraction or its complement, the void fraction, play a critical role in prediction of dynamics. To satisfy the volume-averaged basis of the Navier-Stokes and continuity equations, the calculation of the void fraction should be over a sufficiently large sample of particles to not only give some measure of statistical convergence but also to have a smooth spatial and temporal distribution of the void fraction. Some researchers suggest that the size of the computational cell over which the fluid void fraction is averaged to be ~ 3-4 times that of the particle diameter [6, 161]. Many other researchers use higher ratios [e.g., 162] or diffuse the solid fraction over a larger area [137]. The method of calculating the void fractions in the computational cell can be different as some researchers assume that the full particle is located inside the computational cell in which its center resides (particle center method or PCM) [22] whereas others use only portions (or sectors) of the particle of the volume size that is physically located in the cell (exact method) [163]. The exact method is more accurate but more expensive compared to the PCM. An alternative method (offset method) for calculating the void fraction was suggested by Alobaid, Ströhle [164] in which the void fraction is calculated by averaging the cell-center method results in multiple spatially offset cells. The offset method is reported to improve the accuracy of the predication of the void fraction compared to the PCM [165, 166]. Peng, Doroodchi [167] reported that PCM produces the same results as the exact method if the cell to particle diameter ratio is 3.82. Peng, Doroodchi [167] also reported that the void fraction averaging becomes unsuitable if the cell size is smaller than 1.63 of the particle diameter.

In instances when the fluid grid needs to be of the same order or smaller than the particle diameter, such as in wall bounded turbulent flows, the void fraction can be either calculated on a coarser particle grid that is mapped over the existing fluid grid [18] or smoothed over the neighboring region [137, 168]. These techniques allow for full coupling between the two phases using particle forces as well as void fractions in the fluid momentum equations. However, many past studies in the field of sediment transport have avoided fully coupled simulations because of the inconsistency posed by the volume-averaging assumption and the need to resolve near wall turbulence [41, 91, 96, 169]. Failure to have a smooth variation of void fraction results in long convergence times of the flow solver at each time step, and in extreme cases also leads to numerical instabilities.

The differences between full coupling and partial coupling was investigated by Elghannay and Tafti [145] in sediment transport under turbulent conditions. The fully-coupled method solved the volume averaged Navier-Stokes equations including the effect of void fraction and drag forces from the solid phase. In partial coupling, the void fraction was not considered (defaulted to unity) and only the drag forces were fed back to the fluid momentum balance. It was found that the partial coupling tended to under-predict the mobility of the particles resulting in lower sediment transport compared to full coupling when the same void fraction sensitized drag model is used for both. The deviation increased as more particles were transported as the bed transitioned from the bed-load regime to suspended load. So on one hand, full coupling leads to complications in the calculation of void fraction and numerical difficulties during time integration of fluid equations, while on the other hand, partial coupling eliminates these difficulties but reduces accuracy.

In this paper we suggest a method to bridge the difference between the partial coupling and the full coupling techniques. By doing so it can be possible to take advantage of the fast convergence and numerical stability of partial coupling and at the same time keep the accuracy at par with full coupling. Admittedly the proposed modified partial coupling is still an approximation to the four-way full coupling, but it is shown that using the proposed method gives very close quantitative agreement with fully-coupled simulations at a lower computational cost. Thus, the proposed method should be viewed as a significant improvement over the base partial coupling rather than a substitute for the fully-coupled method. It does not replace the fully-coupled method but can be viewed as a reasonably accurate substitute when the fully-coupled method poses numerical difficulties and partial coupling is the only viable alternative. A bolder interpretation of the proposed method is possible when viewed within the context of other cost-saving model approximations used in the DEM procedure - the proposed modified coupling can be justified as another means of reducing computational complexity of fully-coupled CFD-DEM simulations. This is proven by comparison of the performance of the three coupling techniques on two different applications. The differences in instantaneous and averaged results are discussed along with the computational savings.

6.3 Mathematical Formulation

6.3.1 Particle dynamical equation

In DEM the path of each particle is predicted by the integration of its equation of motion resulting from the application of Newton's law of motion. The equation of motion of particles moving under influence of drag ($\vec{f}_{drag,i}$) and gravity forces ($\vec{f}_{grav,i}$) along with contact forces ($\vec{f}_{contact,i}$) can be expressed as

$$\frac{d\vec{u}_{p,i}}{dt} = \vec{f}_{grav,i} + \vec{f}_{drag,i} + \sum \vec{f}_{contact,i} \tag{6.1}$$

where $\vec{u}_{p,i}$ represents the particle velocity and the force components in the above equation are per unit mass of the particle. Without limiting the generality of the revised partial coupling, for simplicity Eq. (6.1) assumes that the drag force is the only significant fluid-particle interaction force. The contact force ($\vec{f}_{contact,i}$) accounts for both particle-particle interactions and particle-wall interactions. The soft sphere approach is used to account for multiple collisions occurring simultaneously which is predominant in dense particle concentrations. The contact force in the soft sphere model is modelled using a spring-dashpot system in the normal and tangential directions. More details about the linear spring dashpot soft sphere collision model can be found in [18, 22].

The gravity force includes both gravity and buoyancy effects. The submerged weight of the particle (per unit mass of the particle) is given by

$$\vec{f}_{grav} = \left(1 - \frac{\rho}{\rho_p}\right)\vec{g} \tag{6.2}$$

Where ρ is the fluid density and ρ_p is the particle density and g represents the gravitational acceleration. The drag force accounts for the quasi-steady drag in uniform flow and is often a key element in the interaction of dense granular flows and is modeled using the form

$$\vec{f}_{Drag} = \frac{\beta}{\varepsilon(1-\varepsilon)\rho_p}\left(\vec{u} - \vec{u}_p\right) \tag{6.3}$$

where β and $\vec{u}$ are the momentum exchange coefficient and the interstitial fluid velocity. The term ε is the void fraction in each computational cell. A combination of Ergun formula for dense mixtures $\varepsilon < 0.8$ and Wen & Yu drag correlation for dilute mixtures $\varepsilon > 0.8$ is used for the momentum exchange coefficient with a blending function to avoid discontinuity [21].

$$\beta = W\beta_{Ergun} + (1 - W)\beta_{Wen-Yu} \tag{6.4}$$

$$\beta_{Ergun} = 150\mu\frac{(1-\varepsilon)^2}{\varepsilon d_p^2} + 1.75(1-\varepsilon)\frac{\rho}{d_p}\left|\vec{u} - \vec{u}_p\right| \tag{6.5}$$

$$\beta_{Wen-Yu} = \frac{3}{4}C_D\frac{(1-\varepsilon)\varepsilon}{d_p}\rho\left|\vec{u} - \vec{u}_p\right|\varepsilon^{-2.65} \tag{6.6}$$

The blending function W is defined as

$$W = \frac{\tan^{-1}\big(150(\varepsilon - 0.8)\big)}{\pi} + 0.5 \tag{6.7}$$

$$C_D = \begin{cases} 24\big(1.0 + 0.15Re_p^{0.687}\big)/Re_p, & Re_p < 1000 \\ 0.44, & Re_p \geq 1000 \end{cases} \tag{6.8}$$

where C_D is the drag coefficient. Reynolds number Re_p is calculated as

$$Re_p = \frac{\varepsilon\rho d_p\left|\vec{u} - \vec{u}_p\right|}{\mu} \tag{6.9}$$

In Eq. (6.9) μ is the dynamic viscosity of the fluid.

6.3.2 Fluid equations

The carrier phase is modeled using the volume averaged Navier-Stokes equations [20] derived for multiphase flows. The current implementation of the continuous phase is governed by Model-B of Gidaspow [21] in which the pressure drop is accounted for only by the fluid. The fluid equations are written as

$$\frac{\partial(\varepsilon\rho)}{\partial t} + \vec{\nabla}.(\varepsilon\rho\vec{u}) = 0 \tag{6.10}$$

$$\frac{\partial(\varepsilon\rho\vec{u})}{\partial t} + \vec{\nabla}.(\varepsilon\rho\vec{u}\vec{u}) = -\vec{\nabla}p + \vec{\nabla}.(\varepsilon\bar{\bar{\tau}}) + \rho\vec{g} - \sum_{i=1}^{n_p}\frac{m_{p,i}\vec{f}_{fp,i}}{\forall_{cell}} \tag{6.11}$$

where $p\ and\ \bar{\bar{\tau}}$ are the pressure, and viscous shear stress tensor, respectively. While $m_p, \vec{f}_{fp}, \forall_{cell}$ and n_p are the particle mass, the fluid-particle interaction force per unit mass of the particle, the volume of the computational cell, and the number of particles residing in a computational cell.

The flow field is solved on a non-staggered finite-volume grid using a semi-implicit fractional step method. The flow field is advanced in time using the calculated void fractions and drag forces from the previous time step. The calculated fluid velocity field is transferred to the particle grid

and the particles are advanced in time. During this process, the continuous and disperse phases are coupled via the drag force and void fractions. The void fractions and cumulative particle drag forces are calculated in each particle grid cell and transferred to the fluid grid for use in Eqs. (6.3-6.9). The void fraction is calculated by a weighted distribution of particle volumes in a given particle grid cell to the cell vertices and then averaging the cumulative volumes from the vertices to the fluid cells contained in the particle cell. A similar procedure is carried out for transferring the cumulative drag forces from the particle to the fluid grid. A detailed description of the dual-grid formulation is described in [18].

Another technique, which is used in the sediment transport simulations is the use of sub-stepping. In this technique, the particle is advanced multiple time steps during a fluid time step ($\Delta t_p = \Delta t_f / N_{sub}$, where Δt_p is the time step used for the particle calculation, Δt_f is the fluid –or calculation-time step, and N_{sub} is the number of particle sub-steps within a fluid time step). Linear interpolation is used to approximate the fluid velocity between $n\Delta t_f$ *and* $(n+1)\Delta t_f$, where n indicates the number of the fluid time step. Using this technique relaxes the simulation from being advanced in time using the strict time scale imposed by the collision time scale.

6.3.3 Base and revised partial coupling

In the base partial coupling, the void fraction is assumed to be unity ($\varepsilon = 1$) in Eqs. 6.10-6.11 while the conventionally calculated void fraction is used in the drag force model. As mentioned in the introduction section, the base partial coupling was found to consistently under-predict the mobility of the particles. It was reasoned that the under-prediction was caused by a lower drag force on particles. This was attributed to the realization that the interstitial fluid velocity (u) used in the drag force (Eq. 6.3), was being underpredicted in the absence of the void fraction in the fluid momentum equations. In effect, what was being calculated was the superficial velocity ($U = \varepsilon \cdot u$). Thus it was postulated that the under-prediction of particle mobility when using partial coupling could be bridged if the velocity calculated during partial coupling is corrected using the void fraction of the fluid. The base partial coupling uses a void fraction of 1 in Eqs. (6.10-6.11) and an uncorrected relative velocity $\left|\vec{u} - \vec{u}_p\right|$ in Eqs. (6.3-6.9). The revised partial coupling uses a corrected interstitial relative velocity in Eqs. (6.3, 6.5, 6.6, and 6.9) while assuming $\varepsilon = 1$ in Eqs. (6.10-6.11). The corrected relative velocity used is $\frac{|\vec{u}-\vec{u}_p|}{\varepsilon}$. It should be mentioned that using base partial coupling

when simulating fluidized beds is not reported in the literature. The cases are run as a proof of concept.

6.4 Simulation Details and Results

6.4.1 Bubbling fluidized bed

A fluidized bed experiment [6] at a superficial velocity of 0.9 m/s is selected to test the revised partial coupling in a fluidized bed. The selected velocity is three times the minimum fluidization velocity. The simulated fluidized bed has a width, depth/transverse thickness, height of 44 mm × 10 mm × 160 mm, respectively. All side walls were set to no slip boundary condition and the top and bottom wall were set to a permeable wall with velocity equal to the fluidization velocity. The three dimensional simulation was conducted with 9240 particles on a grid which is 12×2×32 cells in the x, y and z directions, respectively. The time step used in all calculation is ~ 5 μs and details of the particle properties and modeling parameters are presented in Table 6.1. Three simulations were conducted using full-coupling (Eqs. 6.10-6.11), partial coupling, and revised partial coupling techniques.

Table 6. 1. Simulation parameters used for Muller's experiment [170].

Particles properties (Poppy seeds)	
Diameter	1.2 mm
Density	1000 kg/m^3
Friction coeff.	0.1
Restitution coeff.	0.98
Stiffness coeff.	800 N/m
Fluid properties (Air)	
Density	1.205 kg/m^3
Viscosity	1.8×10^{-5} kg.m^{-1}s^{-1}

The temporal change of the averaged velocity of all particles is shown in Figure 6.1. The particles are initialized with the initial fluid velocity which is set to the fluidization velocity (U_f = 0.9 m/s). The particles initially move upward, decelerate under the influence of gravity and start descending down as their velocity changes from positive to negative. The base partial coupling degenerates to a static bed after its momentum is lost through collisions and the drag force experienced by the particles is not enough to lift the particles. Whereas, both the full coupling and the revised partial coupling exhibit a fluctuating average particle velocity in a mobile (bubbling) bed. Both bubbling beds show similar bubbling behavior, a central bubble moves up from the center of the bed followed by a recession of the particles down from the side walls. A velocity signal that ramps up from a negative value to a positive value represents an upward motion of a significant cloud of particles, whereas if the majority of the particles are moving down then the averaged particle velocity will be negative.

All simulations were run for approximately 10 seconds and the results were averaged for the last 7.5 seconds. The average void fraction of the three simulations is shown in Figure 6.2 along with the average solid velocity, which is non-dimensionalized with the fluidization velocity. Figure 6.2 clearly demonstrates that the base partial coupling shows poor comparison with the full-coupling approach. In fact, no fluidization or bubbling is observed in this case. The revised partial coupling on the other hand shows almost the same bed-height with slightly faster particles in the core of the bed. In spite of the subtle differences between the revised partial coupling and the full coupling, the revised partial coupling shows significant improvement over the base formulation.

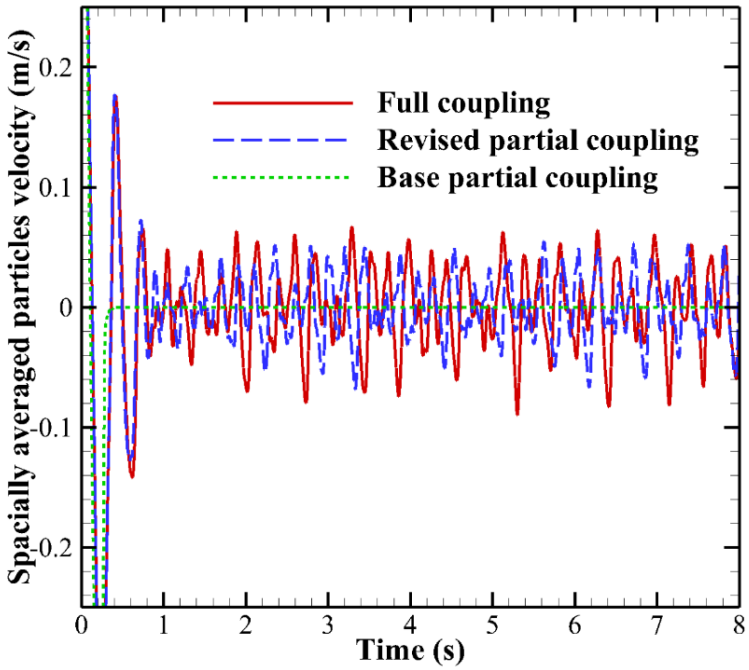

Figure 6. 1. Comparison of domain averaged particles velocity for the different coupling approaches.

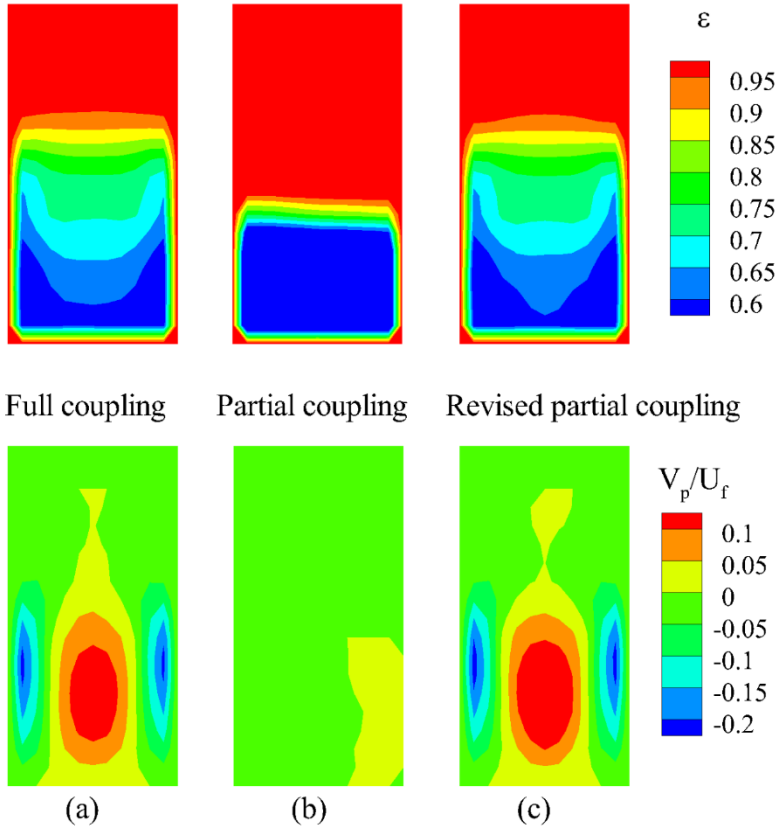

Figure 6. 2. Comparison of averaged void fraction (top) and solids velocity (bottom) for (a) fully coupled simulation, (b) base partial coupling, and (c) revised partial coupling.

It is also worthwhile to examine the interstitial fluid velocity and the pressure drop from using the different coupling techniques. Figure 6.3 shows the average fluid velocity (non-dimensionalized with respect to the fluidization velocity) obtained using the three coupling techniques. It can be seen that both partial coupling techniques show obvious deviations in the velocity flow field. This is not surprising since the single phase flow solution does not account for the presence of the particles. However, it is noteworthy that the true interstitial fluid velocity can be recovered from the revised partial coupling by using the predicted void fraction ($u_{corr} = u/\varepsilon$). Figure 6.4 presents the comparison of the averaged interstitial velocity flow field of the full coupling and the revised partial coupling together with the distribution of the percentage difference. It can be seen that the corrected interstitial velocity shows reasonably good comparison with the full coupling interstitial velocity. The difference is limited to ~10% in most of the domain with small domain of margin error >15%.

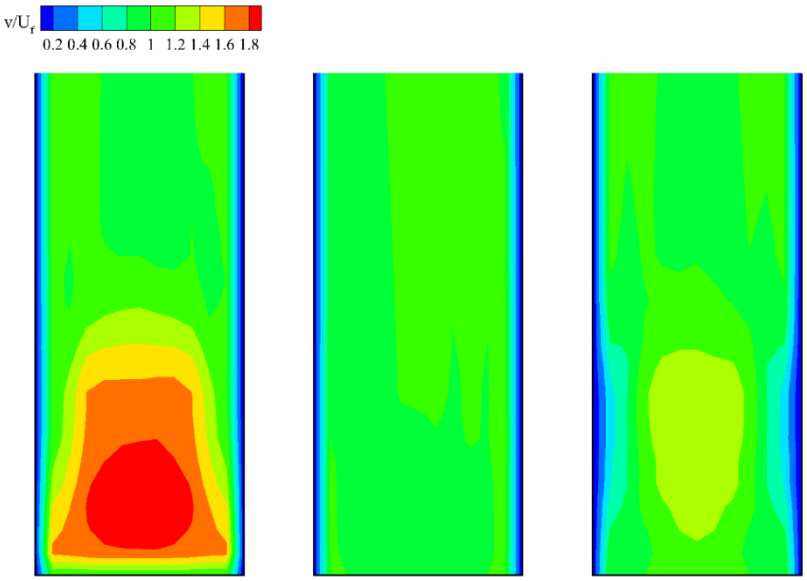

Figure 6. 3. Comparison of averaged interstitial fluid velocity for fully coupled simulation (left), base partial coupling (middle) and revised partial coupling (right).

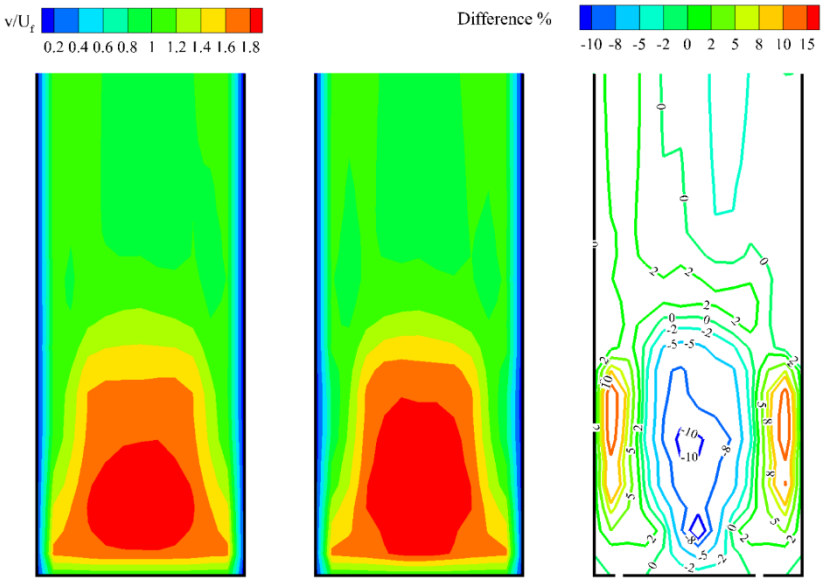

Figure 6. 4. Comparison of averaged interstitial fluid velocity for fully coupled simulation (left), averaged projected interstitial velocity of the revised partial coupling (middle) and the difference between the two (right).

A comparison of the pressure signal at the last ~5 s of the simulations are provided in Figure 6.5. The signal represents the difference between two probes one is located at the bottom wall and the second is located at the top boundary (both adjacent to the side wall). The base partial coupling does not show pressure fluctuations because the bed is not bubbling. Both the full coupling and the revised partial coupling show good comparison of the instantaneous pressure drop signal. The mean pressure drop from the full coupling and the revised partial coupling are found to be 183.8 Pa and 184.3 Pa. The difference between the two is ~0.3%. Both mean pressure drops are slightly less that the weight of the bed of the particles (~ 186.4 Pa). The mean pressure drop from the base partial coupling is found to be ~174 Pa with is ~5.5% less than the mean pressure from the full coupling results. Interestingly this small difference in pressure drop results in significant deviation in results. The r.m.s value of the pressure drop signal for the full coupling and the revised partial coupling is found to be ~36.3 and 23.6 respectively with a difference of 10.1% between the two.

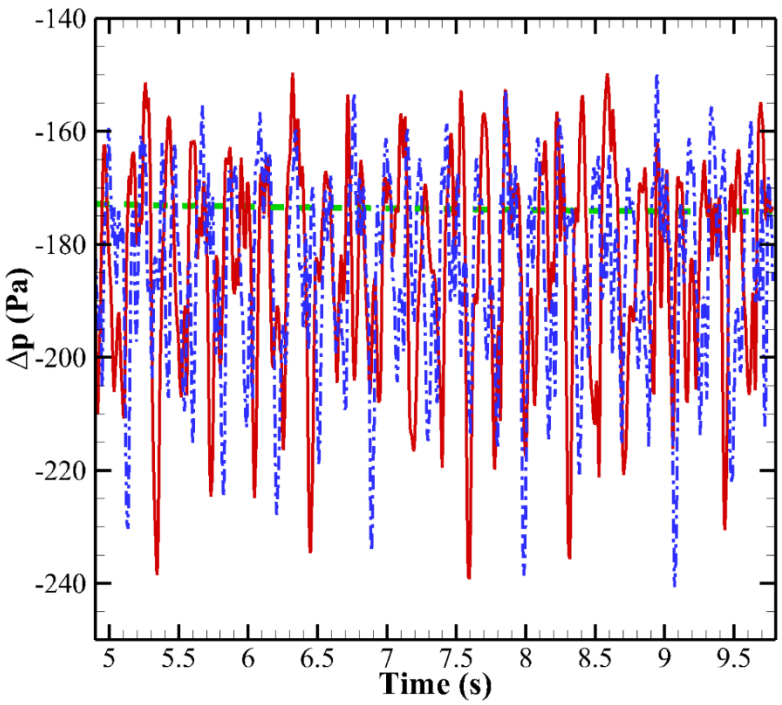

Figure 6. 5. Pressure drop signal of the bubbling fluidized bed at the last 5s of simulations using different coupling methods.

6.4.2 Sediment transport in turbulent open channel

A unidirectional turbulent open channel flow simulation used by Schmeeckle [41] is selected for the investigation of the performance of the different coupling techniques. All the simulations were run in a domain of 0.12×0.06×0.04 m divided into 120, 60, 65 cells in the stream-wise (x), cross-stream (z) and vertical direction (y), respectively. The grid is uniformly spaced in both stream-wise and span-wise directions. The vertical spacing is 0.2 mm in size for the first 20 grid cells above the bottom wall which is then gradually increased in size towards the top boundary. This particle bed height for bedload simulations (~ 2 mm) is encompassed in the uniform grid region. The simulations comprised *O(5)* of mono-sized 0.5 mm spheres of density 2650 kg/m^3 (medium sand) at different flow regimes. The properties of the particles used in the simulation are listed in Table 6.2. The simulations are performed in a turbulent open channel flow (Fig. 6.6) with a velocity slip condition imposed on the top boundary and a no slip condition on the bottom wall. The flow is periodic in both stream-wise and span-wise directions. The imposed mean pressure drop that balances the shear stress determines the value of the mass flowrate inside the channel. The fluid is water with a density of 1000 kg/m^3 and a dynamic viscosity of 8.9x10^{-5} Pa.s.

Our previous work included ten numerical experiments ranging from near incipience of motion of particles to strong suspension of particles [145] . At low flow rates or friction velocity, particle transport occurs in the bedload regime where particles move by rolling, sliding and making small jumps over the bed (saltating). As the flow increases, particles get suspended in the flow by the action of turbulent structures and transport enters the suspended load regime. The transition from bedload to suspended load takes place roughly when the friction velocity ($u_\tau = (\tau_{wall}/\rho)^{1/2}$ where τ_{wall} is the wall shear stress) become comparable to the free fall velocity of the sediment particles (ω). The condition at which incipient particle motion takes place is assumed when the applied non-dimensional shear stress (a.k.a, Shields' parameter $\tau^* \equiv \frac{\tau_{wall}}{(\rho_p - \rho) g d_p}$) reaches a critical threshold [151].

Table 6. 2. Numerical parameters of particles.

Parameter	Value
Particle diameter	0.5 mm
Coefficient of restitution	0.01
Particle density	2650 kg/m^3
Friction Coefficient	0.6
Stiffness coefficient	100 (N/m)
Particle time step	5.3x10^{-5} s

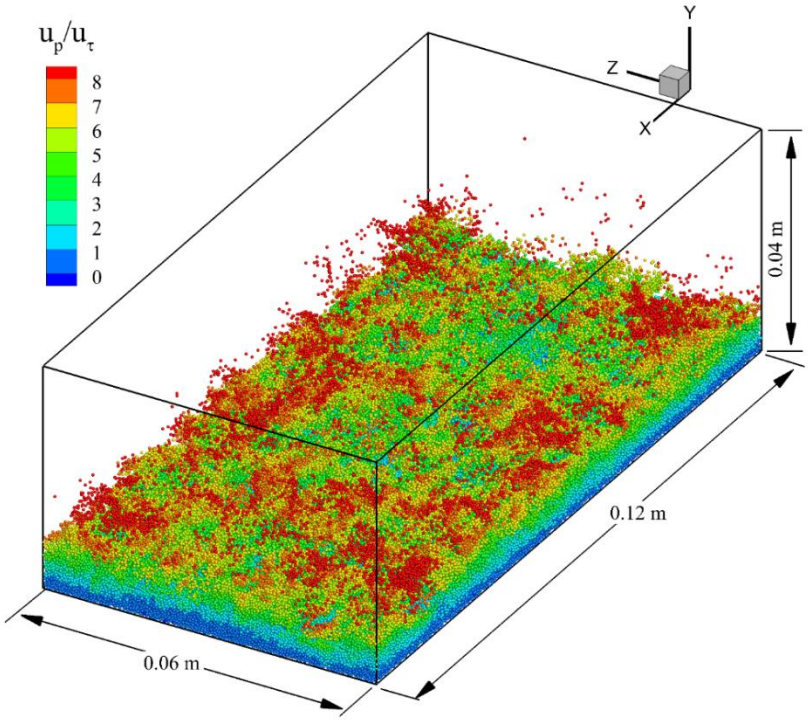

Figure 6. 6. Calculation domain for the turbulent open channel flow.

In earlier work we compared the partial coupling to full coupling approach and found that the differences between the two were smaller in the bedload regime but became more obvious in the suspended load regime [145]. This was because in the bedload regime, most of the particles are static in the bed and the smaller drag force predicted by the partial coupling did not have a large impact, while in the suspended load regime many more particles are mobile and an under-prediction of drag would have a much larger impact on overall particle transport.

In the current work three simulations in different flow regimes are selected to investigate the impact of revised partial coupling on the simulations. The conditions of the selected simulations are presented in Table 6.3. The channel calculations were conducted using the revised particle-coupling and compared to both a fully coupled formulation and a base partial coupling implementation in which the fluid velocity does not account for the presence of the solid. The simulations were run for 30 seconds of real time and the results are averaged in the last 10 seconds. Table 6.4 presents the quantitative values of the channel friction coefficient ($C_f = (u_t/u_b)^2$ where u_b is the bulk fluid velocity in the channel) and sediment transport or particle flux (the particle flux is the summation of the particle volume times the particle velocity) for the three cases along with the percentage error. The first case at a non-dimensional shear stress of $\tau^* \sim 0.0209$ represents a condition near the critical condition of particle movement. The second ($\tau^* \sim 0.288$) and third ($\tau^* \sim 1.558$) cases represent condition of high bedload and suspended load, respectively. As can be seen from the results in Table 6.4, the near incipience of motion and high bedload cases do not show significant change in the channel friction coefficient but the prediction of the particle flux improved noticeably. The improvement is more obvious for the high bedload calculation. The suspended load simulation, on the other hand, shows an improvement in both the predicted channel friction coefficient as well as sediment transport. Although the error in the predicted sediment transport is much smaller, it is over-predicted compared to the fully coupled case by about 15%. The temporal evolution of the mean channel friction and the sediment transport are presented in Figures 6.7*a* and 6.7*b*, respectively, for the suspended load case of $\tau^* = 1.558$. Good agreement of the channel friction coefficient can be seen in Figure 6.7*a* whereas the particle flux is slightly over-predicted. The base partial coupling underpredicts the particle flux because effectively the superficial velocity is used in the drag correlation which gives a lower drag force on the particles – thus less number of particles are set in motion. With the revised partial coupling, the physically

consistent interstitial velocity is used in the drag force calculation thus increasing the force on the particles and making them more mobile. This increases the particle flux. On the other hand, because less number of particles are set in motion with base partial coupling, they collectively resist the fluid motion more than the revised partial coupling, thus increasing the friction coefficient.

Table 6. 3. Simulation conditions for the selected cases.

	u_t (m/s)	Re_τ	Re_b	τ^*	U_s/ω
Case-1	0.013	584	7,820	0.0209	0.239
Case-2	0.0486	2170	22,286	0.288	0.848
Case-3	0.113	5080	53,116	1.558	1.558

Table 6. 4. Mean friction factor (C_f) and sediment transport for the three selected cases.

			Full coupling	Revised partial coupling	Base particle coupling
τ^*=0.0209	C_f	Mean	0.005582	0.006096	0.006176
		Diff. %	--	9.2%	10.6%
	Particle flux (m^4/s)	Mean	1.5×10^{-9}	1.26×10^{-9}	1.14×10^{-9}
		Diff. %	--	-16.2%	-24.4%
τ^*= 0.288	C_f	Mean	0.009488	0.009862	0.0096
		Diff. %	--	3.9%	1.2%
	Particle flux (m^4/s)	Mean	1.31×10^{-7}	1.28×10^{-7}	9.47×10^{-8}
		Diff. %	--	-2.2%	-27.8%
τ^*= 1.558	C_f	Mean	0.009151	0.008956	0.010747
		Diff. %	--	-1.8%	17.9%
	Particle flux (m^4/s)	Mean	4.65×10^{-6}	5.4×10^{-6}	3.7×10^{-6}
		Diff. %	--	14.7%	-21.5%

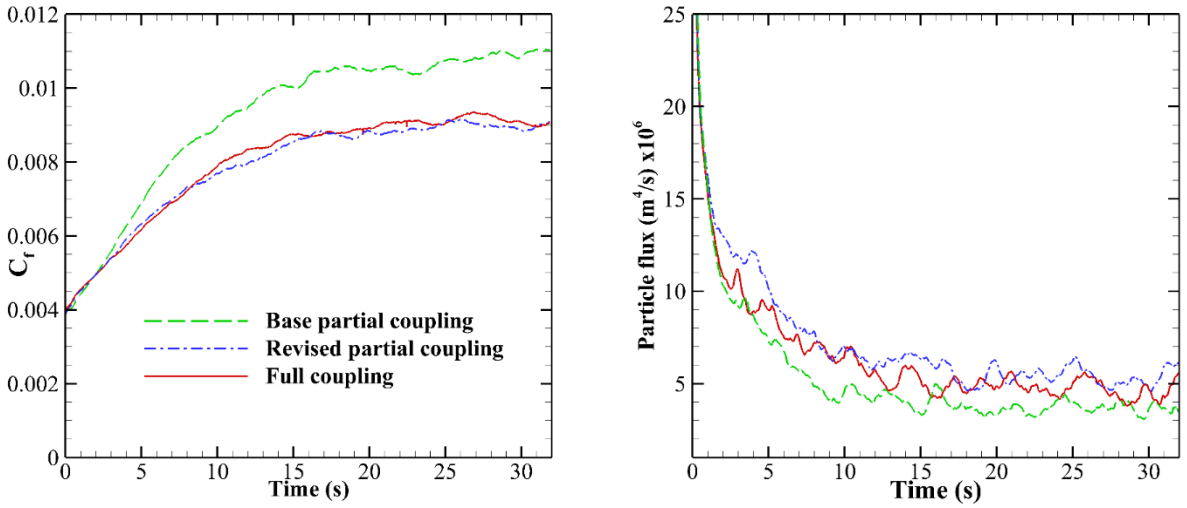

(a) *(b)*

Figure 6. 7. Temporal evolution of *(a)* friction coefficient (C_f) and *(b)* particle flux for case-3 (τ^*~1.56).

6.4.3 Convergence and stability of calculations

As was mentioned earlier in the manuscript, the fully coupled method typically takes many more iterations in the pressure equation to reach convergence because of the inclusion of the void fraction in mass and momentum conservation. Figure 6.8 presents a comparison between the convergence behavior between a fully coupled simulation and revised partial coupling for 25 successive time steps under the same conditions. The interval between time steps is divided into 250 segments representing the maximum number of permissible iterations. The convergence criterion for the pressure equation at each time step is set to a strict value of 1×10^{-6}. As can be seen from Figure 6.8, the revised partial coupling converges in roughly 20 iterations (each marker indicates 5 iterations) whereas the full coupling at most all time steps does not converge to a residual of 1×10^{-6} in the allotted 250 iterations and diverges at the 25th time step. In fact, increasing the maximum number of permissible iterations at each time step, not only increases computational complexity but also makes the solution unstable earlier.

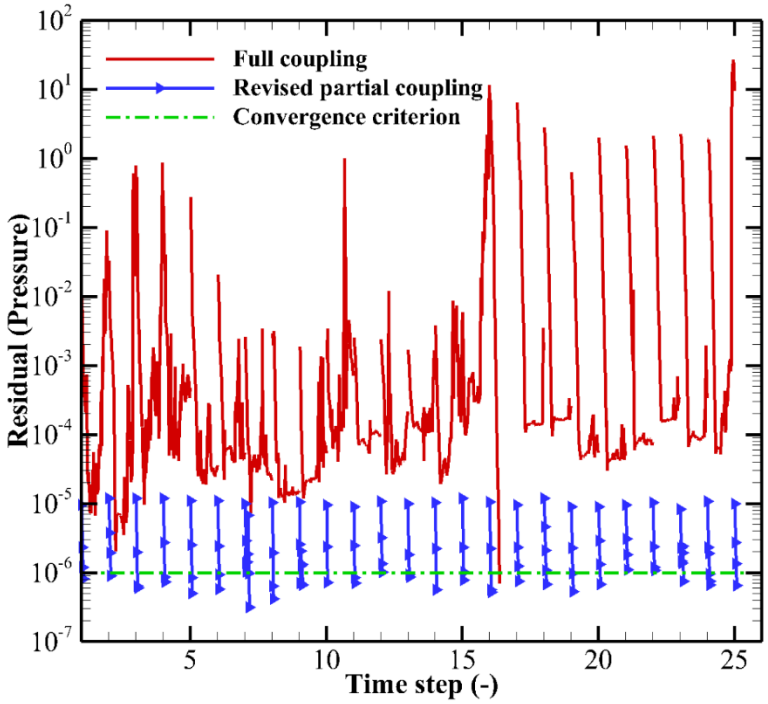

Figure 6. 8. Sample of convergence for successive 25 time step for the sediment transport simulation (τ^*~1.56) for a strict convergence criterion using full coupling and revised partial coupling.

6.4.4 Speed-up of calculations

A summary of the performance outcome of all the conducted simulations is presented in Table 6.5. Since the fluid grid in the fluidized bed simulation is very coarse, the time spent in the fluid part of the calculation is quite small and while improvement in the convergence is evident, the overall impact is minimal. The base partial coupling for the bubbling fluidized bed takes longer time to run because the resultant static bed results in more collisions that need to be processed. For the sediment transport simulations, the fluid solution time increases from bed-load to suspended flow ranging from 25-35% for the fully coupled solution. In contrast, the revised partial coupling varies between 14-21% of the total solution time. For these set of calculations with 10 particle sub-steps for each fluid time step, the savings in total run time using partial coupling are modest ranging from factors of 1.07 to 1.53 with savings in fluid solution time ranging from factors of 1.35 to 4.35. It is projected that for particle transport in high Reynolds number turbulent flows, the savings would be more substantial.

Table 6. 5. Averaged performance for 2.5 seconds of real time for all considered simulations.

		Total Run time (hours)	Fluid Run time (hours)	Run speed-up factor	Fluid solution speed-up factor
Fluidized bed	Full	22.87	1.38	1.0	1.0
	PC-revised	22.81	1.35	1.0	1.02
	PC-base	32.97	1.46	0.69*	0.95
Channel Case-1	Full	38.8	10.4	1.0	1.0
	PC-revised	36.4	7.7	1.07	1.35
	PC-base	33.2	5.7	1.17	1.82
Channel Case-2	Full	47.2	20.5	1.0	1.0
	PC-revised	35.9	7.8	1.31	2.63
	PC-base	33.4	6.4	1.41	3.20
Channel Case-3	Full	109.1	38.7	1.0	1.0
	PC-revised	71.2	10.0	1.53	3.87
	PC-base	84.1	8.9	1.3	4.35

6.5 Conclusions

In this work a revised partial coupling formulation is proposed for use with dense particulate flow systems. The revised coupling assumes a void fraction of unity in the solution of fluid momentum equations but modifies the relative velocity used in point force models to compensate for this omission. Omitting the spatio-temporal variation of void fraction in the momentum equations results in much faster convergence and enhances the numerical stability. This results in faster solution times. Including a modified interstitial relative velocity in point force calculations on the other hand compensates for the lower fluid velocities calculated by the momentum equations. Without this correction, it was found that particle mobility was underpredicted when using partial coupling. The efficacy of the revised partial coupling is demonstrated in two different fluid-particle systems consisting of a bubbling fluidized bed and turbulent sediment transport. In both systems, it is shown that the proposed method shows much better comparison to the fully-coupled approach. In the fluidized bed experiment, without the proposed modification, the bed does not

fluidize in spite of a fluidization velocity which is three times the minimum fluidization velocity. In turbulent sediment transport, the improvement in predictions are more subtle. In the bed-load regime in which particles are not very mobile, the improvements are slight, but as the flow becomes more energetic entraining more particles into suspension, the proposed modification progressively shows more improvement over the base partial coupling.

Using the partial coupling, the fluid solution time was found to be reduced by factors ranging from of 1.35 to 4.35. The reduction in the fluid solution is more significant for simulations that are difficult to converge and those in which the fluid calculation takes a considerable percentage of the overall simulation time. Fully-coupled simulations that exhibit difficult convergence behavior or those which diverge due to numerical instabilities can benefit the most from using this technique

Chapter 7

Alternate Tangential Impact Treatment for the Soft-Sphere Collision Model

Husam A. Elghannay[*] and Danesh K. Tafti[*]

[*]Department of Mechanical Engineering
Virginia Polytechnic Institute and State University
Blacksburg, Virginia 24061

Citation:

Paper submitted to Powder Tech (Jan 2018).

7.1 Abstract

The soft sphere model is used extensively to model particle collisions in dense particle systems. The contact mechanics in the normal and tangential directions is modelled by a spring, damper and dashpot system. The current work evaluates existing modelling strategies in the tangential direction. Existing models require storing the cumulative tangential deformation during the course of the collision for each collision pair. The paper evaluates two existing tangential models (A and B) from the literature and develops alternative methods which do not require storing the tangential deformation (C and D). The models are tested for two canonical single particle experiments of oblique impacts on a surface and sliding particle on a surface. It is shown that neither of the two models A nor B validate with both the test cases. However, limiting the tangential deformation in model A validates both experiments. In Model C, the tangential displacement is approximated as the product of the characteristic time of collision with the instantaneous particle tangential velocity. In Model D, the instantaneous ratio of the tangential to normal impulse is used to characterize the impact according to Maw et al.'s [2] analysis. It is shown that both models give reasonably good predictions in the two test cases with the quality of predictions as good or better than Models A and B which require the storage of the tangential deformation.

7.2 Introduction

The soft sphere collision model is widely used to determine the contact force for particle collisions in Eulerian-Lagrangian multiphase flow simulations. The model allows for interaction forces from multiple simultaneous collisions as they are resolved over a number of time steps within the oscillation time scale of the system (collision time scale). Various normal force formulations are suggested and used in the literature, ranging from using a linear spring-dashpot system [171], employing a Hertzian contact with a viscous damping term [172, 173], or using different loading and unloading stiffness coefficients [174]. A comparison of the existing normal impacts was performed by Shäfer, Dippel [175]. and more recently by Stevens and Hrenya [176]. They found that models that predict a variable coefficient of restitution (COR) at various impact velocities behave quite differently with the increase of the impact speed [176]. Resolved flow simulations are shown to be affected by the collision model adopted even in the case of binary impacts [177, 178].

Similarly, a wide variety of tangential force schemes are suggested and used. The simplest formulation is to assume the tangential force to be equal to the sliding limit opposing the slip [e.g., 179]. The most widely used tangential force model consists of a spring, damper, and slider. The spring and damper together emulate tangential deformation and the slider emulates frictional sliding. When the tangential force exceeds the frictional force in the sliding limit, the force is set to be the product of the sliding friction coefficient and the normal force. Comparison and assessment of the different tangential force schemes has been the topic of many research papers [175, 180, 181]. The tangential force implementations are compared based on the theoretical and experimental work of Maw, Barber [2] and more recently with the experimental work on oblique impact of Kharaz, Gorham [182] and Dong and Moys [183].

In this paper we propose two alternative tangential impact treatments to be used with the soft-sphere collision model. Both suggested approximations eliminate the need to store the tangential displacement for each colliding pair and hence can save memory resources when Computational Fluid-Dynamics-Discrete Element Method (CFD-DEM) is used to simulate dense particulate flow systems. The models are validated with experiments of single particle undergoing oblique impacts with a surface and a spherical particle travelling on a flat plate. Two different existing implementations (Models A and B) of the linear slider-dashpot (LSD) soft-sphere collision model are first investigated. Both existing implementations store necessary information in resolving the tangential impact (tangential displacement) but use different treatments when the sliding limit is reached. It is shown that both existing models (A and B) yield different outcomes when validated with the two experimental test cases. To remedy the inconsistency in the two models, Model AA is proposed which behaves consistently in both test cases. Finally, two additional models (Model C and D) are proposed which do not require storing the history of tangential deformation.

The structure of the paper is as follows: section 7.3 includes the mathematical formulation of the particles equation of motion along with the description of the different implementations of the linear-soft-sphere collision models (Models A and B). A description of one of the suggested tangential treatments (Model C) is also given in this section. The model predictions are presented in section 7.4 where the shortcomings of existing implementations (Models A and B) are investigated and explained for the two test cases. A corrected implementation (referred to as Model AA) is presented at the end of section 7.4 and the validation cases are revisited for the revised

implementation. In section 7.4, a second alternative tangential impact model (Model D) is described and its validation is presented. Finally, concluding remarks related to the performance of the proposed tangential treatments are given in section 7.5.

7.3 Mathematical Formulation

7.3.1 Particle Dynamical Equation

In the absence of fluid forces, the particle equation of motion under the influence of gravity can be expressed as

$$m_p \frac{d\vec{u}_{p,i}}{dt} = \vec{F}_{g,i} + \sum_{N_p} \vec{F}_c \tag{7.1}$$

Here $\vec{u}_p$ is the particle velocity, $\vec{F}_g$ is the gravity force, and $\vec{F}_c$ is the contact force from neighbouring particles and surfaces (N_p). The gravity force is expressed as $\vec{F}_g = \rho_p \forall_p \vec{g}$, where ρ_p is the density of the particle, $\forall_p$ is the volume of the particle, and $\vec{g}$ is the gravitational acceleration. In the current work only gravity and contact forces are of interest.

7.3.2 Collision Mechanics

To calculate the collision forces, the soft sphere collision model is used in which the contact force in both normal and tangential directions is modeled using a linear spring-dashpot-slider system [e.g., 22]. In this framework, the coefficient of restitution is typically an input parameter and is set to a fixed value. The modelled collision between two particles is represented in Fig. 7.1 for particle-particle collision (walls can be assumed as particles with infinite mass and radius). The contact force in the soft sphere model ("$\vec{F}_c$" in Eq. (7.1)) is decomposed into a normal force component and a tangential force component. The spring in both normal and tangential directions accounts for the elastic part of the impact force and the dashpot accounts for the energy loss during the collisions. The slider prevents the tangential force from exceeding a maximum tangential threshold. The contact force components in the normal and tangential direction to the collision plane are expressed as

$$\vec{F}_n = \begin{cases} -k_n \vec{\delta}_n - \eta_n \vec{u}_{n,ij} & for\ \Delta_{ij} > 0 \\ 0 & else \end{cases} \tag{7.2}$$

$$\vec{F}_t = \begin{cases} -k_t\vec{\delta}_t - \eta_t\vec{u}_{t,ij} & for\ |k_t\vec{\delta}_t + \eta_t\vec{u}_{t,ij}| < \mu_f|\vec{F}_n| \\ -\mu|\vec{F}_n| & else \end{cases} \tag{7.3}$$

where; k, δ, η and μ above are the spring constant, particle contact displacement, coefficient of viscous dissipation, and the sliding friction coefficient, respectively. In the above equations, $\vec{u}_{n,ij}$ and $\vec{u}_{t,ij}$ are the normal and tangential component of the relative velocity between the two particles and the parameter Δ_{ij} is the overlap between the two particles (Figure 7.1). The viscous dissipation coefficient is a function of the coefficient of restitution of the particle (e) and the reduced/combined mass of the colliding particles ($m_{ij}= m_i m_j/(m_i+m_j)$) is expressed as

$$\eta = -2\ln(e)\frac{\sqrt{km_{ij}}}{\pi^2 + (\ln(e))^2} \tag{7.4}$$

The normal displacement is given as $\vec{\delta}_{n,ij} = \Delta_{ij}\,\vec{n}_{ij}$ where $\vec{n}_{ij}$ is the unit vector of the normal direction between the two particles.

$$\vec{n}_{ij} = \frac{\vec{r}_j - \vec{r}_i}{|\vec{R}_i| + |\vec{R}_j|} \tag{7.5}$$

The velocity components are calculated as follows

$$\vec{u}_{ij} = \vec{u}_i - \vec{u}_j \tag{7.6}$$

$$\vec{u}_{n,ij} = (\vec{u}_{ij}.\vec{n}_{ij})\vec{n}_{ij} \tag{7.7}$$

the relative translational tangential velocity can be written as

$$\vec{u}_{T,ij} = \vec{u}_{ij} - \vec{u}_{n,ij} \tag{7.8}$$

and the relative tangential velocity at the contact point

$$\vec{u}_{t,ij} = \vec{u}_{T,ij} + \left(|\vec{R}_i|\vec{\omega}_i \times \vec{n}_{ij} - |\vec{R}_j|\vec{\omega}_j \times \vec{n}_{ji}\right) \tag{7.9}$$

where $\vec{\omega}$ is the rotational velocity of the particle. The tangential velocity defined by Eq. (7.9) above is the instantaneous relative slip velocity at the contact point. The relative slip velocity contains a translational (first term) and rotational part (terms within parenthesis) and is typically used to calculate the tangential displacement as

$$\vec{\delta}_t^n = \vec{\delta}_t^{n-1} + \int \vec{u}_{t,ij}\,dt \tag{7.10}$$

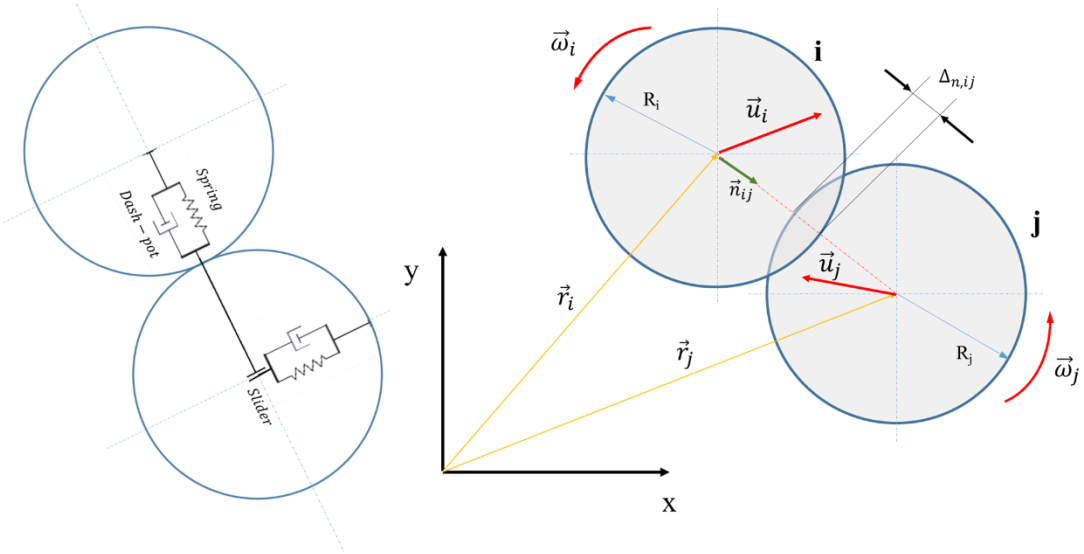

Figure 7. 1. Schematic diagram of soft-sphere collision model (left) and coordinate system (right).

The mathematical formulation described in Equations 7.2-7.10 is the linear soft sphere collision model. The rotational motion of the particle is governed by

$$I_p \frac{d\vec{\omega}}{dt} = \sum_{N_p} \vec{T}_{p,c} \tag{7.11}$$

where $I_p, \vec{T}_{p,c}$ represent the moment of inertia of the particle, and the torque ($\vec{T}_{p,c} = \vec{R}_p \times \vec{F}_c$) acting on the particle from the tangential contact force, where $\vec{R}_p$ is a vector from the mass centre of the particle to the contact point. Integrating Eq. (7.11) updates the angular motion of the particle at each time step.

In the upcoming discussion, the term sliding limit will be used for the case in which the tangential force reaches the maximum threshold of $\pm\mu_f|\vec{F}_n|$. For tangential forces that are less than the sliding limit, parts of the contact area might be in sliding while others in sticking. As can be seen from Equation (7.3), however, the direction of the tangential force is not indicated when the sliding limit is reached. Two different implementations, however, exist for this case. In the first one

(Model A) the direction of the tangential force is opposite to the direction of the tangential force at the instant of sliding such that

$$\vec{F}_t = -\mu\left|\vec{F}_n\right| \frac{k_t\vec{\delta}_t + \eta_t\vec{u}_{t,ij}}{|k_t\vec{\delta}_t + \eta_t\vec{u}_{t,ij}|} \tag{7.12}$$

Generally speaking, for a slider-dashpot system, the damper will either act with the spring (e.g. in the compression stage of a normal impact) or act against it if the spring is the source of the motion (e.g. in the rebound stage of a normal impact). In either case the direction of the tangential force is dictated by the elastic part and thus the direction of the displacement is predominant. Thus, the above equation can be expressed as $\vec{F}_t = -\mu\left|\vec{F}_n\right| \frac{\vec{\delta}_t}{|\vec{\delta}_t|}$ without loss of generality.

In another implementation (Model B), the direction of the tangential force is taken to be that of the velocity at contact ($u_{t,ij}$ defined by Eq. (8.9)), which is opposite to the direction of the velocity at contact

$$\vec{F}_t = -\mu\left|\vec{F}_n\right| \frac{\vec{u}_{t,ij}}{|\vec{u}_{t,ij}|} \tag{7.13}$$

here the quantity $\frac{\vec{u}_{t,ij}}{|\vec{u}_{t,ij}|}$ represents a unit vector parallel to the slip velocity direction. Model-A was first suggested by Cundall and Strack [23] and many researchers have adopted the model-A formulation (e.g. [184-186]). Model-B in which the friction force opposes the slip velocity has also been used (e.g. [22, 157, 180, 187]). Hard-sphere implementations employ model-B formulation since the deformation is not resolved [e.g., 188].

The integrated tangential displacement ($\vec{\delta}_t$ in Eq. (7.10)) has to be stored for each collision pair. For dense particle mixtures of varying sizes each particle can have more than eight neighbours and storing the displacement can consume substantial memory for large systems. In addition, on distributed parallel architectures, the displacements have to be communicated when a particle is transported from one processor to another. An alternative implementation is suggested in which the tangential displacement does not have to be stored but is calculated as

$$\vec{\delta}_t^n = \tau_c\, \vec{u}_{t,ij} \tag{7.14}$$

Here τ_c is the collision duration or time scale which can be pre-estimated using [22]

$$\tau_c = \frac{\pi}{[k_n(1-\gamma^2)/m_{ij}]^{1/2}} \tag{7.15}$$

Where γ is constant given as

$$\gamma = \frac{-\ln(e)}{[\pi^2 + \{\ln(e)\}^2]^{1/2}} \tag{7.16}$$

As can be seen from Eq. (7.3) & (7.14), the tangential force opposes the direction of the slip velocity (in this case it is the same as the direction of the total displacement). For cases in which the sliding limit is reached the force takes the form

$$\vec{F}_t = -\mu\left|\vec{F}_n\right| \frac{\vec{u}_{t,ij}}{|\vec{u}_{t,ij}|} \tag{7.17}$$

the above described formulation (Eqs. 7.14-7.17) is a simplified soft-sphere collision model and will be referred to as Model-C.

7.4 Model Predictions

The performance of the different impact models is investigated in two different single-particle experiments. The first case tested is the impact of a sphere with a wall at different impact angles and the second case tested is the motion of a sphere along a flat-plate. It is found that neither Model A nor B yield consistent results for both cases, but only predict the correct results for one or the other of the two cases. The reason behind these inconsistencies in model predictions is investigated in detail and a modification is proposed to Model A (Model AA) to give the correct predictions for both the cases tested. On the other hand, it is shown that Model-C, in which the tangential deformation is approximated by Eq. (7.14) gives fairly good results for both the test cases.

7.4.1 Model comparison and particle level validation

7.4.1.1 Oblique impact of an elastic sphere

The experimental results of Kharaz, Gorham [182] are used. The experimental work measures the rebound characteristics of a 5 mm diameter aluminum oxide spheres impacting a glass anvil at 3.9 m/s at different angles measured from the surface normal. The numerical and physical parameters used in the validation case are listed in Table 7.1. Note that the input COR in Table 7.1 only characterizes the deformation stage of the collision. The results of the tangential coefficient of restitution (COR) along with the rebound rotational velocity are shown in Figures 7.*2a* and 7.*2b*

for the three different implementations, Model A, B and C. As can be seen from Figure 7.2, the predicted tangential COR by the three models is in a very good agreement with the experimental result when the impact angle is greater than 30 degrees. This regime represents gross slip throughout the impact [2] and can also be well-predicted by the application of Coulomb's law of friction (i.e. $|F_t| = \mu.|F_n|$). For small impact angles, however, both models B and C predict a constant tangential COR of 5/7 which represent the result obtained by rigid body dynamics theory. On the other hand, model-A captures the physical trend at small impact angle where a reduction of the COR takes place to a minimum value at 20 degrees before increasing again with an increase in the impact angle. At small impact angles a competition between slipping and sticking takes place in the contact area [2]. Although some under-prediction can be noted in the current results, very good agreement is reported by [184] for the same experiment when using linear and non-linear model only when values of the stiffness coefficient were made comparable to the physical value. The current results of Model-A were found to be insensitive to the stiffness coefficient. The rebound rotational velocity (Fig. 7.*2b*) shows good agreement with notable under-prediction at 20 degrees for small impact angles and very good agreement at higher impact angles when using both models B and C. Interestingly, Model-A predicts the maximum rotational velocity at 20 degrees, which coincides with the minimum tangential COR, but which is different from the experiment. It should be emphasized that, although Model-B stores the tangential displacement information, it is unable to give predictions that are better than rigid body dynamics theory.

Table 7. 1. Simulation parameters for the oblique impact case.

Parameter	value
stiffness coefficient, k_n	1000 (N/m)
stiffness coefficient, k_t	860 (N/m)
COR	0.98 (-)
Friction factor, μ	0.092 (-)
Diameter	5 (mm)
Time step	1.13 (μs)

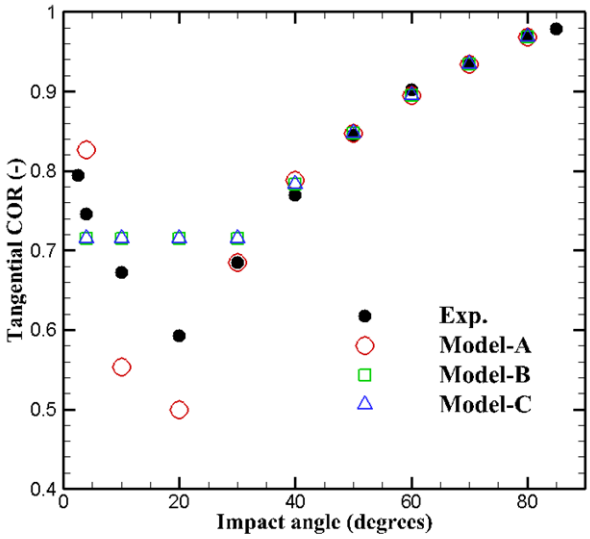

(a) Tangential COR

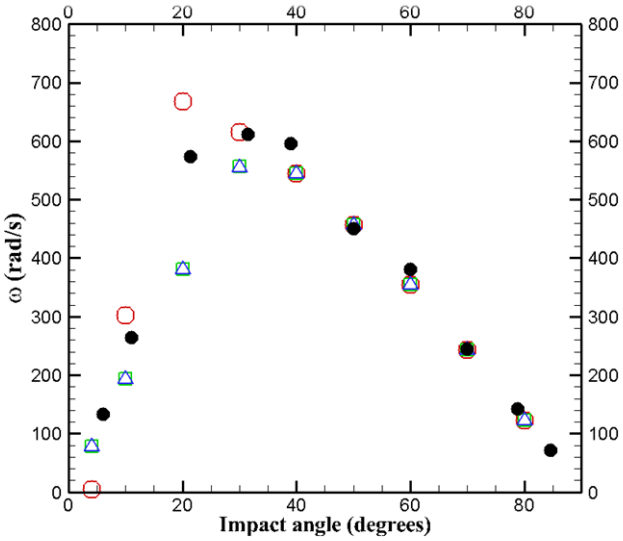

(b) Angular velocity

Figure 7. 2. Comparison of current model with experimental results of an elastic oblique impact.

To get more insight into the predicted results, a comparison of the evolution of the tangential force during the impact duration is presented in Figures 7.3 *a-d* for the three models. The force evolution is shown at 4, 10, 20, 50 degrees which cover different impact regimes. The black solid line represents the sliding limit ($\mp\mu\left|\vec{F}_n\right|$). The tangential force is non-dimensionalized with respect to the weight of the particle whereas the impact time is non-dimensionalized with respect to the collision time. At small impact angle of 4 degrees (Fig. 7.3*a*) the tangential force predicted by both models A and B is found to be governed by the tangential deformation for most of the collision

duration (from the beginning till 85% of the impact time). For Model-A, the tangential force initially opposes the direction of the tangential velocity (with zero spin at instant of impact). The sphere starts picking up a rotational velocity that opposes the direction of the incoming velocity and reduces the slip velocity at the contact point (recall Eq. (7.8)). The tangential force changes its direction as the rotational velocity starts dominating the tangential displacement (governed by Eq. (7.9)). At ~ 85% of the collision time, the tangential displacement increases such that the tangential force exceeds the sliding limit and is governed by the sliding limit ($= \pm\mu_f \left|\vec{F}_n\right|$). Model-B initially matches model-A results when small deformation controls the collision (till ~30% of the collision time). At a certain point, the rotational velocity at the contact point slightly exceeds the translational velocity. At this point the tangential force in Model-B changes its direction by 180 degrees because its direction is dictated by the slip velocity. At the next time step the new tangential force will result in another reversal of the direction of the tangential force as the tangential velocity at the contact point now overcomes the rotational velocity. The tangential displacement at this condition is locked to a specific value and the tangential force will alternate its direction (at constant value) till the end of the collision. Such alternation is not seen in Model-A since the direction of the displacement (rather than the slip velocity) decides the direction of the tangential force. Model-C has a different trend as it directly enters the sliding regime till ~25% of the impact duration. The tangential force during the initial part is pushed to the sliding limit because the particle initially has a high slip velocity (thus high tangential displacement according to Eq. (7.14)). With the increase in the rotational speed the tangential force is continually reduced over a number of time steps over which the tangential force asymptotes to zero. The reduction of the tangential force from the sliding limit takes place before the slip velocity changes its direction (or before reaching a zero value).

The trends are the same at slightly higher impact angle (10 degrees), except that both models A and B will encounter a large initial displacement causing the force to follow the sliding limit ($\pm\mu \left|\vec{F}_n\right|$). At higher impact angles (20 degrees), the tangential force from Model-B starts alternating at ~50% of the collision time, whereas the force from Model-A continues acting in the same direction following the sliding limit throughout the impact duration. The tangential force predicted by model A is maximum because the tangential displacement does not change direction. This is because when the rotational speed exceeds the translational speed the added displacements

do not reverse the cumulative or total- displacement in the direction of the slip velocity. At even higher impact angles (50 degrees), the three models show the same result in which the tangential force coincides with the sliding limit throughout the impact duration. The rotational speed in this case does not reach a point at which it exceeds the translational speed at the contact point and the slip velocity does not change direction.

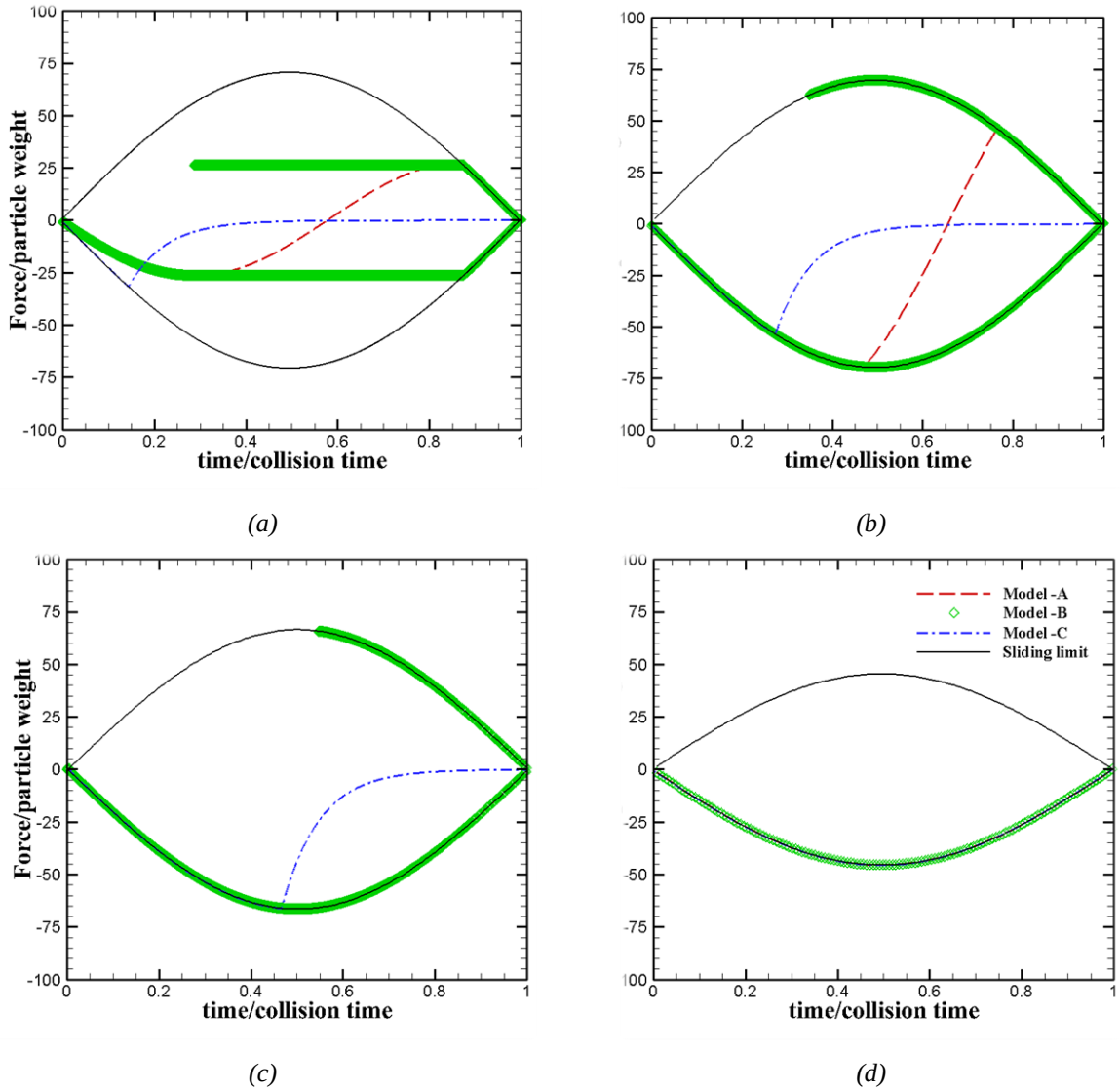

Figure 7. 3. Comparison between tangential force trends for the three models at different impact angles (a) 4 degrees, (b) 10 degrees, (c) 20 degrees, (d) 50 degrees.

Detailed information about the change in tangential displacement and the slip velocity during the impact process for Model-A is provided in Figures 7.4*a –d.* Model-B (not shown in Figure 7.4) has the same trend till the slip velocity reaches zero. The velocities are non-dimensionalized with

respect to the total impact velocity (3.9 m/s) and the tangential displacement is non-dimensionalized with respect to the particle diameter (5 mm). It can be seen that the slip at the contact point decreases from its initial value because of the increase in induced rotational velocity opposite to the velocity direction. For impact degrees of 4 and 10, the slip velocity becomes negative at ~30-40% of the impact time (as can be seen from Fig. 7.4) which corresponds to a peak value of the tangential deformation. This corresponds to the point at which the tangential force starts alternating in figure 7.3*a*. For an impact angle of 20 degrees the slip velocity changes its direction at ~50% of the impact duration. A peak displacement takes place at this point but (unlike 4 and 10 degrees) the deformation direction does not change as the impact proceeds. At even higher impact angles (50 degrees), the impact does not reach the stage at which the slip velocity changes its direction.

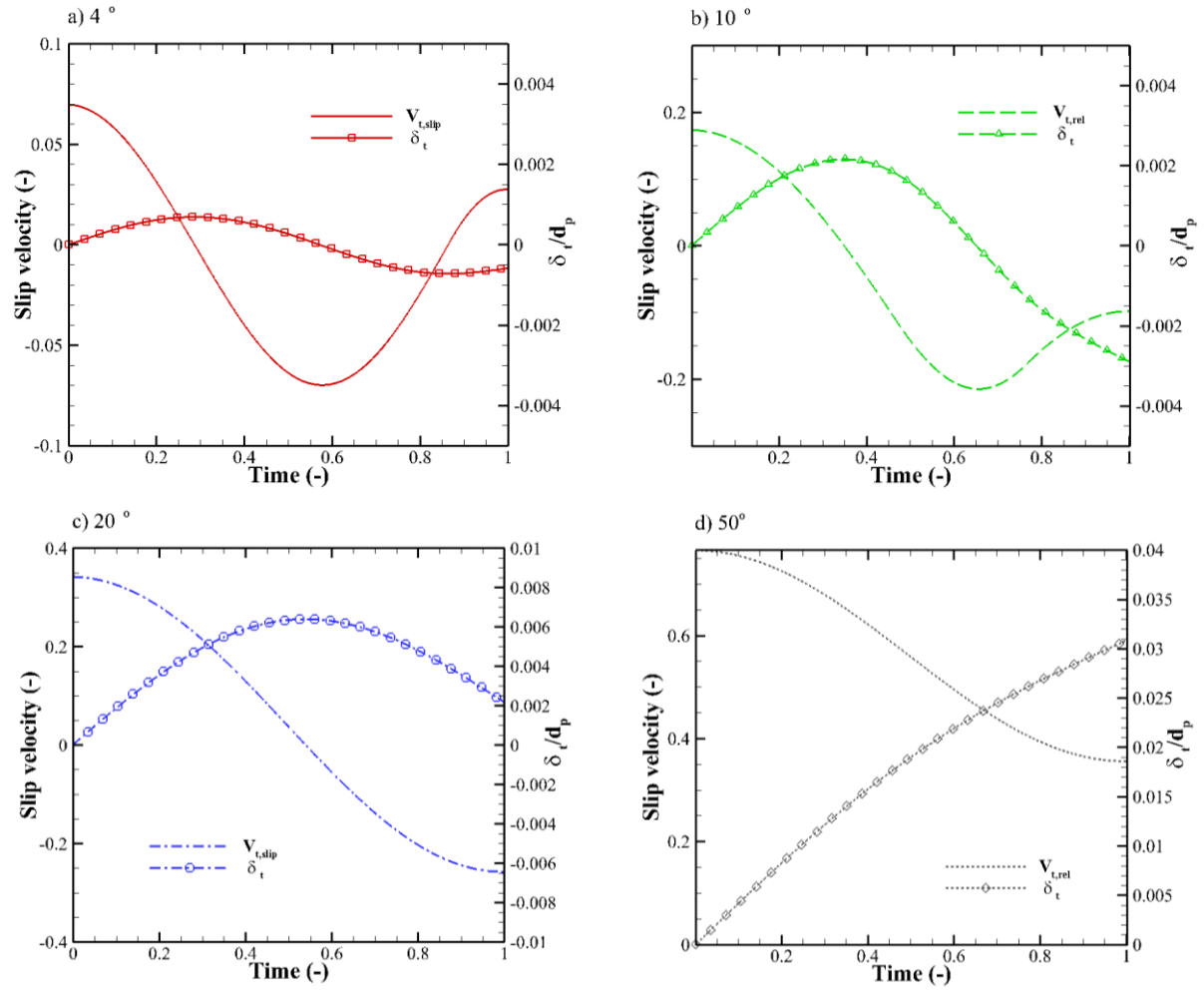

Figure 7. 4. Variation of tangential displacement and the slip velocity during an elastic oblique impact at different angles.

7.4.1.2 Particle on flat plate

If a sphere starts travelling on a flat plate with a certain initial translational velocity (U_i) and zero spin with zero rolling friction between the sphere and the plate (only sliding friction is active), the sliding friction causes the translational velocity to gradually drop while the rotational velocity increases. Once the translational velocity of the sphere reaches $5/7^{th}$ of its initial value a balance between the translational and rotational velocity takes place and the sphere goes into a condition of pure rolling over the flat plate with both its translational velocity and rotational velocity unchanged (see for example, [189]). The particle continues travelling at this condition forever in the absence of dissipation mechanisms other than sliding friction (e.g. rolling friction). The initial and final conditions of this case are indicated in Figure 7.5.

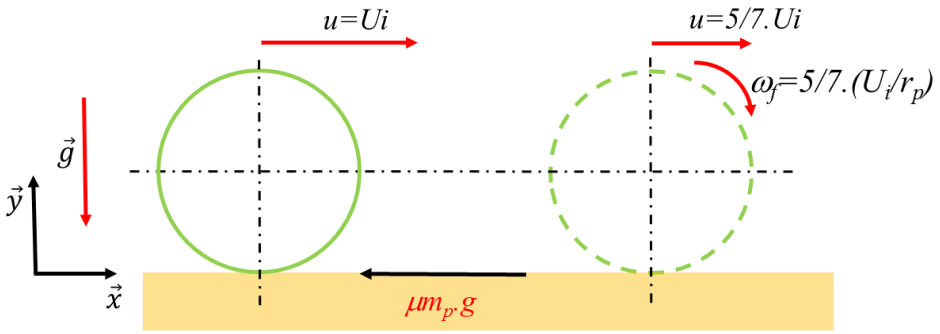

Figure 7. 5. Initial (left) and final (right) condition of sphere travelling on wall experiment in absence of rolling friction.

Numerical simulations of a 10 mm sphere traveling on a flat plate with initial velocity of 1 *m/s* along the x-axis with gravity acting in the negative y-axis were performed. The sphere density is 2500 kg/m^3 and its sliding friction was set to 0.7. The simulation was performed using a time step of 20 μs. The dynamics of a sphere with a sliding friction factor of 0.7 is shown in Figure 7.6 for the three models. It can be seen that for both models B and C, a pure rolling condition is reached in ~ 0.043 s during which the particle translational velocity drops to ~0.714 *m/s* and its rotational velocity ramps up to ~ -143 rad/s. The slip velocity goes to zero at this condition. Both models B and C validate with the theory, however, Model-A fails to capture the mechanics. For model-A, the tangential force continues acting on the sphere when the pure rolling condition is reached (at ~0.043 s) and hence the velocity of the particle keeps decreasing. Similar to models B and C, the

slip velocity reaches zero at ~0.043 s, however, the deformation still has the same direction since the displacement at this point is an accumulation of tangential displacement during ~0.043 s and it takes roughly another 0.043 seconds for the tangential displacement to become zero and change the tangential force direction. The time required for the tangential force to change its direction is thus double that required to reach pure rolling (~0.086 s). This is followed by a decrease in the translation and rotational velocity back to their initial values and the cycle of increasing and decreasing velocities keeps repeating. Interestingly, in spite of the incorrect temporal behavior, the mean translational and rotational velocities equal the correct theoretical asymptotic conditions.

The corresponding tangential friction force for the three models is shown in Figure 7.7. The force is non-dimensionalized with respect of the weight of the particle. A change in the tangential force direction can be seen every ~0.086 s in Model-A (between $\pm\mu.m_p|\vec{g}|$). Interestingly, the friction force asymptotes to zero as the pure rolling condition is reached for Model-C. This is different, as well as more physical, from Model-B in which the particle encounters a continuously alternating force of $\pm\mu.F_n$ *(see also [180])*. The theoretical non-dimensional time to reach the rolling/equilibrium condition from the initial condition is given by $t^* = t.g.\mu/U_i$, where t is the time required to reach a pure rolling condition and U_i is the initial velocity. The validation case was tested at different sliding friction coefficients (0.1, 0.4 and 0.7) and the results are shown in Figure 7.8. It can be seen that the both models B and C show very good agreement with the analytical expression of the non-dimensional time.

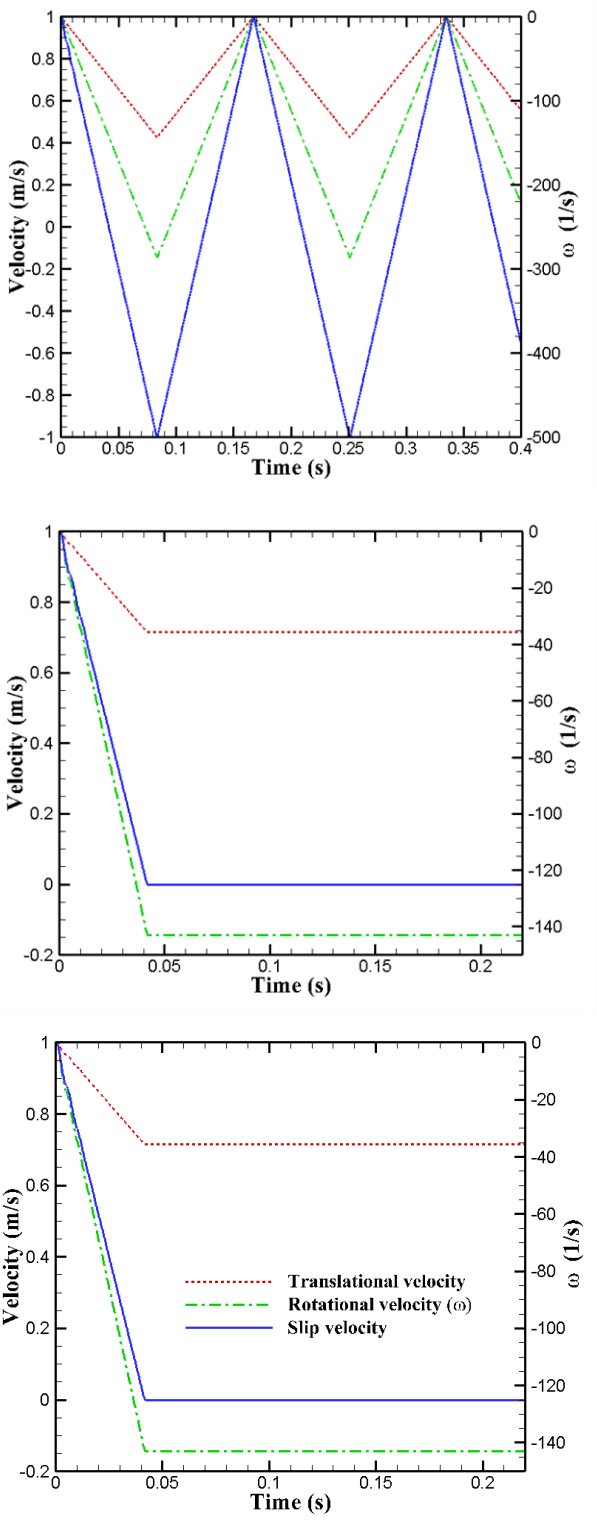

Figure 7. 6. Dynamics of a 10 mm sphere moving on a flat plate without rolling friction and sliding friction factor of 0.7. Top: Model-A, Middle: Model-B, Bottom: Model-C.

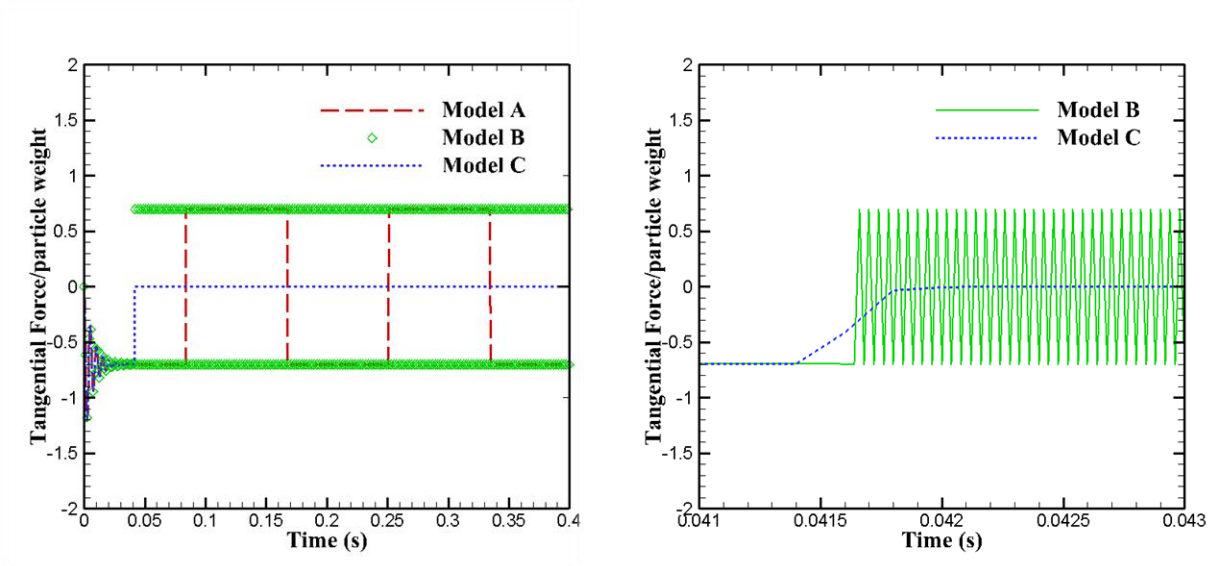

Figure 7. 7. Comparison of the tangential force for particle on wall experiment for the three models. The transition region is exaggerated on right plot for models B and C.

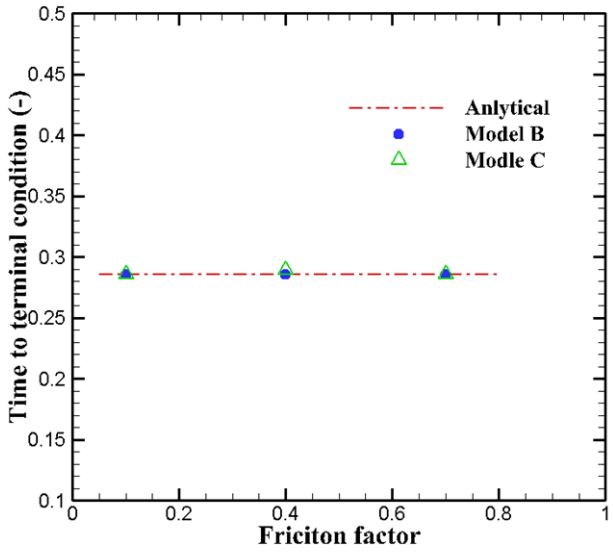

Figure 7. 8. Non-dimensional time to reach pure rolling condition for sphere traveling on a flat plate experiment.

7.4.2 Proper implementation of the tangential linear soft sphere model

As described in the previous section, although both models A and B store and use the tangential displacement information, Model A is unable to validate a particle/sphere moving on a flat plate,

but gives reasonable agreement with experiments on predicting oblique impacts. Model B predictions, on the other hand, is only as good as rigid body impact theory for oblique impacts, but is consistent and correct for a sphere moving on a flat plate. The approximate Model C, which does not store displacement history, was capable of getting the same results as those of Model B in both test cases. In fact, it produces more physical results in the pure rolling regime of a sphere on a flat plate.

In light of these results, it remains to be established that there is one implementation of the linear soft-sphere collision model that can validate both cases. It is shown here that a modified version of Model A can indeed be made to satisfy both cases. The unexpected failure of Model-A for the sphere on wall experiment is a result of using the tangential "displacement" in the tangential force calculation. The tangential "deformation", however, better reflects the physical problem and should be used (rather than tangential displacement). Unlike the tangential displacement, the tangential deformation should be limited and reflects the stored energy in a given situation. A maximum threshold of the tangential deformation is in fact used in some non-linear soft-sphere implementations [190, 191]. The tangential deformation limit employs the ratio of the stiffness in the normal and tangential direction along with the sliding friction and takes the form $\delta_{t.max} = \mu\delta_n (k_n/k_t)$. The ratio of the normal to the tangential stiffness is a function of Poisson ratio such that $k_n/k_t \sim (2- \nu)/(2(1-\nu))$ [2]. Although, the use of $k_n/k_t \sim 1$ was found to have an insignificant effect on the behavior of granular assemblies [23], later studies reported sensitivity to the ratio [175, 184] on individual particle impacts. For instance, a sphere traveling on a flat plate will undergo deformation till δ_t reaches $\delta_{t.max}$, after which the deformation will remain constant at $\delta_{t.max}$ and only change when the calculated δ_t becomes less than $\delta_{t.max.}$

The concept of limiting the tangential displacement (or the deformation) for linear soft-sphere model was proposed by [171]. However, this formulation is far less frequent in the literature [181]. Interestingly, the model used by [171] is Model-B, which in the current work does not benefit from the limit. However, it is shown that Model-A does benefit from the application of an upper bound on tangential deformation. This improved formulation will be referred to as Model-AA and it uses the same formulation of model-A except that if the tangential force reaches/exceeds the gross sliding limit then the tangential displacement is set to [192]

$$\vec{\delta}_{t,max}^{n} = -(1/k_t)\left(\vec{F}_t + \eta_t \vec{u}_{t,ij}\right) \tag{7.18}$$

Figures 7.9*a* and 7.9*b* show the validation of oblique impact using model-AA. As evident, Model-AA is capable of predicting the physics of oblique impact more faithfully compared to Model-A. Besides better agreement in predicting the tangential COR, the maximum rotational speed is now more consistent with the experiment. A comparison between the evolution of the tangential force between Model-A and Model-AA during impact is shown in Figure 7.10 for impact angles of 10 and 20 degrees (largest differences between the model predictions). Figure 7.10 shows that the tangential deformation in the revised model (Model-AA) changes its direction before Model-A since the tangential deformation and thus tangential force is limited.

It is noted that the current results are obtained by defaulting the input tangential COR to be the same as the normal COR [22] for the tangential deformation in Table 7.1. The overall COR is found to be sensitive to the tangential COR where high dissipation (low input COR) in the tangential direction is found to result in recovering the rigid body limit theory at low impact angles. For instance, if the tangential COR is changed to 0.8, 0.5 and 0.01 (while maintaining the normal COR to be 0.98), the calculated overall tangential COR at 20 degrees is 0.627, 0.68, and 0.714, respectively (compared to 0.589 at a tangential COR of 0.98). Similarly at 10 degree impact angle the overall tangential COR becomes 0.7 and 0.713 at a input tangential COR of 0.8 and 0.01, respectively. Although not shown, the trend in tangential force at high dissipation becomes similar to that obtained by Model-C. This trend has also been observed by Thornton [193] in their study of the behaviour of contact models during inelastic impacts.

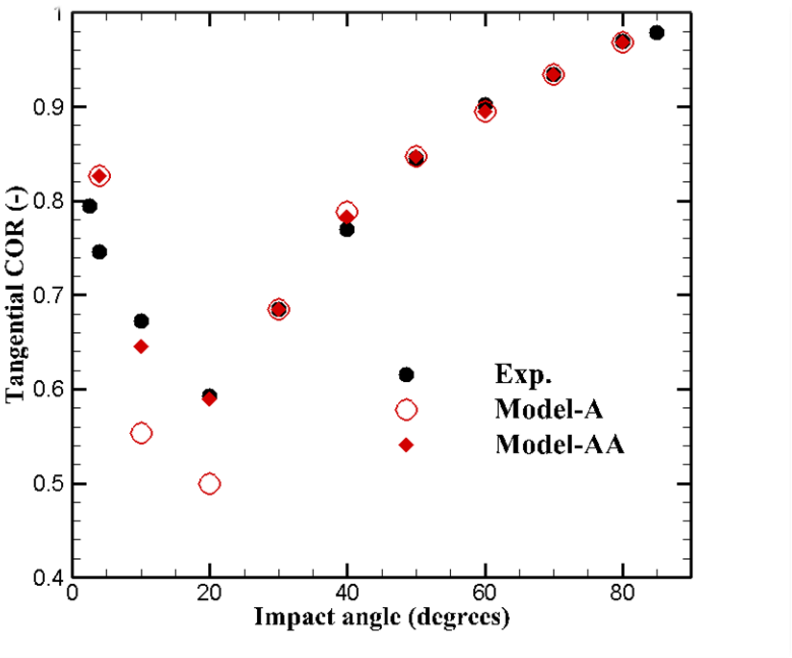

*(a)*Tangential velocity

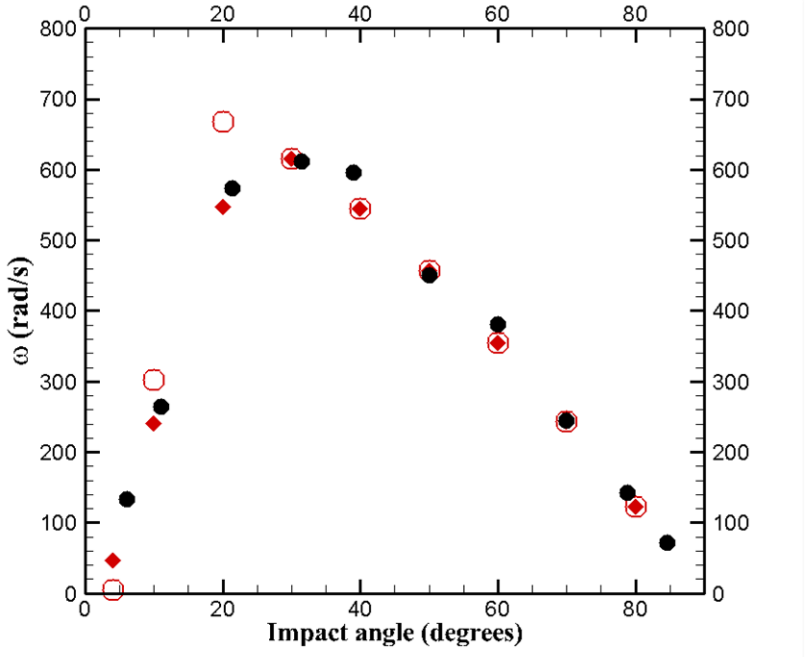

(b) Angular velocity

Figure 7. 9. Comparison of model-A and Model-AA with other models and experimental data of an elastic oblique impact.

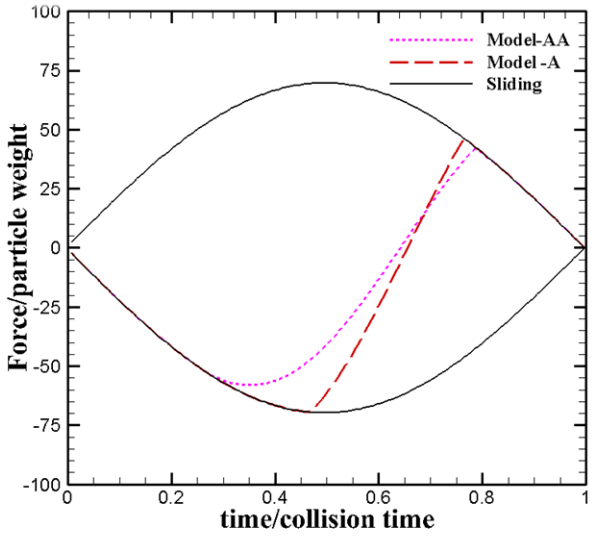

(a)

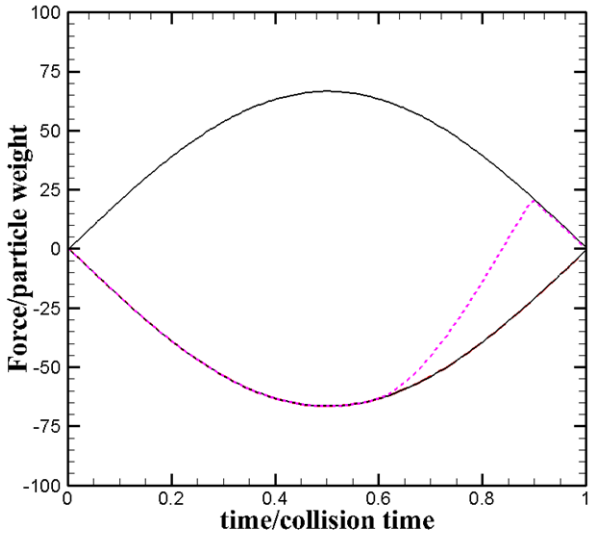

(b)

Figure 7. 10. Comparison between tangential force trends of Model-A and Model-AA at impact angles (a) 10 degrees, (b) 20 degrees.

Figure 7.11 presents the outcome of using Model-AA for the particle-translating-on-wall experiment. Interestingly, the linear and angular velocities show a wavy pattern around the pure rolling velocity. The amplitude of the wavy pattern is found to reduce as the spring stiffness is increased.

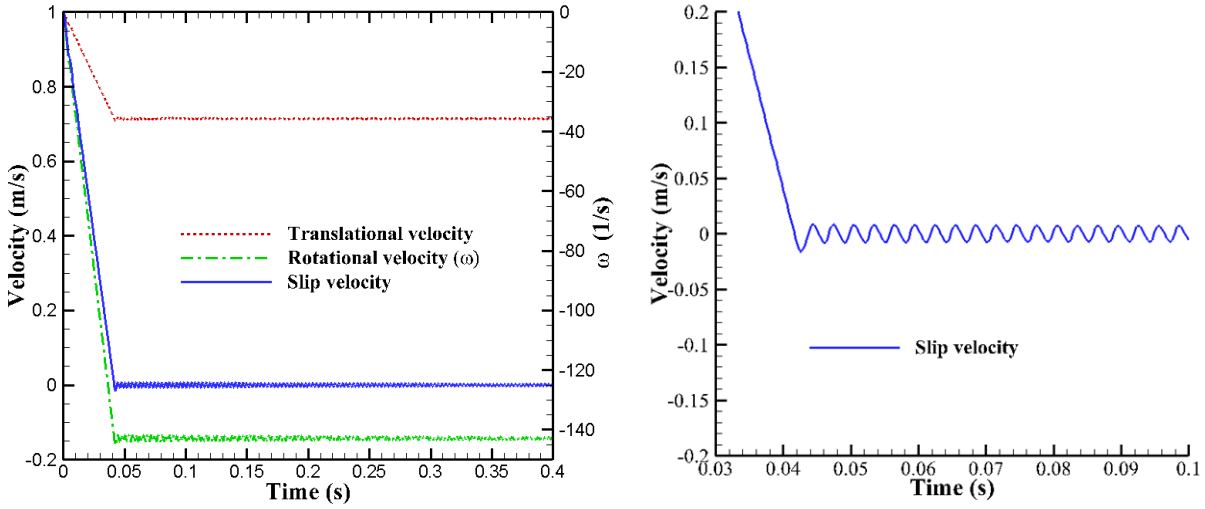

Figure 7. 11. Dynamics of a 10 mm sphere moving on a flat plate using model-AA (left), close up of the slip velocity as it reaches rolling condition is shown on right plot.

While Model-AA does improve on Model-A, Model-B is only as good as Model-C (uses much less storage than Model-B) even if the tangential deformation is limited as in Model-AA. This is a consequence of using the slip velocity to determine the direction of the tangential force. In fact, even non-linear soft sphere implementations that use the slip velocity are prone to the same shortcomings irrespective of the fact that the displacement/deformation may be limited in the formulation.

7.4.3 Alternate formulation

An interesting question that can be raised is whether or not the soft-sphere impact model can result in predictions better than rigid body theory in an oblique impact without storing deformation information and validate with the particle-translating-on-wall experiment as well. In this section an approximate treatment is suggested that can achieve this objective. For typical collisions at relatively small impact angles the contact areas stick and deform with the tangential force typically smaller than the sliding limit. On the other hand, if the impact angle is high enough then the full contact area is in slip mode and the tangential force equals the sliding limit throughout the collision. Between the two extremes there will be competition between sticking and slipping in the contact area. The characterization of the impact condition for an elastic impact was first proposed by [2] who introduced non-dimensional parameters for this purpose. These parameters were

introduced for the same material impacts and were recast in a general form by Di Renzo and Di Maio [184]

$$\kappa = \frac{k_t}{k_n} = \frac{\frac{1-\nu_i}{Gi} + \frac{1-\nu_j}{Gj}}{\frac{1-0.5\nu_i}{Gi} + \frac{1-0.5\nu_j}{Gj}} \tag{8.19}$$

$$\psi_1 = \frac{\kappa}{\mu_f}\frac{v_t}{v_{n1}} \tag{8.20}$$

$$\chi = \frac{\left(1 + \frac{m_p R_p^2}{I_p}\right)\kappa}{2} \tag{8.21}$$

The first parameter is the ratio of the tangential stiffness to the normal stiffness of the particle which is a function of the modulus of rigidity (G) and Poisson ratio (ν) of the two bodies in contact. The second parameter is the non-dimensional impact angle at the incipience of collision (ψ_1),v_{n1} is the normal impact velocity at the incipience of collision (i.e., $\vec{u}_{n,ij}$ at the instance of impact). v_t is the translational tangential velocity ($\vec{u}_{T,ij}$ as defined in Eq. (7.8)). The third parameter represents a combination of a geometrical and physical properties of the bodies in contact. The bracketed combination in Eq. (7.21) =7/2 for a sphere. Table 7.2 provides the three regimes of impact along with the physical mechanics at the contact area. Sticking regime is typically associated with forces that are smaller than the sliding friction limit for most of the impact duration. When slip takes place over all the contact area the tangential force typically becomes equal to the sliding limit. Visual interpretation of the change in tangential force during the impact duration at different impact regimes can be found in [2, 184]. In fact the oblique impact experiment of Kharaz, Gorham [182] at 4 degrees is at relatively low impact angle (see model-A behavior in Figure 7.4a). Similarly impacts at 10 degrees and 50 degrees are at intermediate and high impact angles. The non-dimensional impact angles ψ_1 for these three cases at the incipience of impact are 0.65, 1.65, and 11.14 for 4, 10, and 50, respectively, with the gross slip limit ($\psi_1^{GS} = 4\chi - 1$) of 5.02.

Table 7. 2. Description of different elastic impact regimes.

Description	ψ_1	Contact Mechanics
Relatively small angles of incidence	$\psi_1 \leq 1$	Sticking initially takes place at the contact area. At some instance in the rebound the contact area shrinks and can no longer sustain the traction. Annulus area of slip propagates inward until all the contact area goes into gross slip
Intermediate impact angles	$1 < \psi_1 < (4\chi - 1)$	The impact starts with gross slip during the compression stage. With the increase of the contact area and decrease of the tangential velocity the contact area suddenly changes to sticking. The rebound stage is similar to described above.
Large impact angles	$\psi_1 \geq (4\chi - 1)$	Gross-slip: slip takes place in the whole contact area throughout the impact.

Di Maio and Di Renzo [194]developed an analytical solution for frictional-elastic oblique impacts by coupling the normal and tangential equations of motion with appropriate boundary conditions. They developed analytical expressions for the times at which the impact changes from slip to sticking at intermediate impact angles and the time at which the impact changes from sticking to sliding at low and intermediate angles. Their solution of the system of equation was based on the impact regime, initial impact velocity and time of impact. In the frame work of the hard sphere impact model, Smith [195] used the non-dimensional impact angle at the incipience of impact to improve model predictions at low impact angles. In his work, the impact regime was defined in two stages, a gross sliding and a competition between sliding and sticking regime. He showed good comparisons with oblique impact results at low impact. Since an alternative implementation is sought here which does not require storing contact information, it is assumed that the instantaneous impact angle can be directly used to determine the impact regime. Thus we define

$$\psi^* = \frac{\kappa}{\mu_f}\frac{v_t}{v_n} \tag{7.22}$$

Where ψ^* is the instantaneous non-dimensional impact angle. The characterization of the impact regimes is kept the same as described above. The first step is to calculate the local non-dimensional impact angle ψ^*. The calculation of the force is then made as follows

$$\vec{F}_t = \begin{cases} -\psi^* \mu_f \left|\vec{F}_n\right| \dfrac{\vec{u}_{t,ij}}{|\vec{u}_{t,ij}|} & for\ \psi^* \le 1 \\ -\mu_f \left|\vec{F}_n\right| \dfrac{\vec{u}_{T,ij}}{|\vec{u}_{T,ij}|} & for\ 1 \le \psi^* \le 4\chi - 1 \\ -\mu_f \left|\vec{F}_n\right| \dfrac{\vec{u}_{t,ij}}{|\vec{u}_{t,ij}|} & for\ \psi^* > 4\chi - 1 \end{cases} \tag{7.23}$$

Note that $\vec{u}_{t,ij}$ is the tangential slip velocity, whereas $\vec{u}_{T,ij}$ is the tangential translational velocity. As can be seen from Eq. (7.23), if the impact is characterized to be in the sticking regime ($\psi^* \le 1$), then the tangential force is made smaller than the sliding limit. In this regime, the tangential force is approximated to be directly proportional to the instantaneous non-dimensional impact angle ψ^* with a direction opposite to the slip velocity. If a gross slip condition is assumed ($\psi^* > 4\chi - 1$) the force is simply set equal to the sliding friction limit and made opposite to the slip velocity. At intermediate impact angles ($1 \le \psi^* \le 4\chi - 1$) the force is set to the sliding limit but is assumed to be opposing the translational velocity ($\vec{u}_{T,ij}$) of the particle. This assumption is made to prevent the force from alternating when the slip velocity changes its sign.

A draw back of the model is that it will result in zero force if the particle is initially rotating (without translational tangential impact). To remedy this, Eq. (7.22) is revised as follows

$$\psi^* = \frac{\kappa}{\mu_f} \frac{v_t^c}{v_n} \tag{7.24}$$

here v_t^c is the characteristic tangential impact velocity and is given as

$$v_t^c = \max\left(\left|\vec{u}_{t,ij}\right|, \left|\vec{u}_{T,ij}\right|\right) \tag{7.25}$$

In Eq. (7.25), $\vec{u}_{t,ij}$ represents the tangential slip velocity (Eq. (7.9)), whereas $\vec{u}_{T,ij}$ is the tangential translational velocity (as per Eq. (7.8)). The direction of the friction force in the intermediate regime of Eq. (7.23) is made opposite to the characteristic velocity.

The results of the current model on oblique impact are shown in Fig. 7.12. The results show better agreement with the experimental data compared to Model-C. For a sphere traveling on a wall the

normal velocity is zero and the model directly goes into the gross slip regime. The implementation in this regime is the same as model-B which was shown to agree well with theory.

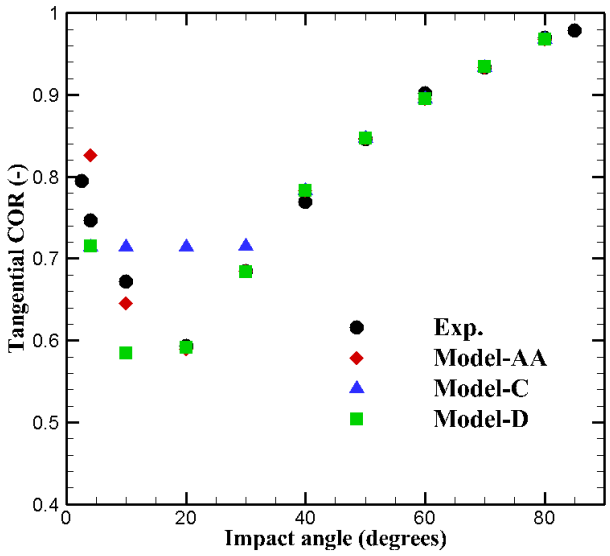

(a)

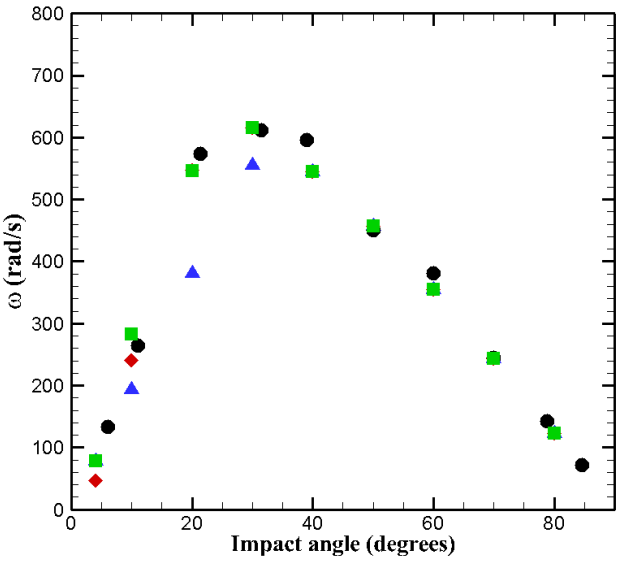

(b)

Figure 7. 12. Performance of the proposed surrogate tangential soft-sphere models on oblique impact results (a) tangential COR, and (b) rebound angular velocity.

7.4.4 Validation on inelastic impacts

In this section we validate the proposed models in inelastic oblique impacts. The experimental data of Dong and Moys [183] is used. The numerical parameters used in the simulation are indicated in

Table 7.3. To incorporate the effect of inelasticity, the non-dimensional impact parameter was defined following Thornton, Cummins [193]

$$\psi^* = \frac{2\kappa}{(1+e_n)\mu_f}\frac{v_t^c}{v_n} \tag{7.26}$$

Where e_n is the normal COR. Equation (7.26) above recovers Eq. (7.24) for elastic impacts. A comparison of the tangential COR and the rebound rotational speed at different impact angles are presented in Figure 7.13 when the particle has no initial spin. Model-C predicts the rigid body theory limit at low impact angles whereas both models AA and D capture some of the physics in this regime. The numerical predictions show reasonable agreement with the experimental data considering that the experiments themselves show notable uncertainty and scatter. As observed by Kruggel-Emden, Wirtz [181], who conducted extensive comparison of different models to this data, considerable deviations existed between the experimental data and the models. In fact deviations between the current experimental data set and the numerical simulations can be observed in the gross sliding regime also.

Table 7. 3. Simulation parameters for the inelastic oblique impact case.

Parameter	value
stiffness coefficient, k_n	100 (kN/m)
stiffness coefficient, k_t	86 (kN/m)
COR	0.9 (-)
Friction factor, μ	0.091 (-)
Diameter	44.45 (mm)
Density	7793 (kg/m^3)
Time step	10 (μs)

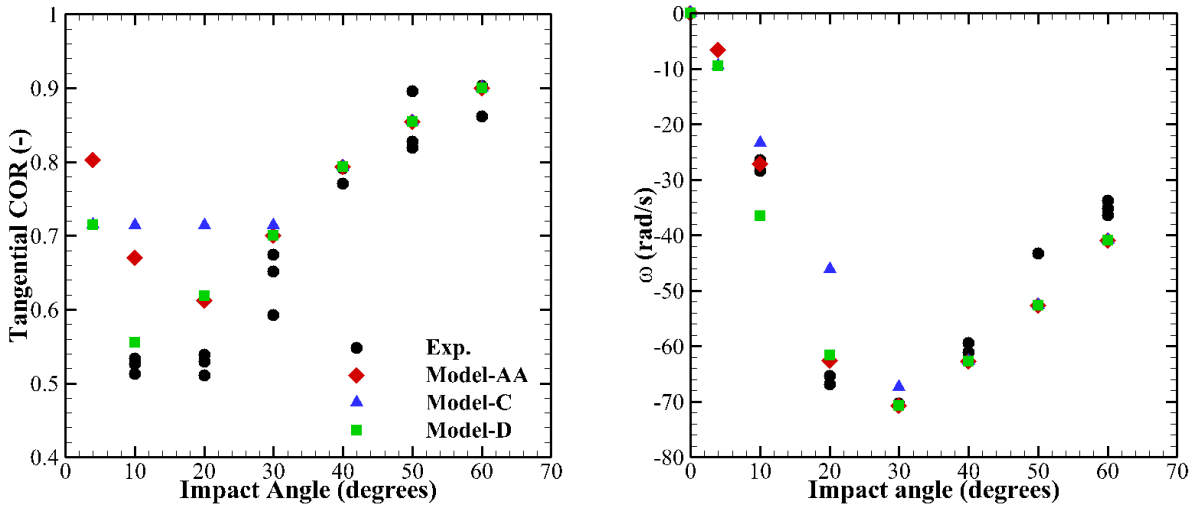

Figure 7. 13. Comparison of the tangential COR (left) and rebound rotational speed (right) for inelastic impact with no initial spin.

Two sets of experiments where performed in addition to the previous case with no initial spin [183]. In one set, the sphere was given a spin of 800 rad/s and in the second set of experiments the initial spin was set to -800 rad/s. A comparison of the results of the resultant tangential COR and the rotational speed for both sets of experiments is provided in Figure 7.14. The legends for the impact angles are the same as those used in Fig. 7.13 where filled symbols represent positive spin and void symbols represent negative initial spin. It can be seen that all models perform the same at impact angles of 20 degrees and higher. At low impact angles and negative rotation (void symbols) the three models show good COR comparisons with the experiments (Fig. 7.14*a*). In fact, all the three models predict a reversal of the translational motion of the sphere at an impact angle of ~5 degrees. However, differences in the rebound rotational speed can be seen. While the experiment and Model-AA show that the sphere loses almost all of its rotational momentum at small impact angles, Models C and D tend to retain a larger portion of the rotational energy for angles less than 10 degrees. Both models C and D under predict the tangential force at low impact angles. Model D could perhaps be refined further by selecting a more appropriate characteristic tangential velocity (Eq. 7.25).

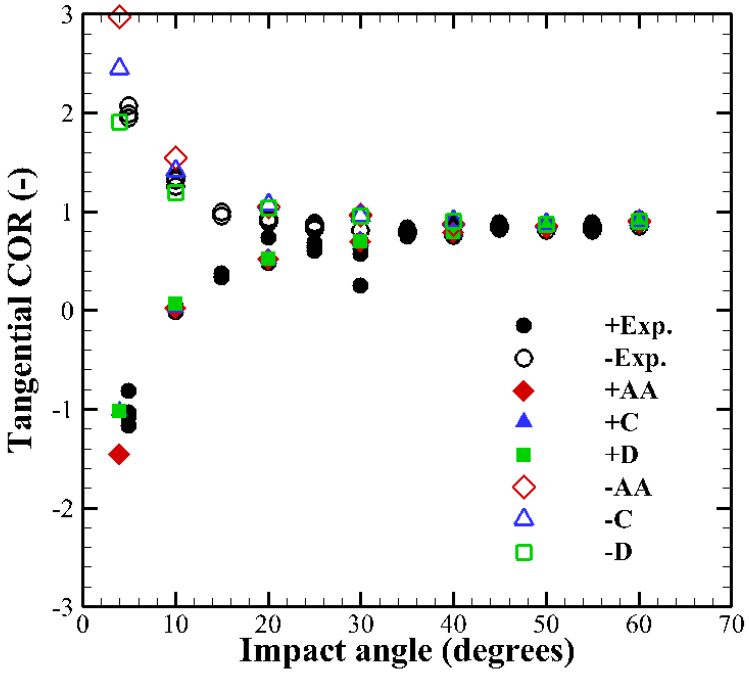

(a)

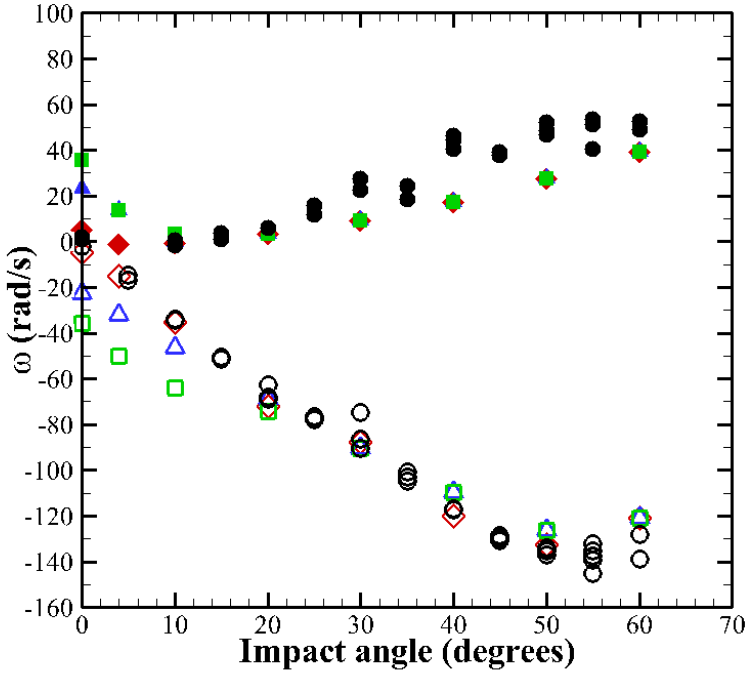

(b)

Figure 7. 14. Comparison of results of inelastic oblique impact with initial spin. a) tangential COR b) rebound rotational speed.

7.5 Conclusions

The current work evaluates existing models (Models A and B) and develops alternative methods (Models AA, C and D) for modeling tangential impacts with the soft-sphere collision model. The models are tested for a single particle in oblique impact with a surface and a single particle sliding on a surface. The paper first demonstrates inconsistencies in the existing model implementations which result in loss of accuracy and incorrect results. It is shown that neither of the models, A nor B give consistent results for both test cases. Model AA is formulated by putting a limit on the allowable tangential displacement to give consistent results in both test cases. Although limiting the tangential displacement was suggested more than a couple of decades ago, only Model-A type implementation benefits from it (this is equally applicable to non-linear soft-sphere models).

Models C and D are specifically developed to eliminate the need to store the tangential deformation for each pairwise collision. The motivation is to save on memory usage for DEM simulations with a large number of polydisperse particles in which a large particle could potentially collide with many small particles. Model C, which calculates the instantaneous displacement as the product of the collision time scale with instantaneous tangential velocity, is easy to implement, however it only recovers the rigid body limit at low impact angles. The second surrogate model attempts to demonstrate the ability of capturing the physics at low impact angles by using the effective instantaneous impact angle with the aid of material properties of the interacting particles or surfaces. Both Models C and D compare well with experiments. In most cases the quality of predictions is as good or better than existing models A and B in the literature.

Chapter 8

Comparison of a Physics Based Hard-sphere Model with the Soft Sphere Model

Husam Elghannay[1], Danesh Tafti[1], Kuahai Yu[2]

1. Mechanical Engineering Department, Virginia Tech., Blacksburg, VA 24061, United States

2. Engineering Mechanics Department, Henan University of Science and Technology, Luoyang 471023, China

Citation:

Paper submitted to Powder Tech (Feb2018).

8.1 Abstract

In this paper we present the application of a physics-based three dimensional hard-sphere impact model to many-particle systems. The hard sphere model is used with conventional time-advancement which is not event driven. A particle relocation technique based on using both pre- and post-collision velocities is developed and validated. Also developed is a parallelization scheme which overcomes the inherent sequential nature of processing collisions with the hard sphere model. The relocation technique is tested in a one-dimensional stack of particles and in the three-dimensional settling of a bed of particles. The technique demonstrates its ability to prevent excessive overlaps and maintaining stable stacks of particles at coefficients of restitutions ranging from 0.0 to 0.98. The model is validated in a bubbling fluidized bed and shows no discernable differences with the soft sphere model but at a computational cost about 23 times less than that of the soft sphere model. The model is used to investigate particle agglomeration in a turbulent ribbed duct flow using LES for particles of size 1 μm and 20 μm. It was found that the 20 μm particles were more prone to agglomerate in regions of low velocity at the upstream and downstream corners of the rib-wall junction. The hard sphere model enabled time steps an order of magnitude larger than that permissible for the soft sphere model which resulted in DEM speedups of more than 20 times, and a corresponding CFD-DEM speed-up of ~5 times.

8.2 Introduction

Simulating dense fluid-particulate systems using the Discrete Element Method (DEM) with CFD is computationally expensive because particle collisions have to be modeled. Two methods are adapted in modeling impact of particles with other surfaces or neighboring particles. These are the soft sphere collision model and the hard sphere collision model. In the soft sphere collision models the contact is modeled using a spring-dashpot-slider system (e.g. [22]) and the collisions are resolved over a number of time steps. Multiple overlaps and interactions are permitted in this frame work. Although the use of proper stiffness is required for accurate resolution of the tangential impact mechanics [184], the stiffness of the particles is typically artificially reduced to allow the use of larger time steps (e.g. [22]). The hard sphere collision model, on the other hand was initially used for binary collisions in molecular dynamics [196] where particles do not overlap and

collisions are modeled in one time step by applying principles of conservation of momentum and energy balance principles. The hard sphere collision model was used in Computational Fluid Dynamics coupled to Discrete Element Method (CFD-DEM) for 2D multiple particle systems using event driven technique (e.g. [163] and [197]). In the event driven technique, all particles are advanced in time using the minimum time step to the next contact without allowing for overlaps between the interacting particles. If this technique is applied to dense particle system in which some of the particles are in continuous contact the resultant time step is extremely restrictive. In fact, formation of a cluster of particles can occur even in the case of dilute granular mixtures causing the time step to approach zero [198, 199]. Moreover, detecting the exact instance of impact can be affected by the limited machine precision leading to stability issues [200]. To prevent the instability initiated by overlaps, the particle diameter was modified (e.g., [201]) leading to solving a slightly different system [200].

In light of these limitations, the soft-sphere model which allows particles to deform elastically has found favor in dense granular flows [198]. At the same time, different techniques have been suggested and used by researchers to extend the use of hard-sphere impact models to dense particulate/granular systems using time advancement techniques rather than event-driven techniques. In the molecular dynamics literature, time advancement was combined with a post-collision adjustment in which the particle positions were reverted back in time if overlaps were detected [e.g., 202, 203].

Helland, Occelli [204] used time-driven advancement technique with the hard sphere collision model in CFD-DEM where they suggested sweeping through computational particle cells in an alternating fashion at each time step to detect and construct collision lists. Once the collision list was constructed, the position of the particles was adjusted to the instance of contact using the overlap distance and relative velocity. The collision dynamics were processed and the interacting particle velocities and positions were changed accordingly. The technique was found efficient but introduced a risk of missing some collisions in dense particle regions [204].

González, Risso [205], in simulating sedimentation under gravity, suggested freezing particles if their velocity exceeded a specified threshold, moving downward and decreasing with a frozen particle below it. A frozen particle is woken-up if it was hit by another particle above a certain velocity threshold and assigned the same energy as when it was put to sleep [205]. Keeping track

of the logic of freezing and awakening particles required considerable book-keeping. McNamara, Flekkøy [206], suggested using the full time step and performing inelastic collision only if the particle did not undergo a collision in the current or preceding time step. This procedure is repeated till all pairs of particles are separate. Guttenberg [198] pointed out that this approach can significantly affect the behavior of dense granular systems. An alternative approach was suggested by Guttenberg [198] in which a list of events that would occur during an upcoming time-step, given the state of the system at the current time step, was collected and executed. Errors introduced by the assumptions in this approach limit its applicability to dense flowing granular systems where static packing of particles is not dominant and where grains are moving locally in the same direction [198].

More recently, Lu, Li [207] proposed using a velocity correction method for the time driven hard sphere algorithm. First a neighbors list was constructed, similar to the soft-sphere collision model, then the collisions were processed for particles that overlap and moving toward each other. Overlaps were reduced by performing a number of sub-steps/iterations of modification of the velocity of the particles which were still in overlap after processing all the collisions. Stiffness and damping coefficients are used during the iterations in a process similar to sub-stepping in the soft-sphere impact model in the normal direction. The velocity correction method showed advantage in maintaining a stationary bed of sediment particles compared to a continuous overlap when no means of resolving the overlap was adopted [208]. However, by modifying the particle post collision velocity, a different effective coefficient of restitution (COR) than the input COR is used.

The objective of this paper is to show that the hard sphere model is a viable, and in many cases necessary alternative to the soft sphere model. By eliminating the collision time scale intrinsic to the soft sphere model, the hard sphere model can operate on larger time scales than the soft sphere model, resulting in savings in computational cost. It is shown that the challenge posed by accommodating only binary collisions at a time and the resulting potential overlaps between particles in the hard sphere framework can be overcome by suitable post-collision re-location of particles after multiple sequential collisions. Another challenge overcome is the inherent sequential nature of the model which prevents parallelization unless special measures are incorporated. With these modifications, the accuracy and efficiency of the hard sphere model is

compared to the soft sphere model in a dense bubbling fluidized bed and in the study of deposition accumulation of micron sized sand particles in a ribbed duct.

The paper is organized as follows: First the governing equations of the fluid and particles are presented. The suggested time advancement method for the particles with the parallelization technique are then described. The validation part includes evaluation of the relocation technique used to resolve overlaps in one and three dimensional systems. The performance of the formulation on particulate flow systems is then evaluated in the fluidized bed system and the turbulent ribbed duct. This is followed by a summary and conclusions.

8.3 Governing Equations and Mathematical Formulation

The methodology employs an Eulerian-Lagrangian approach which involves tracking the individual motion of each particle. The flow is not resolved around the particle surface; instead, point-force expressions are employed to account for different fluid-particle interactions. The fluid governing equations along with the particle equations of motion and the coupling strategy is presented first, followed by a description of the relocation technique used in the time advancement of the hard sphere collision model. A description of the method of parallelization is also provided in this section.

8.3.1 Fluid Equations

The carrier phase is modeled using a volume averaged Navier-Stokes equations derived by Anderson and Jackson [20] for multiphase flows. The current implementation of the continuous phase is governed by Model-B of Gidaspow [209] in which the pressure drop is accounted for only by the fluid. The fluid equations are written as

$$\frac{\partial(\varepsilon\rho)}{\partial t} + \vec{\nabla}.(\varepsilon\rho\vec{u}) = 0 \tag{8.1}$$

$$\frac{\partial(\varepsilon\rho\vec{u})}{\partial t} + \vec{\nabla}.(\varepsilon\rho\vec{u}\vec{u}) = -\vec{\nabla}p + \vec{\nabla}.(\varepsilon\bar{\bar{\tau}}) + \rho\vec{g} - \sum_{i=1}^{n_p} \frac{m_{p,i}\vec{f}_{fp,i}}{\forall_{cell}} \tag{8.2}$$

where $\varepsilon, \rho, \vec{u}, p \; and \; \bar{\bar{\tau}}$ are the fluid void fraction in each computational cell, fluid density, fluid interstitial velocity, pressure, and viscous shear stress, respectively. While $m_p, \vec{f}_{fp}, g, \forall_{cell}$ and n_p are the particle mass, the fluid-particle interaction force per unit mass of the particle, the volume

of the computational cell, the gravitational acceleration, and the number of particles residing in a computational cell, respectively. The void fraction accounts for the presence of particles in the fluid volume.

8.3.2 Particle Dynamical Equation

In DEM the path of each particle is predicted by the integration of its equation of motion resulting from the application of Newton's law of motion. The equation of motion of particles moving under the influence of drag and gravity forces along with contact forces can be expressed as

$$\frac{d\vec{u}_{p,i}}{dt} = \vec{f}_{grav,i} + \vec{f}_{drag,i} + \sum \vec{f}_{c,i} \tag{8.3a}$$

$$\frac{d\vec{x}_{p,i}}{dt} = \vec{u}_{p,i} \tag{8.3b}$$

where force components in the above equation are per unit mass of the particle. In the above equation, the drag force is the only fluid-particle interaction force.

Gravity force herein includes both gravity and buoyancy effects. The submerged weight of the particle (per unit mass of the particle) is given by

$$\vec{f}_{grav} = \left(1 - \frac{\rho}{\rho_p}\right)\vec{g} \tag{8.4}$$

The drag force accounts for the quasi-steady drag in uniform flow and is often a key element in interaction of dense granular flows and is modelled using the form

$$\vec{f}_{drag} = \frac{\beta}{\varepsilon(1-\varepsilon)\rho_p}\left(\vec{u} - \vec{u}_p\right) \tag{8.5}$$

where β, ρ_p, and $\vec{u}_p$ are the momentum exchange coefficient, the particle density, and the particle velocity, respectively. A combination of Ergun formula for dense mixtures $\varepsilon < 0.8$ and Wen & Yu drag correlation for dilute mixtures $\varepsilon > 0.8$ is used for the momentum exchange coefficient with a blending function to avoid discontinuity [21].

$$\beta = W\beta_{Ergun} + (1 - W)\beta_{Wen-Yu} \tag{8.6}$$

$$\beta_{Ergun} = 150\mu\frac{(1-\varepsilon)^2}{\varepsilon d_p^2} + 1.75(1-\varepsilon)\frac{\rho}{d_p}\left|\vec{u} - \vec{u}_p\right| \tag{8.7}$$

$$\beta_{Wen-Yu} = \frac{3}{4} C_D \frac{(1-\varepsilon)\varepsilon}{d_p} \rho \left|\vec{u} - \vec{u}_p\right| \varepsilon^{-2.65} \tag{8.8}$$

Where μ is the dynamic viscosity, d_p is the particle diameter, and W is a blending function defined as

$$W = \frac{tan^{-1}\big(150(\varepsilon - 0.8)\big)}{\pi} \tag{8.9}$$

and C_D is the drag coefficient

$$C_D = \begin{cases} 24\big(1.0 + 0.15 Re_p^{0.687}\big)/Re_p, & Re_p < 1000 \\ 0.44, & Re_p \geq 1000 \end{cases} \tag{8.10}$$

Reynolds number Re_p is calculated as

$$Re_p = \frac{\varepsilon \rho d_p \left|\vec{u} - \vec{u}_p\right|}{\mu} \tag{8.11}$$

The rotational motion of the particle is governed by

$$I_{p,i} \frac{d\vec{\omega}_i}{dt} = \sum\nolimits_{N_p} \vec{T}_{c,i} \tag{8.12}$$

where $I_p, \vec{T}_c$ represent the moment of inertia of the particle, and the torque ($\vec{T}_c = \vec{R}_p \times \vec{F}_c$) acting on the particle from the tangential contact force, where $\vec{R}_p$ is a vector from the mass centre of the particle to the contact point.

Both the soft and the hard sphere model are used to model particle-particle and particle-wall collisions. The contact force in Eq. (8.3a) and contact torque in Eq. (8.12) is only used for the soft sphere model during contact(s). Because of the sequential nature of processing multiple binary collisions in the hard sphere model, multiple simultaneous contacts are more accurately represented by changing the instantaneous velocities of the colliding pair (based on the impact model) before proceeding to the collision with another particle in the sequence. The hard sphere model is limited to binary collisions at a time whereas multiple particle interactions are simultaneously handled in the soft sphere model. The soft sphere and hard sphere contact models are described in the following section.

8.3.3 Soft Sphere Model

The soft sphere collision model is used in which the contact force in both normal and tangential directions is modeled using a linear spring-dashpot-slider system [e.g., 22]. The modelled collision between two particles is represented in Fig. 8.1 for particle-particle collision (walls can be assumed as particles with infinite mass and radius). The contact force in the soft sphere model ("$\vec{F}_{c,i}$" in Eq. (8.3a)) is decomposed into a normal force component and a tangential force component. In this framework, the coefficient of restitution in the normal and tangential direction is typically an input parameter and is set to a fixed value. The spring in both normal and tangential directions accounts for the elastic part of the impact force and the dashpot accounts for the energy loss during the collisions. The slider prevents the tangential force from exceeding a maximum tangential threshold. The contact force components in the normal and tangential direction to the collision plane are expressed as

$$\vec{F}_n = \begin{cases} -k_n\vec{\delta}_n - \eta_n\vec{u}_{n,ij} & for\ \Delta_{ij} < \dfrac{d_{pi}+d_{pj}}{2} \\ 0 & else \end{cases} \tag{8.13}$$

$$\vec{F}_t = \begin{cases} -k_t\vec{\delta}_t - \eta_t\vec{u}_{t,ij} & for\ |k_t\vec{\delta}_t + \eta_t\vec{u}_{t,ij}| < \mu_f|\vec{F}_n| \\ -\mu_f|\vec{F}_n| & else \end{cases} \tag{8.14}$$

where; k, δ, η and μ_f above are the spring constant, particle contact displacement, coefficient of viscous dissipation, and the sliding friction coefficient, respectively. In the above equations, $\vec{u}_{n,ij}$ and $\vec{u}_{t,ij}$ are the normal and tangential components of the relative velocity between the two particles and the parameter Δ_{ij} is the distance between the centres of the two particles. The normal displacement is given as $\vec{\delta}_{n,ij} = \left\{\left(\frac{d_{pi}+d_{pj}}{2}\right) - \Delta_{ij}\right\}\vec{n}_{ij}$ where $\vec{n}_{ij}$ is the unit vector of the normal direction between the two particles while the tangential displacement is approximated as

$$\vec{\delta}_t^n = \vec{\delta}_t^{n-1} + \int \vec{u}_{t,ij}\, dt \tag{8.15}$$

Because the soft sphere model treats collisions over a finite-time scale, the time-advancement is limited by the collision time scale of the system ($\tau_c \propto \sqrt{m_{i,j}/k_n}$), where $m_{i,j}$ is the effective mass of the system. Note that the soft sphere model places a severe restriction on the time step for stiff

particles in the micron range. To alleviate this restriction, the stiffness k_n is artificially lowered to accommodate larger time steps.

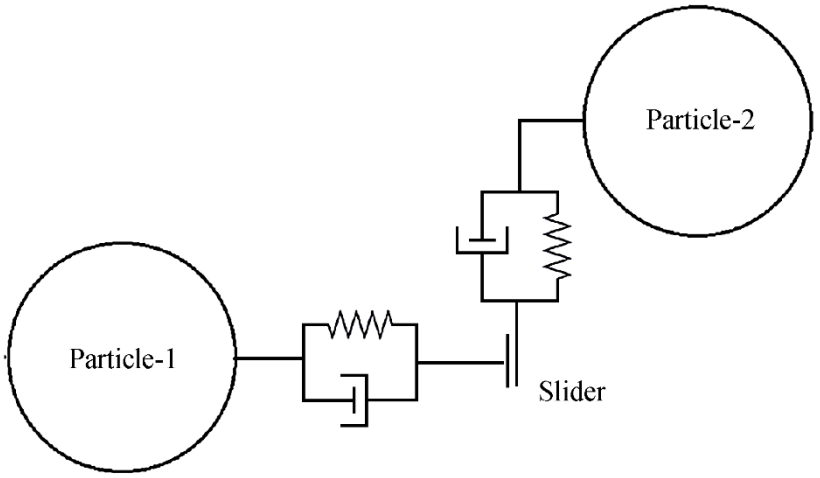

Figure 8. 1. Schematic drawing of the soft-sphere impact model.

8.3.4 Hard Sphere Impulse Based Model

The impulse based collision model developed and validated in Yu and Tafti [210] and Yu, Elghannay [211] is used. It includes the effects of material properties, incident translational and rotational velocities, and angle of impact to give the resultant velocities after impact. The model is developed based on the following assumptions (1) the normal collision is independent of the tangential motion; (2) particles do not deform in the tangential direction – they can only slide or roll during impact; (3) torsion and twisting of the particle is neglected. These assumptions are critically evaluated and validated in Yu, Elghannay [211].

For each collision in the normal direction, depending on the relative normal impact velocity, the impact can go through three compression stages, elastic stage, elastoplastic stage, and full plastic stage [212]. As such there are two critical impact velocities – the first when the impact crosses over from the fully elastic into the elastic-plastic stage which occurs when the material stress exceeds 1.1 times the yield stress, and the second when the particle stress exceeds 2.8 times the yield stress and transitions into the fully plastic regime. Maximum deformation occurs at the end of the compression stage when the particle relative normal velocity is zero. During recovery which is governed by a Young's modulus similarity rule, only the elastic energy is recovered and the plastic strain energy is dissipated during the impact. In addition to plastic deformation losses

during impact, additional losses are incurred in overcoming attractive forces during separation of the two surfaces in contact. The adhesive losses are assumed to be active only during the recovery stage of the collision. The adhesive losses are approximated by an idealized line force based on the material stiffness and surface energy acting on the maximum contact area to represent the work expended to break contact between the two surfaces [213]**.** The adhesive losses become important and dominant at low impact velocities and micron sized particles. If the work of overcoming adhesive forces is less than the recovered elastic energy, then the two particles will move with the same post-collision velocity or in the case of a particle surface impact, the particle will stay on the surface.

With the assumption of rigid body dynamics in the tangential direction, the tangential impact model goes through three stages in the tangential direction, which are (1) sliding; (2) rolling; (3) translation only. A critical tangential impulse defines whether the particle slides or slides and rolls on the surface. When the total tangential impulse is greater than this critical value, rolling between particles or between particle and surface is initiated; otherwise the particle(s) will keep sliding during the whole collision process. The details of the tangential impact model are given in Yu, Elghannay [211].

By modeling the normal and tangential impact, the impact model is capable of predicting the normal, tangential, and total coefficient of restitutions (CORs) for the system as well as for individual particles and gives a physical basis for calculating the post-impact translational and rotational velocities.

8.3.4.1 Particle relocation

For a particle, *i*, colliding with multiple neighbors, *j*, collision (*i,1*) is processed resulting in updated velocities (translational and rotational) for the pair. The next collision (*i,2*) uses the updated velocities of *i* from the (*i,1*) impact as the initial velocity to obtain a resultant velocity for the (*i,2*) pair and so on. The collision is determined between two particles if they are overlapping and moving towards each other (based on relative velocity in the normal direction). After all collisions of particle *i* are processed, additional forces such as fluid drag are calculated (Eq. 8.3(a)) and the particle is advanced in time. Because the time advancement is not event driven but at a constant time scale, it is possible that during time advancement particles will overlap in dense mixtures. The degree to which this problem manifests depends on the mixture density and the time step and

has been one of the main challenges in the implementation of the hard sphere impact model. In the current work, to maintain consistency, an overlap time scale (δt_o) is calculated based on the overlap and the normal velocity.

$$\delta t_o = \frac{\delta_n}{u^n_{p,ij}} \tag{8.16}$$

Here δ_n is the overlap distance and $u^n_{p,ij}$is the relative impact velocity of the interacting particles in the normal direction. The overlap time scale is used to estimate the particle's location before the overlap with the use of the pre-collision velocity. The particle is then advanced in time from that location using the overlap time scale and the post-collision velocity. These two steps can be combined in one step by calculating a relocation displacement as follows

$$\vec{\delta}_{p,i} = (\vec{u}^{post}_{p,i} - \vec{u}^{pre}_{p,i})\delta t_o \tag{8.17}$$

where $\vec{\delta}_{p,i}$, $\vec{u}^{post}_{p,i}$ and $\vec{u}^{pre}_{p,i}$ are the relocation displacement, the particles' post-collision and pre-collision velocities in the *i* direction, respectively. The relocation from collisions with all neighboring particles are accumulated together and applied to the particle in the time advancement step. For binary impacts, the time scale defined by Eq. (8.16) is smaller than the time step used in the time advancement. Equation (8.17) is thus a correction of the time integration process.

Assuming a first order integration in time the updated position (from Eq. (8.3b)) is written as

$$\vec{x}^{n+1}_{p,i} = \vec{x}^{n}_{p,i} + \Delta t.\vec{u}_{p,i} + \vec{\delta}_{p,i} \tag{8.18}$$

8.3.4.2 *Parallelization of particle impacts*

As explained in the previous section, the hard sphere collision process modeling is inherently a sequential process. Parallelization is implemented using a domain decomposition framework in which the spatial domain is divided between different processors. In this framework, particle collisions and building neighbor lists is facilitated by having a layer of ghost particles on each processor. Ghost particles are particles that reside at boundaries of adjoining processor domains which could be colliding with particles on the processor in question. Thus each processor has a list of ghost particles with all relevant information pertaining to their locations, velocities, etc. The ghost particles on a processor only participate in a collision in their designated role as neighbors colliding with a particle on that processor. For example, referring to Figure 8.2, particles P1, P2, P3 residing on processor 1 have their avatars as ghost particles P1g, P2g, P3g on processor 2.

Conversely, the ghost avatars of particles P15, P16 and P18 residing on processor 2 are P15g, P16g and P17g on processor 1. Building ghost particle lists involve message passing across processors and building neighbor lists involve computationally expensive searches and thus both are done only once per particle time step. It is mandatory that ghost particle assembly and the particle neighbor lists are built before invoking the collision model because both the soft sphere and hard sphere model operate on the list of neighbors for each particle. In light of the sequential nature of processing binary collisions in the hard sphere framework, and updating of velocities of the colliding pair before moving on to the next collision, there is a high probability that without any special measures, ghost particles that participate in more than one collision will have at least a few collisions with outdated velocities. These inconsistencies have an adverse effect on the relocation of particles and manifest as sudden unphysical particle movements near processor boundaries.

To overcome the challenge, particle collisions are performed in two steps. Impacts between particles residing on the processor (internal particles) of interest are executed only with ghost particles (if any) in a first pass, followed by a second pass in which impacts between internal particles (particles resident on processor of interest) are considered. The process is described schematically in Figure 8.2. The initial stage shows the particles on two adjacent processors with ghost particle layers on each. Ghost layer 2-1 (particles in cyan) is a copy of the particle information that processor 2 passes to processor 1. Fig. 8.*2b* shows the situation after processing the first pass in which collisions between particles on a given processor are first executed with ghost layer particles (particles in green) on all processors concurrently. In the second pass, the collisions are processed only between particles that exist on the processor (ghost particles excluded) for all processors. Figure 8.2c shows the final state in which all collisions are executed. The main algorithmic elements of the hard sphere model implementation are provided in Figure 8.3.

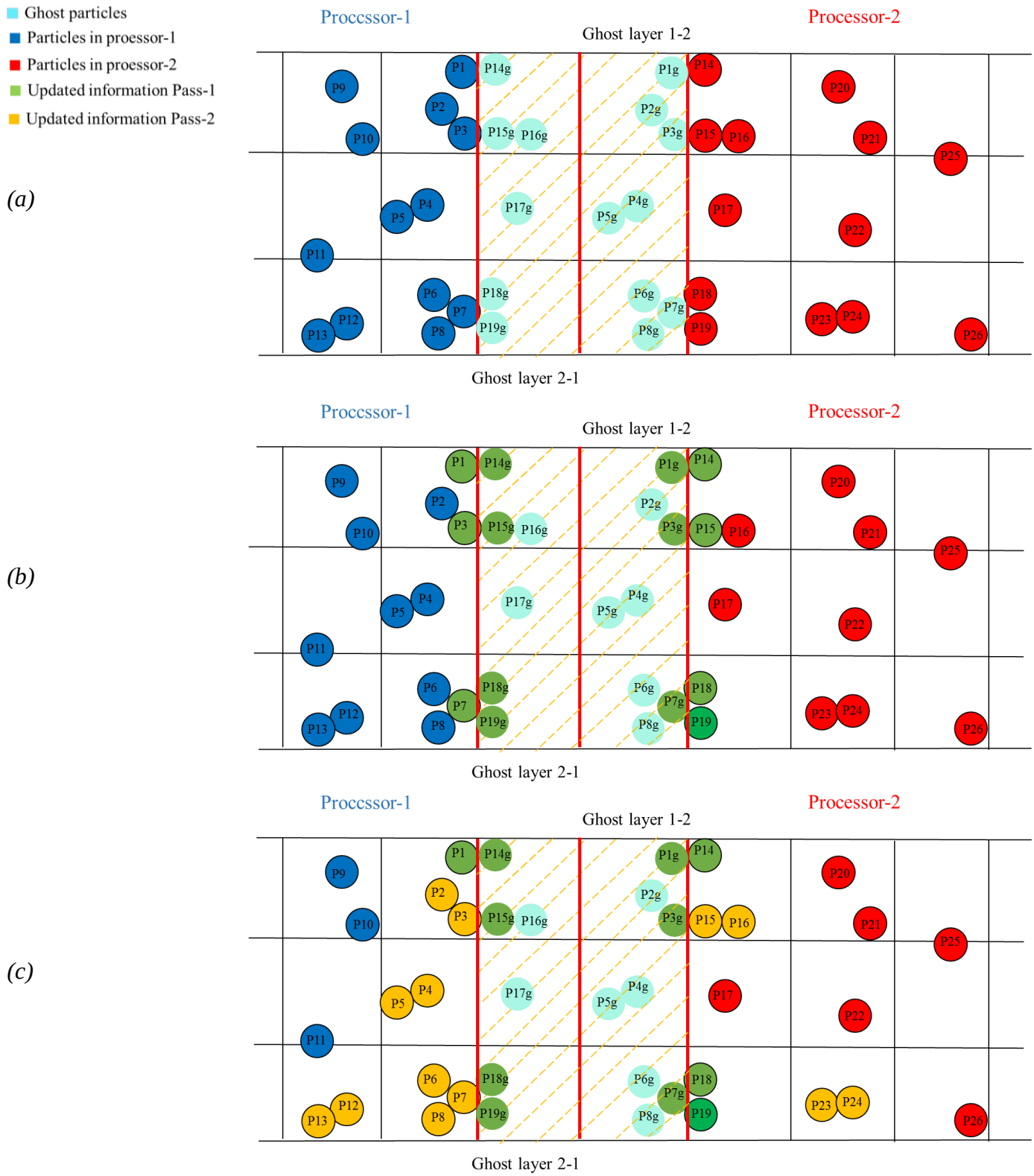

Figure 8. 2. Hard sphere collision model implementation. (a) ghost particles and internal particles on a processor. (b) Collisions only with ghost particles (c) Collisions only with internal particles.

- **Build ghost particle layer on each processor by transferring particle data from adjoining processor**
- **Construct neighbor list for each internal particle using ghost particles**
- **Sequentially loop through all internal particles on processor and execute collisions only with ghost particles (if applicable). Update velocities of colliding pair. Calculate cumulative relocation displacement (Eq. 8.17)**
- **Sequentially loop through all internal particles on processor and execute collisions only with other internal particles. Update velocities of colliding pair. Calculate cumulative relocation displacement**
- **Process particle-wall impacts. Update velocity of particle. Calculate cumulative relocation displacement**
- **Calculate all other relevant forces and torques on particle and update translational and rotational velocities**
- **Update particle locations based on velocities and cumulative relocation (Eq. 8.18).**

Figure 8. 3. Algorithmic elements of hard sphere model implementation.

8.4 Results

First the stability and robustness of the particle relocation technique is evaluated in a single stack of 10 particles using different set values of the coefficient of restitution. This is followed by a particle settling experiment. Two different application are selected to demonstrate the performance and advantages of using the hard sphere model; a small scale bubbling fluidized bed, and the dispersion and accumulation of micron sized particles in a periodic ribbed duct.

8.3.5 **Evaluation of Relocation Technique**

8.3.5.1 ***Evaluation of Relocation Technique in a One-Dimensional Stack of Particles***

Unlike the soft-sphere impact model, no static limit or state of complete rest exists when the hard sphere impact model is used [205] and the problem manifests most critically in stacks of static particles. Thus, in this section the behavior of the relocation technique on a stack of particles under the influence of gravity is investigated. Of primary interest is whether the relocation technique can maintain a stationary position of the particles and the residual velocity induced by the relocation technique. The particle motion is restricted to the direction of gravity and they are initialized to be resting on the top of each other (Fig. 8.4). The direction of negative velocity is in the direction of gravity. The performance of the system can be different depending on the number of the particles stacked on the top of each other. In the current work we examine a stack of ten particles at different input coefficients of restitution. The diameter of the particles is set to 1.2 mm. The simulations were run using a time step of 5 μs and the outcomes where found to be the same for time steps of 0.5 μs and 50 μs.

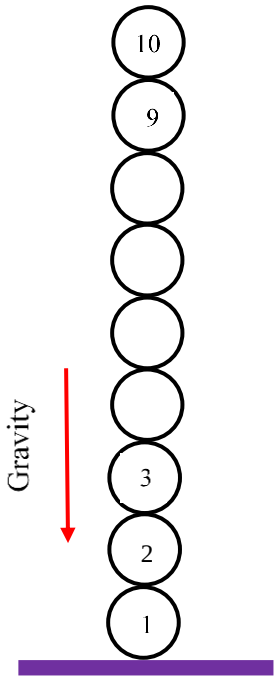

Figure 8. 4. Stack of 10 particles in under the influence of gravity.

Eight different systems with coefficient of restitutions where tested ranging from 0-1. In all the systems the relocation technique was able to prevent the stack of particles from continuously penetrating each other. In fact, the positions where almost stationary with negligible steady fluctuations in most cases. As for the velocity of the particles, steady patterns of velocity fluctuations where found for almost all tested cases. Figure 8.5 presents the stationary velocity tracks for selected simulations normalized with respect to a characteristic reference velocity ($g\Delta t=4.9\times10^{-5}$ m/s). Tracked information (position and velocity) are recorded for the post collision condition. Particle number 1 is the one resting on the wall and particle number 10 is the topmost particle (Fig. 8.4). The particles in between are in ordered numbering. The reference velocity corresponds to the velocity supplied to the particles by virtue of gravity at each time step and it was found that the normalized velocity was independent of the time step used (0.5 μs, 5 μs and 50 μs). The line legends are presented in the case with COR=0.0, the color bands seen for the cases of COR =0.25, 0.5 and 0.75 indicate repeated velocity fluctuating patterns. It is noted that the fully dissipative system shows stable velocity without fluctuations whereas the case of COR=1.0 shows a buildup of the particles fluctuating velocity. The system with COR=0.98 does not show a stationary pattern, but no build-up of velocity fluctuations result. A zoomed-in view of the velocity fluctuations is provided in Figure 8.6 for selected cases, where the markers (when used) indicate a time step. The velocity fluctuations for a system of COR=0.25 are not as uniform as those at COR=0.5 and 0.75. Although not shown, cases with COR=0.85 and 0.9 show uniform velocity fluctuations.

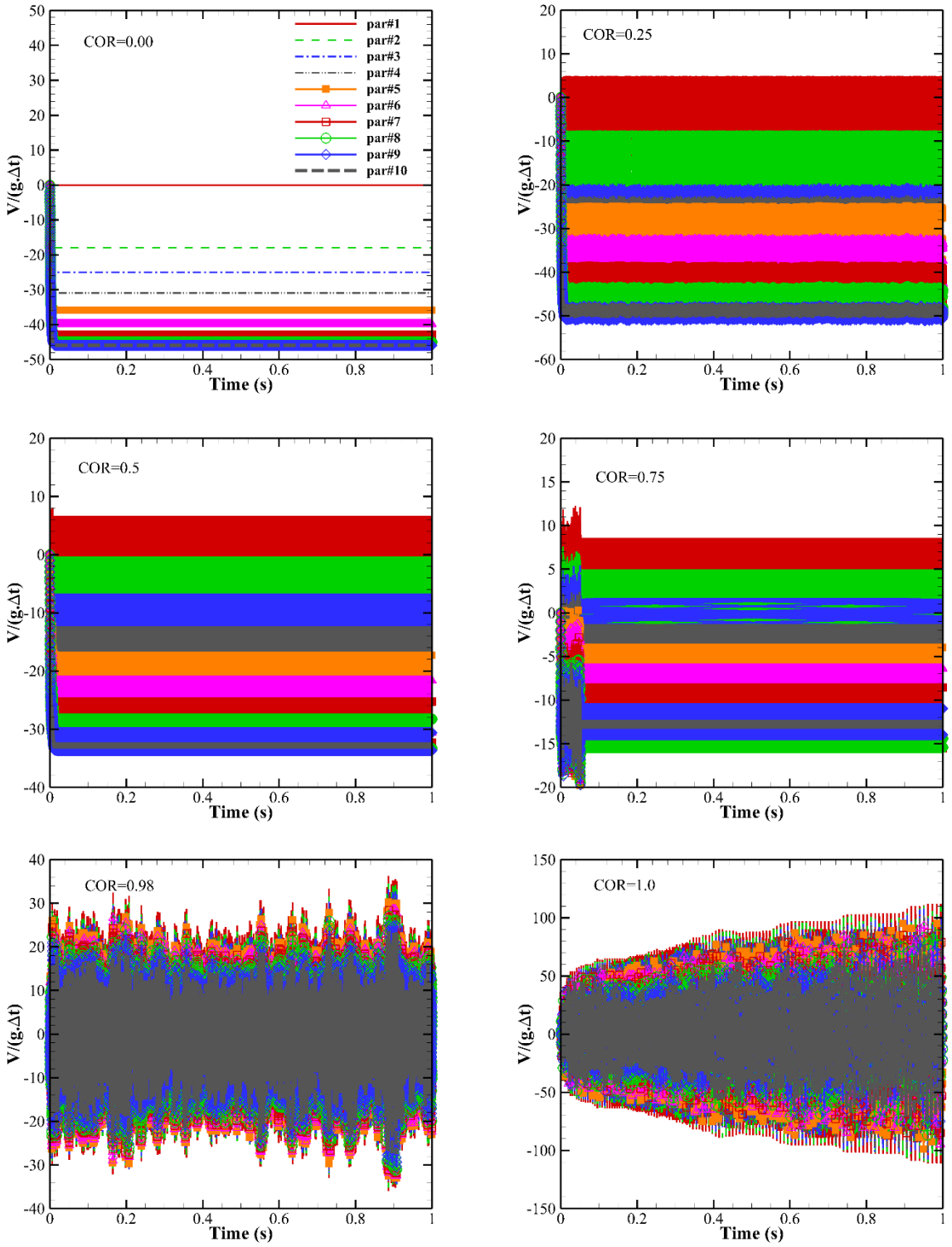

Figure 8. 5. Pattern of velocity track at different COR for a stack of ten particles placed on top of each other.

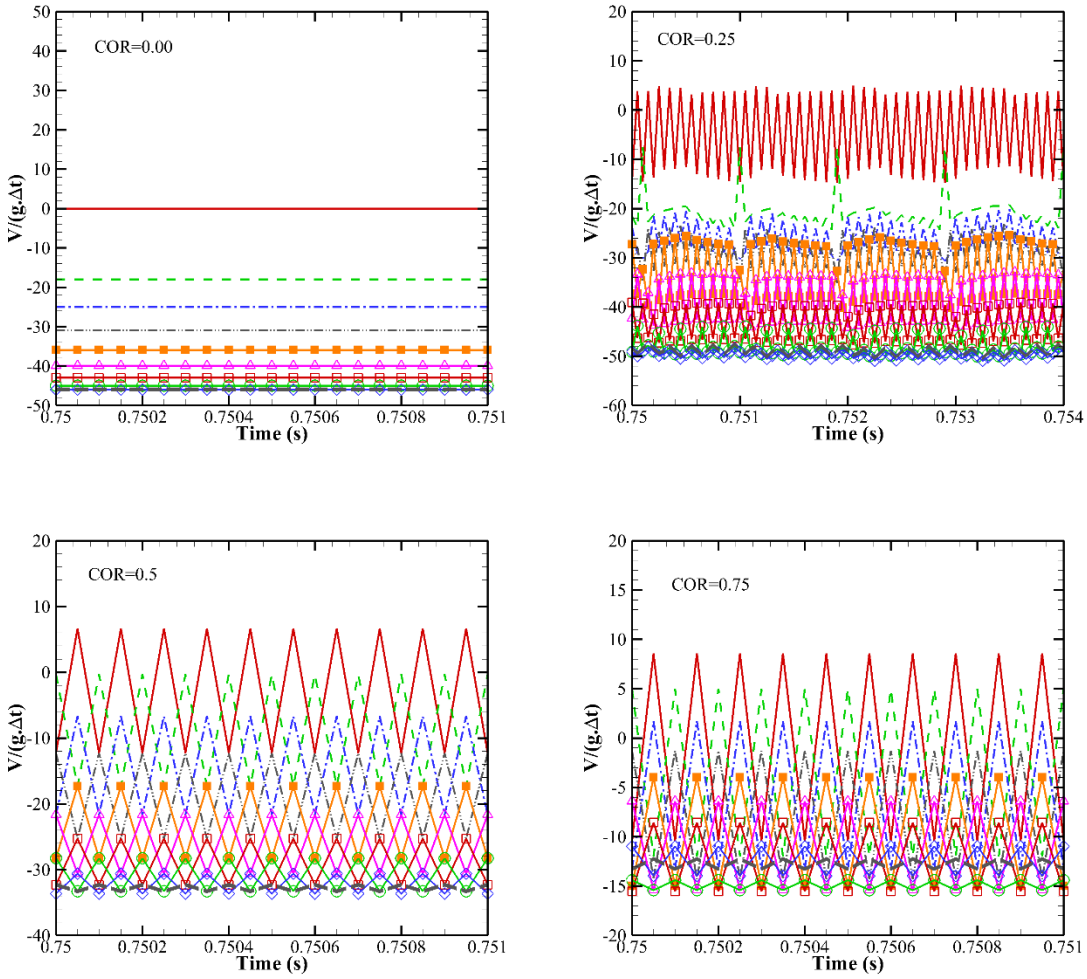

Figure 8. 6. Exaggerated view of the velocity fluctuations for selected cases.

For a fully plastic system (COR=0.0), it is noted that the bottommost particle which is in contact with the wall has a zero velocity. This is because the particle is in continuous impact with the wall which brings its velocity to the wall velocity (recall that particle-wall impacts are executed after calculating all inter-particle collisions). The particle just above the bottom particle (particle number 2) undergoes impacts with particle-1 which has a zero velocity but the final status of the system will be an averaged velocity that is greater than zero. In this dissipative system (COR=0.0) with more than one particle, the value of the velocity of the topmost particle can be approximated by $V_{max} \sim g\Delta t.(\sum n-(n-1))$, where n is the particle number. Intermediate particles will have intermediate values. As the system becomes less dissipative (e.g. COR=0.25), the bottom most

particle gains some inertia after its impact with the wall. Its velocity fluctuates and so does the velocity of all other particles. The induced velocities fluctuate in a repeated pattern and remain bounded and stable. With an even less dissipative system (i.e., COR=0.5), the same patterns are observed. The top most particles show lower fluctuations but with higher magnitudes of velocity. With a further increase in the elasticity of the particles, repeated patterns can still be seen (COR = 0.75-0.9) as the fluctuating particle velocities start approaching each other.

The position of the topmost particle (particle #10) is shown in Figure 8.7 for the different systems. The case with COR=1.0 was excluded since it showed a continuous increase in the particle elevation indicating an unstable system. The zero level indicates the initial location of the particle center which is located at 9.5 diameters above the wall. The deviation from the initial position is non-dimensionalized with respect to $g\Delta t^2$ ($2.45\text{x}10^{-10}$ m or $2\text{x}10^{-7}d_p$) and is indicative of the total overlap of the system. It can be seen that the amount of overlap increases with the increase in dissipation of the system. Although the non-dimensionalized change in position seems to be a large number it does not exceed 0.08% of the particle diameter at the largest overlap for COR=0. It can also be noted that the simulation with COR=0.98 results in an expansion of the particle stack which means that particles are on average separated from each other. The overlap in the system increases with the time step (Fig. 8.8). If the time step is not small enough, however, then the movement can manifest itself as macroscopic movement of the particle which is not desirable. The largest overlap (not shown) is found to be between the bottom-most two particles for a fully dissipative system. However, this observation does not hold for elastic systems. Thus it is challenging to construct a relation between the apparent stiffness of the particles and the time step. It should, however, be accepted that the time step is a measure of the overall apparent stiffness of the system in which decreasing the time step, decreases the overlap between particles. For instance Figure 8.8 presents the effect of changing the time step by two orders of magnitude on the velocity and position of the top most particle. While both the non-dimensional velocity and the normalized overlap of the top most particle are unaffected by the time step, the dimensional velocity and overlap are reduced by factors of Δt and Δt^2, respectively. Thus, the apparent stiffness of the particles can be expected to be inversely proportion to Δt^2.

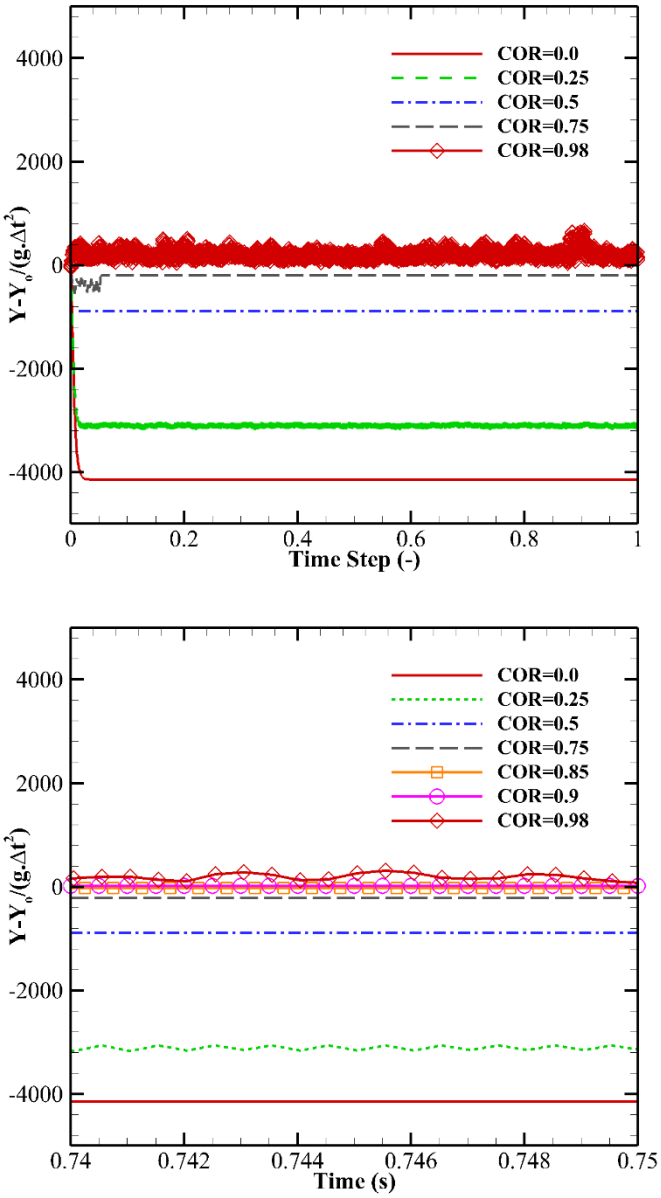

Figure 8. 7. Position of the topmost particles from the initial condition for different coefficients of restitutions (Exaggerated view on bottom figure).

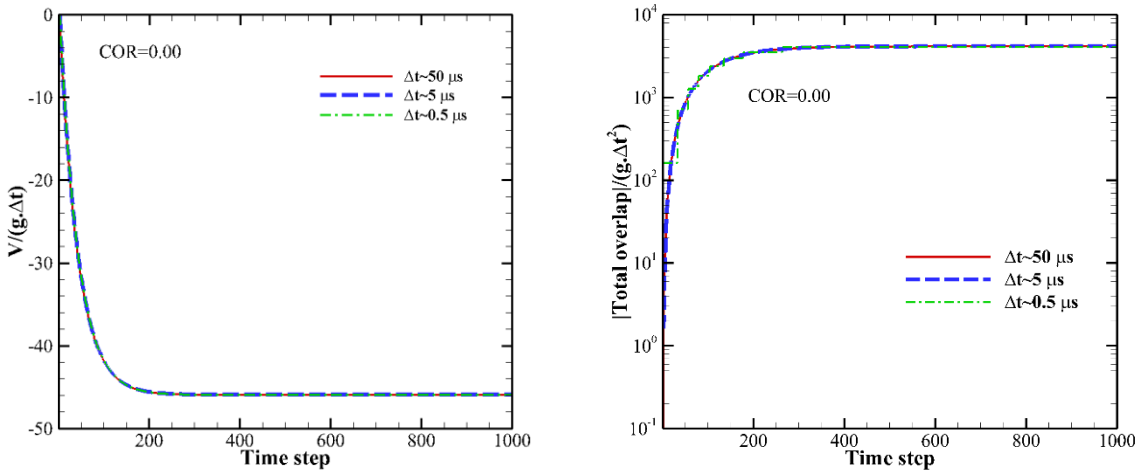

Figure 8. 8. Effect of time step on the velocity and position of the top most particle in a fully dissipative system a) non-dimensional velocity, b) total overlap of the particles stack.

8.3.5.2 Evaluation of Relocation Technique in Settling Bed of Particles

Here the relocation technique is evaluated in a more complex system where both normal and tangential collisions take place. For the current experiment and the fluidized bed experiment (next section) the system under consideration is the same. The material properties used in the simulations are provided in Table 8.1. The time step used to run both calculations is ~5μs. For the settling of particles, all the particles where initially distributed above the bottom wall by keeping a gap between individual particles (Figure 8.9). The particles are allowed to settle and the change of the center of gravity of the system is tracked. Figure 8.10 presents the temporal change in the center of gravity of the system when using the current relocation technique. The hard sphere results are compared to the soft-sphere impact model. It can be seen that the current formulation shows a stable location of the center of gravity of the static bed which is comparable to the soft-sphere model. This indicates that the relocation technique can effectively prevent large overlaps between the particles.

Table 8. 1. Simulation parameters used for 3D settlement of particles and fluidized bed simulations.

Particles properties	
Material	Poppy seeds
Diameter	1.2 mm
Density	1000 kg/m^3
Friction coeff.*	0.1
Restitution coeff.*	0.98
Stiffness coeff.*	800 N/m
Young's modulus	12.0 GPa
Poisson ratio	0.33
Yield stress	100 MPa
Surface energy	0.0124** J/m^2
Wall properties	
Density	2200 kg/m^3
Poisson ratio	0.17
Young's modulus	75.0 GPa
Yield stress	1100 MPa
Surface energy	0.055 J/m^2
Fluid properties (Air)	
Density	1.205 kg/m^3
viscosity	1.8×10^{-5} $kg.m^{-1}s^{-1}$

* values are the same for particle-wall and particle-particle

** value is estimated (not available in literature).

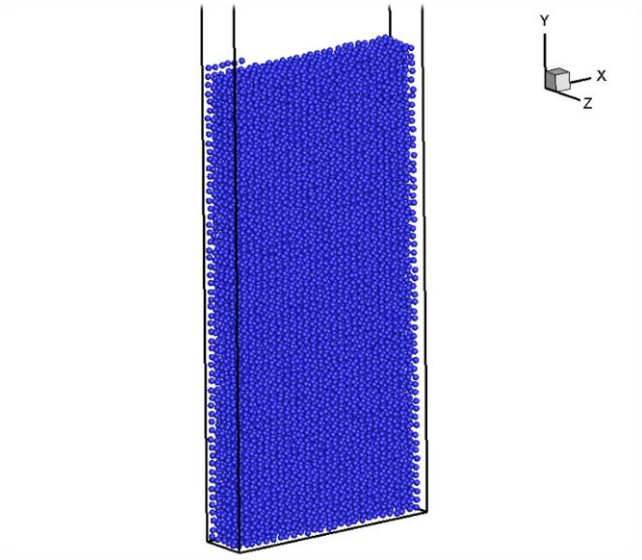

Figure 8. 9. Initial position of particles in 3D settling bed test.

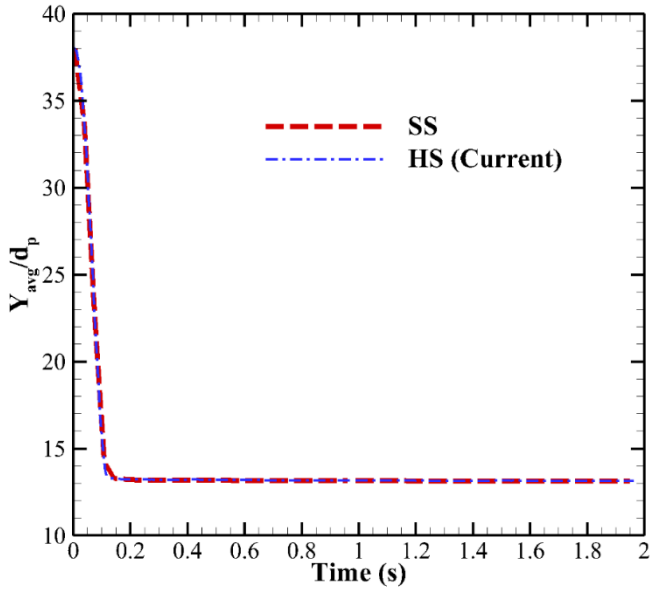

Figure 8. 10. Vertical location of center of gravity of a settling bed of particles

8.3.6 Bubbling fluidized bed

One case of Muller's experiments [6] was selected to validate the implementation and physics of the hard sphere model, validate the parallelization technique, and evaluate the performance and speed-up when using the current time advancement technique compared to the soft-sphere model. The case selected has a superficial velocity of 0.9 m/s which is three times the minimum fluidization velocity of the used beads. The simulated fluidized bed has a width, depth/transverse

thickness and height of 44 mm × 10 mm × 160 mm, respectively. All side walls were set to no slip boundary condition, the top boundary is set to an out flow boundary condition and the bottom boundary set to a permeable wall with velocity equal to the fluidization velocity. The simulation was conducted with 9240 particles on a grid which is 12×2×32 cells in the x, y and z directions, respectively. Details of the particle properties and modeling parameters are presented in Table 8.1. The spring stiffness is used with the soft sphere collision model, whereas the actual material properties of the poppy seeds and wall are used with the hard sphere model. All simulations were run for 10 seconds and the results were averaged for the last 5 seconds. Unless noted otherwise, the time step used for the simulations is ~ 5 μs. The hard sphere simulations are run with the physics based impact model and with a constant COR model and compared to simulations using the soft-sphere collision model with constant COR.

The time-averaged void fraction and solid velocities are provided in Figure 8.11 for the soft-sphere and hard-sphere collision models. The soft sphere model results (Fig 8.11a) are compared to the hard sphere results with a fixed COR=0.98 in Fig. 11b, with variable COR in Fig. 11c, and Fig 11d with a time step 25x larger than the soft sphere model. It can be seen that the four cases show good agreement with each other. Figure 8.11 also shows a comparison of the results for the hard sphere model when the time step is increased by a factor of 25 over the nominal time step of ~5 μs. Both the void fraction distribution and solid velocities are identical and do not show any visible differences. It is noted that it was not possible to run the soft-sphere impact model using such large time steps even if the stiffness was reduced to lower values. By allowing 25× larger time step to be used, the corresponding speed-up in computational time is ~23× using the physics based hard sphere model as compared to soft sphere collision model with k=800N/m.

A more critical comparison is presented in Figure 8.12 of the voidage profile compared to both measurements and simulations done by [6]. They used 2D calculations for the fluid field and a full slip boundary condition for the velocity at side walls. The voidage profiles are shown at two different levels above the distributor plate y=16.4 mm and y=31.2 mm. All DEM simulations performed in the current work and by ([6] show good comparison with measurements at a height of 16.4 mm. At a higher height of 31.2 mm, both simulations show some discrepancy with the experiments away from the bed center. CFD-DEM tends to over predict the void fraction closer to the walls. Fig. 8.13 presents a comparison of the average solid velocity between measurements,

Muller simulation, and current soft-sphere and hard-sphere simulations at three different levels above the distributor, 15, 25, and 35 mm. All the current simulation results show good agreement at the two levels of 15 and 25 mm but under-predicts the solids velocity at 35 mm above the distributor.

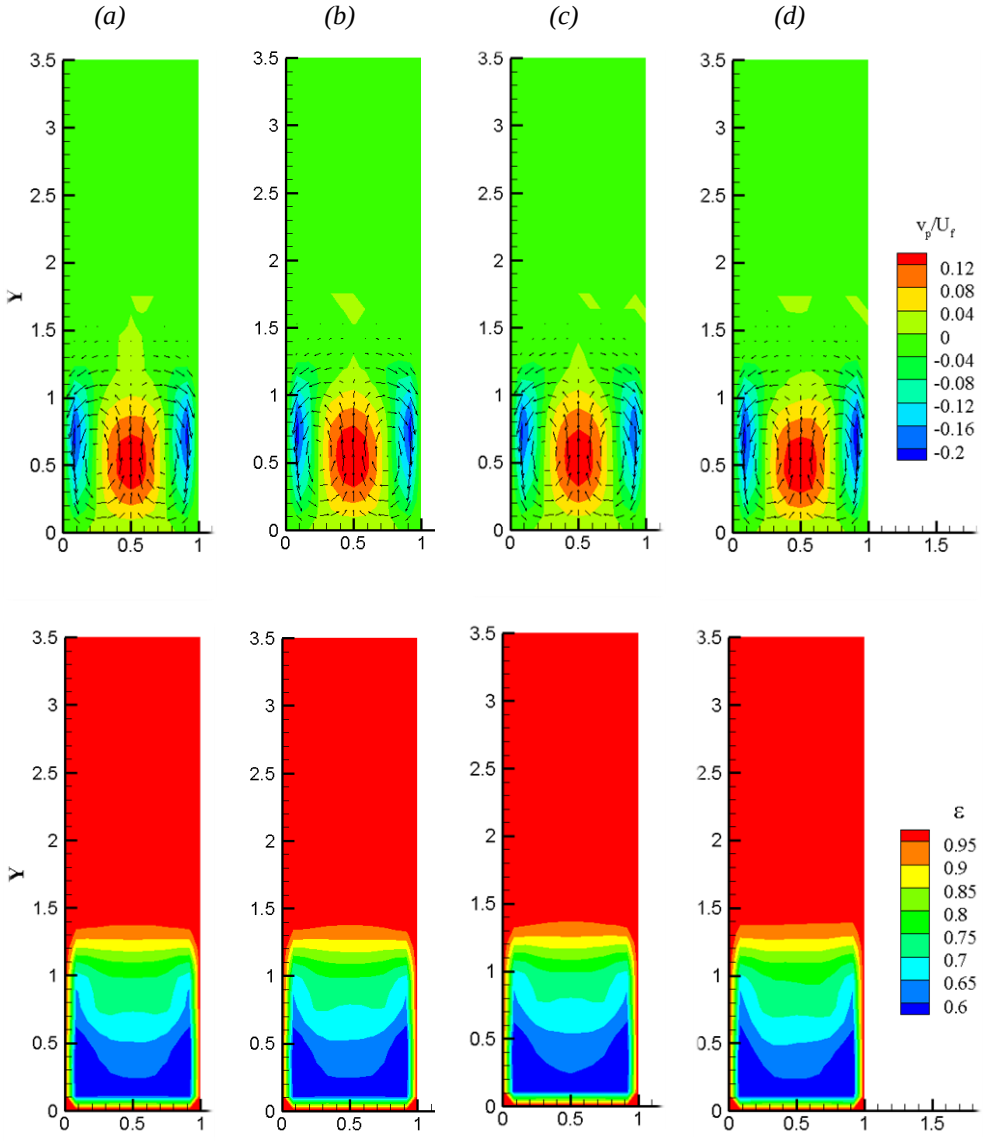

Figure 8. 11. Comparison between averaged void friction (top) and solids velocity (bottom) between *(a)* soft-sphere with COR=0.98 using Δt of ~5μs (b) hard sphere with COR=0.98 using Δt of ~5μs, (c) hard sphere with variable COR using Δt of ~5μs, and (d) hard sphere with variable COR using Δt of ~125μs

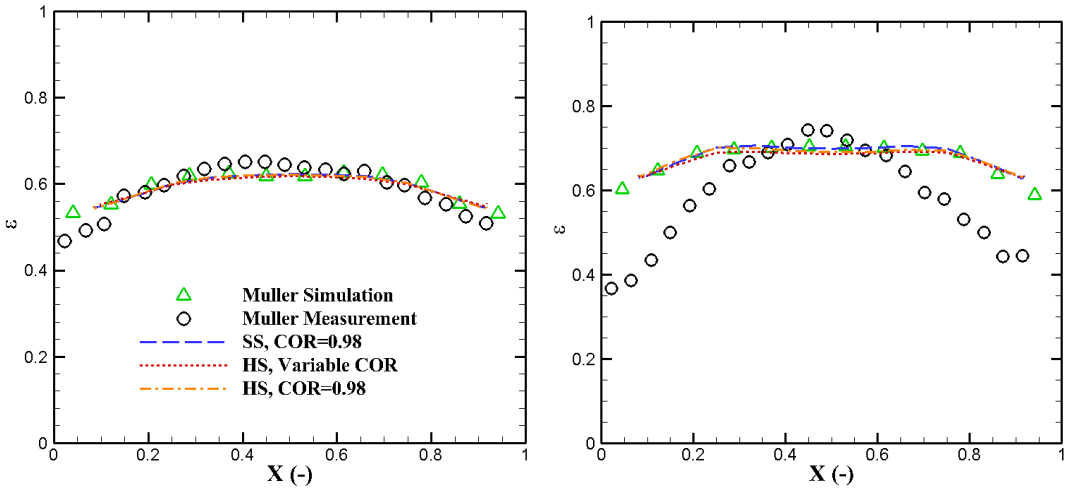

Figure 8. 12. Comparison between averaged void fraction (ε) at 16.4 mm (left) and 32.2 mm (right) above the distributor.

One advantage of the hard sphere model is the embedded physics which allows it to predict the COR based on impact velocities, angle of impact, and material properties. The variation of the coefficient of restitution with the impact speed of the physics based model as compared to the fixed COR value used in the soft sphere model is shown in Fig. 8.14 at different impact velocities for particle-wall normal impact. We assume that most impact velocities in the Muller experiments do not exceed ~0.3 m/s. Judging from the good comparison between the hard sphere model with variable COR and the soft sphere model with fixed COR, it is concluded that the current simulations are not sensitive to the mild changes in COR.

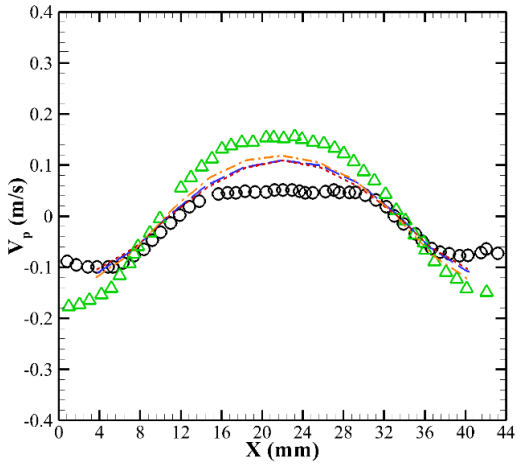

(a)

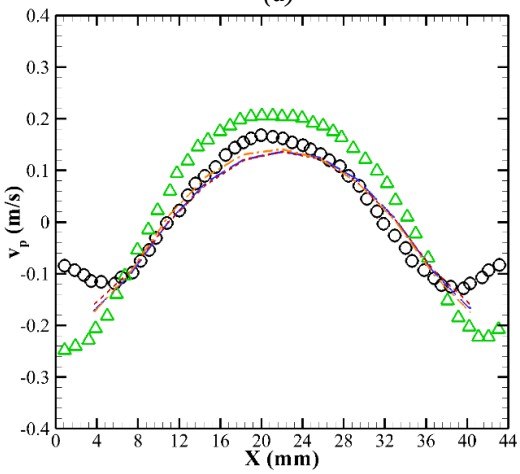

(b)

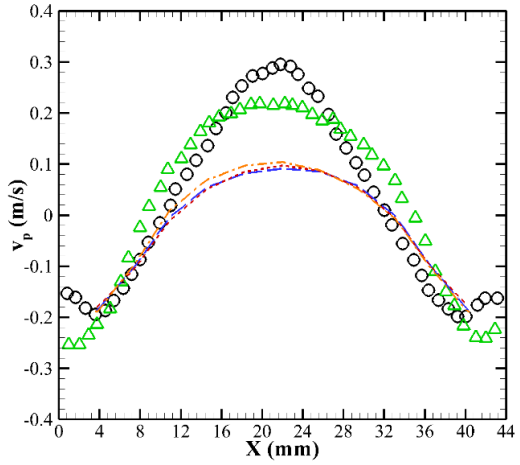

(c)

Figure 8. 13. Comparison of averaged solids velocity at a) 15 b), 25 and c) 35 mm above the distributor. Legends are the same as Figure 8.12.

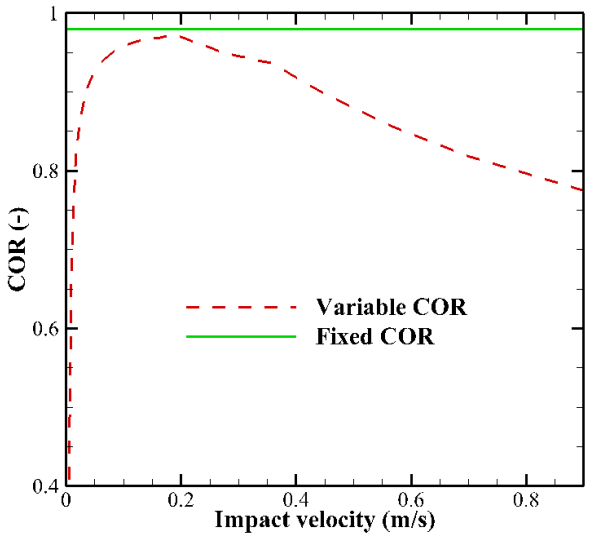

Figure 8. 14. Comparison of the variation of COR of particle-wall impact for the hard sphere and soft sphere simulations.

The last comparison is made to examine the consistency of the proposed parallelization procedure. In this experiment the simulation was run on two processors by decomposing the spatial domain in the x-direction. To increase the probability of any inconsistencies in the sequential treatment of collisions and the proposed treatment of collisions with ghost particles showing up, periodic boundary conditions are used in the depth of the bed (lateral or z-direction). In this scenario ghost particle lists have to be maintained not only at the x-boundary between processor 1 and 2, but also between the lateral boundaries on the same processor. A comparison of the time-averaged results between the hard sphere and soft sphere model is provided in Figure 8.15 validates the parallelization technique.

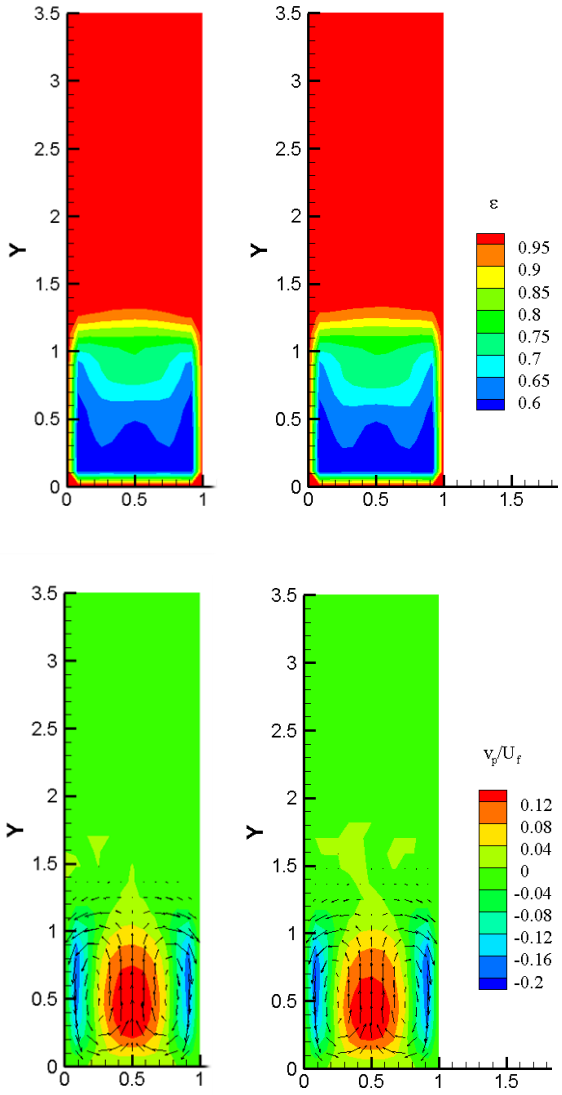

Figure 8. 15. Comparison between averaged void fraction (top) and solid velocity (bottom) of hard-sphere (left) and soft-sphere (right). Simulations are run on two processors with periodicity in the z-direction.

8.3.7 Transport and deposition of micron sized sand particles in a ribbed duct

This section showcases the advantage of the hard sphere model over the soft sphere model in systems where particles are in the micron size range and the soft sphere model becomes increasingly expensive because of the short time scales of collisions. For example, the physical collision time scale of a 10 micron sand particle is of O(10 ns). One such system which is showcased here is an internal cooling duct of a gas turbine blade. Because of the high gas temperatures (1700℃) the high pressure stage of the turbine experiences temperatures well above safe limits to maintain the structural integrity of the blades (800-900℃). Thus active cooling is

incorporated in blade designs where compressor bleed air (500℃) is circulated in internal passages (internal cooling) of the blade and then ejected out on the blade surface (film cooling) through tiny holes (200-300 micron) leading from the cooling channel to the blade surface, to cool the blade. The internal cooling passages are designed with various turbulence generation features such as ribs and pin fins to generate turbulence and enhance cooling.

When aircrafts operate in dusty environments such as during takeoff and landing in desert environments or flying through volcanic ash clouds, the engine ingests sand or ash, which through the compressor circuit finds its way into the internal cooling ducts of the blade. Once in the internal cooling ducts the fine sand particles can form deposits in regions of high temperatures and in flow recirculating regions - not only forming an insulating layer over the blade material but also blocking cooling holes leading to reduced durability of the blades and more frequent servicing.

Both experimental as well as numerical modeling investigations of sand erosion and deposition in gas turbine components has been the subject of much research [e.g., 214, 215], including the investigation of flow, heat transfer [216] and deposition [217-220] in internal cooling passages. In most numerical models (e.g., [217, 218]), only the early stages of deposition are studied, i.e., the effect of deposit formation on the subsequent flow, heat transfer and deposition is not investigated. The exclusion of post-deposition physics leads to considerable numerical simplification, namely, one-way-coupling where only the effect of the flow field on particle transport is considered assuming infrequent interaction between particles during transport, thus eliminating the need for the treatment of particle-particle collisions. In this framework, depositions or wall impacts need only be recorded to form a spatial map of deposition. Since no post-deposition physics is included, the accepted practice is to remove deposited particles from the calculation since they are of no further utility.

One of the important elements of enabling post-deposition physics is to allow particles to interact with each other and with the flow. This allows the formation of particle agglomerates and their removal by inertial eddies which is intrinsic to the overall physics of modeling the effect of deposits on the flow and heat transfer. Thus our primary objective in this section is to show that the hard sphere model is computationally more efficient in these situations than using the soft sphere model for particle-particle and particle-wall collision modeling.

The transport and deposition of fine sand in a representative periodic single pitch square ribbed duct (Fig. 8.16) at a bulk Reynolds number based on mean velocity and hydraulic diameter of 20,000 is studied. The ribbed duct has a rib pitch to rib height ratio of *P/e* =10 and rib height to channel height of *e/H* = 0.1 where *H* is the square duct cross-sectional dimension. A grid of 128×128×128 cells in the stream-wise, wall-normal, and span-wise directions is used with fine grids in the vicinity of all the duct walls and the rib. The calculations utilized 20 processors. A posterior evaluation of the mesh in the wall units based on local friction shows that the first mesh point $\Delta_{\perp}^{+} \ll 1.0$ over the majority of the ribbed duct and rib surfaces ($\Delta_{\perp max}^{+} \sim 3.0$). Large-Eddy Simulations (LES) with the dynamic Smagorinsky subgrid stress model is used for the fluid calculations. The detailed analysis of the turbulent flow and heat transfer are given in [221] and Sewall, Tafti [216] and validation with one-way coupling of particle transport in [222] and [223]. The flow is characterized by a large primary recirculation zone behind the rib that reattaches at a distance of 4.25e behind the rib. Figure 8.17 shows the mean flow field with streamlines. The primary recirculation zone is accompanied by a sympathetic eddy immediately behind the rib, another mean recirculation zone immediately upstream of the rib and a small separated region on top of the rib. Because of the presence of the rib strong secondary flows are set up in the vicinity of the rib [216] which manifest as high span velocities (~0.2 times the mean flow velocity) impinging on the side walls on top of the rib. The flow is highly turbulent the majority of which is produced in the separated shear layer from the rib. Streamwise turbulent rms fluctuations as high as $0.55u_b$ are shown in Figure 8.18 in the separated shear layer at the center plane of the duct (z=0.5) which gradually decays to about 35-40% midway between the ribs. Comparisons with LDV measurements [216] show good agreement with the predictions.

Two mono-sized particle sizes of 1μm and 20 μm are considered in the current study in a channel of 1.0 cm in height. The material properties used in the simulation are listed in Table 8.2. The simulation conditions are listed in Table 8.3 where the mass loading specifies the ratio of the mass flow rate of particles to the mass flow rate of the fluid. The particle response time in the last but one column is defined as ($\tau_p = \frac{\rho_p d_p^2}{18\mu}$) and the mean Stokes number in the last column is defined as ($St_p = \frac{\tau_p . u_b}{H}$) where u_b is the bulk flow velocity.

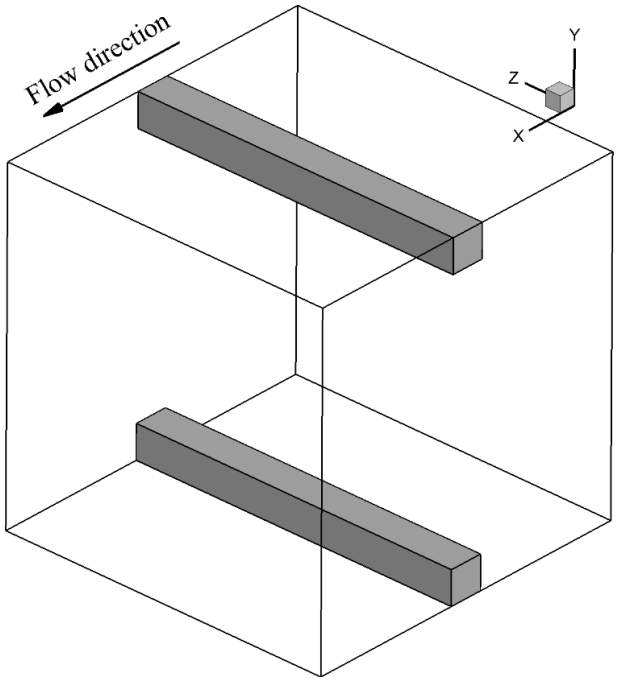

Figure 8. 16. Computational domain for periodic ribbed duct.

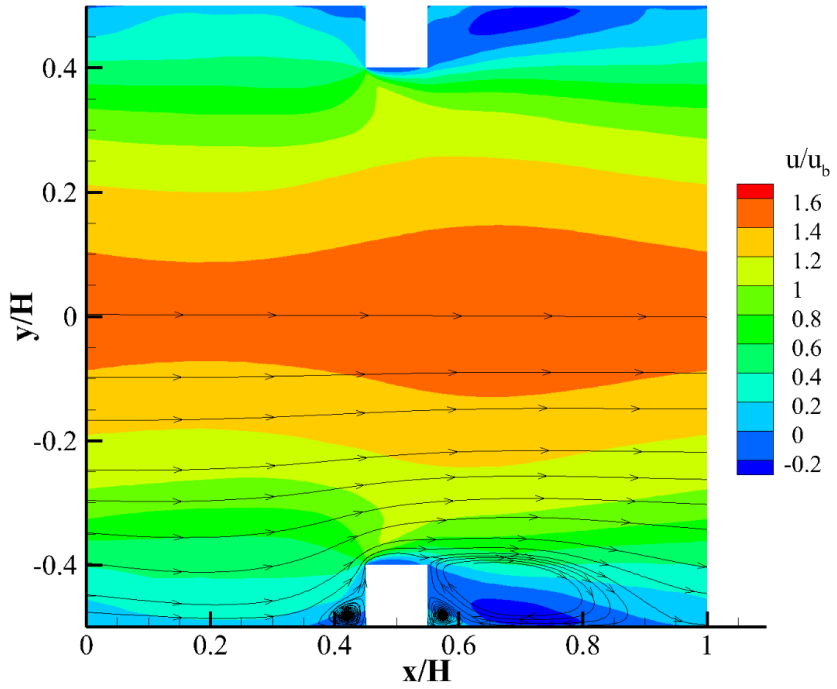

Figure 8. 17. Cross sectional view shows the averaged flow velocity in the domain.

Table 8. 2. Materials properties used in the simulations

Parameters	Density (kg/m^3)	Young's Modulus (GPa)	Yield Stress (MPa)	Poisson's Ratio	Surface energy (N/m)	Sliding friction	Dynamic viscosity (Pa.s)
Particles	2630	191	1057	0.162	0.61	0.1	–
Wall	7850	205	350	0.3	1.62	0.1	–
Fluid	3.67	–	–	–	–	–	4.153×10^{-5}

Table 8. 3. Simulation conditions for the periodic ribbed channel.

	d_p (μm)	Mass loading	Re_{bulk}	τ_p (s)	St_p
Run-1	1	6.36e-5	20,000	3.52×10^{-5}	0.004
Run-2	20	0.57	20,000	1.41×10^{-3}	1.55

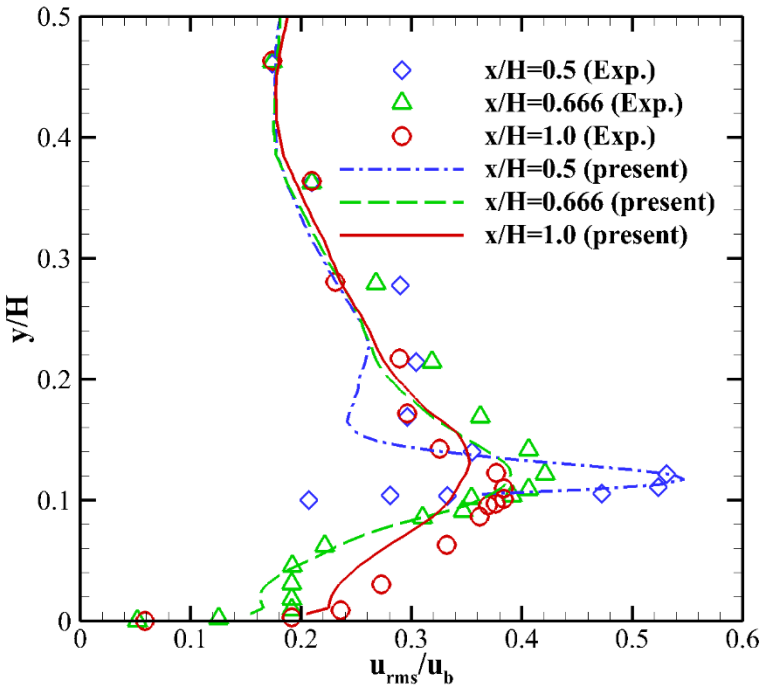

Figure 8. 18. Comparison between mean flow stream turbulent intensity at different locations with experimental data.

The flow was evolved for about 45 flow throughs to reach a stationary state before it was seeded instantaneously with the sand particles at the center of the channel, each particle assuming the local fluid velocity. All simulations were run for more than 100 flow throughs after the injection of particles (physical time after injection ~ 48 ms). Because of the requirements of a fine fluid grid in the vicinity of the ribs and the duct walls, particle dynamics is calculated on a coarser particle grid comprising of a number of fluid cells [18] to maintain a smooth variation of the void fraction in Eqs. (1-2).

Figure 8.20 shows instantaneous snapshots of the volumetric particle distribution in the core of the domain at 20, 60 and 100 fluid flow throughs after the injection of the particles. A plan view at the same times is provided in Figure 21 where only particles that are transported between the top of the rib and the wall are shown. The particles are colorized with respect to their velocity relative to the mean fluid velocity. It can be seen that the 20 μm particles reach the ribbed wall faster than the 1 μm particles. This can be a result of the greater particle-particle interactions that promote the dispersion of particles from their initial injection location in the center of the channel combined with their larger inertia. Most of the 20 μm particles accumulate upstream of the rib in close proximity to the ribbed wall. These particles exhibit both positive and negative velocities which supports the scenario that the particles hit the upstream rib face, bounce back and are redirected back to the rib, till they escape to the center of the channel. High concentration of 20 μm particles can also be seen near the side walls of the channel compared to the 1 μm particles. Figure 8.21 shows that the 20 μm particles are concentrated both immediately upstream and downstream of the rib junction with the side walls. Unlike the 20 μm particles, the 1 μm particles seem to be much more uniformly dispersed in the flow. This is a result of the small Stokes number which allows the particles to follow small instantaneous turbulent flow structures resulting is more uniform dispersion. Furthermore, the 1 μm particles are entrained into the primary recirculation zone behind the rib. As a result, the 20 μm particles are more prone to agglomeration and accumulation in regions of low flow velocity. Figure 8.22 shows the accumulation and agglomeration of 20 μm particles in the corners of the rib-wall junction. There is a steady increase in the size of the agglomerate with the passage of time. This suggests that continual transport of particles into these regions is more dominant over inertial removal of particles by turbulent eddies. Another factor which could play a major role is that as particles agglomerate, turbulent eddies get damped, which

progressively decreases the probability of inertial removal resulting in a non-linear agglomerate growth rate. On the other hand, very few 1 μm particle agglomerates form and even when they do form they are readily swept away by incident turbulent eddies. Table 8.4 summarizes the number of particle-particle and particle-wall impacts as a percentage of the total number of particles present in the calculation over 10 time steps or 1.5 μs; the 20 μm particles exhibit an order of magnitude more impacts with the walls of the duct. These results suggest that based purely on the physics of turbulent transport and particle-wall impact mechanics, larger particles are more susceptible to forming agglomerates and deposits than smaller particles.

To include particle transport and collision modelling in the calculation, the time-step had to be reduced by a factor of two, from 0.30 μs for the turbulent fluid flow alone to 0.15 μs using the hard sphere model. It was not possible to obtain a stable solution with the soft sphere model at this time step. It was found that the largest time step that could be used with the soft sphere model was an order of magnitude smaller than 0.15 μs. Attempts to lower the spring-stiffness to accommodate larger time steps resulted in lost particles at walls and it was not viable to reduce the stiffness below 800 N/m. Thus, the use of the hard sphere model enabled a solution which was about 10 times faster. Attempts at using sub-stepping (multiple particle time steps per fluid time step) with the soft sphere model were successful. By using 10 sub-steps for particle advancement with the soft sphere model, it was possible to use the soft sphere model and reducing the disparity with the hard sphere model to 5x slower (instead of 10x) for the full calculation (fluid+DEM). Just considering DEM, with 10 sub-steps in the SS model, the HS model was 23x faster. No attempts were made to use sub-stepping with the hard sphere model at a fluid time step of 0.3 μs.

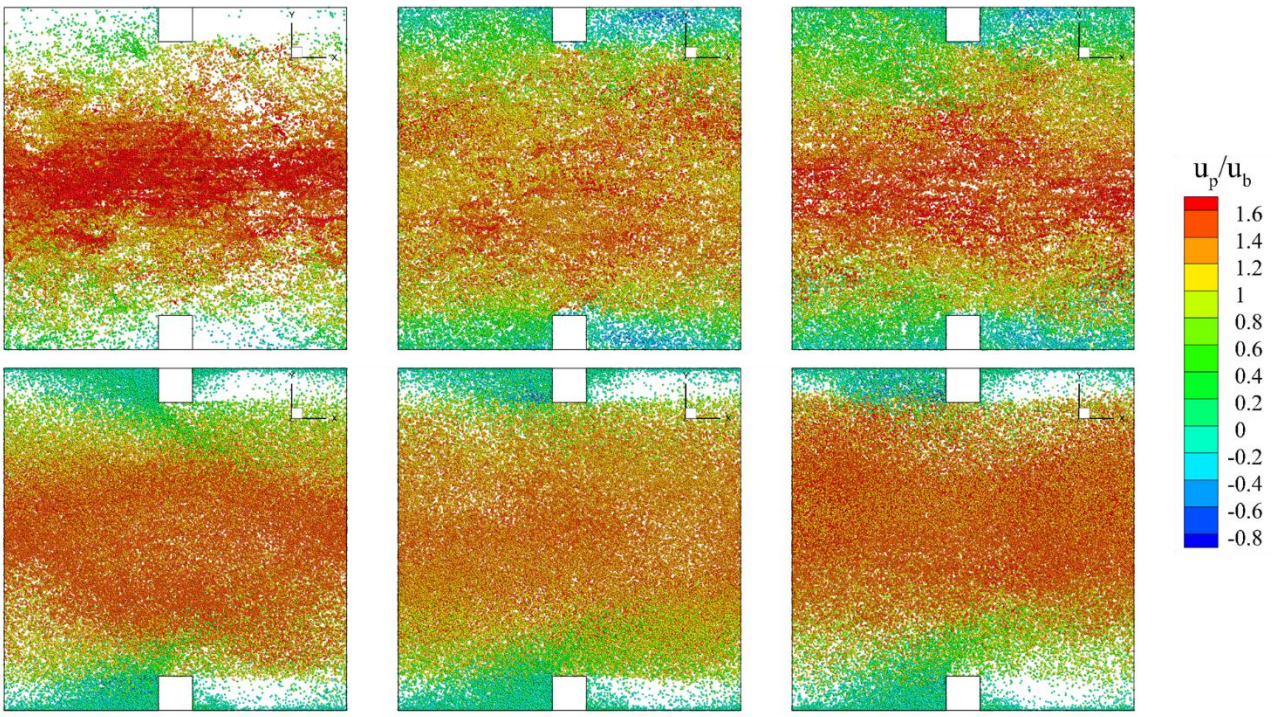

Figure 8. 19. Instantaneous particle location in the middle 50% of the duct at times 8.8 ms, 26.5 ms, and 44.1 ms (left to right) after the injection of the particles for 1 μm (top), and 20 μm (bottom).

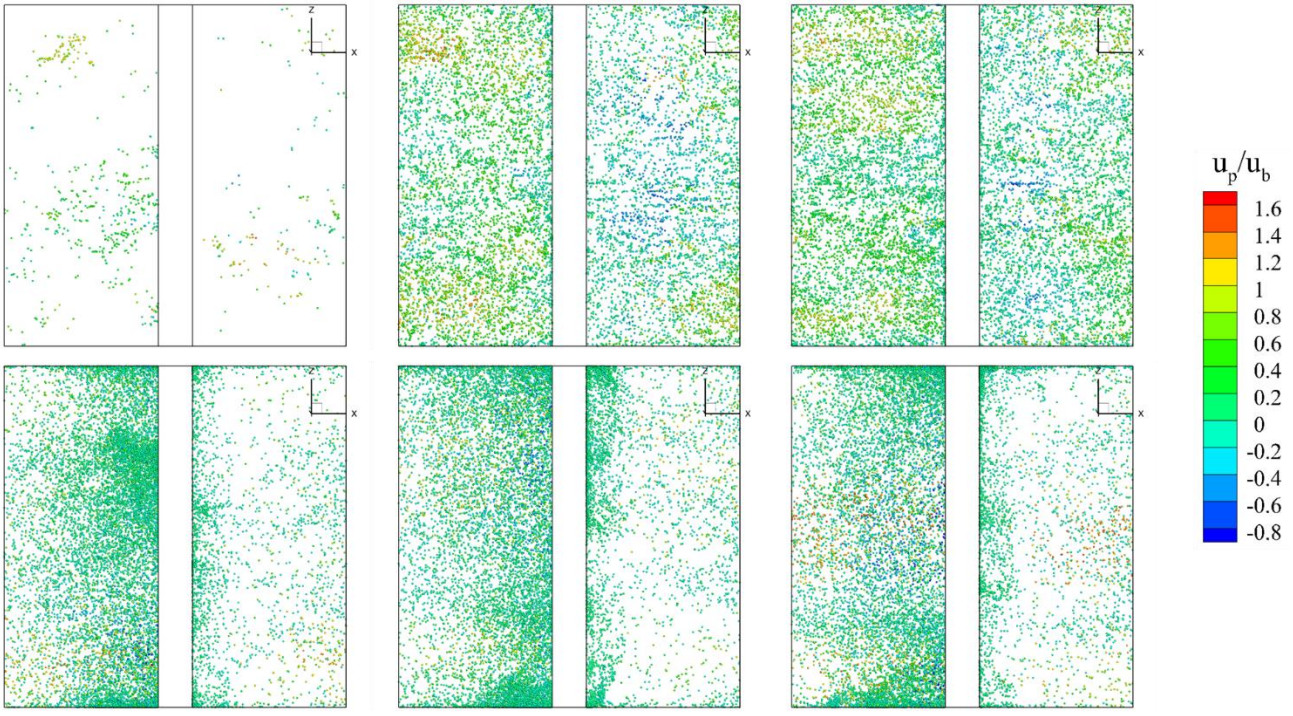

Figure 8. 20. Instantaneous plan view of the location of particles between rib height and wall at times 8.8 ms, 26.5 ms, and 44.1 ms (left to right) after the injection of the particles for 1 μm (top), and 20 μm (bottom).

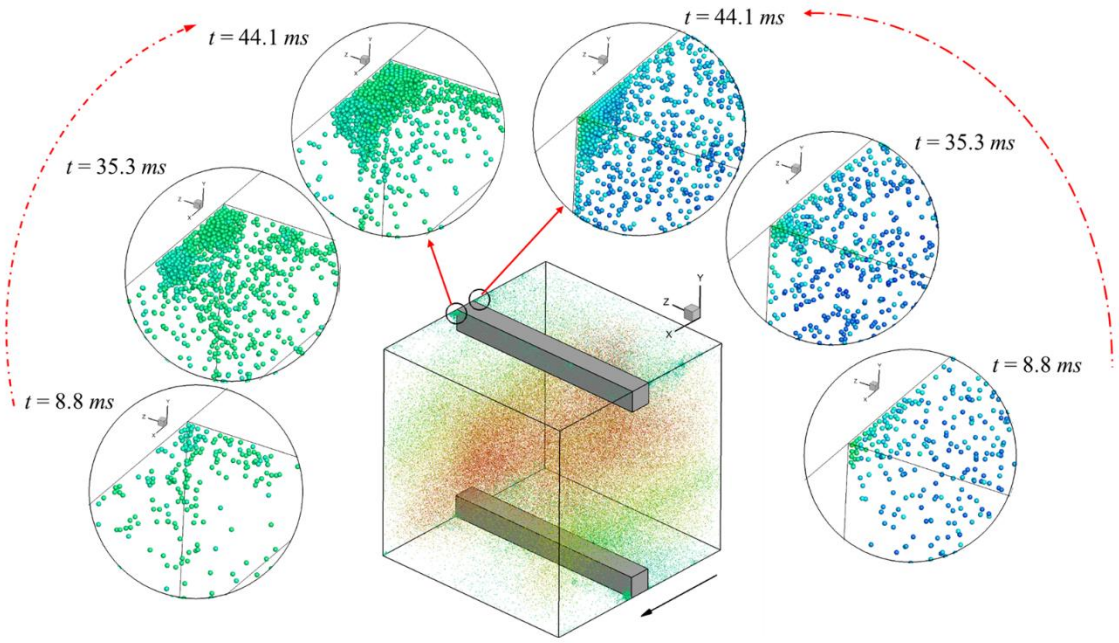

Figure 8. 21. Formation of particle agglomerates with exposure time for 20 μm particles.

Table 8. 4. Number of impacts per 10 time steps as percentage of total number of injected particles.

	Particle-wall	Particle-particle
Run-1	1.3%	0.02%
Run-2	13.9%	5.9%

Figure 8.22 plots the normal coefficient of restitutions calculated by the hard sphere model for 1 μm and 20 μm particles. All calculated normal CORs for the 1 μm particles are zero, indicating that for the 1 μm particles, the work needed to overcome adhesive forces between particle and surface is greater than the rebound energy in the particle. For the same reason, the majority of particle-wall collisions for the 20 μm particles result in a COR=0 whereas a small percentage of impacts have a finite COR. On closer examination of the impacts, the majority of impacts on the ribbed and side walls occur are at very shallow impact angles with a small normal component of velocity which does not provide enough energy for the particle to break free from the adhesive surface forces during rebound. For 20 μm particles, non-zero normal CORs are mostly calculated

at the rib face directly facing the flow, where the impact angle is near normal and the impact velocity is high. It is noteworthy that for the 1 μm particles, in spite of all impacts resulting in a zero normal coefficient of restitution, no substantial accumulation of particles is found. As explained earlier this is because 1 μm particles are much more amenable to inertial removal by turbulent eddies than the 20 μm particles. Another noteworthy observation is that unlike the soft sphere implementation in which the normal coefficient of restitution is a constant input variable to the model, the hard sphere model calculates a physical COR, which would be quite difficult to estimate *a-priori*.

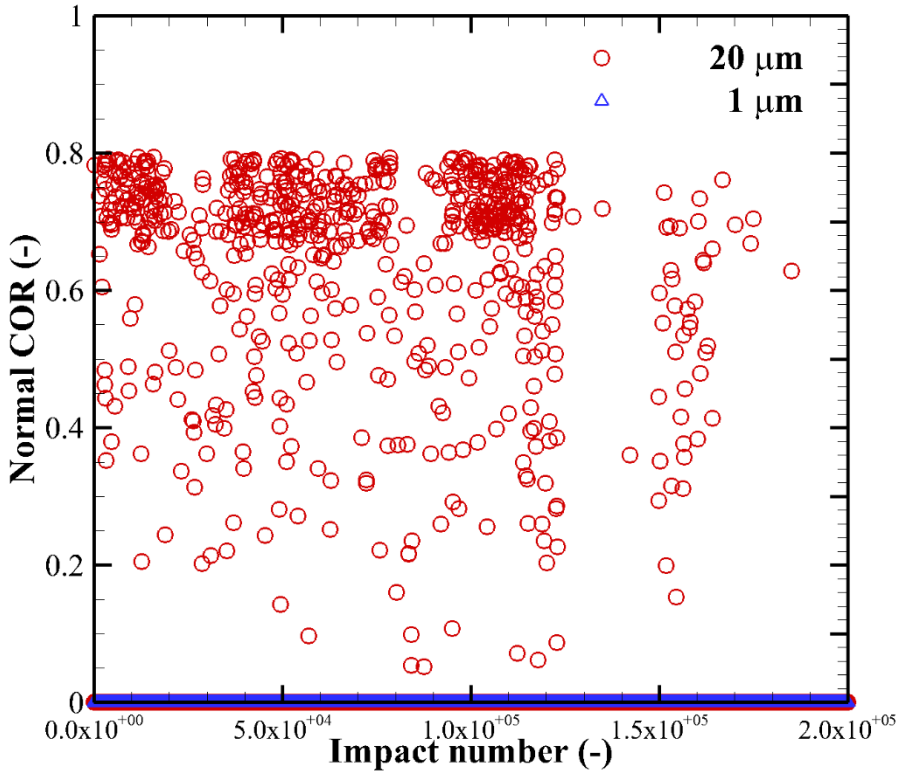

Figure 8. 22. Representative normal restitution coefficients of particle-wall impacts for 1 μm and 20 μm particles.

8.5 Summary and Conclusions

In the current work we present a comparison between a physics based hard sphere model with the soft sphere model. A physics-based hard sphere model is proposed using conventional time-advancement which is not event driven. The challenge of the hard sphere model only admitting sequential binary collisions in dense particle systems and its consequences on particle overlaps and overall stability is investigated. A particle relocation technique based on using both pre- and post-collision velocities is proposed. Also proposed is a parallelization scheme which bypasses the inherent sequential nature of processing collisions with the hard sphere model. The proposed technique is tested in a one-dimensional stack of particles and in the settling of a bed of particles. The proposed relocation technique demonstrates its ability to prevent excessive overlaps and maintaining stable stacks of particles at coefficients of restitutions ranging from 0.0 to 0.98. In a fully elastic system with COR of 1.0, the accumulation of numerical errors results in an increase in system energy and renders it unstable. The resulting system behavior for a three-dimensional bed of settling particles is in very good agreement with results obtained from the soft-sphere model. The model was then validated in a bubbling fluidized beds with no discernable differences in the predicted void fraction and solid velocities with the soft sphere model but at a computational cost about 23 times less than the soft sphere model. The proposed parallelization technique showed results consistent with a single processor calculation. Finally particle agglomeration was investigated in a turbulent ribbed duct flow using LES for particles of size 1 μm and 20 μm. It was found that the 20 μm particles were more prone to agglomerate in regions of low velocity at the upstream and downstream of the rib-wall junction. In this system also, the hard sphere model enabled time steps an order of magnitude larger than that permissible for the soft sphere model resulting in DEM speedups of more than 20×, and a corresponding CFD-DEM speed-up of ~5×.

In conclusion, it is shown that a physics based hard sphere model is a viable alternative to the soft sphere model in dense fluid-particulate systems at a lower computational cost.

Chapter 9

Summary and Conclusions

The main objective of the current work was to develop and validate alternative models that can be used to reduce the computational cost of CFD-DEM without significant loss of accuracy. These techniques targeted different aspects of CFD-DEM frame work such as implementation of force models, coupling between the two phases, coarse graining, contact mechanics, and time advancement for hard-sphere simulations. A summary with important findings and conclusions are highlighted below.

Blind Validation of CFD-DEM

Blind DEM-CFD predictions using the in-house code GenIDLEST are compared to experimental measurements of a small scale challenge problem set by NETL for validating multiphase flow codes. The experiment comprises a bubbling fluidized bed with Geldart group D particles at three superficial velocities. Comparisons of mean and rms of velocity and pressure along with third and fourth-order moments of velocity components are presented. In spite of quantitative differences between the measured and simulated values of mean and rms pressure, there is agreement in the changing trends as fluidization velocity increases. The mean vertical velocities are represented reasonably well by the simulations, whereas the simulated trends in the horizontal velocity are different than experiments. The rms velocities are predicted with reasonable accuracy. The simulated skewness and flatness indicate a close to Gaussian distribution for the vertical and horizontal velocities. This agrees reasonably well with the experiments at the center of the bed, but larger differences exist at the side walls. Where appropriate, the possible reasons for the discrepancies are discussed.

CFD-DEM clearly falls into the realm of complex multi-physics simulations, with drag models, methods used to transfer fluid-to-particle and particle-to-fluid quantities, size of fluid and particle grid [18] influencing the prediction accuracy. Considering all these challenges, GenIDLEST

performed reasonably well with good qualitative agreement but fair quantitative agreement with experiments.

Evaluation of Coarse Graining DEM using Representative Particle (RP) Model

Implementation of coarse graining using Representative Particle (RP) Model was validated and evaluated by comparison with unscaled simulations in two different applications. The RP model showed good/reasonable predictions as compared to unscaled simulations over wide operation regimes of the two different systems. For the sediment transport simulations, it was found that using the same particle grid for the unscaled and scaled simulations resulted in better predictions as compared to using a coarser particle grid proportional to the scaled particle diameter. It was found that the scaled sediment transport calculations performed well in the bed-load regime but did show some deviations in the suspended load regime. The fluidized bed simulation showed better agreement in both pressure drop and bed height, however, the averaged solids velocity was found to decrease with the increase in scaling factor.

Deviations in RP model prediction can be caused by the main assumption of lumping particles together where the particle mobility (e.g. granular temperature) is inherently reduced. Moreover, the RP model formulation does not consider the inter-parcel collisions when two parcels are interacting [4]. This source of deviation becomes significant in systems where energy dissipation determines the behavior of the system (e.g., fluidized beds). In addition to that there are differences associated with the response of a lumped particle to flow structures (for instances when a transient flow structure is capable of entraining a number of particles less than the particles actually lumped in the model). The feedback from such deviations to the coupled carrier fluid can add to the deviation in predictions.

The DEM speed-up from using RP model is proportional to the scaling factor. For a scaling factor of 2 the fully-3D DEM simulation speeds up with more than eight times since in addition to the number of simulated particles being reduced by 8, the number of collisions are reduced along with communication between processors. The overall speed-up however, is affected by the carrier fluid simulation time which is not scaled by the RP model. As such the overall speed-up depends on the percentage of DEM time to the overall time. The later can be affected by both the ratio of the number of computational cells to the number particles in the simulation and to the convergence

behavior. A scaling factor of 2 was used in the current work in which 8 original particles are lumped in a single representative particle. The speed-up in DEM alone is >8 in all cases (since collisions are less and there is an additional saving in the communication and other particle-calculations). The overall saving depends on the percentage of time taken by the DEM calculation to the fluid calculation. For instance if DEM constitutes 50% of the simulation, then eliminating DEM altogether may only result of a speed-up of 2x. In the current work the maximum speed-up of DEM was ~14-16x with a corresponding CFD-DEM speed-up of ~5-6x achieved when DEM constitutes more than 90% of the overall simulation time in the framework of MPI parallelization.

Development and Validation of Reduced History Force Model

A new modeling approach for history force was proposed. The new model saved both CPU time and memory resources. The model showed very good agreement with settling particle simulations for a wide range of Reynolds number ranging from ~1 to ~ 260. Some deviation was noticed at smaller Reynolds numbers ~1, which can be attributed to the rapid change in acceleration in a short time which may not be consistent with the assumptions made in deriving the proposed formulation.

The model also showed good agreement when compared to available experimental data of oscillating spheres at different frequencies and amplitudes, and spheres rebounding from a wall over a wide range of Reynolds numbers and density ratios. The current model efficiently calculated the history force in terms of both memory resources and calculation time. The memory resources were reduced to saving only 5 parameters per particle for the whole simulation compared to 3n per particle when using the full force calculation method using the Basset kernel and few hundreds per particle when using the window model [29]. The large savings in memory resource and computational time makes this formulation a good candidate for use in application where large number of particles are simulated for long times. Although validating the performance of the model in a complex flow-field was not tested, the validation of the model in basic modes of motion, however, indicated that it could produce quantitative/qualitative agreement in a combination of these modes. The model was developed and validated assuming/using a constant time step. The applicability of the model was limited to cases where Basset or Mei and Adrain kernel are applicable (e.g. Mei and Adrian kernel may not be applicable if the particle is ingested into its own wake). The model deviated from experiments when large variations in acceleration took place

within the memory time period. These deviations were noted as discontinuities for settling spheres with small Stokes numbers (~0.1).

LES-DEM Simulations of Sediment Transport

Computational Fluid Dynamics (CFD) was coupled with the Discrete Element Method (DEM) to simulate sediment transport in a turbulent open channel flow. Combining the DEM with LES poses contradictory requirements of a fine fluid grid to resolve small scale turbulent structures versus DEM requirements of a grid larger than the particle size for proper volume averaging to avoid near-discrete jumps in the void fraction field. To bypass this challenge, past work has used reduced or partial coupling between the continuous and dispersed phases. In the current work, a dual-grid formulation was used to allow for full four-way coupling. The differences between simulation results using partial and full coupling methods are given.

The predicted sediment transport rate was in good agreement with empirical bed load formula and showed a correct dependency in the suspended-load regime. Transport rates predicted by using partial coupling showed good agreement with full-coupling in the bedload regime, but under-predicted transport in the suspended load regime. The friction factor was found to increase in the bedload regime reaching a maximum when the friction velocity equaled the settling velocity, and then decrease in the suspended-load regime. The maximum resistance to flow, thus, took place in the transition from the bedload to the suspended load regime. This is because of the competition between the increase in the energy extracted by the stationary sediment particles and the decrease in energy extracted by the suspended particles with the increase in flow energy.

A sensitivity analysis of collision parameters on the numerical simulations of sediment transport using CFD-DEM framework was conducted. The sensitivity to friction factor, restitution coefficient and particle stiffness was examined for sediment transport cases in different flow regimes. It was found that the simulation results were sensitive to changes in friction factor in suspended load regime but showed lesser sensitivity in the bed-load regime when moderate changes in friction factor were considered. The increase in coefficient of restitution from the base value of 0.01 to 1.0, resulted in an increase in the particle flux and the flowrate. This is brought about by less dissipation of energy during collisions and a subsequent increase in the mobility of particles, which extract less energy from the fluid. Results from using restitution coefficient of 0.6

were, however, comparable to those from the reference calculation with a coefficient of restitution of 0.01. A change of the particle stiffness by two-orders of magnitude, showed insignificant impact on both particle transport and flow rate. Between the three parameters varied in the sensitivity analysis, the friction factor had the largest effect on the simulation results.

Revised Partial Coupling for Dense Fluid-Particulate Systems

A revised partial coupling formulation was proposed for use with dense particulate flow systems. The revised coupling assumes a void fraction of unity in the solution of fluid momentum equations but modifies the relative velocity used in point force models to compensate for this omission. Omitting the spatio-temporal variation of void fraction in the momentum equations resulted in much faster convergence and enhanced the numerical stability. This resulted in faster solution times. Including a modified interstitial relative velocity in point force calculations on the other hand compensated for the lower fluid velocities calculated by the momentum equations. Without this correction, it was found that particle mobility was underpredicted when using partial coupling. The efficacy of the revised partial coupling is demonstrated in two different fluid-particle systems consisting of a bubbling fluidized bed and turbulent sediment transport. In both systems, it is shown that the proposed method showed much better comparison to the fully-coupled approach. In the fluidized bed experiment, without the proposed modification, the bed did not fluidize in spite of a fluidization velocity which was three times the minimum fluidization velocity. In turbulent sediment transport, the improvement in predictions were more subtle. In the bed-load regime in which particles are not very mobile, the improvements were slight, but as the flow became more energetic entraining more particles into suspension, the proposed modification progressively showed more improvement over the base partial coupling.

Using the partial coupling, the fluid solution time was found to be reduced by factors ranging from 1.35 to 4.35. The reduction in the fluid solution was more significant for simulations that were difficult to converge and those in which the fluid calculation took a considerable percentage of the overall simulation time. Fully-coupled simulations that exhibit difficult convergence behavior or those which diverge due to numerical instabilities can benefit the most from using this technique.

Alternate Tangential Impact Treatment for the Soft-Sphere Collision Model

The current work evaluates existing models (Models A and B) and develops alternative methods (Models AA, C and D) for modeling tangential impacts with the soft-sphere collision model. The models were tested for a single particle in oblique impact with a surface and a single particle sliding on a surface. Inconsistencies in the existing model implementations are first demonstrated which result in loss of accuracy and incorrect results. It is shown that neither of the models, A nor B give consistent results for both test cases. Model AA was formulated by putting a limit on the allowable tangential displacement to give consistent results in both test cases. Although limiting the tangential displacement was suggested more than a couple of decades ago, only Model-A type implementation benefits from it (this is equally applicable to non-linear soft-sphere models).

Models C and D are specifically developed to eliminate the need to store the tangential deformation for each pairwise collision. The motivation was to save on memory usage for DEM simulations with a large number of polydisperse particles in which a large particle could potentially collide with many small particles. Model C, which calculated the instantaneous displacement as the product of the collision time scale with instantaneous tangential velocity, was easy to implement, however it only recovered the rigid body limit at low impact angles. The second surrogate model attempted to demonstrate the ability of capturing the physics at low impact angles by using the effective instantaneous impact angle with the aid of material properties of the interacting particles or surfaces. Both Models C and D compared well with experiments. In most cases the quality of predictions was as good or better than existing models A and B in the literature.

Comparison of a Physics Based Hard-sphere Model with the Soft Sphere Model

A comparison between a physics based hard sphere model with the soft sphere model was presented. A physics-based hard sphere model was proposed using conventional time-advancement which was not event driven. The challenge of the hard sphere model only admitting sequential binary collisions in dense particle systems and its consequences on particle overlaps and overall stability was investigated. A particle relocation technique based on using both pre- and post-collision velocities was proposed. Also proposed was a parallelization scheme which bypassed the inherent sequential nature of processing collisions with the hard sphere model. The proposed technique was tested in a one-dimensional stack of particles and in the settling of a bed

of particles. The proposed relocation technique demonstrated its ability to prevent excessive overlaps and maintaining stable stacks of particles at coefficients of restitutions ranging from 0.0 to 0.98. In a fully elastic system with COR of 1.0, the accumulation of numerical errors resulted in an increase in system energy and rendered it unstable. The resulting system behavior for a three-dimensional bed of settling particles was in very good agreement with results obtained from the soft-sphere model. The model was then validated in a bubbling fluidized beds with no discernable differences in the predicted void fraction and solid velocities with the soft sphere model but at a computational cost about 23 times less than the soft sphere model. The proposed parallelization technique showed results consistent with a single processor calculation. Finally, particle agglomeration was investigated in a turbulent ribbed duct flow using LES for particles of size 1 μm and 20 μm. It was found that the 20 μm particles were more prone to agglomerate in regions of low velocity at the upstream and downstream of the rib-wall junction. In this system also, the hard sphere model enabled time steps an order of magnitude larger than that permissible for the soft sphere model resulting in DEM speedups of more than 20 times. In conclusion, it was shown that a physics based hard sphere model was a viable alternative to the soft sphere model in dense fluid-particulate systems at a much lower computational cost.

References

1. Gopalan, B. *Small Scale Challenge Problem*. in *Workshop on Multiphase Flow Science*. 2013.
2. Maw, N., J. Barber, and J. Fawcett, *The oblique impact of elastic spheres.* Wear, 1976. **38**(1): p. 101-114.
3. Boyce, C.M., et al., *Adapting Data Processing To Compare Model and Experiment Accurately: A Discrete Element Model and Magnetic Resonance Measurements of a 3D Cylindrical Fluidized Bed.* Industrial & Engineering Chemistry Research, 2013. **52**(50): p. 18085-18094.
4. Benyahia, S. and J.E. Galvin, *Estimation of Numerical Errors Related to Some Basic Assumptions in Discrete Particle Methods.* Industrial & Engineering Chemistry Research, 2010. **49**(21): p. 10588-10605.
5. Mokhtar, M.A., et al., *Validation of the similar particle assembly (SPA) model for the fluidization of Geldart's group A and D particles.* AIChE Journal, 2012. **58**(1): p. 87-98.
6. Müller, C.R., et al., *Validation of a discrete element model using magnetic resonance measurements.* Particuology, 2009. **7**(4): p. 297-306.
7. Link, J.M., et al., *Flow regimes in a spout–fluid bed: A combined experimental and simulation study.* Chemical Engineering Science, 2005. **60**(13): p. 3425-3442.
8. Shaffer, F., et al., *High speed imaging of particle flow fields in CFB risers.* Powder Technology, 2013. **242**(0): p. 86-99.
9. Mudde, R.F., *Time-resolved X-ray tomography of a fluidized bed.* Powder Technology, 2010. **199**(1): p. 55-59.
10. Shadle, L., et al., *Model Validation Challenges: Next Steps,* in *NETL 2011 Workshop on Multiphase Flow Science*. August 16-18, 2011: Airport Marriott Station Square, Pittsburgh, PA.
11. Laguerie, C., Large, J.F, in *Fluidization VIII Workshop*. May 14-19, 1995: Tours, France.
12. Kwauk, M., Li, J., Yang, W-C. in *Fluidization X Workshop*. May 20-25, 2001. Beijing, People Republic of China.
13. Li, T., J.-F. Dietiker, and M. Shahnam, *MFIX simulation of NETL/PSRI challenge problem of circulating fluidized bed.* Chemical Engineering Science, 2012. **84**(0): p. 746-760.
14. Shadle L., e.a. *Challenge Problem III*. in *CFB X Workshop*. May, 3, 2011. Sun Rivere, Oregon.
15. Ozarkar, S., Sanyal, J., Liu, F., Srinivasa, M. *Comparison of Three Numerical Approaches for Modeling Poly-Disperse Dense Particulate Flows*. in *NETL 2011 Workshop on Multiphase Flow Science*. August 16-18, 2011.
16. Gopalan, B. *Small Scale Challenge Problem*. in *Workshop on Multiphase Flow Science*. Aug 6-7, 2013. Morgantown, WV.
17. Tafti, D.K. *GenIDLEST – a scalable parallel computational tool for simulating complex turbulent flows*. in *Proceedings of the ASME Fluids Engineering Division*. 2001. New York, NY 10016-5990, United States.
18. Deb, S. and D.K. Tafti, *A novel two-grid formulation for fluid–particle systems using the discrete element method.* Powder Technology, 2013. **246**(0): p. 601-616.
19. Amritkar, A., S. Deb, and D. Tafti, *Efficient parallel CFD-DEM simulations using OpenMP*. Journal of Computational Physics, 2014. **256**(0): p. 501-519.

20. Anderson, T.B. and R. Jackson, *Fluid mechanical description of fluidized beds. Equations of motion.* Industrial & Engineering Chemistry Fundamentals, 1967. **6**(4): p. 527-539.
21. Lu, H., et al., *Size segregation of binary mixture of solids in bubbling fluidized beds.* Powder Technology, 2003. **134**(1–2): p. 86-97.
22. Tsuji, Y., T. Kawaguchi, and T. Tanaka, *Discrete particle simulation of two-dimensional fluidized bed.* Powder Technology, 1993. **77**(1): p. 79-87.
23. Cundall, P.A. and O.D. Strack, *A discrete numerical model for granular assemblies.* geotechnique, 1979. **29**(1): p. 47-65.
24. Saxena, S.C. and V.L. Ganzha, *Heat transfer to immersed surfaces in gas-fluidized beds of large particles and powder characterization.* Powder Technology, 1984. **39**(2): p. 199-208.
25. Bi, H.T., et al., *A state-of-the-art review of gas–solid turbulent fluidization.* Chemical Engineering Science, 2000. **55**(21): p. 4789-4825.
26. Germano, M., et al., *A dynamic subgrid-scale eddy viscosity model.* Physics of Fluids A: Fluid Dynamics, 1991. **3**(7): p. 1760-1765.
27. Gopalan, B. and F. Shaffer, *A new method for decomposition of high speed particle image velocimetry data.* Powder Technology, 2012. **220**(0): p. 164-171.
28. *Private communications with Dr. Gopalan.* January 31, 2014.
29. Dorgan, A. and E. Loth, *Efficient calculation of the history force at finite Reynolds numbers.* International journal of multiphase flow, 2007. **33**(8): p. 833-848.
30. González, A., F. Bombardelli, and Y. Niño. *Improving the prediction capability of numerical models for particle motion in water bodies*. in *Proceedings of the 7th Int. Conf on Hydroscience and Engineering*. 2006.
31. Bombardelli, F.A., A.E. González, and Y.I. Niño, *Computation of the particle Basset force with a fractional-derivative approach.* Journal of Hydraulic Engineering, 2008. **134**(10): p. 1513-1520.
32. Niño, Y. and M. García, *Using Lagrangian particle saltation observations for bedload sediment transport modelling.* Hydrological Processes, 1998. **12**(8): p. 1197-1218.
33. Niño, Y. and M. García, *Gravel saltation: 2. Modeling.* Water resources research, 1994. **30**(6): p. 1915-1924.
34. Lukerchenko, N. *Basset history force for the bed load sediment transport*. in *First IAHR European Division Congress Edinburgh FMIId*. 2010.
35. Bialik, R.J., *Particle–particle collision in Lagrangian modelling of saltating grains.* Journal of Hydraulic Research, 2011. **49**(1): p. 23-31.
36. Bialik, R., V. Nikora, and P. Rowiński, *3D Lagrangian modelling of saltating particles diffusion in turbulent water flow.* Acta Geophysica, 2012. **60**(6): p. 1639-1660.
37. Bialik, R.J. and W. Czernuszenko, *On the numerical analysis of bed-load transport of saltating grains.* International Journal of Sediment Research, 2013. **28**(3): p. 413-420.
38. Schmeeckle, M.W. and J.M. Nelson, *Direct numerical simulation of bedload transport using a local, dynamic boundary condition.* Sedimentology, 2003. **50**(2): p. 279-301.
39. Kholpanov, L. and R. Ibyatov, *Mathematical modeling of the dispersed phase dynamics.* Theoretical Foundations of Chemical Engineering, 2005. **39**(2): p. 190-199.
40. Lee, H.-Y., et al., *On three-dimensional continuous saltating process of sediment particles near the channel bed.* Journal of Hydraulic Research, 2006. **44**(3): p. 374-389.
41. Schmeeckle, M.W., *Numerical simulation of turbulence and sediment transport of medium sand.* Journal of Geophysical Research: Earth Surface, 2014. **119**(6): p. 1240-1262.

42. Mordant, N. and J.-F. Pinton, *Velocity measurement of a settling sphere.* The European Physical Journal B-Condensed Matter and Complex Systems, 2000. **18**(2): p. 343-352.
43. Armenio, V. and V. Fiorotto, *The importance of the forces acting on particles in turbulent flows.* Physics of Fluids (1994-present), 2001. **13**(8): p. 2437-2440.
44. Michaelides, E.E., *A novel way of computing the Basset term in unsteady multiphase flow computations.* Physics of Fluids A: Fluid Dynamics (1989-1993), 1992. **4**(7): p. 1579-1582.
45. Tatom, F., *The Basset term as a semiderivative.* Applied Scientific Research, 1988. **45**(3): p. 283-285.
46. Van Hinsberg, M., J. ten Thije Boonkkamp, and H. Clercx, *An efficient, second order method for the approximation of the Basset history force.* Journal of Computational Physics, 2011. **230**(4): p. 1465-1478.
47. Maxey, M.R. and J.J. Riley, *Equation of motion for a small rigid sphere in a nonuniform flow.* Physics of Fluids (1958-1988), 1983. **26**(4): p. 883-889.
48. Lamb, H., *Hydrodynamics Dover.* New York, 1945. **43**.
49. Rivero, M., J. Magnaudet, and J. Fabre, *Quelques résultats nouveaux concernant les forces exercées sur une inclusion sphérique par un écoulement accéléré.* Comptes rendus de l'Académie des sciences. Série 2, Mécanique, Physique, Chimie, Sciences de l'univers, Sciences de la Terre, 1991. **312**(13): p. 1499-1506.
50. Mei, R., C.J. Lawrence, and R.J. Adrian, *Unsteady drag on a sphere at finite Reynolds number with small fluctuations in the free-stream velocity.* Journal of Fluid Mechanics, 1991. **233**: p. 613-631.
51. Chang, E.J. and M.R. Maxey, *Unsteady flow about a sphere at low to moderate Reynolds number. Part 1. Oscillatory motion.* Journal of Fluid Mechanics, 1994. **277**: p. 347-379.
52. Chang, E.J. and M.R. Maxey, *Unsteady flow about a sphere at low to moderate Reynolds number. Part 2. Accelerated motion.* Journal of Fluid Mechanics, 1995. **303**: p. 133-153.
53. Basset, A.B., *On the motion of a sphere in a viscous liquid.* Philosophical Transactions of the Royal Society of London. A, 1888: p. 43-63.
54. Czernuszenko, W., *Lagrangian Model for a Single Saltating Grain in the Near-Wall Region of an Open-Channel Flow.* Archives of Hydro-Engineering and Environmental Mechanics, 2014. **60**(1-4): p. 31-50.
55. Odar, F. and W.S. Hamilton, *Forces on a sphere accelerating in a viscous fluid.* Journal of Fluid Mechanics, 1964. **18**(02): p. 302-314.
56. Crowe, C., J. Chung, and T. Troutt, *Particle mixing in free shear flows.* Progress in energy and combustion science, 1988. **14**(3): p. 171-194.
57. Mei, R. and R.J. Adrian, *Flow past a sphere with an oscillation in the free-stream velocity and unsteady drag at finite Reynolds number.* Journal of Fluid Mechanics, 1992. **237**: p. 323-341.
58. Loth, E., *Particles, drops and bubbles: Fluid dynamics and numerical methods*. 2010, University of Illinois at Urbana-Champaign & University of Virginia. Book Draft for Cambridge University Press. Available on (May 7, 2010): http://www.ae.illinois.edu/loth/CUP/Loth.htm.
59. Lawrence, C.J. and R. Mei, *Long-time behaviour of the drag on a body in impulsive motion.* Journal of Fluid Mechanics, 1995. **283**: p. 307-327.

60. Lovalenti, P.M. and J.F. Brady, *The force on a sphere in a uniform flow with small-amplitude oscillations at finite Reynolds number.* Journal of Fluid Mechanics, 1993. **256**: p. 607-614.
61. Kim, I., S. Elghobashi, and W.A. Sirignano, *On the equation for spherical-particle motion: effect of Reynolds and acceleration numbers.* Journal of Fluid Mechanics, 1998. **367**: p. 221-253.
62. Rostami, M., et al., *Can the history force be neglected for the motion of particles at high subcritical Reynolds number range?* International Journal of Engineering Transactions B Applications, 2006. **19**(1): p. 23.
63. Moorman, R.W., *Motion of a spherical particle in the accelerated portion of free fall*. 1955, University of Iowa.
64. Ten Cate, A., et al., *Particle imaging velocimetry experiments and lattice-Boltzmann simulations on a single sphere settling under gravity.* Physics of Fluids (1994-present), 2002. **14**(11): p. 4012-4025.
65. Michaelides, E.E. and A. Roig, *A reinterpretation of the Odar and Hamilton data on the unsteady equation of motion of particles.* AIChE Journal, 2011. **57**(11): p. 2997-3002.
66. Gondret, P., M. Lance, and L. Petit, *Bouncing motion of spherical particles in fluids.* Physics of Fluids, 2002. **14**(2): p. 643-652.
67. Taneda, S., *Experimental investigation of the wake behind a sphere at low Reynolds numbers.* Journal of the Physical Society of Japan, 1956. **11**(10): p. 1104-1108.
68. Dey, S., *Entrainment threshold of loose boundary streams*, in *Experimental Methods in Hydraulic Research*. 2011, Springer. p. 29-48.
69. Chanson, H., *Hydraulics of open channel flow*. 2004, Oxford: Butterworth-Heinemann.
70. Diplas, P., et al., *The role of impulse on the initiation of particle movement under turbulent flow conditions.* Science, 2008. **322**(5902): p. 717-720.
71. Papanicolaou, A.N., et al., *Sediment transport modeling review—Current and future developments.* Journal of Hydraulic Engineering, 2008. **134**(1): p. 1-14.
72. Bai, J., H. Fang, and T. Stoesser, *Transport and deposition of fine sediment in open channels with different aspect ratios.* Earth Surface Processes and Landforms, 2013. **38**(6): p. 591-600.
73. Zedler, E.A. and R.L. Street, *Sediment transport over ripples in oscillatory flow.* Journal of Hydraulic Engineering, 2006. **132**(2): p. 180-193.
74. Milioli, C.C. and F.E. Milioli, *On the accuracy of two-fluid model predictions for a particular gas–solid riser flow.* Applied Mathematical Modelling, 2010. **34**(3): p. 684-696.
75. Jha, S.K. and F.A. Bombardelli, *Modeling the diffusion and transport of suspended sediment in open channels, using two-phase flow theory*, in *Modelling and Simulation of Diffusive Processes*, S.K. Basu and N. Kumar, Editors. 2014, Springer: Gewerbestrasse. p. 51-68.
76. Chiodi, F., P. Claudin, and B. Andreotti, *A two-phase flow model of sediment transport: Transition from bedload to suspended load.* Journal of Fluid Mechanics, 2014. **755**: p. 561-581.
77. Maurin, R., J. Chauchat, and P. Frey, *Dense granular flow rheology in turbulent bedload transport.* Journal of Fluid Mechanics, 2016. **804**: p. 490-512.
78. Exner, F.M., *Uber die wechselwirkung zwischen wasser und geschiebe in flussen.* Akademie der Wiss in Wien, Math-Naturwissenschafliche Klasse, Sitzungsberichte, Abt IIa, 1925. **134**: p. 165-203. (in German).

79. Paola, C. and V. Voller, *A generalized Exner equation for sediment mass balance.* Journal of Geophysical Research: Earth Surface, 2005. **110**(F4).
80. Charru, F., B. Andreotti, and P. Claudin, *Sand ripples and dunes.* Annual Review of Fluid Mechanics, 2013. **45**: p. 469-493.
81. Sotiropoulos, F. and A. Khosronejad, *Sand waves in environmental flows: Insights gained by coupling large-eddy simulation with morphodynamics.* Physics of Fluids, 2016. **28**(2): p. 021301.
82. Doré, A., et al., *Numerical modeling of subaqueous sand dune morphodynamics.* Journal of Geophysical Research: Earth Surface, 2016. **121**(3): p. 565-587.
83. Zhao, M., L. Cheng, and Z. Zang, *Experimental and numerical investigation of local scour around a submerged vertical circular cylinder in steady currents.* Coastal Engineering, 2010. **57**(8): p. 709-721.
84. Wang, H.-W., H.-Y. Lee, and P.-N. Lee, *Three-dimensional saltating processes of multiple sediment particles.* International Journal of Sediment Research, 2009. **24**(1): p. 16-32.
85. Jiang, Z. and P. Haff, *Multiparticle simulation methods applied to the micromechanics of bed load transport.* Water resources research, 1993. **29**(2): p. 399-412.
86. Drake, T.G. and J. Calantoni, *Discrete particle model for sheet flow sediment transport in the nearshore.* Journal of Geophysical Research: Oceans (1978–2012), 2001. **106**(C9): p. 19859-19868.
87. McEwan, I. and J. Heald, *Discrete particle modeling of entrainment from flat uniformly sized sediment beds.* Journal of Hydraulic Engineering, 2001. **127**(7): p. 588-597.
88. Chang, Y.S. and A. Scotti, *Entrainment and suspension of sediments into a turbulent flow over ripples.* Journal of turbulence, 2003. **4**(19): p. 1-22.
89. Chang, Y.S. and A. Scotti, *Turbulent convection of suspended sediments due to flow reversal.* Journal of Geophysical Research: Oceans (1978–2012), 2006. **111**(C7).
90. Durán, O., B. Andreotti, and P. Claudin, *Numerical simulation of turbulent sediment transport, from bed load to saltation.* Physics of Fluids, 2012. **24**(10): p. 103306.
91. Escauriaza, C. and F. Sotiropoulos, *Lagrangian model of bed-load transport in turbulent junction flows.* Journal of Fluid Mechanics, 2011. **666**: p. 36-76.
92. Nabi, M., et al., *Detailed simulation of morphodynamics: 2. Sediment pickup, transport, and deposition.* Water resources research, 2013. **49**(8): p. 4775-4791.
93. Nabi, M., et al., *Detailed simulation of morphodynamics: 3. Ripples and dunes.* Water resources research, 2013. **49**(9): p. 5930-5943.
94. Kim, H.S., et al., *Numerical investigation of local scour at two adjacent cylinders.* Advances in Water Resources, 2014. **70**: p. 131-147.
95. Schmeeckle, M.W., *The mechanics of bedload sediment transport*, in *Department of Geography*. 1998, Department of Geography, University of Colorado at Boulder.
96. Schmeeckle, M., *The role of velocity, pressure, and bed stress fluctuations in bed load transport over bed forms: Numerical simulation downstream of a backward-facing step.* Earth Surface Dynamics, 2015. **3**(1): p. 105.
97. Nelson, J.M., et al., *Role of near-bed turbulence structure in bed load transport and bed form mechanics.* Water Resources Research, 1995. **31**(8): p. 2071-2086.
98. Vowinckel, B., T. Kempe, and J. Fröhlich, *Fluid–particle interaction in turbulent open channel flow with fully-resolved mobile beds.* Advances in Water Resources, 2014. **72**: p. 32-44.

99. Kidanemariam, A.G. and M. Uhlmann, *Interface-resolved direct numerical simulation of the erosion of a sediment bed sheared by laminar channel flow.* International Journal of Multiphase Flow, 2014. **67**: p. 174-188.
100. Ji, C., et al., *Saltation of particles in turbulent channel flow.* Physical Review E, 2014. **89**(5): p. 052202.
101. Sun, R. and H. Xiao, *SediFoam: A general-purpose, open-source CFD–DEM solver for particle-laden flow with emphasis on sediment transport.* Computers & Geosciences, 2016. **89**: p. 207-219.
102. Hilton, J. and P. Cleary. *Comparison of resolved and coarse grain DEM models for gas flow through particle beds*. in *Ninth International Conference on CFD in the Minerals and Process Industries, Melbourne*. 2012.
103. Najjar, F. and D. Tafti, *Study of discrete test filters and finite difference approximations for the dynamic subgrid-scale stress model.* Physics of Fluids, 1996. **8**(4): p. 1076-1088.
104. Patankar, S., C. Liu, and E. Sparrow, *Fully developed flow and heat transfer in ducts having streamwise-periodic variations of cross-sectional area.* ASME J. Heat Transfer, 1977. **99**(2): p. 180-186.
105. Tafti, D.K., *Time-accurate techniques for turbulent heat transfer analysis in complex geometries*, in *Computational Fluid Dynamics and Heat Transfer*, R. Amano and B. Sunden, Editors. 2011, WIT Press: Southampton, UK. p. 217-264.
106. Maxey, M.R. and J.J. Riley, *Equation of motion for a small rigid sphere in a nonuniform flow.* Physics of Fluids, 1983. **26**(4): p. 883-889.
107. Ergun, S., *Fluid flow through packed columns.* Chem. Eng. Prog., 1952. **48**: p. 89-94.
108. Wen, C.Y. *Mechanics of fluidization*. in *Chem. Eng. Prog. Symp. Ser. (in Japanese)*. 1966.
109. Elghannay, H.A. and D.K. Tafti, *Development and validation of a reduced order history force model.* International Journal of Multiphase Flow, 2016. **85**: p. 284-297.
110. Ferrante, A. and S. Elghobashi, *On the physical mechanisms of two-way coupling in particle-laden isotropic turbulence.* Physics of Fluids, 2003. **15**(2): p. 315-329.
111. Gopalakrishnan, P. and D. Tafti, *Development of parallel DEM for the open source code MFIX.* Powder technology, 2013. **235**: p. 33-41.
112. al-Khayat, O., A.M. Bruaset, and H.P. Langtangen, *Particle collisions in a lumped particle model.* Communications in Computational Physics, 2011. **10**(04): p. 823-843.
113. Snider, D., *An incompressible three-dimensional multiphase particle-in-cell model for dense particle flows.* Journal of Computational Physics, 2001. **170**(2): p. 523-549.
114. Washino, K., et al., *Similarity model for DEM simulation of fluidized bed.* Journal of the Society of Powder Technology, Japan, 2007. **44**(3): p. 198-205.
115. Liu, Z., et al., *Use of similarities in CFD-DEM simulation of fluidized bed*, in *14th International Conference on Fluidization - From Fundamentals to Products*. 2013, Engineering Conferences International (ECI): Noordwijkerhout, The Netherlands.
116. Sakano, M., T. Yaso, and H. Nakanishi, *Numerical simulation of two-dimensional fluidized bed using discrete element method with imaginary sphere model.* Japanese Journal of Multiphase Flow, 2000. **14**(1): p. 66-73.
117. Kuwagi, K., *The similar particle assembly (SPA) model, an approach for large-scale discrete element (DEM) simulation.* Fluidization, 2004: p. 243-250.
118. Sakai, M. and S. Koshizuka, *Large-scale discrete element modeling in pneumatic conveying.* Chemical Engineering Science, 2009. **64**(3): p. 533-539.

119. Dietrich, W.E., *Settling velocity of natural particles.* Water resources research, 1982. **18**(6): p. 1615-1626.
120. Elghannay, H.A. and D.K. Tafti, *Sensitivity of numerical parameters on DEM predictions of sediment transport*, in *2nd International Conference on Powder, Granule and Bulk Solids' Innovations and Applications*. 2016: Jaipur, India.
121. Brownlie, W.R., *Prediction of flow depth and sediment discharge in open channels*, in *Department of Civil Engineering*. 1982, Department of Civil Engineering, California Institute of Technology.
122. Bagnold, R.A., *An approach to the sediment transport problem from general physics*. 1966: US government printing office.
123. Meyer-Peter, E. and R. Müller. *Formulas for bed-load transport*. 1948. IAHR.
124. Wong, M. and G. Parker, *Reanalysis and correction of bed-load relation of Meyer-Peter and Müller using their own database.* Journal of Hydraulic Engineering, 2006. **132**(11): p. 1159-1168.
125. Engelund, F. and E. Hansen, *A monograph on sediment transport in alluvial streams*. 1967, Copenhagen: Teknisk Forlag.
126. USACE, *Flume tests made to develop a synthetic sand which will not form ripples when used in movable bed models*, in *Technical Memo*, U.S.W.E. Station, Editor. 1936: U. S. Waterways Experiment Station, Vieksburg, Mississippi.
127. Miller, M.C., I.N. McCave, and P.D. Komar, *Threshold of sediment motion under unidirectional currents.* Sedimentology, 1977. **24**(4): p. 507-527.
128. Dennis, D.J., *Coherent structures in wall-bounded turbulence.* Anais da Academia Brasileira de Ciências, 2015. **87**(2): p. 1161-1193.
129. Jeong, J., et al., *Coherent structures near the wall in a turbulent channel flow.* Journal of Fluid Mechanics, 1997. **332**: p. 185-214.
130. Heathershaw, A. and P. Thorne, *Sea-bed noises reveal role of turbulent bursting phenomenon in sediment transport by tidal currents.* Nature, 1985. **316**(6026): p. 339-342.
131. Rashidi, M., G. Hetsroni, and S. Banerjee, *Particle-turbulence interaction in a boundary layer.* International Journal of Multiphase Flow, 1990. **16**(6): p. 935-949.
132. Dwivedi, A., et al., *Flow structures and hydrodynamic force during sediment entrainment.* Water Resources Research, 2011. **47**(1).
133. Marchioli, C. and A. Soldati, *Mechanisms for particle transfer and segregation in a turbulent boundary layer.* Journal of fluid Mechanics, 2002. **468**: p. 283-315.
134. McEwan, I., et al., *Probabilistic modeling of bed-load composition.* Journal of Hydraulic Engineering, 2004. **130**(2): p. 129-139.
135. Bhuiyan, F., *Stochastic and Deterministic Methods of Computing Graded Bedload Transport*, in *Sediment Transport-Flow and Morphological Processes*. 2011, InTech.
136. Dey, S., *Entrainment Threshold of Loose Boundary Streams*, in *Experimental Methods in Hydraulic Research*, P. Rowinski, Editor. 2011, Springer Berlin Heidelberg. p. 29-48.
137. Capecelatro, J., O. Desjardins, and R.O. Fox, *Numerical study of collisional particle dynamics in cluster-induced turbulence.* Journal of Fluid Mechanics, 2014. **747**: p. R2.
138. Uhlmann, M., *Direct numerical simulation of sediment transport in a horizontal channel*. 2006: Ciemat.
139. Niño, Y., M. García, and L. Ayala, *Gravel saltation: 1. Experiments.* Water resources research, 1994. **30**(6): p. 1907-1914.

140. Schmeeckle, M.W., et al., *Interparticle collision of natural sediment grains in water*. Water Resources Research, 2001. **37**(9): p. 2377-2391.
141. Moreno-Atanasio, R., B. Xu, and M. Ghadiri, *Computer simulation of the effect of contact stiffness and adhesion on the fluidization behaviour of powders.* Chemical engineering science, 2007. **62**(1): p. 184-194.
142. Derksen, J.J., *Simulations of granular bed erosion due to laminar shear flow near the critical Shields number.* Physics of Fluids, 2011. **23**(11): p. 113303.
143. Heald, J., I. McEwan, and S. Tait, *Sediment transport over a flat bed in a unidirectional flow: simulations and validation.* Philosophical Transactions-Royal Society of London Series a Mathematical Physical and Engineering Sciences, 2004. **362**: p. 1973-1986.
144. Basset, A.B., *On the motion of a sphere in a viscous liquid.* Philosophical Transactions of the Royal Society of London. A, 1888. **179**: p. 43-63.
145. Elghannay, H. and D. Tafti, *LES-DEM Simulations of Sediment Transport.* international journal of sediment research, 2017.
146. van Rijn, L.C., *Sediment transport, part II: Suspended load transport.* Journal of hydraulic engineering, 1984. **110**(11): p. 1613-1641.
147. Bagnold, R., *An approach to the sediment transport problem.* General Physics Geological Survey, Prof. paper, 1966.
148. Wong, M. and G. Parker, *The bedload transport relation of Meyer-Peter and Mller overpredicts by a factor of two.* Journal of Hydraulic Engineering, 2006. **132**: p. 1159-1168.
149. Dey, S. and A. Papanicolaou, *Sediment threshold under stream flow: A state-of-the-art review.* KSCE Journal of Civil Engineering, 2008. **12**(1): p. 45-60.
150. Bravo, R., P. Ortiz, and J. Luis Pérez–Aparicio, *Analytical and discrete solutions for the incipient motion of ellipsoidal sediment particles.* Journal of Hydraulic Research, 2017: p. 1-15.
151. Shields, A., *Application of similarity principles and turbulence research to bed-load movement*. 1936, Soil Conservation Service.
152. Kramer, H. *Sand mixtures and sand movements in fluvial models*. in *Proceedings of the American Society of Civil Engineers*. 1934. ASCE.
153. Bravo, R., P. Ortiz, and J. Pérez-Aparicio, *Incipient sediment transport for non-cohesive landforms by the discrete element method (DEM).* Applied Mathematical Modelling, 2014. **38**(4): p. 1326-1337.
154. Fenton, J. and J. Abbott. *Initial movement of grains on a stream bed: The effect of relative protrusion*. in *Proceedings of the Royal Society of London A: Mathematical, Physical and Engineering Sciences*. 1977. The Royal Society.
155. Li, T., et al., *The NETL MFiX Suite of multiphase flow models: A brief review and recent applications of MFiX-TFM to fossil energy Technologies.* Chemical Engineering Science, 2017. **169**: p. 259-272.
156. Chan-Braun, C., *Turbulent open channel flow, sediment erosion and sediment transport*. Vol. 2011. 2012: KIT Scientific Publishing.
157. Luo, K., et al., *Particle-resolved direct numerical simulation of gas–solid dynamics in experimental fluidized beds.* AIChE Journal, 2016. **62**(6): p. 1917-1932.
158. Elghannay, H.A. and D.K. Tafti. *Evaluation of Coarse Graining DEM Using Representative Particle Model*. in *Proceedings of the 7th International Conference on Discrete Element Methods*. 2017. Springer.

159. Elghobashi, S., *On predicting particle-laden turbulent flows.* Applied scientific research, 1994. **52**(4): p. 309-329.
160. Sangani, A.S., D. Zhang, and A. Prosperetti, *The added mass, Basset, and viscous drag coefficients in nondilute bubbly liquids undergoing small-amplitude oscillatory motion.* Physics of Fluids A: Fluid Dynamics, 1991. **3**(12): p. 2955-2970.
161. Li, T., et al., *CFD–DEM study of effect of bed thickness for bubbling fluidized beds.* Particuology, 2012. **10**(5): p. 532-541.
162. Kerst, K., et al., *CFD-DEM simulations of a fluidized bed crystallizer.* Chemical Engineering Science, 2017. **165**: p. 1-13.
163. Hoomans, B., et al., *Discrete particle simulation of bubble and slug formation in a two-dimensional gas-fluidised bed: a hard-sphere approach.* Chemical Engineering Science, 1996. **51**(1): p. 99-118.
164. Alobaid, F., J. Ströhle, and B. Epple, *Extended CFD/DEM model for the simulation of circulating fluidized bed.* Advanced Powder Technology, 2013. **24**(1): p. 403-415.
165. Götz, S., *Gekoppelte CFD-DEM-Simulation blasenbildender Wirbelschichten*. 2006: Shaker.
166. Alobaid, F., *3D Modelling and Simulation of Reactive Fluidized Beds for Conversion of Biomass with Discrete Element Method*. 2013, Technische Universität.
167. Peng, Z., et al., *Influence of void fraction calculation on fidelity of CFD-DEM simulation of gas-solid bubbling fluidized beds.* AIChE Journal, 2014. **60**(6): p. 2000-2018.
168. Rui, S. and X. Heng, *Diffusion-Based Coarse Graining in Hybrid Continuum--Discrete Solvers: Theoretical Formulation and A Priori Tests*. 2014.
169. Chang, Y.S. and A. Scotti, *Turbulent convection of suspended sediments due to flow reversal.* Journal of Geophysical Research: Oceans, 2006. **111**(C7).
170. Müller, C., et al., *Granular temperature: comparison of magnetic resonance measurements with discrete element model simulations.* Powder Technology, 2008. **184**(2): p. 241-253.
171. Tsuji, Y., T. Tanaka, and T. Ishida, *Lagrangian numerical simulation of plug flow of cohesionless particles in a horizontal pipe.* Powder technology, 1992. **71**(3): p. 239-250.
172. Lee, J., *Density waves in the flows of granular media.* Physical Review E, 1994. **49**(1): p. 281.
173. Kuwabara, G. and K. Kono, *Restitution coefficient in a collision between two spheres.* Japanese journal of applied physics, 1987. **26**(8R): p. 1230.
174. Walton, O.R. and R.L. Braun, *Viscosity, granular-temperature, and stress calculations for shearing assemblies of inelastic, frictional disks.* Journal of Rheology, 1986. **30**(5): p. 949-980.
175. Shäfer, J., S. Dippel, and D. Wolf, *Force schemes in simulations of granular materials.* Journal de physique I, 1996. **6**(1): p. 5-20.
176. Stevens, A. and C. Hrenya, *Comparison of soft-sphere models to measurements of collision properties during normal impacts.* Powder Technology, 2005. **154**(2): p. 99-109.
177. Uhlmann, M., *Interface-resolved direct numerical simulation of vertical particulate channel flow in the turbulent regime.* Physics of Fluids (1994-present), 2008. **20**(5): p. 053305.
178. Glowinski, R., et al., *A fictitious domain approach to the direct numerical simulation of incompressible viscous flow past moving rigid bodies: application to particulate flow.* Journal of Computational Physics, 2001. **169**(2): p. 363-426.

179. Haff, P. and B. Werner, *Computer simulation of the mechanical sorting of grains.* Powder Technology, 1986. **48**(3): p. 239-245.
180. Elperin, T. and E. Golshtein, *Comparison of different models for tangential forces using the particle dynamics method.* Physica A: Statistical Mechanics and its Applications, 1997. **242**(3): p. 332-340.
181. Kruggel-Emden, H., S. Wirtz, and V. Scherer, *A study on tangential force laws applicable to the discrete element method (DEM) for materials with viscoelastic or plastic behavior.* Chemical Engineering Science, 2008. **63**(6): p. 1523-1541.
182. Kharaz, A., D. Gorham, and A. Salman, *An experimental study of the elastic rebound of spheres.* Powder Technology, 2001. **120**(3): p. 281-291.
183. Dong, H. and M. Moys, *Experimental study of oblique impacts with initial spin.* Powder technology, 2006. **161**(1): p. 22-31.
184. Di Renzo, A. and F.P. Di Maio, *Comparison of contact-force models for the simulation of collisions in DEM-based granular flow codes.* Chemical Engineering Science, 2004. **59**(3): p. 525-541.
185. Schwartz, S.R., D.C. Richardson, and P. Michel, *An implementation of the soft-sphere discrete element method in a high-performance parallel gravity tree-code.* Granular Matter, 2012. **14**(3): p. 363-380.
186. Mokhtar, M., et al., *Validation of the similar particle assembly (SPA) model for the fluidization of Geldart's group A and D particles.* AIChE Journal, 2012. **58**(1): p. 87-98.
187. Xu, B. and A. Yu, *Numerical simulation of the gas-solid flow in a fluidized bed by combining discrete particle method with computational fluid dynamics.* Chemical Engineering Science, 1997. **52**(16): p. 2785-2809.
188. Kondic, L., *Dynamics of spherical particles on a surface: collision-induced sliding and other effects.* Physical Review E, 1999. **60**(1): p. 751.
189. Panyapiang, T., et al., *Skuba 2012 extended team description*. 2013, RoboCup.
190. Zhou, Y., et al., *An experimental and numerical study of the angle of repose of coarse spheres.* Powder technology, 2002. **125**(1): p. 45-54.
191. Langston, P., U. Tüzün, and D. Heyes, *Discrete element simulation of granular flow in 2D and 3D hoppers: dependence of discharge rate and wall stress on particle interactions.* Chemical Engineering Science, 1995. **50**(6): p. 967-987.
192. David, C.T., et al., *Powder flow testing with 2d and 3d biaxial and triaxial simulations.* Particle & Particle Systems Characterization, 2007. **24**(1): p. 29-33.
193. Thornton, C., S.J. Cummins, and P.W. Cleary, *An investigation of the comparative behaviour of alternative contact force models during inelastic collisions.* Powder technology, 2013. **233**: p. 30-46.
194. Di Maio, F.P. and A. Di Renzo, *Analytical solution for the problem of frictional-elastic collisions of spherical particles using the linear model.* Chemical Engineering Science, 2004. **59**(16): p. 3461-3475.
195. Smith, C.E., *Predicting rebounds using rigid-body dynamics.* ASME Journal of Applied Mechanics, 1991. **58**(3): p. 754-758.
196. Alder, B.J. and T. Wainwright, *Studies in molecular dynamics. I. General method.* The Journal of Chemical Physics, 1959. **31**(2): p. 459-466.
197. Huilin, L., et al., *Prediction of particle motion in a two-dimensional bubbling fluidized bed using discrete hard-sphere model.* Chemical Engineering Science, 2005. **60**(12): p. 3217-3231.

198. Guttenberg, N., *Approximate hard-sphere method for densely packed granular flows.* Physical Review E, 2011. **83**(5): p. 051306.
199. McNamara, S. and W. Young, *Inelastic collapse in two dimensions.* Physical review E, 1994. **50**(1): p. R28.
200. Bannerman, M.N., et al., *Stable algorithm for event detection in event-driven particle dynamics.* Computational Particle Mechanics, 2014. **1**(2): p. 191-198.
201. Pöschel, T. and T. Schwager, *Computational granular dynamics: models and algorithms*. 2005: Springer Science & Business Media.
202. McNeil, W.J. and W.G. Madden, *A new method for the molecular dynamics simulation of hard core molecules.* The Journal of Chemical Physics, 1982. **76**(12): p. 6221-6226.
203. Stratt, R.M., S.L. Holmgren, and D. Chandler, *Constrained impulsive molecular dynamics.* Molecular Physics, 1981. **42**(5): p. 1233-1143.
204. Helland, E., R. Occelli, and L. Tadrist, *Computational study of fluctuating motions and cluster structures in gas–particle flows.* International Journal of Multiphase Flow, 2002. **28**(2): p. 199-223.
205. González, S., D. Risso, and R. Soto, *Extended event driven molecular dynamics for simulating dense granular matter.* The European Physical Journal-Special Topics, 2009. **179**(1): p. 33-41.
206. McNamara, S., E.G. Flekkøy, and K.J. Måløy, *Grains and gas flow: Molecular dynamics with hydrodynamic interactions.* Physical review E, 2000. **61**(4): p. 4054.
207. Lu, L., T. Li, and S. Benyahia, *An efficient and reliable predictive method for fluidized bed simulation.* AIChE Journal, 2017.
208. Ouyang, J. and J. Li, *Particle-motion-resolved discrete model for simulating gas–solid fluidization.* Chemical Engineering Science, 1999. **54**(13-14): p. 2077-2083.
209. Gidaspow, D., *Multiphase flow and fluidization: continuum and kinetic theory descriptions*. 1994: Academic press.
210. Yu, K. and D. Tafti, *Impact model for micrometer-sized sand particles.* Powder Technology, 2016. **294**: p. 11-21.
211. Yu, K., H.A. Elghannay, and D. Tafti, *An impulse based model for spherical particle collisions with sliding and rolling.* Powder Technology, 2017. **319**: p. 102-116.
212. Stronge, W.J., *Impact mechanics*. 2004: Cambridge university press.
213. Timoshenko, S., S. Timoshenko, and J. Goodier, *Theory of Elasticity, by S. Timoshenko and JN Goodier*. 1951: McGraw-Hill book Company.
214. Grant, G. and W. Tabakoff, *Erosion prediction in turbomachinery resulting from environmental solid particles.* Journal of Aircraft, 1975. **12**(5): p. 471-478.
215. Hamed, A., W. Tabakoff, and R. Wenglarz, *Erosion and deposition in turbomachinery.* Journal of propulsion and power, 2006. **22**(2): p. 350-360.
216. Sewall, E.A., et al., *Experimental validation of large eddy simulations of flow and heat transfer in a stationary ribbed duct.* International journal of heat and fluid flow, 2006. **27**(2): p. 243-258.
217. Singh, S., et al., *Sand transport in a two pass internal cooling duct with rib turbulators.* International Journal of Heat and Fluid Flow, 2014. **46**: p. 158-167.
218. Dowd, C., D. Tafti, and K. Yu. *Sand Transport and Deposition in Rotating Two-Passed Ribbed Duct With Coriolis and Centrifugal Buoyancy Forces at Re= 100,000*. in *ASME Turbo Expo 2017: Turbomachinery Technical Conference and Exposition*. 2017. American Society of Mechanical Engineers.

219. Schneider, O., et al. *Investigations of dust separation in the internal cooling air system of gas turbines*. in *ASME Turbo Expo 2003, collocated with the 2003 International Joint Power Generation Conference*. 2003. American Society of Mechanical Engineers.
220. Peterson, B.A., *A Study of Blockage due to Ingested Airborne Particulate in a Simulated Double-Wall Turbine Internal Cooling Passage*. 2015, The Ohio State University.
221. Tafti, D., *Evaluating the role of subgrid stress modeling in a ribbed duct for the internal cooling of turbine blades.* International Journal of Heat and Fluid Flow, 2005. **26**(1): p. 92-104.
222. Shah, A.P., *Development and application of a dispersed two-phase flow capability in a general multi-block Navier Stokes solver*. 2005, Virginia Tech.
223. Shah, A. and D.K. Tafti, *Transport of particulates in an internal cooling ribbed duct.* Journal of Turbomachinery, 2007. **129**(4): p. 816-825.
224. Sakai, M., et al., *Verification and validation of a coarse grain model of the DEM in a bubbling fluidized bed.* Chemical Engineering Journal, 2014. **244**: p. 33-43.
225. Al-Khayat, O., A.M. Bruaset, and H.P. Langtangen, *A lumped particle modeling framework for simulating particle transport in fluids.* Communications in Computational Physics, 2010. **8**(1): p. 115-142.
226. al-Khayat, O., A. Magnus Bruaset, and H. Petter Langtangen, *Particle collisions in a lumped particle model.* Communications in Computational Physics, 2011. **10**(4): p. 823.
227. Kazari, M., et al. *A Study on Conditions for Similarity of Particles Motion in Numerical Simulation of Dense Gas-Solid Two Phase Flow*. in *Proceedings of the 2nd Int. Conf. on Multiphase Flow\'95, Kyoto*. 1995.
228. Kawaguchi, T., et al. *DEM Simulation of 2-D Fluidized Bed using Similarity Model*. in *Discrete Element Methods: Numerical Modeling of Discontinua: Proceedings of the Third International Conference, September 23-25, 2002, Santa Fe, New Mexico, USA*. 2002. American Society of Civil Engineers.
229. Liu, Z., et al., *Use of Similarities in CFD-DEM Simulation of Fluidized Bed.* 2013.
230. Kuwagi, Takeda, and Horio. *The Similar Particle Assemblage (SPA) Model, An Approach to Large Scale DEM Simulation*. in *Fluidization XI*. 2004. Brooklyn, NY 11201, USA: Engineering Conference International.
231. Sakai, M., et al., *Large-scale discrete element modeling in a fluidized bed.* International Journal for Numerical Methods in Fluids, 2010. **64**(10-12): p. 1319-1335.
232. Sakai, M., et al., *Study on a large-scale discrete element model for fine particles in a fluidized bed.* Advanced Powder Technology, 2012. **23**(5): p. 673-681.
233. Hilton, J. and P. Cleary. *Comparison of resolved and coarse grain DEM models for gas flow through particle beds*. in *Proceedings of the Ninth International Conference on CFD in the Minerals and Process Industries*. 2012.
234. BRAUN, M., M. SRINIVASA, and S. GOHEL. *Validation of an Efficient CFD-DEM Model for Large Scale Fluidized Beds*. in *Ninth International Conference on CFD in the Minerals and Process Industries,*. 2012. CSIRO, Melbourne, Australia, 10-12 December 2012.
235. Elghannay, H.A. and D.K. Tafti. *DEM Predictions of NETL Small Scale Challenge Problem*. in *ASME 2014 4th Joint US-European Fluids Engineering Division Summer Meeting collocated with the ASME 2014 12th International Conference on Nanochannels, Microchannels, and Minichannels*. 2014. American Society of Mechanical Engineers.

236. Simpson, T.W., et al., *Comparison of response surface and kriging models in the multidisciplinary design of an aerospike nozzle*. 1998: Institute for Computer Applications in Science and Engineering, NASA Langley Research Center.
237. Chung, H.-S. and J.J. Alonso, *Using gradients to construct cokriging approximation models for high-dimensional design optimization problems.* AIAA paper, 2002. **317**: p. 14-17.
238. Kennedy, M.C. and A. O'Hagan, *Predicting the output from a complex computer code when fast approximations are available.* Biometrika, 2000. **87**(1): p. 1-13.
239. Forrester, A.I., A. Sóbester, and A.J. Keane. *Multi-fidelity optimization via surrogate modelling*. in *Proceedings of the Royal Society of London A: Mathematical, Physical and Engineering Sciences*. 2007. The Royal Society.
240. Han, Z.-H., S. Görtz, and R. Zimmermann, *Improving variable-fidelity surrogate modeling via gradient-enhanced kriging and a generalized hybrid bridge function.* Aerospace Science and Technology, 2013. **25**(1): p. 177-189.
241. Coukuyt, I., T. Dhaene, and P. Demeester, *ooDACE toolbox, a matlab kriging toolbox: getting started.* J Mach Learn Res, 2013. **15**: p. 3183-3186.
242. Gibilaro, L., et al., *On the apparent viscosity of a fluidized bed.* Chemical engineering science, 2007. **62**(1): p. 294-300.
243. Kafui, K., C. Thornton, and M. Adams, *Discrete particle-continuum fluid modelling of gas–solid fluidised beds.* Chemical Engineering Science, 2002. **57**(13): p. 2395-2410.

Appendix A

On the Improvement of CFD-DEM Coarse Graining Predictions

Husam A. Elghannay[1], Kuahai Yu[2], and Danesh K. Tafti[1]

[1]Department of Mechanical Engineering
Virginia Polytechnic Institute and State University
Blacksburg, Virginia 24061

[2]Department of Engineering Mechanics

Henan University of Science and Technology

Luoyang, Henan, China 471023

Citation:

Elghannay, Husam, Kuahai Yu, and Danesh Tafti. "On the Improvement of CFD-DEM Coarse Graining Predictions." ASME 2016 Fluids Engineering Division Summer Meeting collocated with the ASME 2016 Heat Transfer Summer Conference and the ASME 2016 14th International Conference on Nanochannels, Microchannels, and Minichannels. American Society of Mechanical Engineers, 2016.

Abstract

Discrete Element Method (DEM) coupled to Computational Fluid Mechanics (CFD) is a powerful tool for simulating complex multiphase flows. The cost of this Eulerian- Lagrangian description, however, increases with the increase of the number of particles ~O(N_p) which limit its use in natural and industrial scale systems. Efforts to reduce the cost of CFD-DEM capability include reducing the total number of simulated particles by lumping them in larger size representative particles (RP Model). The scaled Representative Particle simulations are less compute intensive compared to the more expensive high fidelity un-scaled/resolved simulations. The prediction accuracy of the RP model, however, decreases as larger scaling factors are used. In the current work, we study the possibility of getting improved results from RP model by using two different techniques. First attempts will be made to identify reasons for reduction in RP model prediction accuracy, then different techniques for improvement of RP model are suggested and tested. In the second part, the ability of the co-kriging surrogate model to improve CFD-DEM predictions by combining many reduced-order RP model simulations with a few high-fidelity unscaled calculations is tested. Appropriate systems are selected to evaluate each method.

Nomenclature

C_D	drag coefficient (-)
d_p	particle diameter (m)
e	coefficient of restitution (-)
f	force per computational cell volume (N/m^3)
F_p	force on particle (N)
g	acceleration of gravity (m/s)
I_p	particle moment of inertia (kg.m^2)
l	scaling factor (-)
m_p	mass of particle (kg)
N_p	number of particles in computational cell (-)
n_{pP}	number of particles lumper in each parcel

p	pressure (N/m^2)
Re	Reynolds number (-)
t	time (s)
T_p	torque on particle (N.m)
u	fluid velocity (m/s)
v_p	particle velocity (m/s)
V_p	particle volume (m^3)
W	smoothing function (-)

Greek letters

β	momentum exchange coefficient ($kg/(m^3.s)$
ε	computational cell void fraction (-)
ρ	density (kg/m^3)
τ	viscous shear tensor (Pa.s)
ω	rotational velocity (s^{-1})
ω_s	free-fall velocity of particle (m/s)
μ	dynamic viscosity (kg/(m.s)

Introduction

Typically, billions of particles exist in most practical/ industrial systems (e.g. fluidized/spouted beds, conveying, mixing and coating of aggregates, milling of mineral rock,); whereas the number of particles that have been included in recent studies have at most been a few million using parallel computing techniques with large number of processors [19, 111, 224]. Several attempts have been made to overcome the computational complexity of CFD-DEM simulations. These range from collecting particles in an averaged Eulerian frame work [113, 225, 226] or using a modified Largangian representation of lumped particles. Two different techniques are employed for Lagrangian representation of lumped particles; in one method increasing the particle size is associated with changing the particle and fluid properties according to similarity laws and in the second approach the physical properties of the particle and fluid are retained.

The use of particles of larger size (also known as parcels or representative particles) instead of a group of smaller/original size particles was first proposed by Kazari et al. in 1995 [227] using a similarity model. The model was validated in a 2-D fluidized bed; however, good agreement was not obtained neither for the pressure drop nor for the bubble behavior [5]. Some investigators [228] studied the limitation of Kazari et al.'s similarity model on a 2-D fluidized bed and hypothesized that the smaller predicted bubble velocity with larger representative particles was because of the unsuitability of the grid size used to correctly calculate the void fractions.

Sakano et al. [116] assumed an imaginary-particle of larger diameter and lower density containing original particles at a specified void fraction. The model was tested on a 2-D fluidized bed with diameters of about 4 and 10 times that of the actual diameter. Results obtained from the imaginary particle model revealed differences in bubble size and expanded bed height above distributor. Better results of bubble size and distribution with the imaginary-particle model were obtained by assuming a modified void fraction for a Face Centered Cubic (FCC) packing structure. The physical meaning of the assumed particle structure was, however, not justified [5].

Wasio et al. [114] used a similarity model in simulating fluidized and spouted beds, in which both the gas and solid densities are modified together with the superficial fluidization velocity. The model was tested in pseudo-3D fluidized bed and spouted bed systems using representative particles up to 13.3 times larger than the original. The model showed reasonable agreement in bubble behavior in the fluidized bed system and the mean bubble size in the spouted bed. In more

recent work Liu et al. [229] used a similarity model which retained the particle density while changing fluid properties. The flow patterns of the fluidized bed showed qualitative agreement when using a scaling factor of up to 16 times the original size. The reported results showed good agreement with experiment for mean bubble velocity and frequency for bubbles sizes larger than 0.15 m.

In 2004, Kuwagi et al. [230] proposed the "similar particle assembly" (SPA) in which groups of the original particles having the same density and chemical composition are replaced in large-sized particles termed "representative particles". Similar to Kazari et al. [227] and Sakano et al.'s work [116] this model did not consider particle-particle interactions and was developed by focusing on the drag force. Validation of the model on a 2-D fluidized bed showed fair agreement indicating the potential of the SPA concept [230]. Sakai & Koshizuka [118] pointed out that simulation results obtained by these models are not always accurate in various gas–solid flow systems because the energy dissipation due to collisions cannot be negligible in many gas–solid flow systems.

This issue was considered in the coarse grain model of Sakai and Koshizuka [118] who extended the modeling approach developed in the SPA model for particles of the same density to particle-particle interaction forces with additional relationship of the rotational motion of the particles. The model validation was considered in two different particulate systems; a pneumatic conveyer [118] and a 2-D fluidized bed [231, 232]. For the 2-D fluidized bed, quantitative comparisons were based on expanded bed height and pressure drop at different superficial velocities by using coarse-graining ratio of two and three. Good agreement was achieved of the selected parameters without reporting quantitative comparisons in bubble size and velocities or model deviations at different flow regimes [5]. More recently, Sakai et al. [224] compared results from DEM simulations using coarse graining ratio of two and three with original size DEM results in fluidized state and fixed bed state to show the adequacy of the coarse grain model. Quantitative agreement in pressure drop and expanded bed height was achieved between coarse grain model simulations using scaling factors of two and three and original DEM simulations and qualitative agreement was observed regarding bubbling and splashing. Results from larger coarse-graining ratio of 5 were then compared to an experiment of a fluidized bed which contained about 29 million particles. Quantitative agreement in pressure drop and expanded bed height was reported between experiment and model using a scaling factor of 5.

Many researchers validated or used the RP model on fluidized bed systems [4, 5, 233, 234], and pneumatic conveying system [118]. The superiority of one model over the others cannot be judged since these models are validated using different systems and by examining different parameters. The RP model used in the current work does not include changing the physical fluid and particle properties, and the collision parameters (namely the particle stiffness). The current work, investigates techniques to obtain enhanced predictions from RP model simulations. Two different strategies are suggested and tested. In the first strategy, efforts are carried out to enhance each RP simulation prediction, whereas in the other strategy, a few unscaled simulations are added to a set of RP model simulations to get improved prediction of the overall trend. In the latter, a co-kriging surrogate model is suggested for use.

The governing equations of the CFD-DEM are presented along with the assumptions and changes required for implementation of the RP model. A brief description of the co-kriging surrogate model is also presented in the next section. The results include presenting a validation case to show the performance of RP model at different scaling factors. Efforts to improve the RP model prediction are presented and evaluated in a separate section. Then the ability of using co-kriging model is tested on two different systems by examining two data sets of results simultaneously.

Materials and Methods

The in-house flow solver GenIDLEST [17] (Generalized Incompressible Direct and Large Eddy Simulation of Turb-ulence) was coupled with an implementation of DEM to solve for individual particle motion for simulating particulate flows. Serial and parallel DEM implementation was validated in previous work [18, 19, 235]. The implementation of RP model to the current CFD-DEM implementation is validated in different systems by the authors, one of which is presented in the current work.

Governing equations

The Eulerian-Lagrangian framework involves solving the volume averaged Naveir-stokes equations derived by Anderson and Jackson [20] for the carrier phase. Model B of Gidaspow is adapted in which the pressure drop is accounted for only by the fluid. The continuous phase is governed by

$$\frac{\partial(\varepsilon\rho)}{\partial t} + \vec{\nabla}.(\varepsilon\rho\vec{u}) = 0 \tag{A.1}$$

$$\frac{\partial(\varepsilon\rho\vec{u})}{\partial t} + \vec{\nabla}.(\varepsilon\rho\vec{u}\vec{u}) = -\vec{\nabla}p + \vec{\nabla}.(\varepsilon\bar{\bar{\tau}}) + \rho\vec{g} - \vec{f}_{drag} \tag{A.2}$$

Where $\varepsilon, \rho, \vec{u}, p, \bar{\bar{\tau}}$ and $\vec{f}_{drag}$ are the volume fraction, density, fluid interstitial velocity, pressure, viscous stress and drag force per unit volume, respectively. The drag force represents the particle fluid interaction and is defined as

$$\vec{f}_{Drag} = \sum_{n=1}^{N_p} \frac{\beta V_p}{(1-\varepsilon)}\left(\vec{u} - \vec{v}_p\right) \tag{A.3}$$

where $\beta, V_p, \vec{u}$ and $\vec{v}_p$ are the momentum exchange coefficient, the particle volume, the average fluid velocity, and the particle velocity, respectively. N_p represents the number of particles in each computational cell. A combination of Ergun and Wen & Yu drag correlation with a blending function to avoid discontinuity is used for the momentum exchange coefficient [21].

$$\beta = W\beta_{Ergun} + (1-W)\beta_{Wen-Yu} \tag{A.4}$$

$$\beta_{Ergun} = 150\mu\frac{(1-\varepsilon)^2}{\varepsilon d_p^2} + 1.75(1-\varepsilon)\frac{\rho}{d_p}\left|\vec{u} - \vec{u}_p\right| \tag{A.5}$$

$$\beta_{Wen-Yu} = \frac{3}{4}C_D\frac{(1-\varepsilon)\varepsilon}{d_p}\rho\left|\vec{u} - \vec{u}_p\right|\varepsilon^{-2.65} \tag{A.6}$$

where W is the blending function given by

$$W = \frac{\tan^{-1}\left(150(\varepsilon - 0.8)\right)}{\pi} + 0.5 \tag{A.7}$$

$$C_D = \begin{cases} 24\left(1.0 + 0.15Re_p^{0.687}\right)/Re_p, & Re_p < 1000 \\ 0.44, & Re_p \geq 1000 \end{cases} \tag{A.8}$$

where Reynolds number Re_p is defined as

$$Re_p = \frac{\varepsilon d_p\left|\vec{u} - \vec{u}_p\right|\rho}{\mu} \tag{A.9}$$

in the above equations d_p represents the particle diameter, C_D is the drag coefficient solid phase, and μ denotes the fluid viscosity.

The motion of each particle is governed by Newton's law of motion

$$m_p \frac{d\vec{v}_p}{dt} = V_p(\rho_p - \rho)\vec{g} + \vec{F}_{p,drag} + \sum \vec{F}_{p,coll} \quad \text{(A.10)}$$

$$I_p \frac{d\vec{\omega}_p}{dt} = \vec{T}_{p,coll} \quad \text{(A.11)}$$

where m_p, I_p and ω_p, are the particle's mass, mass moment of inertial, the angular velocity, respectively. $F_{p,coll}$, and $T_{p,coll}$ stand for the force and torque resulting from the particle collisions with walls or with each other. Soft or hard sphere models are commonly used to model particle-particle interactions in DEM simulations. The soft sphere approach is used to account for multiple interactions occurring at the same time which are predominant in dense fluidized beds. The contact force in the soft sphere model is decomposed into a normal force component and a tangential force component. Normal and tangential force component are modelled using spring-dashpot-slider system. Details of the soft sphere model can be found in [22, 23].

A semi-implicit fractional step method is used to solve the flow field on a non-staggered finite-volume grid. The flow field is advanced in time using calculated void fractions and drag forces from the previous time step. For detailed description about the numerical algorithm and the coupling between the two phases, the reader is referred to [18].

Representative particle model

In the currently used RP model, both the fluid and particle properties are retained while the particle diameter is increased. Figure A.1 shows an unscaled system of particles along with a corresponding representative particle.

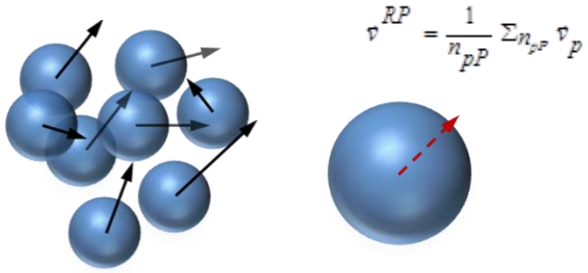

Figure A. 1. Unscaled system of spheres (left) lumped in one representative sphere (right) moving with average velocity.

For simplicity assume a particle moving under drag and buoyancy effects only (recall Eq. A.10). The equation of motion of original particles assuming binary collision between particles

$$m_p \frac{d\vec{u}_p}{dt} = V_p(\rho_p - \rho)\vec{g} + \vec{F}_{p,drag} + \vec{F}_{coll,t} + \vec{F}_{coll,n} \tag{A.12}$$

the LHS represents the rate of change in particle momentum and terms in RHS represent, the net particle weight, the drag force, and the normal and tangential collision forces. The number of particles in each representative particle (or parcel) can be found as

$$n_{pP} = \frac{m_{RP}}{m_p} = \left(\frac{d^{RP}}{d_p}\right)^3 = l^3 \tag{A.13}$$

here; l is the scaling factor (or graining ratio). Taking the sum of both sides over the number of particles inside each computational parcel gives

$$m_p \sum\nolimits_{n_{pP}} \frac{d\vec{v}_p}{dt} = n_{pP} V_p(\rho_p - \rho)\vec{g} + \sum\nolimits_{n_{pP}} \left(\vec{F}_{p,drag} + \vec{F}_{coll,t} + \vec{F}_{coll,n}\right) \tag{A.14}$$

The velocities of the representative particles are assumed to be the average of the original scale particles

$$\vec{v}^{RP} = \frac{1}{n_{pP}} \sum\nolimits_{n_{pP}} \vec{v}_p \tag{A.15}$$

Since the collective mass of the particles inside each parcel is equal to the representative particle mass ($m_{RP}=n_{pP}\, m_p$), Eq. (A.10) we can written as

$$m^{RP}\frac{d\vec{v}^{RP}}{dt} = V^{RP}(\rho_p - \rho)\vec{g} + \sum\nolimits_{n_{pP}} \left(\vec{F}_{p,drag} + \vec{F}_{coll,t} + \vec{F}_{coll,n}\right) \tag{A.16}$$

it is assumed that, when two parcels collide, all original particles within colliding parcels are undergoing the same collision (n_{pP} collisions occur). Such that

$$\vec{F}^{RP}_{coll,n} = \sum_{n_{pP}} \vec{F}_{coll,n} = -k_n \sum_{n_{pP}} \vec{\delta}_n - \eta_n \sum_{n_{pP}} \vec{v}_{p,n} \tag{A.17}$$

assuming the original and representative particles to have the overlap $\delta_n = \delta_n^{RP}$, hence

$$\vec{F}^{RP}_{coll,n} = n_{pP}\left(-k_n\vec{\delta}_n - \eta_n\vec{v}_{p,n}\right) \tag{A.18}$$

such that an equivalent representative particle viscous dissipation and spring constant can be set as

$$k_n^{RP} = n_{pP}k_n \;\&\; \eta_n^{RP} = n_{pP}\eta_n \tag{A.19}$$

then Eq. (A.18) can thus be written as

$$\vec{F}^{RP}_{coll,n} = -k_n^{RP}\vec{\delta}_n - \eta_n^{RP}\vec{u}_n^{RP} \tag{A.20}$$

similar treatment is done to the tangential direction.

As for the rotational motion

$$\frac{d\vec{\omega}_p^{RP}}{dt} = \frac{\vec{T}^{RP}_{p,coll}}{I_p^{RP}} = \frac{\vec{r}_p^{RP} \times \vec{F}^{RP}_{coll,n}}{I_p^{RP}} \tag{A.21}$$

Eq. (A.21) above yields

$$\frac{d\vec{\omega}_p^{RP}}{dt} = \frac{1}{l}\frac{d\vec{\omega}_p}{dt} \tag{A.22}$$

The drag force for particles within each representative particle can be expressed as (recall Eq. A.3)

$$\vec{F}^{RP}_{Drag} = \sum_{n_{pP}} \vec{F}_{Drag} = \frac{\beta V_p}{(1-\varepsilon)} \sum_{n_{pP}} \left(\vec{u} - \vec{v}_p\right) \tag{A.23}$$

the momentum exchange coefficient β is assumed to be constant and evaluated for the original size particles. Assuming the fluid velocity to be the same for both representative particle and original scale particles within them and for uniform size particles, we can write

$$\vec{F}_{Drag}^{RP} = \frac{\beta V^{RP}}{\varepsilon(1-\varepsilon)}(\vec{u} - \vec{v}^{RP}) \quad \text{(A.24)}$$

where the drag force on the representative particle is calculated using the momentum exchange coefficient based on the original particle. Implementing RP model to an existing CFD-DEM solver is described in the work of Hilton and Cleary [233].

For multiphase flows, the volume averaged NS equations require the computational grid to be larger than the particle size to avoid discontinuities and allow for proper voidage averaging. In many instances, the size of the computational grid limits the use of larger scaling factor when using RP model. Although the void fraction can be smoothed over distance larger than the computational grid (e.g., the use of two-grid formulation), excessively smoothing the void fraction can affect the quality of results in cases where the two phases are essentially separated by a distinguished surface (e.g., sediment transport in bed-load regime).

Co-Kriging surrogate Model

Kriging is a popular statistical interpolation method that uses the spatial correlation between given sample points to enhance prediction accuracy. The model first builds a regression function that captures the main trends of the data followed by application of a stochastic Gaussian process to reduce the residuals. In general a kriging model can be expressed as

$$y(x) = \boldsymbol{\beta Y} + Z(x) \quad \text{(A.25)}$$

β is the weights matrix which are chosen to minimize the variance of the estimation error. **Y** is the sample points matrix, and Z(x) is s stationary Gaussian (or stochastic) process that generates localized deviation from the global model [27]. The interpolation of the sampled data is carried out using a maximum likelihood estimation procedure (unlike RMS) which allows for capturing of multiple local extrema [236]. In the original Kriging method, the stationary random process *Z(.)* has a zero mean and a covariance matrix of [237]

$$Z9x) = Cov\left[y\left(x^i\right), y\left(x^j\right)\right] = \sigma^2 R\left(x^i, x^j\right) \quad \text{(A.26)}$$

Here σ^2 is the process variance of *Z(.)* and $R(x_i,x_j)$ is the spatial correlation functions (e.g. Gaussian exponential correlation function). The co-kriging surrogate model is an extension of the kriging model that incorporates multi fidelity sample points to exploit the cross-correlated information contained in the two sets of data to reduce the variance of the estimation error (to enhance the

prediction ability of the surrogate model).The covariant matrix in the direct co-kriging is modified to incorporate gradient information along with function values at sample points. The gradient information in the direct co-kriging method is estimated from the low-fidelity data. In the auto-regression model of Kennedy and O'Hagan [238] the high fidelity data is approximated as the low fidelity data multiplied by a scaling factor plus a Gaussian process $Z_d(.)$ that represents the difference between the high fidelity data and the scaled low fidelity data [239]

$$Z_h(x) = Z_l(x) + Z_d(x) \tag{A.27}$$

Here $Z_l(.)$ and $Z_h(.)$ represent the Gaussian processes of the low and high fidelity data, respectively. The constructed covariance matrices are more complicated than that presented in Eq. (A.24).

Partially co-allocated data is required for estimation of scaling parameter between the two data-sets, however, it is possible to construct co-kriging model with completely non-collocated points by using kriging estimates [239]. These surrogate models were found to be very useful for optimization, visualization, and prototyping, and sensitivity analysis. A detailed description of kriging and co-kriging model formulation and development can be found in [237, 239, 240]. In the current work, Matlab ooDACE (object oriented Design and Analysis of Computer Experiments) Toolbox [241] was used to perform the co-kriging predictions inexpensively.

Results

The results contain three sections. A validation case is first presented to demonstrate the applicability and limitations of the implemented RP model. The selected case is a 3D fluidized bed at specific fluidization velocity. The RP model predictions are performed at two different scaling factors and are compared to unscaled simulation. In a second section, deviations in RP model predictions are discussed and different attempts to bridge these deviations are suggested and tested. Finally, the ability of the co-kriging surrogate model to get improved results by adding few unscaled calculations to RP model results is tested on two different systems. The first system compromises a pseudo-3D fluidized bed at different fluidization velocity. The second system is for a unidirectional open turbulent channel flow at transport stage range from essentially no particle motion to strong suspension.

Validation case

The CFD–DEM solver is validated using a selected case from Muller's experiments [6]. The selected case has a superficial velocity of 0.9 m/s which is three times the minimum fluidization velocity of the beads used. The simulated fluidized bed has a width, depth/transverse thickness, height of 44 mm × 10 mm × 160 mm, respectively. All side walls were set to no slip boundary condition and the top and bottom wall were set to a permeable wall with velocity equal to the fluidization velocity. The three dimensional simulation was conducted with 9240 particles on a grid which is 12×2×32 cells in the x, y and z directions, respectively. Details of the particle properties and modeling parameters are presented in Table A.1. The RP model simulation was conducted using scaling factor of 2 and 3 (8 and 27 particle are lumped in a single representative particle, respectively). All simulations were run for approximately 10 seconds and the results were averaged for the last 5 seconds.

Fig. A.2 shows the averaged voidage and solids velocity in the bed for the three simulations using unscaled particles, scaling factor of 2 and scaling factor of 3. It can be seen that as the scaling factor increases more particles tend to settle down above the bottom boundary (distributer). The averaged solids velocity shows that the mobility of the particles decreases with the increase of the scaling ratio.

Table A. 1. Simulation parameters used for Muller's simulation.

Particles properties	l=1	l=2	l=3
Material	Poppy seeds		
Diameter	1.2 mm	2.4 mm	4.8 mm
Density	1000 kg/m^3		
Friction coeff.	0.1		
Restitution coeff.	0.9 m/s		
Stiffness coeff.	100 N/m	800 N/m	2700 N/m
Fluid properties (Air)			
Density	1.205 kg/m^3		
viscosity	1.8×10^{-5} kg.m^{-1}s^{-1}		

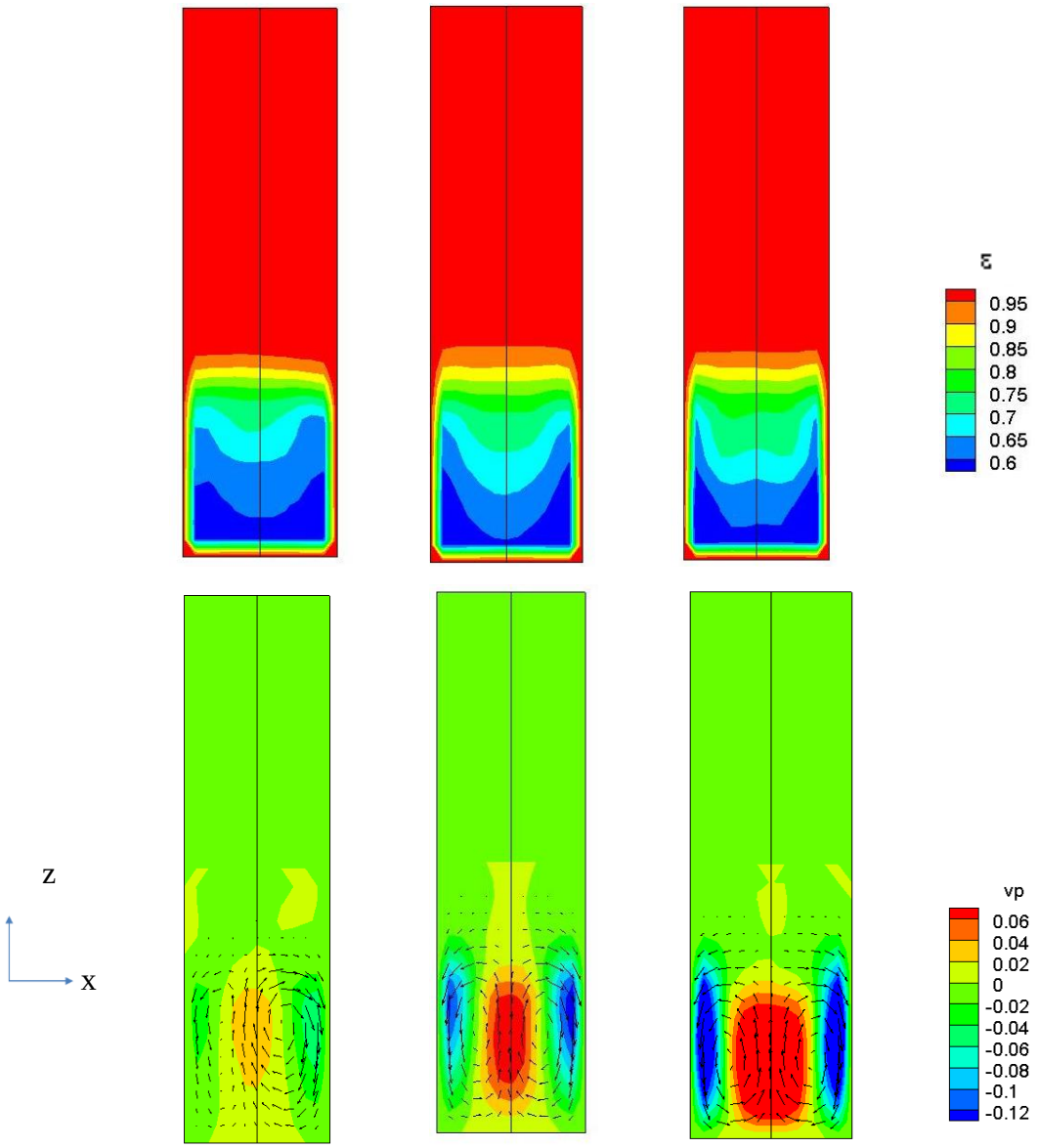

Figure A. 2. Averaged voidage (top) and solids velocity (bottom) for unscaled simulation (right), RP model (l=2; middle) and (l=3; left).

A quantitative comparison is presented in Fig. A.3 for the voidage profile obtained from all current simulations along with both measurements and simulation done by Muller et al. The voidage profiles are shown at two different levels above the distributor plate y=16.4 mm and y=31.2 mm. Muller et al used 2D calculations for the fluid field and a full slip boundary condition for the velocity at side walls. It can be seen that results from current unscaled simulation compare

well with those of Muller et al.'s at both elevations. Both the DEM simulations performed by us and [6] (using original particle size) show good comparison with measurements at height of 16.4 mm. At a higher height of 31.2 mm, both resolved simulations show some discrepancy with the experiments away from the bed center. DEM over predicts the void fraction values closer to the walls. Although the RP model with scaling factor of 2 shows good comparison with unscaled simulation results at both elevations, it can be seen that using a scaling factor of 3 shows notable deviation. With the increase of scaling factor, the void fraction above the distributor is decreased as a result of the presence of more particles.

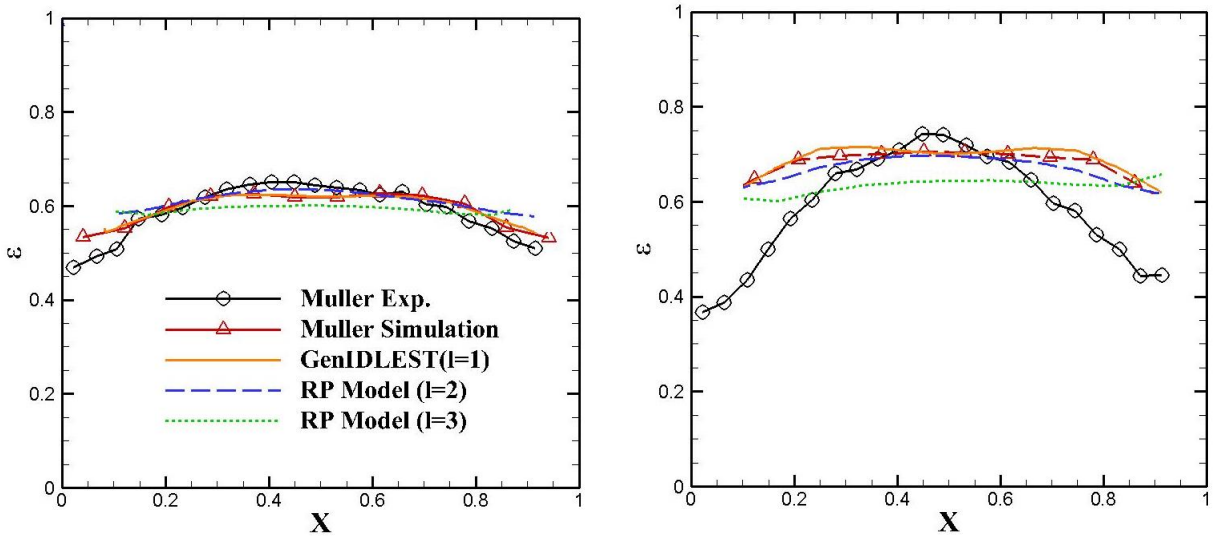

Figure A. 3. Comparison of average void fraction at 16.4 mm above the distributor (left) and 31.2 mm above the distributor (right).

Endeavors to improve RP Model prediction

The identification of reasons for reduction in the accuracy of RP model predictions is not an easy task due to the complex nature of the particle-particle and particle-flow interactions. In this section, efforts will be carried out to isolate main reasons of deviation between the scaled and unscaled system in a fluidized bed system. Instead of studying a complex system, it would be easier to reduce the interactions between the continuous and the dispersed phase. To simplify the task, the continuous and dispersed phases are completely decoupled and the particle-wall interactions from side walls are excluded by considering a periodic domain. In an actual fluidized-bed system simulation, the concentration of the particles will lead to an increase in the interstitial fluid velocity

as well as an increase in the drag force exerted on the particles. In the currently adapted decoupled system, the fluid will not get any feedback from the particles such that the fluid velocity from the distributor remains constant throughout the whole domain. The void fractions are, however, still used in the calculation of the drag force on the particles (Eqs. A.3-A.9). It is suggested that if the model predictions are improved in a decoupled system then they will also improve when both phases are coupled.

Classification of deviation types in RP model

Deviations in RP model prediction can be classified into three categories; firstly differences caused by the main assumption of lumping particles together by which their mobility (e.g. granular temperature) is inherently reduced. This type of deviation may be hard to recover. Secondly, are differences caused by a reduction in the collision frequency in the RP system. This source of deviation becomes significant in systems where energy dissipation determines the behavior of the system (e.g., fluidized beds). Thirdly differences associated with the response of a lumped particle to flow structures and their feed back to the fluid. The former may include instances where a transient flow structure is capable of entraining a number of particles less than the particles actually lumped in the model. This can be the case for erosion of particles from particle bed. The third type also includes the feedback from the particles to the fluid which will not be exactly the same (e.g. difference in the rate of change in void fraction in computational cells). For simplicity in the current work only the first two types will be dealt with and the third type will not be considered.

The system used in the current work is shown in Fig. A.4, where 10164 particles are placed in a periodic fluidized bed system. The top and bottom boundaries are set as permeable walls. The grid is uniform in all directions compromising 6x42x6 cells in the x, y and z directions indicated in Fig. A.4. The particles and fluid considered in the current system are identical to those in Muller et al.'s experiments as listed in Table A.1 with the only exception that the particle stiffness was increased to 1000 N/m. Both the width and breadth of the domain are 22 mm (~$18d_p$) and the overall height of the computational domain is 150 mm (~$128d_p$). The number of particles is selected such that it retains the number density of particles per unit area as of Muller's system. To initialize a simulation; the particles are first arranged above the distributor and allowed to settle under the effect of gravity after which the drag force from a fluidization velocity of 1.5 m/s is activated on the particles. The simulation was advanced in time using a time step of ~$3x10^{-6}$ s to 9 seconds. In

an actual system the currently used fluidization velocity is corresponding to 5x of the minimum fluidization velocity of the beads used.

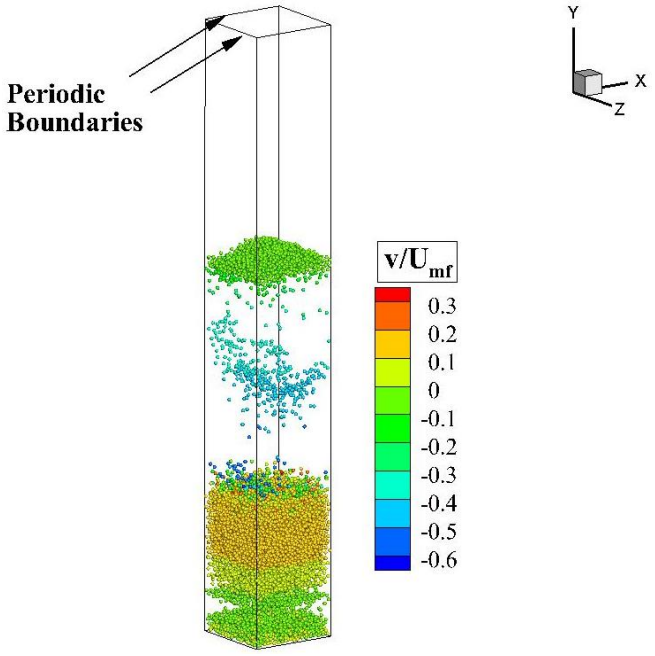

Figure A. 4. The periodic fluidized bed system.

Further simplification of the system can be done by fluidizing ideal particles (using frictionless perfectly elastic particles). The time series and the domain averaged void fractions and vertical solids velocity (~ 6 s) are presented in Figs. A.5 and A.6 respectively.

Fig. 5 presents the time series results of particle transport in the vertical direction ($flux_y = \sum_{N_p} V_p v_p$). Both "Ideal" spheres (*f=0.0 and e=1.0*) and a system of "real" spheres with dissipative properties (*f = 0.1, e=0.9*) are represented. Unscaled simulation (with 10164 particles) and RP model simulation using scaling factor of 2 (1270 particles) are shown. The time series shown in Fig. A.5 is for 3 s of real time. It can be seen from the time series results that the scaled and unscaled ideal systems are in better agreement as compared to the system with real particle properties. Interestingly, it can also be seen that the unscaled system shows near identical repeated pattern of fluidization every 30 time units (~1 s of real time). Animation of the results shows that bubbles/slugs are actually formed even in the case of ideal systems which may not be the case for coupled systems with ideal spheres. The higher positive particle flux corresponds to an up rise of

a packet of particles moving upward (hence a gas slug is formed beneath). As the particles cloud moves upward it starts eroding from the bottom possibly as a results of loss of momentum of lower particles as they push and interact with particles above them. The particles showers from the particle cloud, mix with the particles above the distributor and at a particular instance the existing bed height will be enough to lift another particle cloud by forming a slug/ bubble at a location above the distributor plate. On some occasions, the most recent packet of particles moving upward interacts with the falling remnants of particles from a previous particle cloud. The new particle cloud will, generally, be energetic enough to push it upward again. Such interaction can be observed in the real unscaled system by two successive peaks in Fig. A.5.

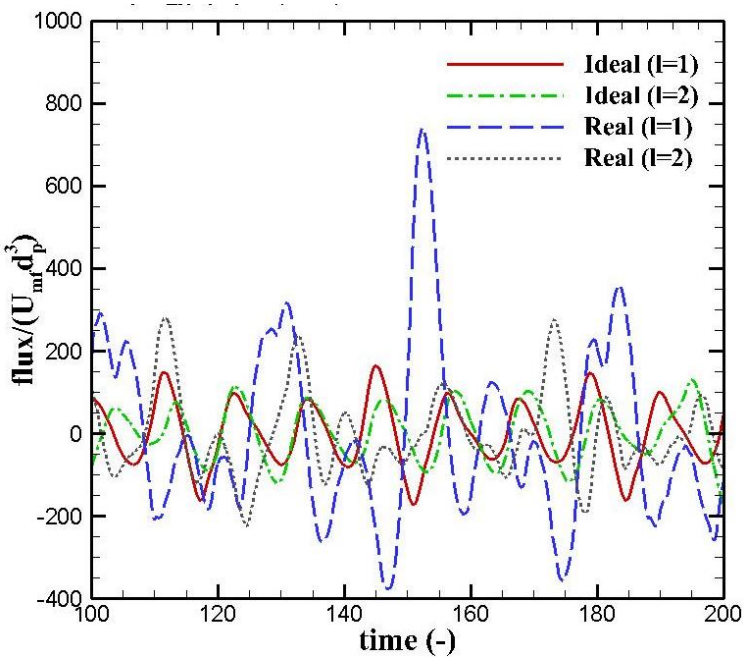

Figure A. 5. Time series of vertical particle flux for decoupled ideal and real systems for both unscaled and scaled simulation.

Fig. A.6 shows the domain averaged results over 6s of real time for both void fractions and vertical solids velocity for both systems with ideal and real –dissipative- particles. The averaged solids velocity is negative because particles will fall (in individual fashion) in velocity higher that their upward velocity. It can be seen that the ideal system is much less energetic as compared to a system with dissipative spheres. Also it can be seen that a difference between the scaled and unscaled system exists even in the case of ideal spheres. This difference in fact represents the loss of mobility due to lumping particles together.

The difference between the scaled and unscaled simulation in the ideal spheres system reflects the first type of deviations discussed earlier. It can be seen that the expanded bed height is approximately the same. The averaged solids velocity is also in agreement but almost double for the unscaled system compared to the scaled system (l =2) at the top part of the bed. For a real system, the difference in bed height between the scaled and unscaled systems is obvious (>25%) whereas the maximum solids velocity in the unscaled system is now ~ 5x of the scaled system. This difference contains both first and second type of differences described earlier and as the dissipative properties are reduced it will retrieve the ideal system.

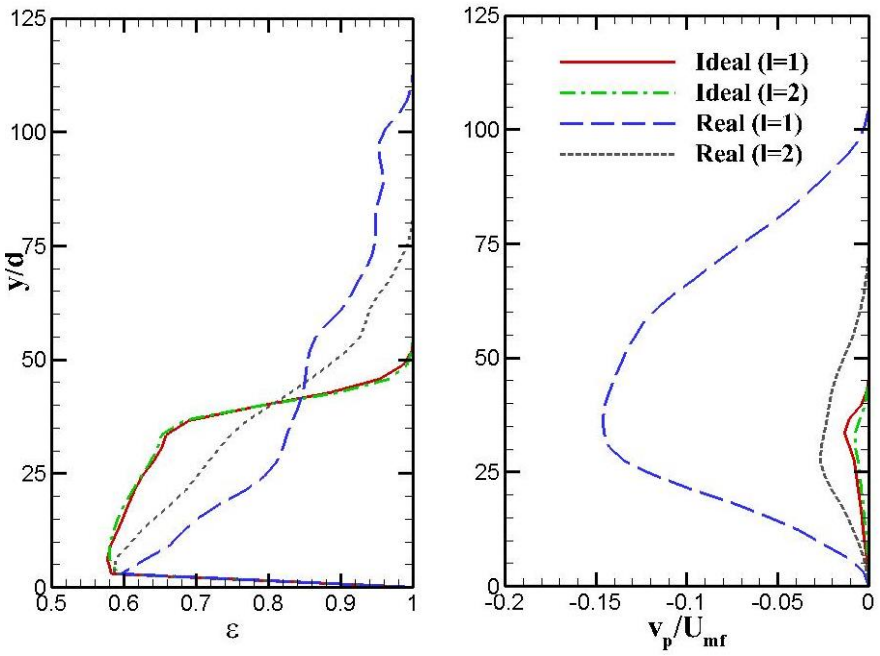

Figure A. 6. Comparison between average void fraction and solids velocity for both ideal and dissipative spheres.

Benyahia and Galvin [4] pointed out that when two parcels (representative particles) collide the number of collisions assumed in the model does not account for the collision between the particles inside each parcel. They suggested reducing the restitution coefficient of the representative particles in order to account for the additional energy loss during collisions. Their formula for the modified restitution coefficient has a singularity that limits its application for finite restitution coefficients to relatively small scaling factors (e.g., for e~0.55 the scaling factor is limited to ~3 or less). To the best of the authors' knowledge, no other technique is reported or used elsewhere

in the literature. It should be mentioned that Benyahia and Galvin's approach targets only losses due to unresolved collisions and doesn't explain or justify differences in the ideal system. In the next section different techniques will be suggested to improve the prediction of RP model results. A comparison with Benyahia and Galvin approach will also be performed. In the following section only a system with dissipative properties will be tested; the potential of improvement is the same for an ideal system.

Attempts to improve RP Model predictions

A number of techniques are suggested to improve the RP model predictions in this section. The proposed methods are tested on the decoupled system in a fully periodic domain described earlier. The main idea is to increase the mobility or energy dissipated through collisions of the RP model particles by using local flow variables. Some techniques which were tested with limited or no success will be mentioned in brief at the end of this section. The suggested methods are conceptual, and hence lack rigid mathematical formulation. As such, parametric testing was performed to study their impact on improving the RP model prediction. Based on our understanding of factors that lead to reduction in model performance, the current techniques try to recover part of the reduction in mobility of the representative particles. A brief introduction of the underlying concept behind each technique is provided in the following sub-sections and the performance of these techniques is discussed in the next section.

Extrapolating of parcel impact velocity

The first method assumes that RP model collisions are not equivalent to unscaled model. For instance if a falling parcel is in collision with a fixed wall the most appropriate velocity to be used as an average is that of a particle located in the center of that parcel. In reality if a falling parcel is in collision with a fixed wall its collision velocity will be that achieved when the particle reaches the surface which is -in fact- less than that of a particle located in the center of the parcel. The representative particle impact velocity should, thus, be extrapolated assuming the particle to be moving at constant acceleration at current time step. To test this technique, equations of motion with constant acceleration are used ($v'=v+2ad_p$). If the particle is found to reverse its motion during the extrapolation process its velocity is set to zero. It was found that if both particles are

extrapolated simultaneously, the qualitative agreement between scaled and unscaled simulations is lost.

Random walk technique

In this method it is assumed that a secondary collision "or force" will exist as a result of unresolved inter-particle collisions. In the current formulation the magnitude of this force is assumed to be proportional to the mobility of the parcels. It is suggested that the random walk force to have the form

$$\vec{f}_{RandWalk} = C_{RW} G\left(\vec{u} - \vec{v}_p\right) \tag{A.27}$$

Where G is a unit variance random number and C_{RW} is a proportionality constant. The constant C_{RW} could be higher for higher scaling factors since the mobility is reduced more in such cases. The above formula suggests that no random force will exist if the particle velocity is equal to the average flow field velocity. The proportionality constant (C_{RW}) used in the current work was set to 0.2. Alternative formulation can also be tried by assuming the random force to be proportional to the change in rms values of velocity (or to the acceleration of the parcel). Similar concept –though different formulation- is used to model the Brownian motion resulting from molecular interactions with sub-micron particles or to account for particle eddy interactions within a RANS framework [58].

Direct increase of energy dissipation though collisions

In this method the collision dissipation is increased by directly changing the velocities used in collision mechanics. The particle velocity is used to calculate the inelastic part of collision (please refer to soft sphere collision model). Since it was found that the mobility is reduced for scaled systems, it is suggested that a higher relative velocity be used when resolving collisions. Namely by changing the relative velocity used in calculating the damping force in the collision. This method is similar in concept to Benyahia and Galvin but will overcome the limitation in their formulation since the change in relative velocity can be performed without restrictions.

Reassessment of drag force

In this method it is hypothesized that the loss in the bed height could be in-part caused by the equivalence in drag between unscaled and scaled system. It is surmised that the momentum

exchange coefficient (or drag coefficient) for the representative particle is less because of using a single value of velocity to calculate it. It is suggested that the results will improve if normal distribution of particle velocity is used. Alternatively, the drag is assumed to be different if a distribution of velocities is given during the calculation of the drag force. In this technique a normal distribution of velocity was given to the particle velocity using the particles' granular temperature as a standard deviation. No significant change of the averaged results was obtained (results will not be presented) possibly because of the small sample of particles included in the current simulation (only 8). It should be mentioned that this technique has over-head calculation in looping through particles in each parcel along with the generation of random number.

Besides the above mentioned technique if both systems are coupled, it is suggested that fluid viscosity could be modified for representative particles simulations to account for sub parcel unresolved feedback from the particles to the fluid which may not be accounted by in the discussed techniques. A similar concept in which the fluid viscosity is modified to account for the particle mobility and interactions is suggested by Gibilaro et al. [242].

Discussions on improvement outcomes

Fig. A.7 shows a comparison of the domain averaged void fraction and solids velocity for dissipative system along with averaged results from extrapolating the particle velocity (Extrp.), random walk (RW), direct increase of the relative collision velocity by 2 and 8 times factor (vpx2 &vpx8) along with using BenYahia and Galvin (B&G) approach. It can be seen that increasing the energy dissipation will improve the bed height predictions without any significant increase in the averaged solids velocity. The extrapolation of particle velocity results in an increase in the bed height and change in solids velocity. The change is however, negligibly small. On the other hand, the Random-walk technique used can be seen to increase the mobility of the particles (since the peak velocity in increased) with the unfavourable result of further decreasing the bed height. For B&G case the restitution coefficient is changed to ~0.73 based on the formula provided in their work (8 particles in each parcel with e=0.9). It can be seen that the suggested treatment shows improved results in terms of both bed height and solids velocity. Similar to the extrapolation technique, the change however, is not significant as compared to the overall difference seen between model and unscaled simulation. It should be mentioned that although both direct dissipation of energy used herein (with double of the solids velocity) and Benyahia and Galvin

formulation yielded the same average results, it was found that the current method will result in an increase in the granular temperature of the particles whereas Benyahia and Galvin formulation will lead to lower granular temperature in the currently used system.

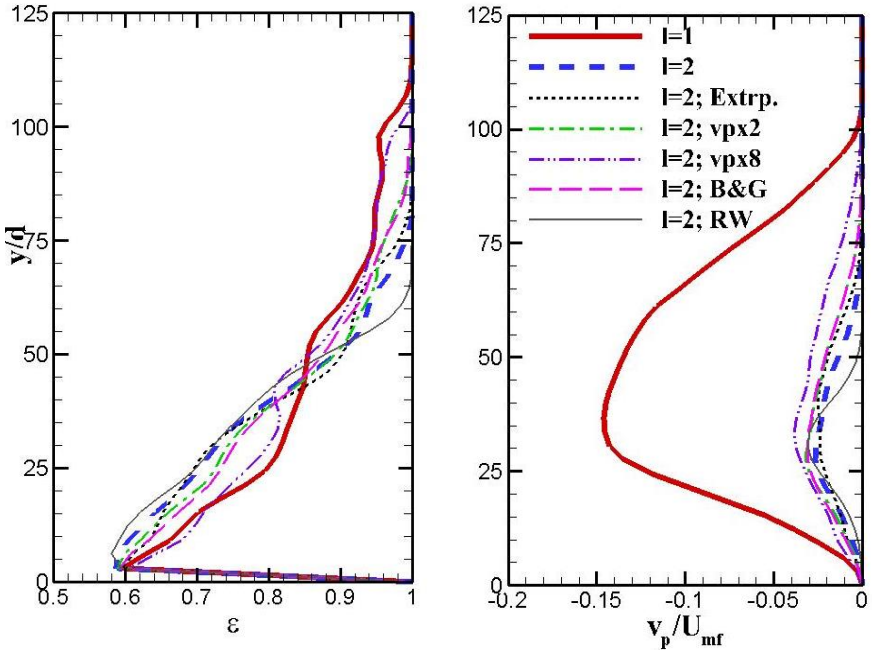

Figure A. 7. Results from extrapolation of particle velocity and random walks concepts.

It should also be mentioned that although individual improvement show small/negligible change in the simulation predictions, a combination of the above mentioned three techniques results in an energetic fluidization with bed height higher than the currently used domain. As such further refinement is required to test the overall impact of a combination of these techniques.

Co-kriging Predictions

In this section we test the capability of the co-kriging surrogate model to get improved predictions by combining few unscaled (high fidelity) predictions with the results obtained from the RP model. Unlike previous techniques which target improving the prediction of individual RP model simulation, this technique is used to get better prediction of an overall trend from a relatively large set of numerical experiments. Two different systems are employed for this purpose, a pseudo-3D

fluidized bed simulation over a wide range of fluidization velocities and a unidirectional turbulent flow over a bed of particles in a channel at different flow regimes from essentially no bed motion to a state of strong suspension. Results from using unscaled particles are available for both systems and are used as the accurate solution to which the surrogate model predictions are compared. For each validation case two different outputs are examined together to ensure that the application of RP model ensures improved prediction for both model outputs. The abscissa is normalized with respect to the maximum value on that axis.

Fluidized bed case

The simulation set by Sakai et al. [232] is selected for the purpose of the evaluation of the co-kriging surrogate model. The selected simulation is a pseudo 3D fluidized bed (symmetric boundary conditions in the y-direction) with no adhesion forces. The calculation domain is a 30 mm x 360 mm rectangular fluidized bed as shown in Figure 8. The system was fluidized with air at 1.0 kg/m^3 density and $1.8x10^{-5}$ Pa-s viscosity. Scaling factors 2 and 3 where tested along with the original size of the particles. The simulation parameters used for the particles are listed in Table 2. More information about the setup of the problem can be found in [118]. For evaluation of the co-kriging surrogate model, only data from using scaling factor of 2 will be considered along with the unscaled data.

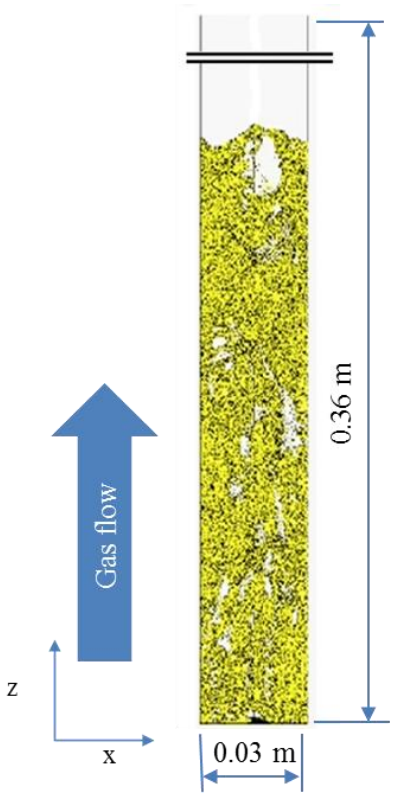

Figure A. 8. Calculations domain for Sakai simulation.

Table A. 2. Simulation parameters of the particles.

Parameter	l =1	l =2	l =3
Diameter (μm)	200	400	600
Rest. Coefficient	0.9	0.9	0.9
Density (kg/m^3)	800	800	800
Friction Coeff.	0.3	0.3	0.3
Stiffness (N/m)	20	160	540
# of particles	90,000	22,500	10,000
Fluid density	1.8×10^{-5} Pa-s		
Fluid viscosity	1.0 kg/m^3		

Fig. A.9 presents both the pressure drop and bed height vs. the fluidization velocity for the pseudo-2D fluidized bed system at different fluidization velocities using scaling factor of 2. The x-axis is

normalized by the value of the maximum fluidization velocity of the data in (=0.05 m/s). Three unscaled (high fidelity) data points are selected to construct the co-kriging model along with the full set of RP model data using scaling factor of 2 (low fidelity). Since the number of low fidelity data points is not large, the number of high fidelity data points used for co-kriging was limited to only 3 points. The current strategy for selecting the data points is to consider two end points along with an intermediate data point. It can be seen from Fig. A.10 that, the co-kriging model shows improved prediction as compared to the kriging model constructed based on the available high fidelity data (broken black line) for both pressure drop and bed height. Although small deviation can be noticed in pressure drop (at u/u_{fmax} ~0.3) the co-kriging can be seen to correctly capture both the qualitative and quantitative values of both parameters. By testing the prediction of the co-kriging model on different set of results it was found that the co-kriging model will result in erratic predictions if the RP model fails to capture the qualitative trend of the unscaled system.

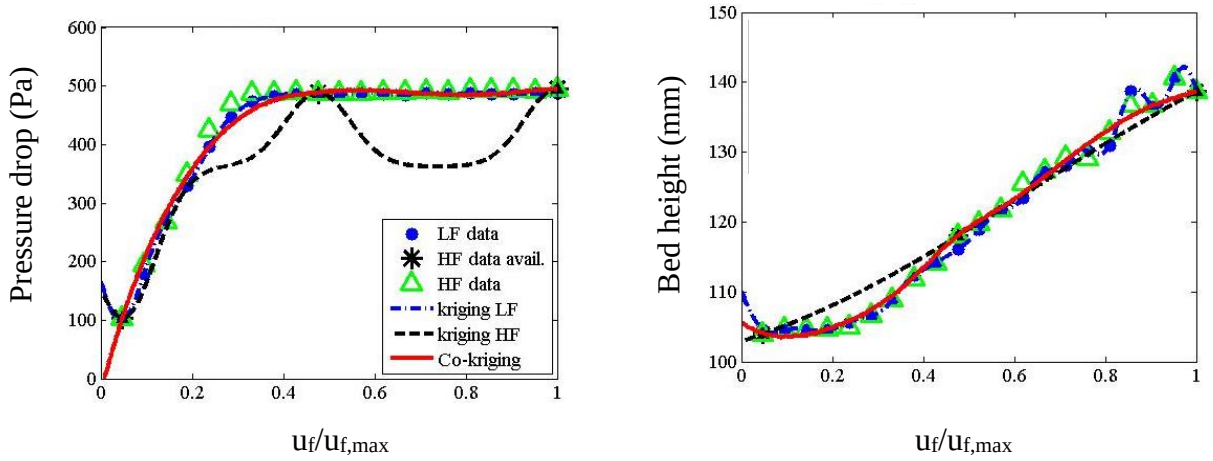

Figure A. 9. Kriging and co-kriging for pressure drop (left) and bed height (right) for a pseudo-2D fluidized bed.

Open turbulent channel flow

A unidirectional open channel flow simulation set by Shchmeeckle [41] is selected. The simulations comprise of ten numerical experiments of medium sand in water. The simulation is performed in a turbulent open channel flow (Fig. A.10) with a velocity slip condition imposed on the top wall and a no slip condition on the bottom wall. The flow is periodic in both stream-wise

and cross-stream directions. The pressure drop that balances the imposed shear stress will determine the value of the mass flowrate inside the channel. Simulation parameters pertaining to particle and fluid properties are provided in

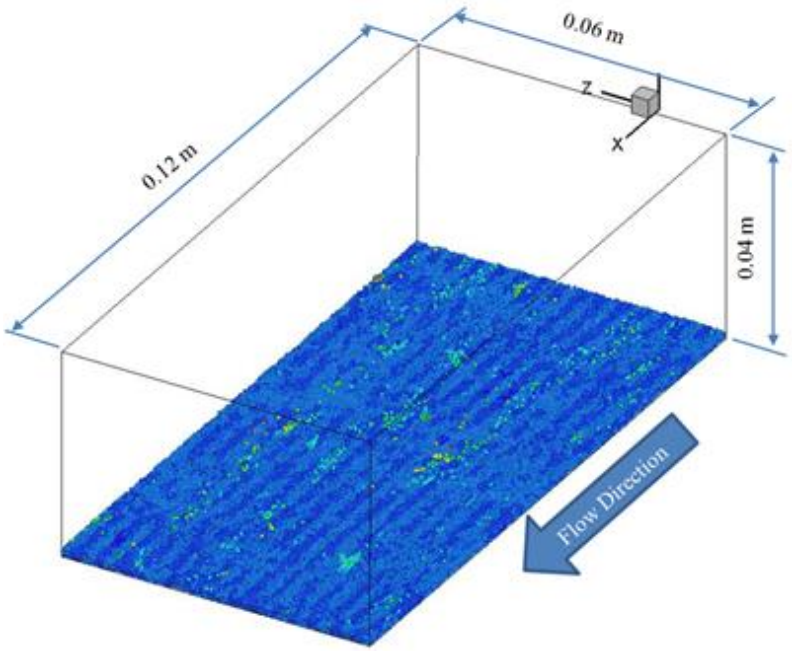

Figure A. 10. Simulation domain of unidirectional flow simulation.

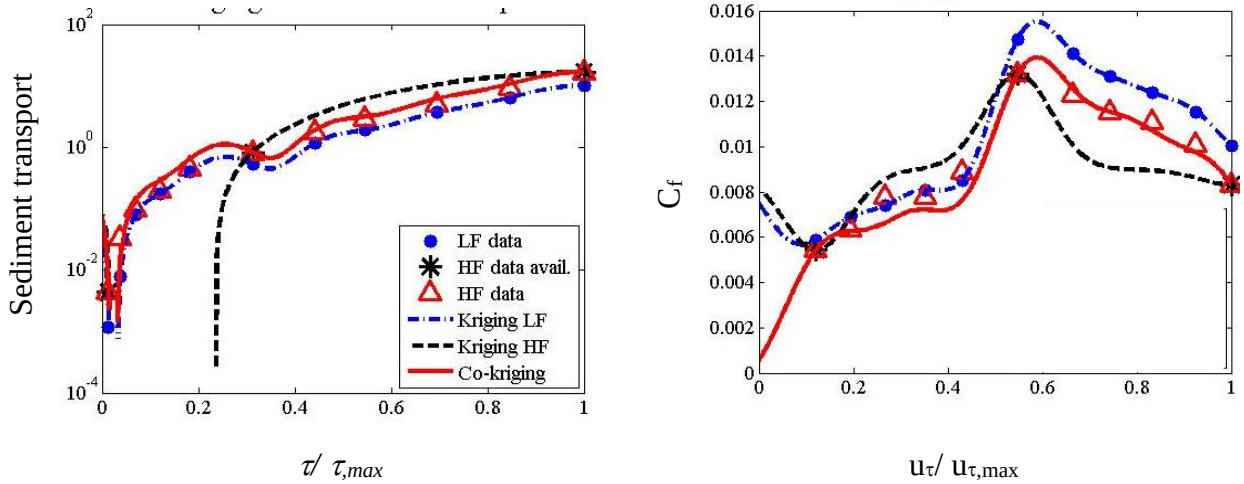

Figure A. 11. Kriging and co-kriging models for sediment transport (left) and friction factor (right) of a psudo-2D fluidized bed.

Fig. A.11 (top) shows the non-dimensional sediment transport (AKA Einstein number) vs. the non-dimensional shear stress (AKA Shields parameter). The x- axis is normalized by the maximum value of the largest Shields' parameter used (θ_{max} ~1.6) for the sediment transport diagram and the maximum non-dimensional velocity for the friction factor ($[u_\tau/\omega]|_{max}$ ~2.0). The strategy of selection of points is similar to described earlier. It can be seen that for the current simulations, although the co-kriging surrogate model results in improved prediction in both sediment transport and friction factor compared to simulation results from RP model by itself in the suspended load regime, some deviations in bedload regime can be observed. Such deviation in bedload regime predictions can be because of the fact that two out of the three selected points belong to the suspended load regime. It should be mentioned that, the prediction can be different if the selected points are changed. To eliminate this dependency, additional HF data points may be necessary.

Conclusions

This paper focuses on improving the RP model prediction. Two different methodologies are presented in the current work. In one method attempts are made to identify the reasons of reduction in RP model predictions and a number of techniques are suggested and tested on a representative system. In the second approach, co-kriging surrogate model is suggested for use for cases which have a relatively large number of experimental data. In this method a few resolved simulations (or experimental data) are added to the full set of results from RP model such that better predictions can be obtained by using co-kriging surrogate model. The latter method is applicable when the RP model is applied for a large number of data points covering a wide range of operation/flow conditions, whereas the first technique focuses on improving accuracy of individual/single simulation.

To test the suggested techniques, a periodic fluidized bed was employed to eliminate collisions with side walls and the continuous and dispersed phases were decoupled. By using some of the suggested techniques it was found that the bed height predictions can be improved significantly. The technique was tested for a scaling factor of 2 where the maximum averaged solids velocity in the domain was found to drop to only about 20% of the unscaled simulation and the averaged bed height was found to be less by ~ 30%. Although the suggested techniques are conceptual and include some parametric evaluation of some parameters, an improvement in RP model predictions was obtained. The improvement in the solids velocity obtained by any individual technique was

found to be marginal relative to the unscaled simulation. The inherent loss of mobility in particles by lumping them together makes it more challenging to get improved results in the averaged solids velocity.

On the other hand, the use of a co-kriging surrogate model showed that it is possible to get improved results if enough coarse grained data is available. The authors also found that co-kriging surrogate model can results in unrealistic behavior/trend in cases where the RP model fails to capture the qualitative trends of the unscaled simulation or experimental data.

Appendix B

Evaluation of Coarse Graining DEM Using Representative Particle Model

Husam A. Elghannay[*] and Danesh K. Tafti[*]

[*]Department of Mechanical Engineering
Virginia Polytechnic Institute and State University
Blacksburg, Virginia 24061

Citation:

Elghannay, Husam A., and Danesh K. Tafti. "*Evaluation of Coarse Graining DEM Using Representative Particle Model.*" International Conference on Discrete Element Methods. Springer, Singapore, 2016.

Abstract

The application of Computational Fluid Mechanics (CFD) coupled to Discrete Element Method (DEM) to simulate industrial and natural scale system requires integrating large number of particles for long times which can make these simulations impractical. One method to reduce the computational cost of DEM simulations is by lumping particles in representative particles of larger diameters to reduce the total number of particles in the simulations. In this work the applicability and limitation of using a representative particle model is evaluated in engineering and natural systems, a fluidized bed system at different fluidization velocities and scaling ratios and a unidirectional open turbulent channel flow in flow regimes ranging from essentially no motion to suspended sediment.

Introduction

Typically, billions of particles are required in most practical/industrial systems (e.g. conveying, milling of mineral rock, fluidized/spouted beds); whereas the number of particles that could be handled in recent studies was at most a few millions using parallel computational techniques with large number of processors [19, 111, 224] . Several attempts have been made to overcome the computational limitation due to number of particles in CFD-DEM simulations by collecting particles in an averaged Eulerian frame work [113, 225, 226] or in a Largangian representation. Two different techniques are used for Lagrangian representation of lumped particles; in one method increasing the particle size is associated with changing the particle and fluid properties according to similarity models [114-116] and in the second approach the physical particle and fluid properties are retained [118, 230].

These models are validated or used on fluidized bed systems [4, 5, 230, 233, 234], spouted beds [114], and pneumatic conveying system [118]. Qualitative and quantitative agreement is reported with the use of different scaling factors (ratio between original particle diameter and representative particle diameter) for up to 16. A scaling factor of 5 allowed for simulating up to 25 Million of particles in a fluidized bed with good quantitative agreement reported. Since these models were validated on different systems and by examining different parameters, it is hard to determine the superiority of one over the other. The currently used model does not include changing the physical fluid and particle properties, some collision parameters, however, are subject to change. The

simulations where performed using the in-house code GenIDLEST [17]. The assumptions and changes required for implementation of the model are described in the next section.

Mathematical Formulation

Governing Equations

The carrier phase is modeled using a volume averaged Navier-Stokes equations derived by Anderson and Jackson [20]. Model-B of Gidaspow [21] in which the pressure drop is accounted for only by the fluid is used in the current work

$$\frac{\partial(\varepsilon\rho)}{\partial t} + \vec{\nabla}.(\varepsilon\rho\vec{u}) = 0 \tag{B.1}$$

$$\frac{\partial(\varepsilon\rho\vec{u})}{\partial t} + \vec{\nabla}.(\varepsilon\rho\vec{u}\vec{u}) = -\vec{\nabla}p + \vec{\nabla}.(\varepsilon\bar{\bar{\tau}}) + \rho\vec{g} - \sum^{n_p} \frac{\vec{F}_{drag}}{\forall_{cell}} \tag{B.2}$$

Where ε, ρ, $\vec{u}$,p and $\bar{\bar{\tau}}$ are the fluid volume fraction in each computational cell, fluid density, fluid interstitial velocity, pressure, and viscous shear stress, respectively. While m_p, $\vec{F}_{drag}$, $\forall_{cell}$ and n_p are the particle mass, the drag force on the particle, the volume of the computational cell, and the number of particles residing in the current computational cell, respectively. The last term on the right-hand side (RHS) of Eq. (B.2) accounts for the interaction forces between dispersed phase and the continuous phase from drag on particles. For cases in which the particle size is larger or comparable to the grid size, a particle grid with appropriate size is mapped over the fluid grid for proper volume averaging and coupling [18]. The particle equation of motion is established by applying Newton's law of motion to each individual particle. Assuming only drag and gravitational effects we can write

$$m_p \frac{d\vec{u}_p}{dt} = V_p(\rho_p - \rho)\vec{g} + \frac{\beta V_p}{\varepsilon(1-\varepsilon)}(\vec{u} - \vec{u}_p) + \sum \vec{F}_{coll} \tag{B.3}$$

The terms on RHS accounts for gravitational effects, drag force, and contact force, respectively. In the current work, a combination of Ergun formula and Wen & Yu drag correlation is used for the momentum exchange coefficient β [21]. The soft sphere method is used to account for multiple contact interactions occurring at the same time which are predominant in dense particulate systems. In the soft sphere model, the contact force is modelled using spring-dashpot-slider

system. More details about soft sphere model can be found in [22, 23]. The rotational motion is governed by

$$\frac{d\vec{\omega}_p}{dt} = \frac{\vec{T}_{p,collision}}{I_p} \tag{B.4}$$

where I_p and ω_p, are the particle's mass moment of inertia, and the angular velocity, respectively. $T_{p,collision}$ stand for the force and torque resulting from the particle contact with wall boundaries or with neighbouring particle.

Representative Particle Model

The number of particles in each representative particle (or parcel) can be found as

$$n_{pP} = \frac{m_{RP}}{m_p} = \left(\frac{d^{RP}}{d_p}\right)^3 = l^3 \tag{B.5}$$

The velocities of the representative particles are assumed to be the average of the original scale particles

$$\vec{u}^{RP} = \frac{1}{n_{pP}} \sum\nolimits_{n_{pP}} \vec{u}_p \tag{B.6}$$

For simplicity assuming only binary collision between two representative particles, from Eqs. (B.3), (B.5) and (B.6) we thus can write

$$m^{RP} \frac{d\vec{u}^{RP}}{dt} = V^{RP}(\rho_p - \rho)\vec{g} + \sum\nolimits_{n_{pP}} \left(\vec{F}_{p,drag} + \vec{F}_{coll,t} + \vec{F}_{coll,n}\right) \tag{B.7}$$

it is assumed that, when two parcels collide, all original particles within the colliding parcels are encountering the same collision (n_{pP} collisions occur). Such that

$$\vec{F}^{RP}_{coll,n} = \sum_{n_{pP}} \vec{F}_{coll,n} = -k_n \sum_{n_{pP}} \vec{\delta}_n - \eta_n \sum_{n_{pP}} \vec{u}_{p,n} \tag{B.8}$$

assuming the original and representative particles to have the same overlap $\delta_n = \delta_n^{RP}$, hence

$$\vec{F}^{RP}_{coll,n} = n_{pP}\left(-k_n \vec{\delta}_n - \eta_n \vec{u}_{p,n}\right) \tag{B.9}$$

such that an equivalent representative particle viscous dissipation and spring constant can be set as

$$k_n^{RP} = n_{pP} k_n \;\&\; \eta_n^{RP} = n_{pP} \eta_n \tag{B.10}$$

It should be mentioned that Eq. (B.10) implies that only the particle stiffness need to be changed for RP model since the viscous dissipation coefficient will follow ($\eta \sim (m_{eff}.k)^{1/2}$), as such the physical coefficient of restitution of both scaled and unscaled systems is the same. Then Eq. (B.8) can be written as

$$\vec{F}_{coll,n}^{RP} = -k_n^{RP} \vec{\delta}_n - \eta_n^{RP} \vec{u}_n^{RP} \tag{B.11}$$

Similar treatment can be done for the tangential direction.

The drag force for representative particles can be expressed as (recall Eq. B.3)

$$\vec{F}_{Drag}^{RP} = \sum_{n_{pP}} \vec{F}_{Drag} = \frac{\beta V_p}{(1-\varepsilon)} \sum_{n_{pP}} (\vec{u} - \vec{u}_p) = \frac{\beta V^{RP}}{(1-\varepsilon)} (\vec{u} - \vec{u}^{RP}) \tag{B.12}$$

where the drag force on the representative particle is calculated using the momentum exchange coefficient based on the original particle.

Simulation Details and Results

Unidirectional Flow Channel

A unidirectional open turbulent channel flow simulation set by Schmeeckle [41] is selected (Fig. B.1). A velocity slip condition imposed on the top wall and a no slip condition on the bottom wall. The flow is periodic in both stream-wise and cross-stream directions. All the simulations were run in a domain of is 0.12x0.06x0.04 m divided into 120, 60, 65 segments in the shown x, y, z directions respectively. The grid is uniformly spaced in both stream-wise (x) and cross stream (z) directions, whereas vertical spacing is 0.2 mm in size in the first 20 cells adjacent to the bottom wall then gradually increased toward the top wall. Simulation parameters pertaining particle properties are listed in Table B.1. A total of ten numerical experiments were selected that cover a range of sediment transport modes ranging from essentially no-motion to strong suspension. Simulations that cover the bed-load regimes were performed using 115,728 particles whereas

simulations that cover the suspended-load were performed with 330,028 particles. The simulations were run for up to 30s of real time and the presented results are averaged for the last 10s.

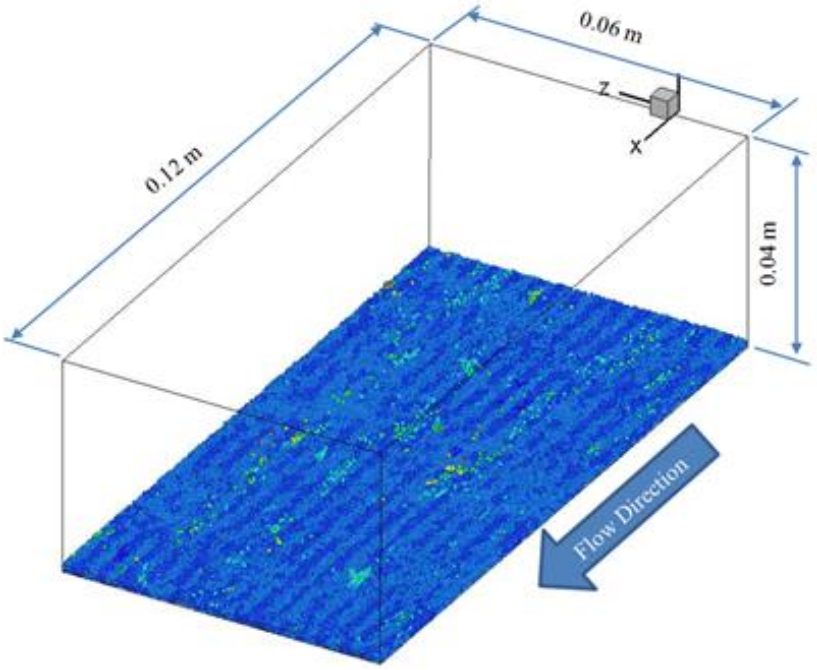

Figure B. 1. Simulation domain for unidirectional open channel flow simulation.

Table B. 1. Numerical parameters for open channel flow.

Parameter	Value
Particle diameter	0.5 mm
Coefficient of restitution	0.01
Particle density	2650 kg/m^3
Friction coefficient	0.6
Stiffness coefficient	100 (N/m)
Time step	5.3x10^{-4} s

Fig. B.2a presents the non-dimensional sediment transport ($q^*= q_{sx}/(u_g.d_p)$) vs. the non-dimensional shear stress ($\tau^*= u_\tau^2/u_g^2$) using unscaled and scaled simulations. Here u_g is a characteristic velocity defined as $u_g = (\rho_p/\rho-1)g.d_p$ and q_{sx} is the volumetric volume flux of particles in the stream direction divided by the surface area of the channel. The first five

experiments are in the bed load regime, in which there is a distinguishable interface between the two phases, compare well with empirical fits for both bedload [148] and total load [125]. The simulations with higher shear stress are in the suspended-load regime since the friction velocity is higher than the estimated free fall velocity for the sediment particles (ω_s~0.057 m/s). In general, good overall agreement is achieved by the scaled simulations ($l=2$) with some under prediction of sediment transport in the suspended load regime. A similar trend exist for the prediction of the friction factor ($C_f = u_\tau^2/u_b^2$), which increases in the bed load regime as the wall shear stress increases, but decreases in the suspended load regime with further increase in wall shear stress (Fig. B.2b).

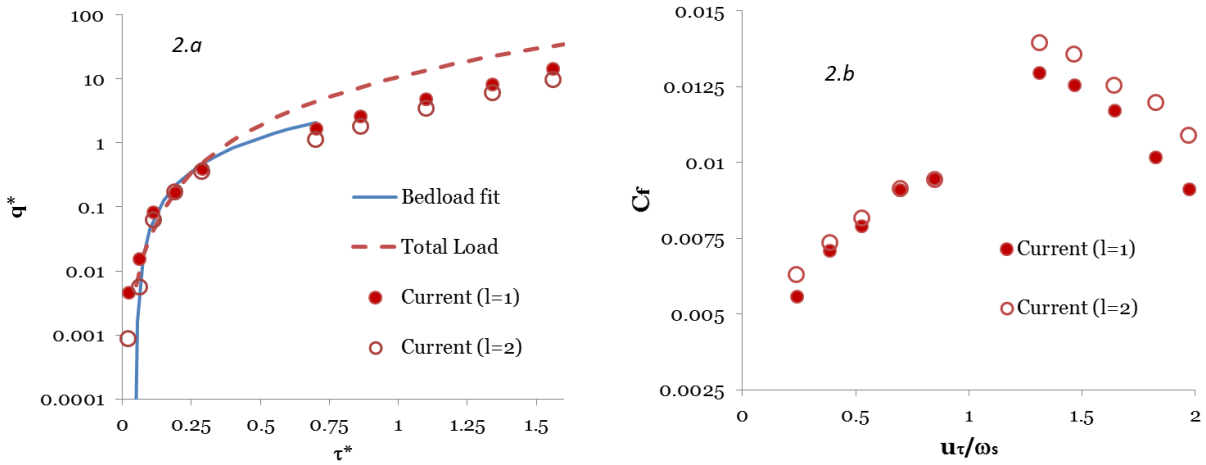

Figure B. 2. Comparison between scaled and unscaled simulations for open channel simulation: a) sediment transport and b) friction factor.

Pseudo-3D Fluidized bed

The selected simulation is pseudo-3D fluidized bed (Fig. B.3) with no adhesion forces set by Sakai et al. [232]. A uniform grid of 10x240 cells was used for the current simulation with symmetric boundary condition in the y-direction. Two scaling factors 2 and 3 where tested along with the original size of the particles. The simulation parameters used for particles are listed in table B.2. In the current study, only 9 simulation points where selected and run for four seconds and the average is considered for the last two seconds.

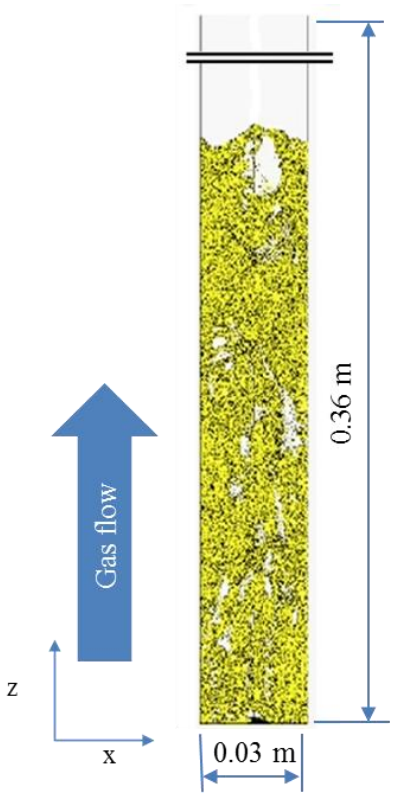

Figure B. 3. Calculations domain for psudu-3D fluidized bed case.

Table B. 2. Simulation parameters for psudu-3D fluidized bed case.

Parameter	l =1	l =2	l =3
Diameter (μm)	200	400	600
Rest. Coefficient	0.9	0.9	0.9
Density (kg/m^3)	800	800	800
Friction Coeff.	0.3	0.3	0.3
Stiffness (N/m)	20	160	540
# of particles	90,000	22,500	10,000
Fluid density	1.8×10^{-5} Pa-s		
Fluid viscosity	1.0 kg/m^3		

Figure B.4a and 3.4b show a comparison of bed-height and pressure drop between the current simulation results and Sakai et al.'s results. It can be seen that a good agreement is found between

original and representative particle model with scaling factors of 2 and 3 in both, the current set of results and Sakai et al.'s results. The bed height predicted by current simulations is higher by about 5 mm as compared to Sakai's simulation. This difference can be due to the presence of air pockets which can exist in the bed [243]. This could result from the use of different model formulations (Model A of Gidaspow is used by Sakai versus Model B used in this work). Good agreement in pressure drop results is achieved between current simulation and those of Sakai's. When the superficial velocity reaches the minimum fluidization velocity, the pressure drop reaches approximately constant value which is corresponding to the weight of the bed. The minimum fluidization velocity is estimated to be at 0.022 m/s [232].

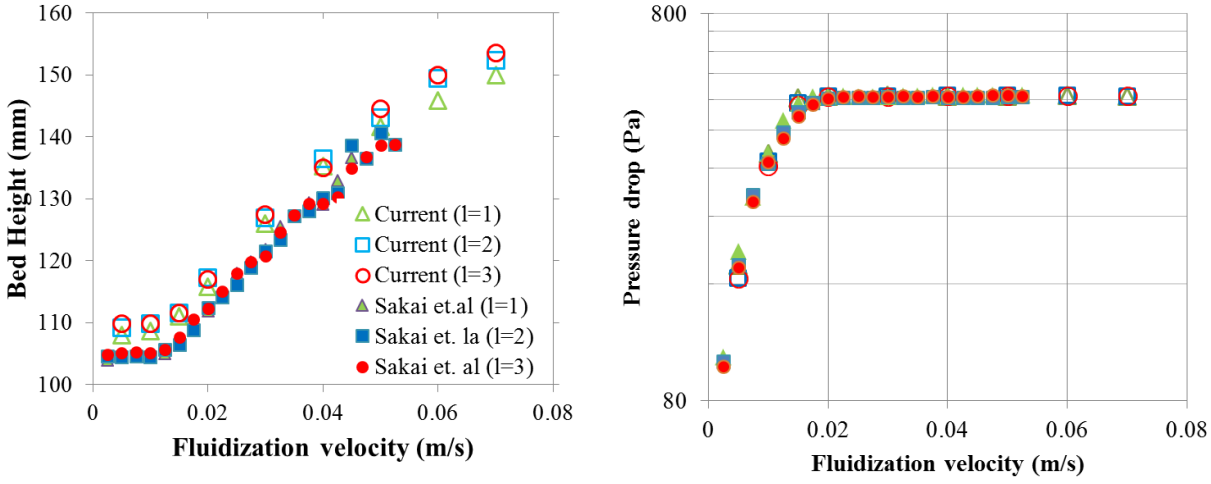

(a) *(b)*

Figure B. 4. Code-to-code comparisons to Pseudo-3D fluidized bed simulation at different scaling factors: a) bed height, b) pressure drop.

Discussions and Conclusions

The RP model has shown to provide good/reasonable predictions as compared to unscaled simulations at wide operation regimes of two different systems. For the sediment transport results it was found that using the same particle grid for the unscaled and scaled simulations resulted in better predictions as compared to using a coarser particle grid proportional to the scaled particle diameter. As seen from results of sediment transport in an open channel, the scaled calculations perform well in the bed load regime but do show some deviations in the suspended load regime. The fluidized bed simulation show better agreement in both pressure drop and bed height,

however, both measures may not be considered to completely describe the fluidization behaviour, the averaged solids velocity is found to decrease with the increase in scaling factor.

Deviations in RP model prediction can be caused by the main assumption of lumping particles together where the particle mobility (e.g. granular temperature) is inherently reduced. Moreover, the RP model formulation does not consider the inter-parcel collisions when two parcels are interacting [4]. This source of deviation becomes significant in systems where energy dissipation determines the behaviour of the system (e.g., fluidized beds). In addition to that there are differences associated with the response of a lumped particle to flow structures (for instances when a transient flow structure is capable of entraining a number of particles less than the particles actually lumped in the model). The feedback from such deviation to the coupled carrier fluid can add to the deviation in predictions.

The DEM speed-up from using RP model is proportional to the scaling factor. For a scaling factor of 2 the fully-3D DEM simulation will speed up with more than eight times since in addition to the number of simulated particles being reduced by 8, the number of collisions are reduced along with communication between processors. The overall speed-up however, will be affected by the carrier fluid simulation time which is not scaled by the RP model. As such the overall speed-up depends on the percentage of DEM time to the overall time. The later can be affected by both the ratio of the number of computational cells to the number particles in the simulation and the convergence behaviour. From the current work it was found that RP model speed-up of more than 5 is more likely achieved when unscaled DEM constitutes about more that 90% in the frame work of MPI parallelization.